CHARACTERIZING IMAGE QUALITY OF SOLAR ULTRAVIOLET IMAGING TELESCOPE ON BOARD ADITYA L1-MISSION AND LONG-TERM STUDY OF THE SUN

A Thesis

Submitted for the Degree of

Doctor of Philosophy (Technology)

Submitted by

SUBHAMOY CHATTERJEE

Department of Applied Optics & Photonics

University College of Technology

University of Calcutta

March 2019

This thesis is dedicated to my Family, Friends and Teachers...

Publications, Talks

Peer Reviewed Journals (Published/Accepted)

1. **Subhamoy Chatterjee**, Dipankar Banerjee, B. Ravindra, *A Butterfly Diagram and Carrington Maps for Century-long Ca II K Spectroheliograms from the Kodaikanal Observatory*, The Astrophysical Journal, Vol. 827:87, 2016.[1]

2. **Subhamoy Chatterjee**, Sudip Mandal, Dipankar Banerjee, *Variation of Supergranule Parameters With Solar Cycles: Results From Century-Long Kodaikanal Digitized Ca II K Data*, The Astrophysical Journal, Vol. 841:70, 2017.[2]

3. **Subhamoy Chatterjee**, Manjunath Hedge, Dipankar Banerjee and B. Ravindra, *Long-term Study of the Solar Filaments from the Synoptic Maps as Derived from H_α Spectroheliograms of the Kodaikanal Observatory*, The Astrophysical Journal, Vol. 849:44, 2017.[3]

4. **Subhamoy Chatterjee**, Dipankar Banerjee, Scott W. McIntosh, Robert J. Leamon, Mausumi Dikpati, Abhishek K. Srivastava and Luca Bertello, *Signature of Extended Solar Cycles as Detected from CaII K Synoptic Maps of Kodaikanal and Mount Wilson Observatory*, The Astrophysical Journal Letters, Vol. 874:1, 2019.

5. Sudip Mandal, **Subhamoy Chatterjee**, Dipankar Banerjee, *Association of Supergranule Mean Scales with Solar Cycle Strengths and Total Solar Irradiance*, The Astrophysical Journal, Vol. 844:24, 2017.

6. Sudip Mandal, **Subhamoy Chatterjee**, Dipankar Banerjee, *Association of Plages with Sunspots: A Multi-Wavelength Study Using Kodaikanal Ca II K and Greenwich Sunspot Area Data*, The Astrophysical Journal, Vol. 835:158, 2017.

[1] This work has been presented in Chapter 5 of this thesis.
[2] This work has been presented in Chapter 6 of this thesis.
[3] This work has been presented in Chapter 7 of this thesis.

7. Sudip Mandal, **Subhamoy Chatterjee**, Dipankar Banerjee, *Solar Active Longitudes from Kodaikanal White-light Digitized Data*, The Astrophysical Journal, Vol. 835:62, 2017.

8. Durgesh Tripathi, A.N. Ramaprakash, Aafaque Khan, Avyarthana Ghosh, **Subhamoy Chatterjee**, Dipankar Banerjee et al., *The Solar Ultraviolet Imaging Telescope on-board Aditya-L1*, Current Science, Vol. 113, No. 4, 2017.[4]

9. Abhishek K. Srivastava, Scott W. McIntosh, N. Arge, Dipankar Banerjee, Mausumi Dikpati, Bhola N. Dwivedi, Madhulika Guhathakurta, B.B. Karak, Robert J. Leamon, Shibu K. Matthew, Andres Munoz-Jaramillo, D. Nandy, Aimee Norton, L. Upton, **Subhamoy Chatterjee**, Rakesh Mazumder, Yamini K. Rao and Rahul Yadav, *The Extended Solar Cycle: Muddying the Waters of Solar/Stellar Dynamo Modeling or Providing Crucial Observational Constraints?*, Front. Astron. Space Sci., 22 November 2018.

10. Mausumi Dikpati, Scott W. McIntosh, **Subhamoy Chatterjee**, Dipankar Banerjee, Ron Yellin-Bergovoy and Abhishek Srivastava, *Triggering The Birth Of New Cycle's Sunspots By Solar Tsunami*, Scientific reports, Vol. 9, 2035, 2019.

Conference proceedings (Publsihed/Accepted)

1. Avyarthana Ghosh, **Subhamoy Chatterjee** et al., *The Solar Ultraviolet Imaging Telescope onboard Aditya-L1*, Proc. SPIE 9905, Space Telescopes and Instrumentation 2016: Ultraviolet to Gamma Ray Vol. 9905, 990503-1, 2016.[5]

Selected Conference Abstracts (talk/poster)

1. **Subhamoy Chatterjee**, Dipankar Banerjee, Manjunath Hegde and B. Ravindra, *Generation of Carrington maps and automated feature detection from Ca II K spectroheliograms of Kodaikanal Solar Observatory*, IAUS 340, Jaipur, February 19-24, 2018.

2. **Subhamoy Chatterjee**, Dipankar Banerjee, Scott W. McIntosh, *Detection and Time-latitude Study of Network Bright Elements from Century-long Kodaikanal Ca II K Data*, IAUS 340, Jaipur, February 19-24, 2018.

[4]Part of this work has been presented in Chapter 2 of this thesis.
[5]Part of this work has been presented in Chapter 2 of this thesis.

3. Manjunath Hegde, **Subhamoy Chatterjee**, Dipankar Banerjee and B. Ravindra, *Long term study of the solar filaments from the Synoptic Maps as derived from H_α Spectroheliograms of Kodaikanal Observatory*, IAUS 340, Jaipur, February 19-24, 2018.

4. **Subhamoy Chatterjee**, Dipankar Banerjee, *Extraction of Features and their Long-term Evolution from Century-long Ca II K data of Kodaikanal Observatory*, ASI meeting, Jaipur, March 6-10, 2017.

5. **Subhamoy Chatterjee** et al., *Butterfly Diagram and Carrington Maps from Century-Long CaK Spectroheliograms*, Accepted in the XXXIV Meeting of Astronomical Society of India Srinagar, India during May 10-13, 2016.

6. **Subhamoy Chatterjee** et al., *Scattering Study for Solar Ultraviolet Imaging Telescope*, International conference titled 'Dynamic Sun 1: MHD Waves and Confined Transients in the Magnetized Atmosphere' organized by IIT-BHU and University of Sheffield, UK held at IITBHU, Varanasi, India during February 22-26, 2016.

7. **Subhamoy Chatterjee** et al., *Tolerance Analysis of Solar Ultraviolet Imaging Telescope Optics*, International conference titled 'Coupling and Dynamics of Solar Atmosphere' held at IUCAA, Pune, India during November 10-14, 2014.

Under Revision/Preparation

1. **Subhamoy Chatterjee**, Manjunath Hedge, Dipankar Banerjee and B. Ravindra, *Detecting Prominences for 10 solar cycles: A study using Kodaikanal, Meudon and Kanzelhohe Data* [under revision][6]

2. **Subhamoy Chatterjee**, Aafaque R. Khan, A.N. Ramaprakash, Avyarthana Ghosh, Durgesh Tripathi, Dipankar Banerjee, *Scattering Analysis and Design of Baffles for the Solar Ultraviolet Imaging Telescope (SUIT) on-board Aditya-L1* [under preparation][7]

3. A. N. Ramaprakash, Durgesh Tripathi, Aafaque R. Khan, Avyarthana Ghosh, **Subhamoy Chatterjee**, P. Sreejith, Dipankar Banerjee, Pravin Chordia, Achim Gandorfer, Natalie Krivova, Dibyendu Nandy, Chaitanya Rajarshi, Sami K. Solanki,

[6]This work has been presented in Chapter 8 of this thesis.
[7]This work has been presented in Chapter 3 of this thesis.

Design and Development of the Solar Ultraviolet Imaging Telescope (SUIT) on board Aditya L1 [under preparation][8]

[8]Part of this work has been presented in Chapter 2 of this thesis.

Abstract

Spatially resolved solar near ultraviolet (NUV, 200-400 nm) observation is important to understand the coupling between different layers of solar atmosphere and its impact on Earth's climate. Again, solar features in NUV regime are crucial in budgeting long-term variation of solar irradiance and probing solar magnetic cycle. Contextually, Solar Ultraviolet Imaging Telescope (SUIT), on-board upcoming ADITYA-L1 mission, attempts full-disc solar imaging with 1.4" resolution in NUV through 11 filters.

Thesis starts with optimization of SUIT optics incorporating design requirements, constraints to generate an off-axis Ritchey-Chretien configuration. Ghost flux minimization produces tilted filter configuration. Afterwards, fabrication, alignment and thermal tolerances are derived constraining image quality. Scattering caused by optical surface micro-roughness and particulate contamination is analysed producing requirements on surface polish and assembly environment. SUIT baffles are designed to restrict scatter from entrance aperture. A flat-field model is developed using light emitting diodes. Also, a plan for SUIT optical alignment is rendered.

Having relevance to SUIT observation, digitized Ca II K and H_α spectroheliograms from Kodaikanal Solar Observatory (KoSO) are analysed. Plages are detected through an automated method from Ca II K series (1907-2007). Carrington maps are generated and correlated with modern magnetic maps for overlapping times confirming locational correspondence between plages and magnetic patches. The Ca II K series is also used in automated detection of supergranules, which represents solar magneto-convection. Time evolution of their morphological parameters near and away from active region depict contrasting correlations with sunspot cycle hinting different dynamos involved. Full disc KoSO H_α images are calibrated for the period 1914-2007 and Carrington maps are generated. A semi-automated technique is developed to detect filaments from Carrington maps. Time-latitude distribution of filaments reveals polar rush and its role in polar field reversal. Prominences are detected through an automated method

for 10 solar cycles from a combined dataset with a major share from KoSO Ca II K disc-blocked series (1906-2002). Results illustrate nonlinear profile of poleward migration for all cycles and may provide constraints in deriving solar meridional flow rate. Thus this long-term study can complement SUIT data pipeline with relevant algorithms and build confidence for future cycle predictions.

Contents

List of Figures

List of Tables

List of Abbreviations

AIA Atmospheric Imaging Assembly

AoI Angle of Incidence

AR Active Region

BBSO Big Bear Solar Observatory

BSDF Bidirectional Scattering Distribution Function

CCD Charge Coupled Device

CME Coronal Mass Ejection

CMOS Complementary Metal-Oxide Semiconductor

CR Carrington Rotation

EIT Extreme-ultraviolet Imaging Telescope

EUV Extreme UltraViolet

FFT Fast Fourier Transform

FG FilterGram

FoV Field of View

FWHM Full Width Half Maxima

HASTA H-Alpha Solar Telescope for Argentina

HMI Helioseismic and Magnetic Imager

KoSO Kodaikanal Solar Observatory

KSO Kanzelhoehe Solar Observatory

LOS Line Of Sight

LSO Lomnicky Solar Observatory

MDI Michelson Doppler Imager

MTF Modulation Transfer Function

MWO Mount Wilson Observatory

NAOJ National Astronomical Observatory of Japan

NASA National Aeronautics and Space Administration

NSO National Solar Observatory

NUV Near UltraViolet

OAD Off Axis Distance

PROBA PRoject for Onboard Autonomy

PSD Power Spectral Density

PSF Point Spread Function

PSPT Precision Solar Photometric Telescope

QR Quiet Region

QS Quiet Sun

RMS Root Mean Square

RoC Radius of Curvature

ROI Region Of Interest

SDO Solar Dynamics Observatory

SG SpectrohelioGram

SIDC Solar Influences Data analysis Center

SoHO Solar and Heliospheric Observatory

STEREO Solar TErrestrial RElations Observatory

SuFI Sunrise Filter Imager

SUIT Solar Ultraviolet Imaging Telescope

SWAP Sun Watcher using Active Pixel system detector and image processing

TSI Total Solar Irradiance

UV UltraViolet

VELC Visible Emission Line Coronagraph

WMO World Metrological Organization

Chapter 1

Introduction and Review of Literature

1.1 Introduction

The Sun, our nearest star, is the very reason that all of us exist. It took birth from interstellar cloud [Priest 2014] and currently falls in the main sequence star category depicted by *Hertzsprung-Russell diagram* [Karttunen 1996]. Solar observation and modelling predicts the Sun to be composed of 6 layers. It fuses hydrogen to helium at the core. The outward pressure caused by the hydrogen fusion balances the inward pressure from gravity and brings stability [Priest 2014]. The energy produced at the core is carried through the radiative zone and passes a convective zone next to finally reach the surface, the photosphere. There lies a thin layer above photosphere which presents plethora of structures, surrounded by the low density solar atmosphere consisting of transition region and corona. To resolve these structures and understand their dynamics, high spatial and temporal resolution observation is essential. Solar observation ranges from imaging to spectroscopy and spectropolarimetry [Priest 2014, Schlichenmaier, R. & Collados, M. 2002]. Solar irradiance is solely responsible for the life on Earth. Thus, it is necessary to understand variability of solar irradiance over different time scales. Also, energetic solar events such as Coronal Mass Ejections (CMEs) can disrupt the communication on Earth affecting our day-to-day life. Among different wavelength regimes, the irradiance variability is higher in ultraviolet (UV) and it al-

lows us to observe the precursors of CMEs namely flares [Hudson 2010]. Space-based observations for UV is necessary because of its absorption by Earth's atmosphere [Gray et al. 2010, Ermolli et al. 2013]. Different space-based solar observatories such as SoHO, STEREO, SDO have been consistently observing the Sun in extreme ultraviolet probing flares, CMEs [Delaboudinière et al. 1995, Jean-Pierre Wuelser 2004, Lemen et al. 2012]. However, solar observation in near ultraviolet (NUV) has been limited though it allows to understand the physics of coupling between different heights of solar atmosphere and has immense effect on Earth's climate dynamics. First attempt to observe the Sun in NUV has been by ballon-borne Sunrise Filter Imager, recording partial field of solar disc [Gandorfer et al. 2011]. However, full-disc synoptic observation for longer time is necessary for recording the spatially resolved irradiance variation [Tripathi et al. 2017] and evolution of different structures such as sunspots, plages, filaments/prominences, supergranular networks etc. Solar magnetic field is the reason behind all these structures at diverse spatial scales [Solanki et al. 2006]. Observation of solar magnetic field through magnetograms started only after 1967 at low resolution in different ground-based observatories namely NSO/Kitt Peak and Wilcox Solar Observatory [Livingston & Harvey 1971, Henney & Harvey 2001, Harvey & Munoz-Jaramillo 2015, Murdin 2000, Bogart et al. 1992]. Currently, the space-based instruments SoHO/MDI and SDO/HMI are recording high resolution magnetograms [Scherrer et al. 1997, Scherrer & HMI Team 2010] . Thus, before 1960's there has been no direct observation of magnetograms. But, different observatories across the globe started observing the sun in different wavelengths from early 1900's probing the magnetic proxies. Kodaikanal Solar Observatory (KoSO) has been one among the most consistent, recording solar images through plates/films in three different wavelengths on almost daily basis over the last century. Kodaikanal historical data have been recently digitised enabling the scientific community to detect different solar features and study their temporal evolution [Ravindra et al. 2013, Mandal et al. 2017, Priyal et al. 2014b, Chatterjee et al. 2016, 2017]. The temporal evolution of those features often produces cycles of period $\approx$ 11 years, named as solar cycle. The solar cycle is a direct consequence of solar magnetic cycle [Hathaway 2015]. Thus, long-term evolution of solar magnetic field can be explored well through those long-term datasets. These datasets have been handled

manually in past to detect the solar features [Ananthakrishnan 1952, 1954, Xu et al. 2018]. Though an experienced human eye can not be replaced by a machine, change of human operators brings inconsistency in detection. Thus, semi-automated and fully automated computer codes are inevitable to avoid human bias in processing long-term datasets. Appropriate algorithms developed for a long-term datasets can be useful in data-pipeline of a telescope imaging the Sun in relevant wavelengths.

In this context, present thesis carries out optical design optimisation with related characterization of an upcoming space telescope aimed to image full disc of the Sun in NUV and presents consistent automated/semi-automated detection of magnetic proxies primarily from Kodaikanal long-term data. Those detected features will provide us indirect evidence for long-term solar magnetic evolution and help in developing data-pipeline to identify similar structures from the NUV telescope.

1.2 Review of Literature

1.2.1 Layers of the Sun

The Sun, is known to be composed of six layers (Figure 1.1). Going away from centre the are namely:

1. **The Core:** Half of solar mass is concentrated at the core with a radius of 150 Mm which is roughly a quarter of solar radius (Figure 1.1). However, 99% of solar energy is generated from the core. This energy is produced majorly by proton-proton chain reaction, fusing hydrogen nuclei to helium nuclei and is responsible for all the heat and light that we receive on the Earth. The process of the energy escape from solar interior is complex. As we can not see inside the Sun, most of the knowledge about solar interior comes from combination of theoretical models and observational facts namely mass, surface temperature, and luminosity (total energy output from the surface). The temperature of the core is as high as 15.7×10^6 kelvin (K).

2. **The Radiative Zone:** Above the core, there lies a region extending till $0.7R_{Sun}$ carrying energy outwards though radiation (Figure 1.1). This region is called

"radiative zone". In this domain of the Sun's interior, the radiation does not travel directly outwards. The plasma density here is very high, average temperature is about 4×10^6 K and the photon gets absorbed and re-emitted countless number of times finally reaching the convective zone through "Random Walk". It takes several hundred thousand years for radiation to make its way from the core to the top of the radiative zone.

3. **The Convective Zone:** By the time the radiation reaches the top of radiative zone ($0.7R_{Sun}$) the temperature drops below 10^6 K. At the point, the magnitude of temperature gradient becomes too high making the plasma too opaque to allow radiation to pass [Priest 2014]. This is how convective instability starts and hot plasma moves up from solar interior through turbulent cells towards the surface (Figure 1.1). At the surface the opacity is insufficient to restrict the escape of radiation and thus plasma expands, radiate and cools down to start descending motion. This cycle continues in the convective zone. Energy transport in the convective zone is much quicker compared to the radiative zone.

4. **The Photosphere:** Above convection zone, there lies the Sun's visible surface, the Photosphere. It only few 100 km thick and has an average temperature of about 5,800 K. It is the region from which most of Sun's visible light is emitted. The most intriguing structures seen in photosphere are dark sunspots (Figure 1.1), bright faculae near active regions at limb and the granulation of 1 Mm scale.

5. **The Chromosphere and Transition Region:** The chromosphere lies just above the photosphere stretching over about 2000 km (Figure 1.1). Through the chromosphere the temperature rises from 4300 K to 25000 K. Through a transition region few 100 km thick above chromosphere the temperature increases exponentially from 25000 K to 10^6 K (Figure 1.2). These two layers are highly non-uniform and dynamic. As can be noted from Figure 1.2, chromosphere can be observed through different spectral lines. The commonly used ones are Ca II K (3933.67Å) and H_α (6563Å). The structures clearly seen in Ca II K are plages, supergranular boundaries/networks whereas dark on-disc filaments or bright off-limb prominences are the features clearly seen in H_α. Apart from sunspots, these structures

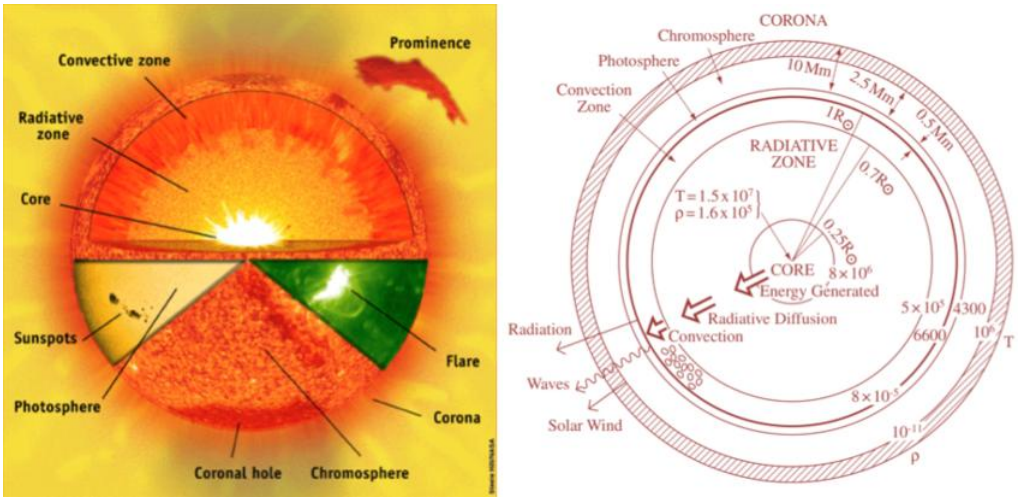

Figure 1.1: *Left panel* shows different layers of the Sun with observed features in those; *Right panel* shows thicknesses, densities (in kg.m^{-3}) and temperatures (in K) of different layers. Layers thicknesses are not shown in scale. The chromosphere and corona boundary, depicted by shaded region, is variable between 2.5 and 15 Mm. Image Source: https://soho.nascom.nasa.gov/classroom/ and Priest [2014]

have immense importance in understanding long-term evolution of solar activity.

6. **The Corona:** Above the transition region, there lies the corona which is dominated by magnetic field. The temperature of corona is about 2×10^6 K. Because of its very low density it was first discovered at eclipse. It has been a mystery for decades how the atmosphere gets so hot. Space observatories such as SoHO, SDO are helping to solve this mystery. Features and events at diverse spatial and temporal scales such as coronal bright points, solar wind, CMEs are observed in corona, some of which dictate the space weather conditions.

1.2.2 Solar Magnetic Cycle

Solar cycle was first discovered through sunspot observation which increases and decreases in number (Figure 1.3) over a period of $\approx$ 11 years and repeats itself [Schwabe 1844, Hathaway 2015]. Same cyclic behaviour was observed through sunspot areas (Figure 1.3). It was soon realised that solar cycle is actually magnetic in nature and is best depicted through magnetic flux. A theoretical framework, called 'solar dynamo theory' was deviced to explain such oscillation of solar magnetic field and this theory was even able to explain the origin of sunspots. Flux-transport dynamo [Dikpati &

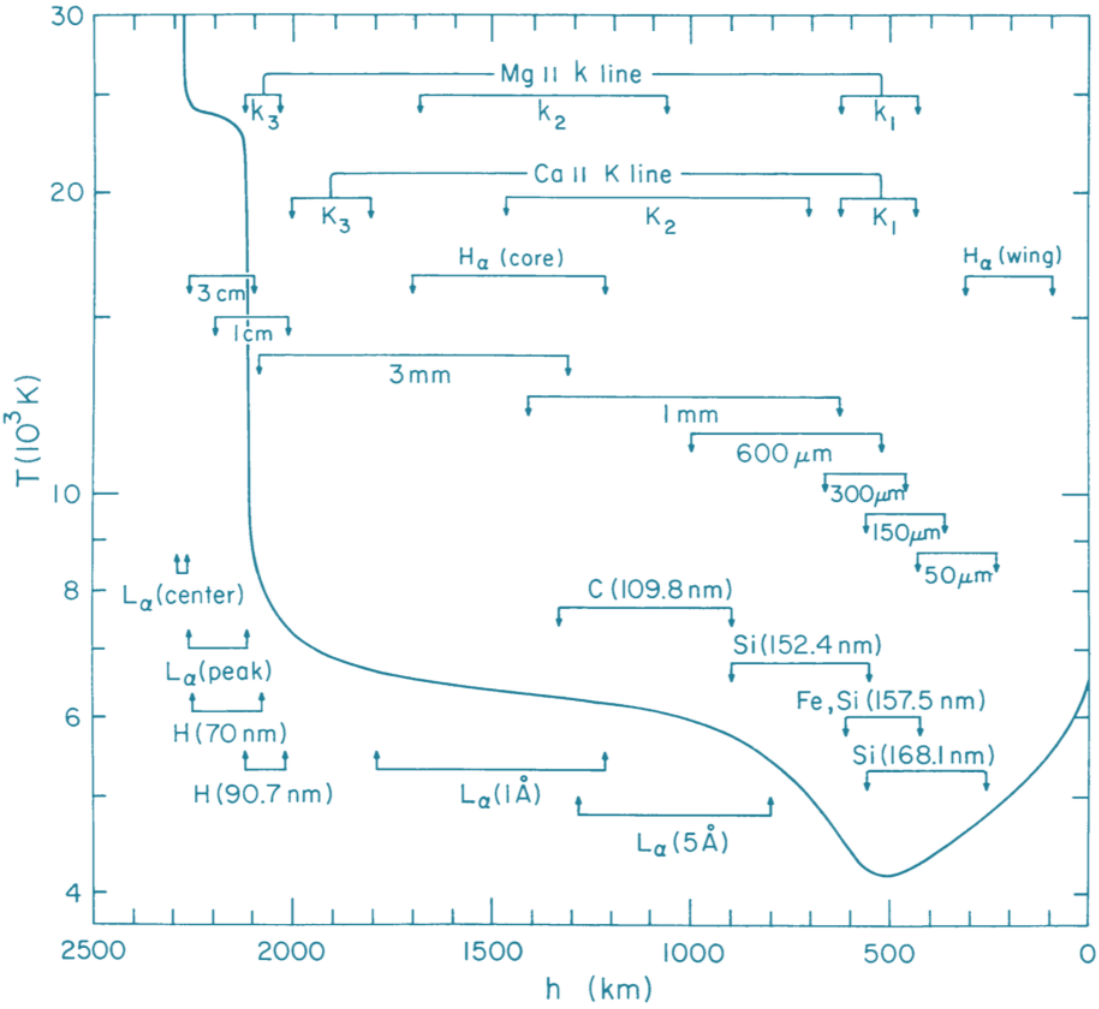

Figure 1.2: Temperature plot of the solar atmosphere. In the plot the formation heights of different spectral lines are indicated. Adapted from: Vernazza et al. [1981]

Gilman 2006, 2007, Choudhuri et al. 2007] has been the most successful in reproducing the observational facts such as equator-ward migration, polar reversal observed in a magnetic butterfly digram (Figure 1.4). This theory considers a tachocline, at the bottom of convection zone, which is the region of concentrated differential rotation. The differential rotation produces strong toroidal field which rises to the solar surface due to magnetic buoyancy ultimately producing sunspots (Figure 1.5). The Babcock Leighton mechanism [Babcock 1961, Leighton 1964] acts at the surface on the decaying sunspots generating the poloidal field. Meridional circulation [Choudhuri et al. 1995] carries this poloidal field poleward which is also observed in the magnetic butterfly diagram. The poloidal field cancels the old poloidal field and builds up new opposite polarity. This poloidal field then brought to the bottom of convection zone being affected by strong differential rotation. This is how the cycle continues (Figure 1.5). Though there has been advancement in dynamo theory to explain many observational facts, but some of the observational features and irregularities in the cyclic behaviour are still not explained completely by dynamo theory. It is thus necessary to understand how consistent are the observations. Regular direct observations of solar magnetic field started only after1970's [Livingston & Harvey 1971, Henney & Harvey 2001, Harvey & Munoz-Jaramillo 2015, Murdin 2000, Bogart et al. 1992]. However, magnetic field is ubiquitous on the Sun and expressed itself through different structures of varied spatial scale [Solanki et al. 2006]. Those are called 'magnetic proxies'. Apart of sunspot there are other magnetic proxies such as plages, filaments/prominences which were regularly observed from different places across the globe from early 1900's. Thus, those records are extremely important to understand solar magnetic evolution for several cycles strengthening the observational inputs for theoreticians.

1.2.3 Magnetic Proxies

1.2.3.1 Sunspots

Sunspots are the areas of intense magnetic field. It appears dark because of the inhibition of energy transport from interior by magnetic field. It is cooler by 1000 K to 3000 K with respect to surrounding Quiet Sun. Sunspots occur in pairs that have magnetic

fields pointing in opposite directions being modelled by foot points of magnetic flux tubes. A typical sunspot consists of a dark umbra, surrounded by a fainter penumbra. An average sunspots is of the same size as the Earth (Figure 1.6). As already described, the solar cycle was first discovered through sunspot counts. Later the same behaviour was found from sunspot area and magnetic flux in sunspots. The equator-ward pattern of magnetic butterfly is reproduced also by sunspots. Sunspots appear first at about 30° latitude and slowly migrate towards equator [Hathaway 2015]. They serve as excellent proxies for the study of long-term variations of solar magnetic evolution, as sunspot observations are available for past 400 years. It is known that flares are precursors of CMEs which are known as drivers of space weather condition. It has been observed that sunspot activity is positively correlated with flare events. Thus, also from space climate perspective sunspots play crucial role. Historically, low sunspot activity has been correlated with 'little ice age' on Earth known as "maunder minimum". Thus, it is apparent that Earth's climate is affected by sunspot activity or more precisely solar magnetic activity.

1.2.3.2 Plages, Networks

The chromosphere of the Sun shows bright regions called plages, typically found near sunspots. These are particularly visible when the Sun imaged in hydrogen and calcium lines (Figure 1.6). They are mostly co-spatial with photospheric faculae seen near limb, but bigger in size. The plages appear along supergranular boundaries or chromospheric networks (Figure 1.6) where magnetic field is concentrated through supergranular flow. Plages appear bright, though they are regions of magnetic concentration in contrast to sunspots. This is modelled by size of flux tubes. Thin flux tubes are bright where as thicker ones are dark. Plages being collection of thin flux tubes appear bright [Solanki 1999]. Though sunspots are found to be associated with plages, there are plage regions where no sunspot is found. Plage latitude follows butterfly pattern similar to sunspots although, smaller plages can appear till latitudes about 50°. Also, increase of solar irradiance is seen to be a competition between dark sunspots and numerous bright plages. These plages are important magnetic proxies to consider and historical chromospheric datasets are valuable in this regard.

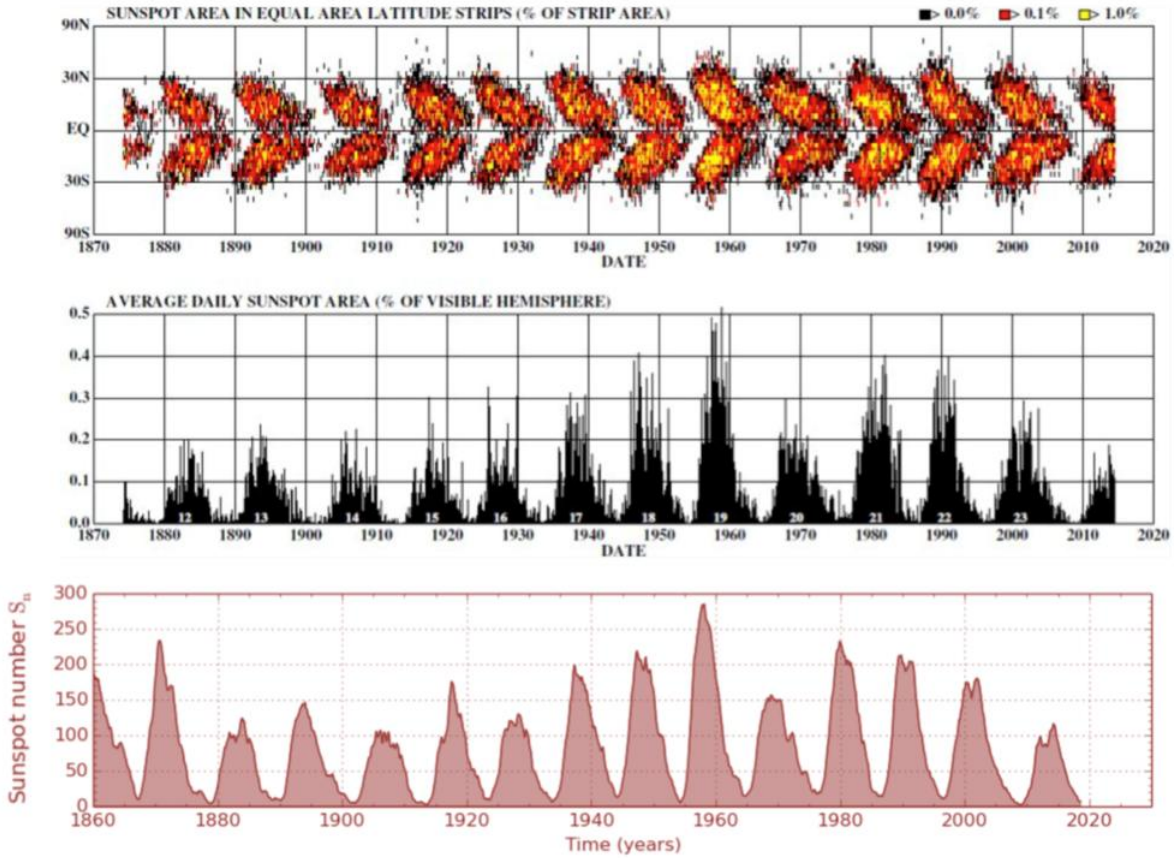

Figure 1.3: *Top panel* shows Sunspot butterfly diagram where sunspot area is mapped against latitude and time. *Middle panel* shows the mean daily sunspot area for e very solar rotation starting from May 1874 as a function of time. *Bottom panel* shows SIDC monthly smoothed sunspot number. Image Source: Hathaway [2015], `http://www.sidc.be/silso/datafiles`.

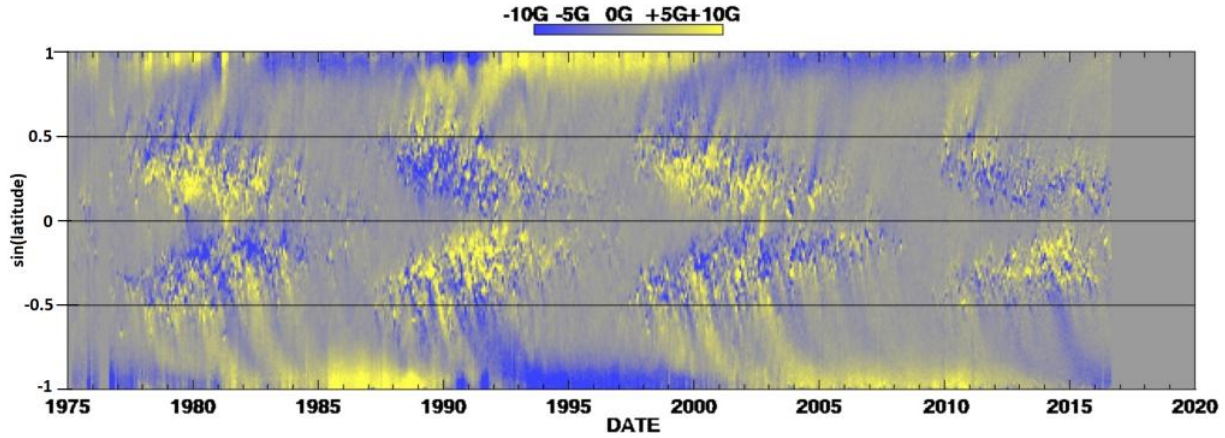

Figure 1.4: Latitudinal depiction of Solar magnetic cycle derived from longitudinally averaged radial magnetic field from NSO/Kitt Peak and SoHO/MDI. Additional feature observed is poleward migration and polar magnetic field reversal with of opposite polarity fields. Image Source: Hathaway [2015].

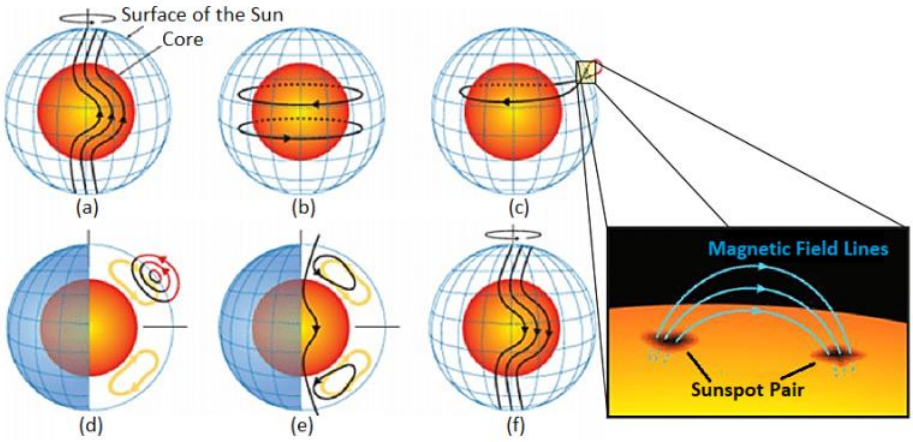

Figure 1.5: Cartoon of solar flux transport dynamo. (a) shows how the poloidal magnetic field lines are deformed by differential rotation at the bottom of solar convection zone. (b)shows formation of toroidal field after few such rotations. This in turn generates flux tube structures. (c) depicts how the flux tubes start rising towards the surface because of magnetic buoyancy. It ultimately pops up from the photosphere creating a pair of sunspots. (d) shows how the decay fo the sunspots will again generate poloidal magnetic field which is then transported towards the poles through meridional circulation (depicted in yellow lines). (e) shows creation of poloidal field having opposite polarity followed by (f) creation of new orientation of toroidal fields due to differential rotation. Image Source: NASA

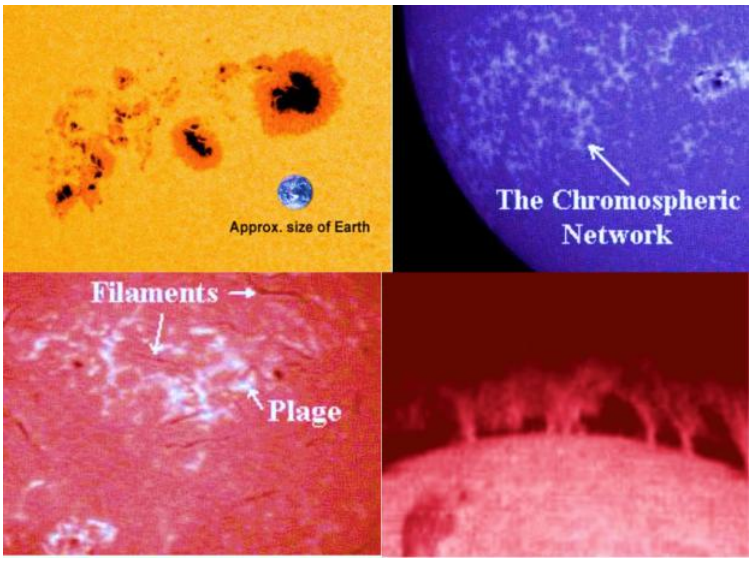

Figure 1.6: Magnetic Proxies seen in different wavelengths. *Top left panel* shows sunspots with dark umbra and fainter penumbra in white light. *Top right panel* shows chromospheric network in Ca II K. *Bottom left panel* shows plages and filaments in H_α. *Bottom right panel* shows off-limb counter part of filaments called 'prominences' in H_α. Image Source: https://solarscience.msfc.nasa.gov/

1.2.3.3 Filaments/Prominences

Filament are the on-disc dark thread like features seen in chromospheic lines such as H_α. Prominence are essentially filaments observed off-limb. When seen off-limb because of absence of background the prominence appear bright in contrast to filaments (Figure 1.6). There are different classes of these structure based on their size and evolution time scale. Quiescent prominences can reach the corona and be there as stable structures slowly evolving over several solar rotations. Prominences can also be eruptive being correlated to solar events such as CMEs. These structures are often found near sunspot activity regions. However, prominences are found all over the solar surface whereas sunspot appearance is limited within mid-latitudes. There is clear association prominences with solar magnetic field. The filaments are seen to be aligned along polarity inversion lines i.e. boundary between opposite magnetic polarity regions [Gibson 2018]. Apart from equator-ward migration of sunspots another interesting feature observed in magnetic butterfly is the poleward migration. Latitudinal locations of filaments and prominences are found to reproduce this feature confirming their role in polar reversal. Thus, through long-term H_α datasets, the history of polar magnetic field reversal can be traced.

1.2.4 Solar Irradiance Cycle

Like solar magnetic field the electromagnetic energy output of the Sun is seen to vary in a cyclic manner with same period. When integrated over all the wavelengths irradiance is seen to vary only by 0.1% from solar minima to maxima (Figure 1.7). However, the scenario changes when the irradiance variation is studied spectrally. The irradiance variation is much stronger in UV and X-ray as compared to other wavelength regimes (Figure 1.8). Also, UV observations are important from the sense that they affect the Earth's stratosphere by photochemical reactions involving ozone. Now, different features on the Sun help in the understanding of the budget of irradiance variation. As for example, the excess radiation from plage more than balances the reduction in radiation from sunspots [Solanki & Fligge 2002]. Thus, spatially resolved UV observation is vital.

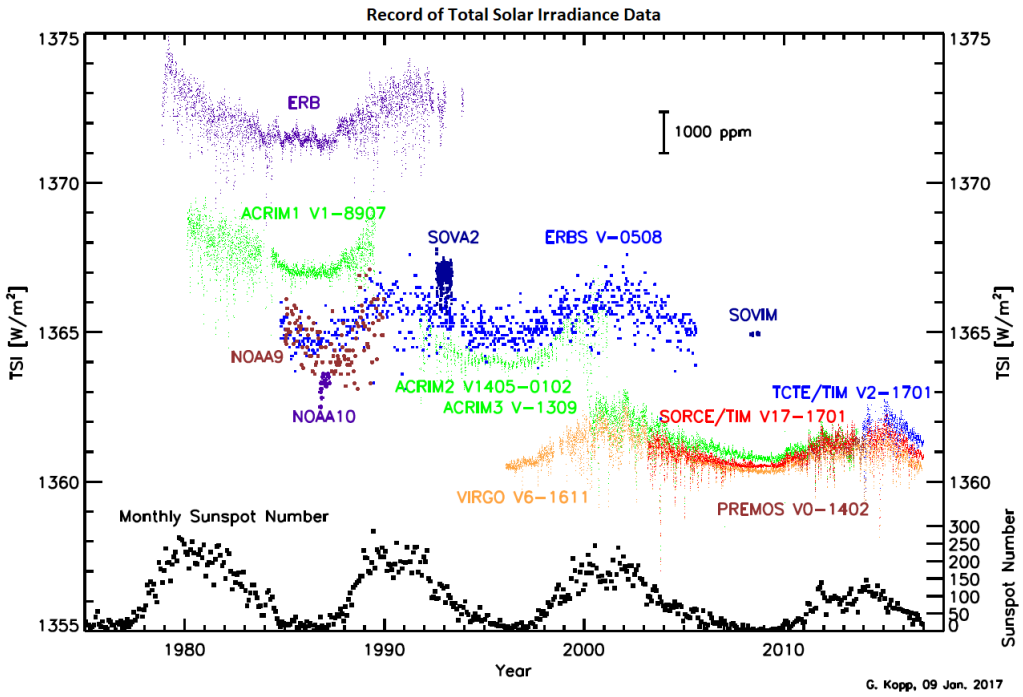

Figure 1.7: TSI measurements from space-based sources. The time series with black dots at the bottom of the plot depicts monthly sunspot number. Image Source: Kopp [2016]

1.2.5 Solar Observation in Ultraviolet

Because of high temperature, upper atmosphere of the Sun radiates in UV, Extreme UV (EUV) and X-rays. These wavelengths are often used to probe highly energetic solar flares which are often associated with CMEs having direct impact on space-climate. Such observations also strengthen our understanding of basic physical processes connecting magnetic fields on the Sun to enable prediction of major solar events. Those events have enough potential to disrupt our terrestrial systems related to power and communication. Also, the UV and X-rays get absorbed by Earth's atmosphere necessitating the space-based observation of the Sun. Solar and Heliospheric Observatory (SoHO), Solar TErrestrial RElations Observatory (STEREO) and Solar Dynamics Observatory (SDO) instruments have been endeavours in the context of solar EUV imaging. These provided novel insight about physical mechanisms behind extreme heating of solar corona, acceleration of solar wind and also ensured continuous monitoring of solar atmosphere imaging the faint emission from corona .

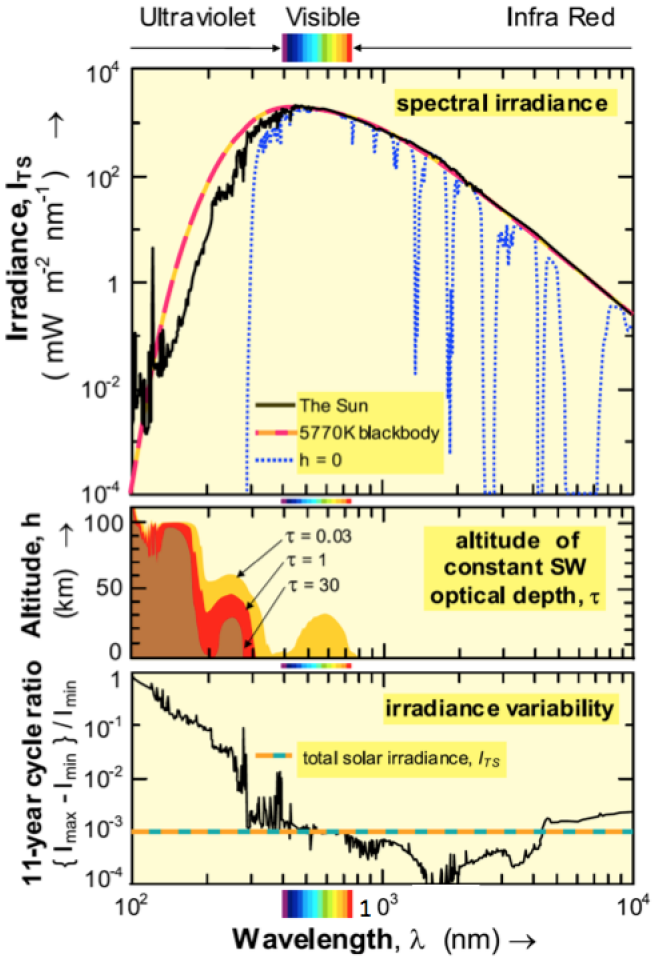

Figure 1.8: *Top panel* shows solar irradiance spectrum is black along with the spectrum for blackbody radiator at a temperature of 5770 K in red. Spectrum of solar radiation on Earth's surface is depicted by blue dotted line. *Middle panel* indicates the the altitudes till which shortwave solar radiation can penetrate for three different smoothed optical depths. *Bottom panel* depicts the variability of solar Spectral irradiance from cycle minimum to maximum based on two solar cycles. Total solar irradiance variability is depicted by the horizontal dashed line. Image Source: Gray et al. [2010]

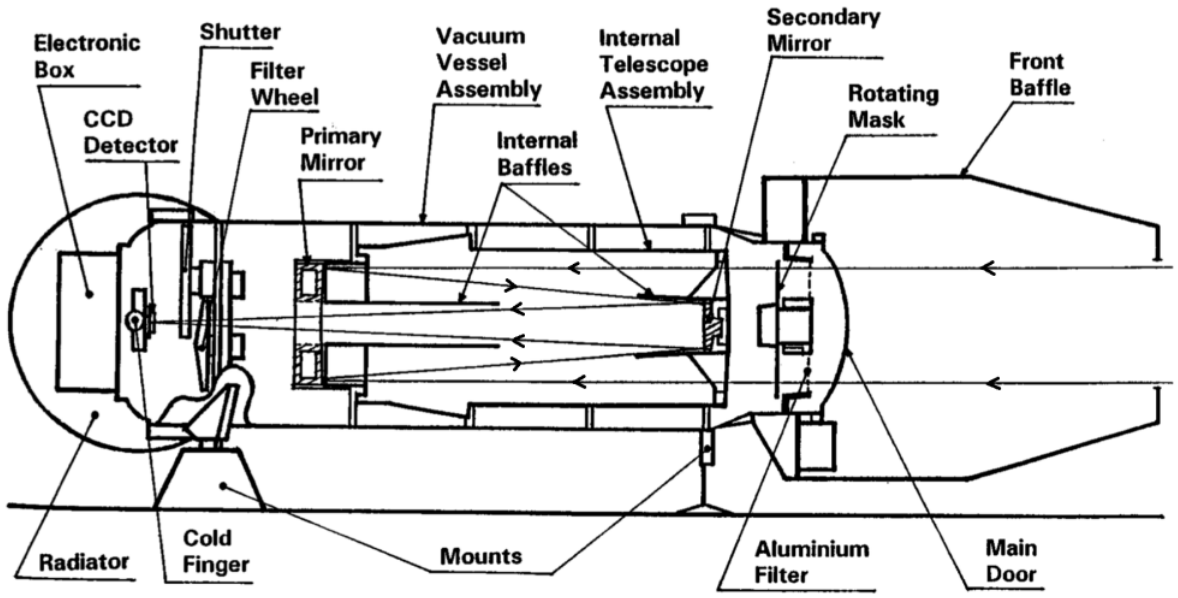

Figure 1.9: EIT optics and major subsystems. Image Source: Delaboudinière et al. [1995]

1.2.5.1 Existing UV Telescopes

1. **SoHO/EIT:** The Extreme-ultraviolet Imaging Telescope (EIT), on-board SoHO, was lunched back in December 2, 1995 at Lagrangian-1 point making observations uninterrupted by Earth's occultations. EIT was aimed to observe transition region and inner corona studying structures such as chromopsheric network, coronal holes and active regions. It was the first dedicated EUV instrument to image the Sun up to $1.5R_{Sun}$ (Field of View $45' \times 45'$) through four different wavelengths namely Fe IX (171 Å), Fe XII (195 Å), Fe XV (284 Å), and He II (304 Å) on long-term basis. The multi-layer normal incidence telescope optical design (Figure 1.9) was based on a Ritchey-Chretien configuration with primary and secondary mirrors divided into four quadrants [Delaboudinière et al. 1995]. The quadrants were multi-layer (molybdenum and silicon) coated and matched between primary and secondary to perform imaging in four wavelengths [Delaboudinière et al. 1995]. EIT used back-illuminated CCD cooled at $-80°$ with a pixel scale of 2.6" achieving a spatial resolution $\approx$ 5.2". Currently, EIT performs full disc observation at least once a day in four wavelengths.

2. **STEREO-SECHHI/EUVI:** The Extreme UltraViolet Imager (EUVI) of SECHHI

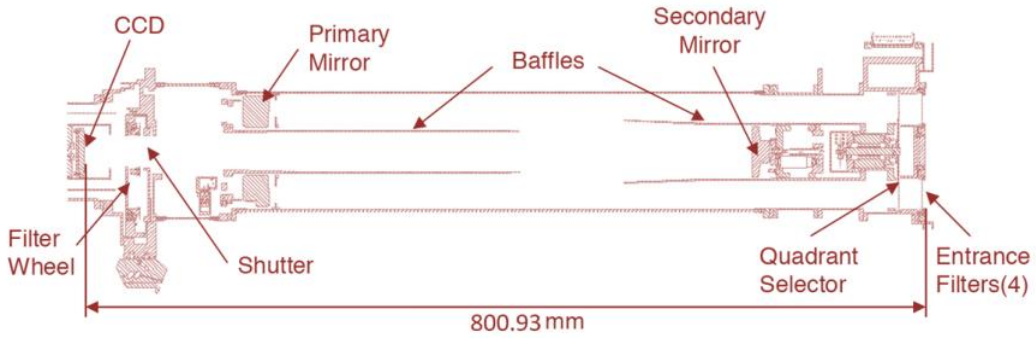

Figure 1.10: Cross-section of EUVI telescope depicting difference optical components. Image Source: Jean-Pierre Wuelser [2004]

(Sun Earth Connection Coronal and Heliospheric Investigation) instrument suite onboard STEREO-A and STEREO-B spacecrafts were launched in 2006 to observe the Sun from two vantage points enabling a 3-dimensional reconstruction of different solar structures. EUVI makes observation of the chromosphere and low corona through four EUV lines namely He II 304 Å, Fe IX 171 Å, Fe XII 195 Å, and Fe XV 284 Å. The normal incidence EUV optics (Figure 1.10) is based on Ritchey-Chretien configuration with an entrance filter for heat rejection [Jean-Pierre Wuelser 2004]. The imaging is performed through a 2048 × 2048 back-illuminated CCD providing pixel scale of 1.6" and therefore allowing a FoV of $1.7R_{Sun}$. It thus achieved a substantial improvement in spatial resolution and also in cadence capturing 1 image in every 3 minutes as compared to EIT/SoHO.

3. **SDO/AIA:** The Atmospheric Imaging Assembly (AIA) on-board the Solar Dynamics Observatory (SDO) was launched on February 11, 2010 at an inclined geosynchronous orbit. AIA aims at understanding the evolution of magnetic environment in solar atmosphere with plasma interaction. AIA consists of four telescopes (Figure 1.11) based on Cassegrain configuration [Lemen et al. 2012]. Each of them has 20 cm primary with an active secondary mirror (Figure 1.11). Imaging is performed through 9 different wavelengths (lines and continuum) namely Fe XVIII (94 Å), Fe VIII,XXI (131 Å), Fe IX (171 Å), Fe XII,XXIV (193 Å), Fe XIV (211 Å), He II (304 Å), Fe XVI (335 Å), C IV (near 1600 Å) and nearby continuum (1700 Å) probing temperature minimum, chromosphere, transition region, active region and quiet corona (Figure 1.11). AIA uses 4096 × 4096 back-

illuminated CCD achieving a FoV of about $1.3R_{Sun}$ along detector axis from center. It significantly improves in spatial resolution (1.5") and temporal resolution (12 seconds) over SoHO/EIT and STEREO/EUVI.

4. **PROBA 2/SWAP:**

   SWAP (Sun Watcher using Active Pixel system detector and image processing) on-board PROBA 2 mission was flown in November, 2009 following a sun-synchronous orbit. This enables continuous monitoring of the Sun. SWAP is an EUV telescope relying on an off-axis Ritchey-Chretien configuration (Figure 1.13). The optics uses an elliptical primary mirror combined with a spherical secondary through quasi-normal incidence [Berghmans et al. 2006]. It achieves a FoV of 54' (about $1.8R_{Sun}$) through an EUV enhanced APS 1024×1024 pixel CMOS detector. SWAP performs imaging of solar corona at 1 min intervals through a bandwidth of 15 Å, centered at 175 Å. Solar flares or EIT-waves and their association with early phase of CMEs are probed with such observations.

1.2.6 Need of Solar Observation in Near Ultraviolet

Earth's atmosphere absorbs high-energy radiation (X-rays and UV). Schematic presented in Figure 1.14 shows reach of the UV radiation in the Earth's atmosphere. The solar UV radiation can be divided into three regions, namely UV-A, UV-B and UV-C. As can be observed from Figure 1.14, Earth's atmosphere absorbs almost all the UV-C and UV-B radiation. The main source of absorption below 200 nm is oxygen (O_2). For radiation within the range 200-240 nm, both O_2 and O_3 play major roles and radiation above 242 nm is mostly absorbed by O_3 [Tripathi et al. 2017]. UV radiation above 310 nm penetrates into the Earth's atmosphere. Therefore, the radiation from the Sun within the wavelength range 200-400 nm is crucial in order to understand the effects of solar radiation on Earth's climate. Total energy output from the Sun <400 nm is just ≈ 8% of the total solar energy output, i.e. total solar irradiance (TSI). However, more than 60% variability over a solar cycle is recorded in the radiation below 400 nm . This should be noted that the variability in TSI over a solar cycle is about 0.1%. Measurements by the SIM instrument on SORCE suggested changes between 2007 and 2004 which were

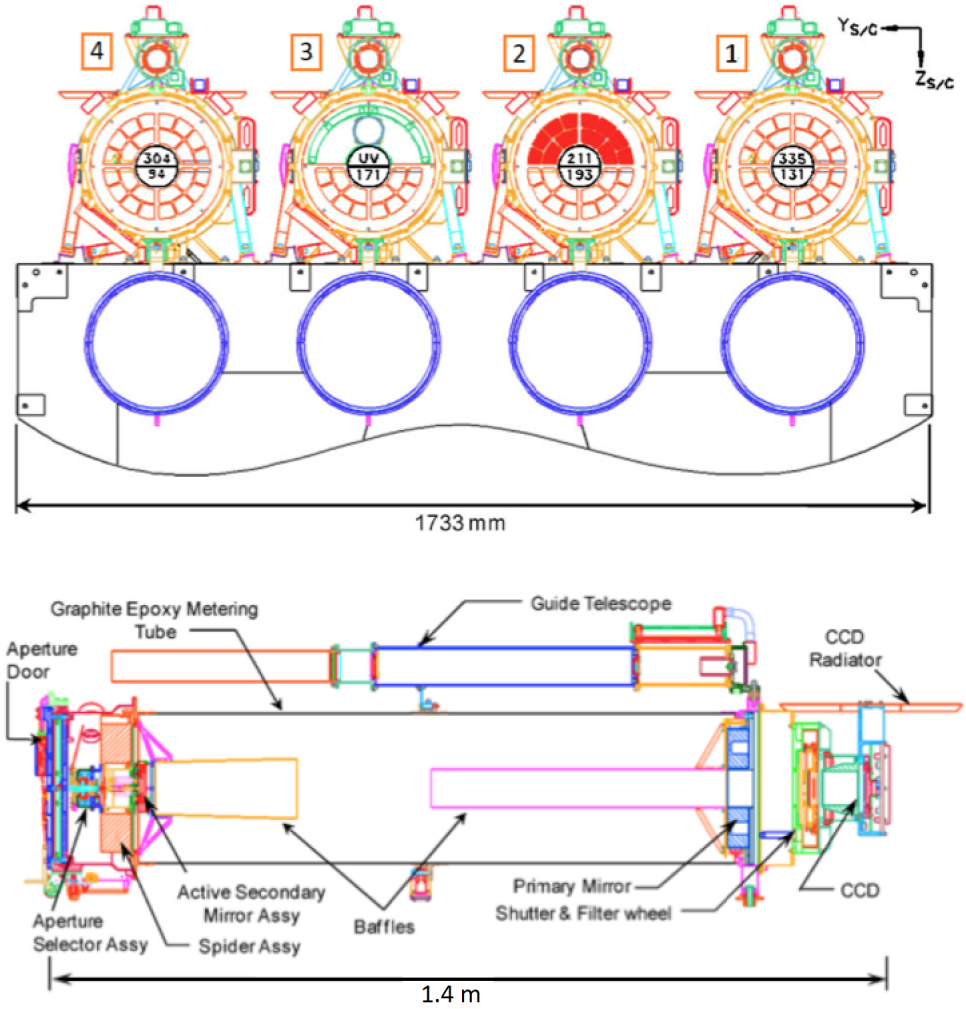

Figure 1.11: *Top panel* shows the wavelength channel layout in each of four AIA telescopes. All the telescopes except 'telescope 2' use filters on filter wheels for selecting different wavelengths. An aperture blade is used for 'telescope 2' to select different wavelengths. 'Telescope 3' uses a MgF_2 window at the top half with a coating centered at 1600 Å. *Bottom panel* shows the cross section of AIA 'telescope 2' with its guide telescope. The entrance filters are protected by the aperture door during launch. The guide telescope for every AIA telescopes provides a signal to the active secondary mirror for stabilizing the image on CCD. Image Source: Lemen et al. [2012]

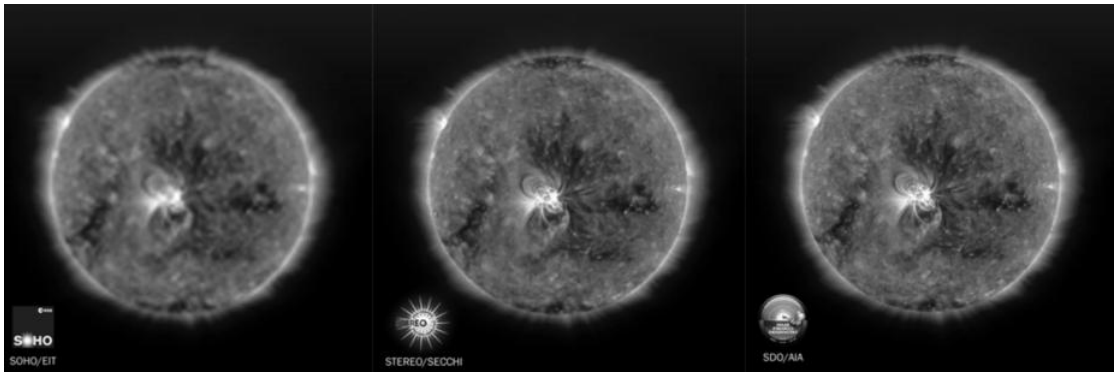

Figure 1.12: Image resolution comparison between SoHO/EIT, STEREO-SECCHI/EUVI and SDO/AIA. Image Source: https://sdo.gsfc.nasa.gov/mission/

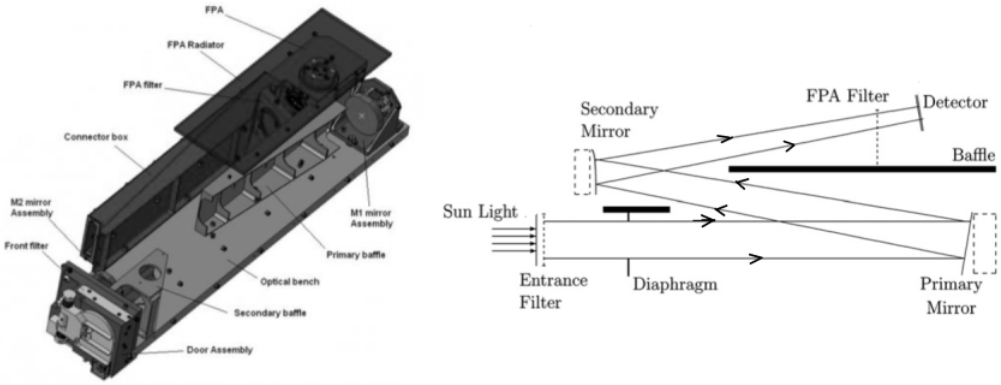

Figure 1.13: *Left panel* shows different components of the SWAP telescope with their assembly. *Right panel* Optical layout of SWAP depicting the off-axis design. Image Source: Berghmans et al. [2006] and http://proba2.sidc.be/

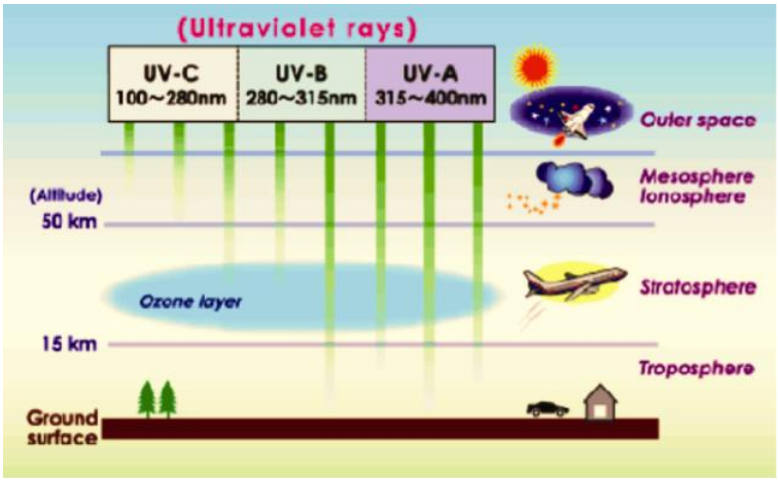

Figure 1.14: Penetartion of UV rays into Earth's atmosphere. Image Source: Centre for Global Environment Research, National Institute for Environmental Studies, Japan.

a factor of 3-6 stronger than possibly predicted by state-of-the-art models. We note here that these measurements are based on Sun-as-a-star observations, i.e. considering the Sun as a point source and without resolving the individual surface structures that cause the irradiance changes. Modern observations of the Sun show that the solar atmosphere consists of a plethora of structures with different temperatures, densities and length scales, and they radiate at different temperatures. Therefore, the results obtained using Sun-as- a-star measurements, though of extreme importance, do not really provide enough insights into the causes of the observed variability. One needs to address the following questions: (a) Coupling and dynamics of the solar atmosphere: What are the processes through which the energy is channellized and transferred from the photosphere to the chromosphere and then to the corona? (b) Prominence studies: What are the mechanisms responsible for stability, dynamics and eruption of solar prominences? (c) Initiation of CMEs and space weather: What is the kinematics of erupting prominences during the early phase. (d) Sun's climate studies with SUIT: How strongly does the solar spectral irradiance of relevance for the Earth's climate vary? [Tripathi et al. 2017]

1.2.6.1 Sunrise/SuFI

Sunrise is a balloon-borne solar observatory with a telescope with an aperture of 1 m (Figure 1.15), working in the visible and near ultraviolet spectral domain. It was aimed to understand the structure and dynamics of the magnetic field in the atmosphere of the Sun. SuFI, Sunrise Filter Imager, [Gandorfer et al. 2011] is one of the post focus instruments of main telescopes providing high resolution near-ultraviolet images of the photosphere and chromosphere. SuFI uses the design of a modified Schwarzchild microscope imaging 20"×40" of the Sun in UV enhanced fast CCD camera through 214 nm, 300 nm, 312 nm, 388 nm and 397 nm filters (Figure 1.15). It also embeds phase diversity capability to correct for residual aberrations due to thermoelastic deformations of the telescope during flight (Figure 1.15). Half area of the CCD captures the focused image, while through the optical delay line second image with a defocus of approximately one wave is formed on the other half of CCD. Post-flight restoration of the images free from static aberrations of the optical path can thus be achieved. SUNRISE completed two flights of several days for scientific solar observation each from ESRANGE near Kiruna, Sweden in June 2009 and June 2013 being in quiet and active phase of solar cycle respectively.

1.2.7 ADITYA-L1 mission and Solar Ultraviolet Imaging Telescope

Aditya-L1, India's first multi-wavelength solar observatory in space, aims to provide continuous coverage of the Sun's atmosphere using remote sensing from Lagrangian one point [Ghosh et al. 2016]. In addition, it will also provide in-situ measurement of particle flux as well as heliospheric magnetic field. Aditya-L1 will carry a payload composed of seven instruments, namely, the Visible Emission Line Coronagraph (VELC), the Solar Ultraviolet Imaging Telescope (SUIT), the High Energy L1 Orbiting Spectrometer (HEL1OS), the Soft X-ray Low Energy X-ray Spectrometer (SoLEX), the Plasma Analyzer Package for Aditya (PAPA), Aditya Solarwind and Particle Experiment (ASPEX) and a Magnetometer (Figure 1.16). SUIT is inspired by the light weight design of SWAP and NUV capabilities of SuFI (Figure 1.16). It aims to provide full disc images of the Sun in Near Ultraviolet (200-400 nm) with a spatial resolution similar to

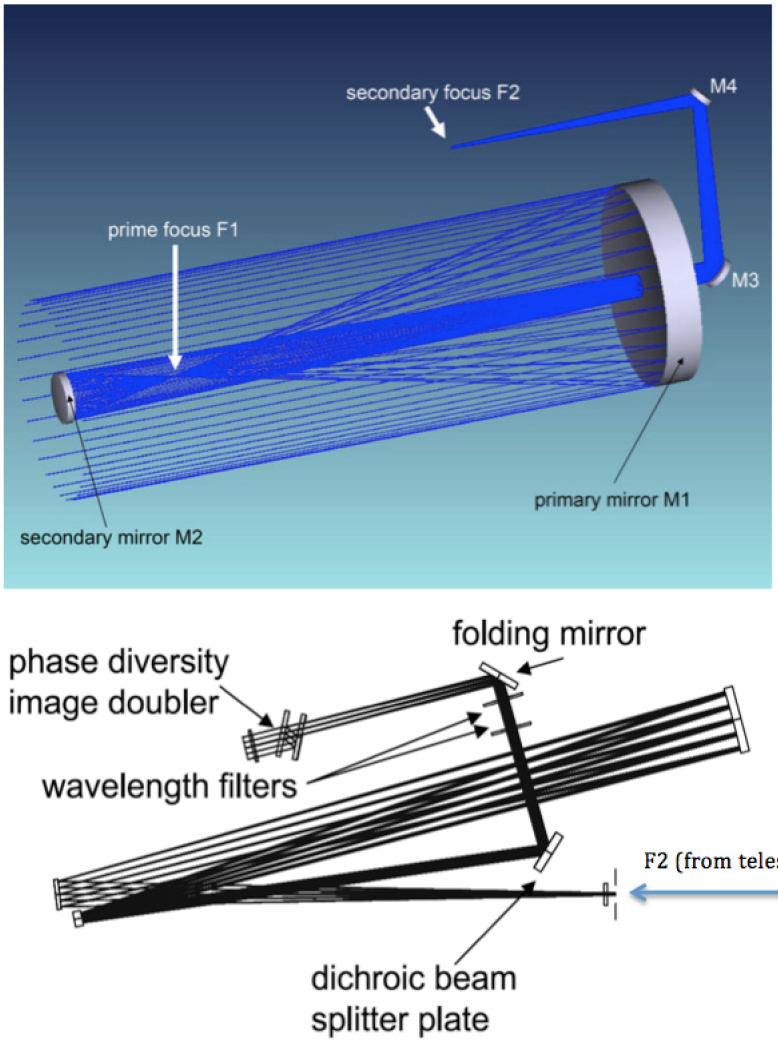

Figure 1.15: *Top panel* shows optical path of the Sunrise Telescope through ray diagram. *Bottom panel* optical design of SuFI with light fed for imaging from main Sunrise telescope. Image Source: Gandorfer et al. [2011] and https://www.mps.mpg.de/solar-physics/sunrise-telescope

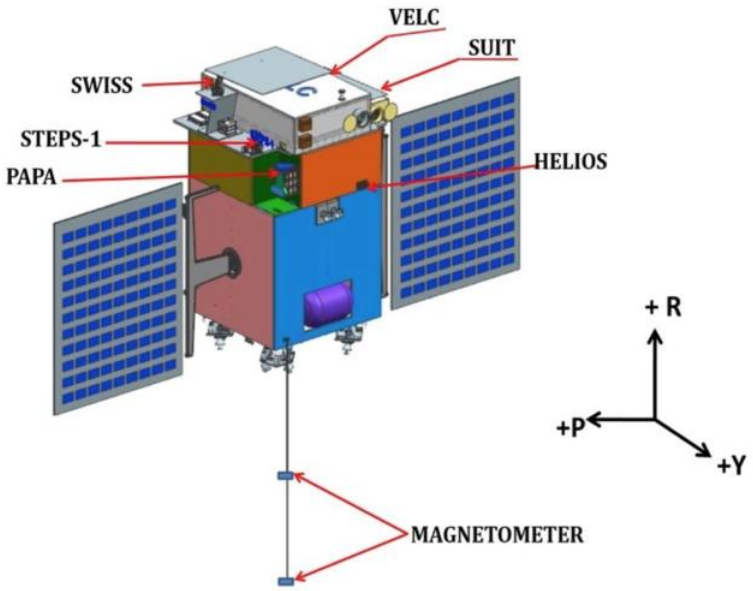

Figure 1.16: Solar Ultraviolet Imaging Telescope (SUIT) as one of the payloads on the ADITYA-L1 satellite. The image is not to scale. Image Source: Indian Space Research Organisation (ISRO), Ghosh et al. [2016]

SDO/AIA (Figure 1.12).

1.2.8 SUIT and Long-term Study of The Sun

SUIT will observe the Sun 24×7 from L1 point remaining uninterrupted by Earth's occultation. It will capture full-disk images of the Sun in all its 11 filters every 30 minutes. These will be in one-hand useful for long-term study of solar spectral irradiance. Also the data, being spatially resolved, will provide opportunity to detect features at varied spatial scales such sunspots, plages, chromospheric networks, magnetic bright points, filaments and prominences. These features are manifestations of solar magnetic field. Thus, detection of those will allow us to understand long-term solar magnetic evolution. As most of those features are visible through ground-based chromospheric datasets, long-term Ca II K and H_α observations can act as test-bed. Algorithms developed for feature detection from those datasets can be used in the data pipeline of SUIT. Though it is challenging to perform irradiance studies from historical ground-based datasets, morphological informations of the features can be used for performing irradiance budgeting and estimation of magnetic flux.

1.2.9 Long-term Chromospheric Datasets

Historically solar chromosphere has been sampled through two different wavelengths namely Ca II K and H_α from several ground based observatories as shown in Table 1.1. Intensities observed through Ca II K line are correlated with strength of magnetic field. Networks and concentrated network brightenings (plages) are the main features observed in the K_3 (3933.67Å) region of this line (Figure 1.17). Filaments/prominences are other faint features observed in this line. However, filaments become much more prominent in the other chromospheric Balmer absorption line H_α (Figure 1.17), appearing as dark elongated on-disc structure with bright background. Historically full-disc solar images in these two wavelengths have been recorded either in form of spectroheliograms (SG) or in the form of filtergrams (FG). SGs are recorded through an instrument called spectroheliograph and filtergraphs are used for recording FGs as described below.

1. **The Spectroheliograph:** This is an instrument used to image sun in specific wavelengths through dispersers such as prisms or diffraction gratings. George E. Hale invented this instrument back in 1889 and photographed Sun in Ca II H and K lines with 2 inch disc diameter observing faculae and bright prominences at Kenwood AstroPhysical Observatory [Hale 1893]. Figure 1.18 shows a typical optical arrangement of Ca II K and H_α spectroheliographs at Kodaikanal Solar Observatory. The solar image is first created on the entrance slit (S1) plane through a siderostat mirror and a triplet lens. The narrow strip of the Sun entering through S1 is re-collimated through a doublet lens and dispersed through two prisms (mirrors with grating in case of H_α). The spectrum is then focused through a doublet lens passing through an appropriate filter (F1)finally creating the image of narrow strip at desired wavelength on photographic material (P). For creating the full-disc image on P, the solar image and P are synchronously moved with respect to the entrance slit. The advantage of this instrument is the narrow achievable bandwidth centered at the science wavelength. But, disadvantages are the scanning time and artefacts introduced in the image due to non-uniform scanning speed.

2. **The Filtergraph:** Filtergraphs are more common now a days which perform full-disc imaging of the Sun using appropriate filters. The advantages of filtergraph over spectroheliograph are the smaller exposure time because of simultaneous imaging of full disc, less distortions and simpler optical configuration avoiding dispersers. However, constraint of filtergraph is the bandwidth of filter. In case of spectroheliograph much narrower bandwidth can be achieved.

As can be observed from Table 1.1, that most of the historical chromospheric datasets are recorded as spectroheliograms. However, some of them are not available in digitised form. The observers diligently recorded feature from photographic plates manually and preserved those detection as Synoptics maps as for example Meudon Observatory H_α synoptic maps (Figure 1.19). Those are maps of the entire sun on rectangular grid of latitude and longitude through synoptic observation for one solar rotation. These maps are valuable for data-driven dynamo simulation.

One of the problem in dealing with these datasets is the non uniformity. One can notice from Figure 1.20, that change of wavelength pass band changes the contrast and may very well affect the area of detected features. Interestingly, for Kodaikanal Observatory the instruments for recoding spectroheliograms remained unchanged for entire observation period. Also, among all the observatories Kodaikanal started observing at the earliest and covered almost entire 20th century for both Ca II K and H_α. These facts inspired us to use Kodaikanal chromospheric dataset as primary test-bed for feature detection and long-term study.

1.2.10 Kodaikanal Solar Observatory

Kodaikanal Observatory (Figure 1.21), established in 1899, has been observing almost on daily basis for more than 100 years (starting in 1904) in three different wavelengths, namely white light, Ca II K and H_α providing simultaneous observation of photosphere, lower and upper chromosphere almost on simultaneous basis. The white light images are essentially filtergrams whereas the Ca II K and H_α images are full-disc spectroheliograms. The spectroheliograms were recorded through spectroheliographs (Figure 1.22) fed by a siderostat as described in previous section. There datasets were

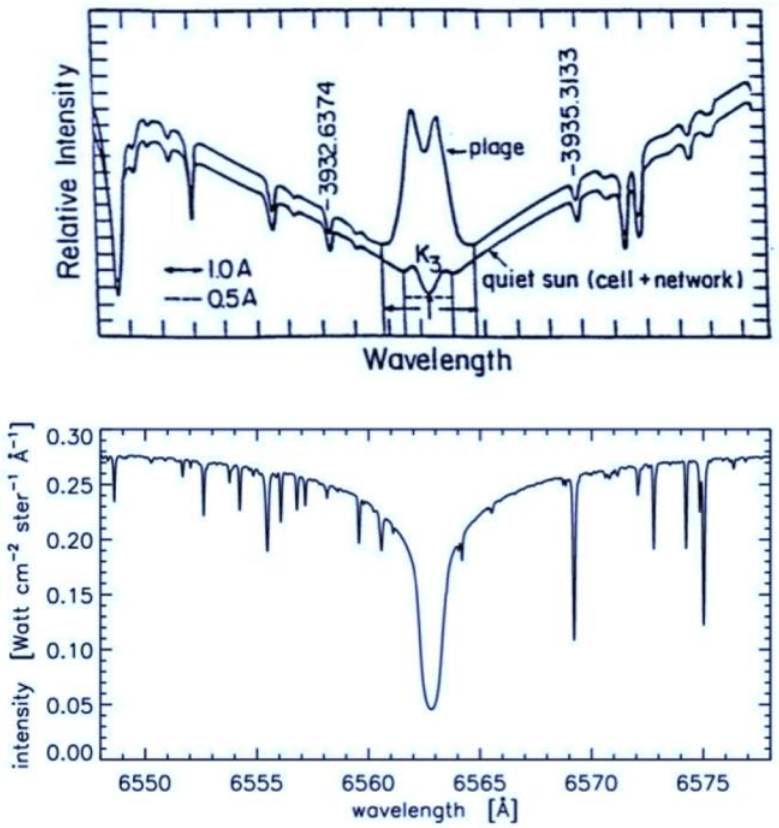

Figure 1.17: *Top panel* shows the Ca II K line for Quiet Sun and in presence of Plages. *Bottom panel* shows the H_α line. Image source:http://www.staff.science.uu.nl/~rutte101/dot/

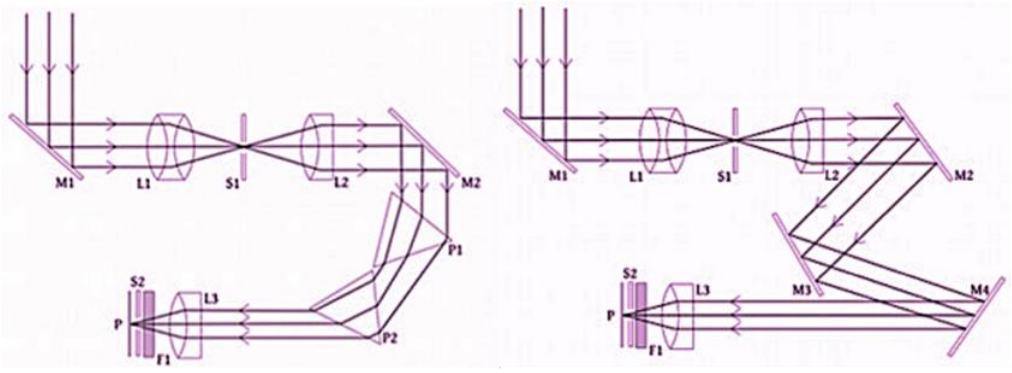

Figure 1.18: *Left panel* shows siderostat and optical arrangement of Ca II K spectroheliograph at Kodaikanal Observatory. *Right panel* shows siderostat and optical arrangement of H_α spectroheliograph at Kodaikanal Observatory. Image source:https://kso.iiap.res.in/new/instruments

Table 1.1: List of ground-based Chromospheric datasets

Wavelength	Time Span	Data	Observatory	References, Links
Ca II K	1904-2007	Full Disc SG	Kodaikanal	Priyal et al. [2014b], Chatterjee et al. [2016],https://kso.iiap.res.in/new
Ca II K	1926-2007	Full Disc SG	Coimbra	Garcia et al. [2011]
Ca II K	1931-1974	Full Disc SG	Arcetri	https://arxiv.org/abs/1710.04949
Ca II K	1963-1977	Full Disc SG	Catania	https://arxiv.org/abs/1902.07483
Ca II K	1915-1985	Full Disc SG	Mount Wilson	Bertello et al. [2010]
Ca II K	1926-1969	Full Disc SG	Kyoto	Kitai et al. [2013]
Ca II K	1917-1974	Full Disc SG	Mitaka	Hanaoka [2013]
Ca II K	1963-2002	Full Disc SG	Sacramento Peak	Tlatov et al. [2009]
Ca II K	1942-1979	Full Disc SG	McMath-Hulbert	Mohler & Dodson [1968]
Ca II K	1996-	Full Disc FG	Rome/PSPT	https://arxiv.org/abs/1710.04949
Ca II K	2008-2013	Full Disc FG	Kodaikanal Twin Telescope	http://adsabs.harvard.edu/abs/2012arXiv1202.5910S
Ca II K	1971-2005	Full Disc FG	Big Bear	Zirin [1974], Naqvi et al. [2010]
Ca II K	1986-	Full Disc FG	San Fernando	Chapman et al. [1997]
H_α	1912-2007	Full Disc SG	Kodaikanal	Chatterjee et al. [2017],https://kso.iiap.res.in/new
H_α	1919-	Hand-drawn Synoptics maps (from 1919) and Full Disc SG (from 1980)	Meudon	Tlatov et al. [2016b]
H_α	1982-	Full Disc FG	Big Bear	http://www.bbso.njit.edu/
H_α	1973-	Full Disc FG	Kanzelhohe	http://cesar.kso.ac.at/synoptic/ha_years.php
H_α	2010-	Full Disc FG	GONG	http://halpha.nso.edu/archive.html
H_α	1998-	Full Disc FG	HASTA	Bagalá et al. [1999],http://www.oafa.fcefn.unsj-cuim.edu.ar/hasta/
H_α	2014-	Full Disc FG	Catania	http://www.oact.inaf.it/weboac/sun/
H_α	2012-	Full Disc FG	ChroTel	http://www.kis.uni-freiburg.de/en/observatories/chrotel/
H_α	2002-	Full Disc FG	Crimean	http://swc.craocrimea.ru/
H_α	1989-	Full Disc FG	Huairou	http://sun.bao.ac.cn/
H_α	1949-	Full Disc FG	NAOJ	http://solarwww.mtk.nao.ac.jp/en/database.html
H_α	1979-	Synoptics maps of Filaments	Kislovodsk	Tlatov et al. [2016b]
H_α	2005-2015	Full Disc FG	SMART, Hida	http://www.hida.kyoto-u.ac.jp/SMART/
H_α	2000-	Full Disc SG	Yunnan	http://www.bbso.njit.edu/Research/Halpha/

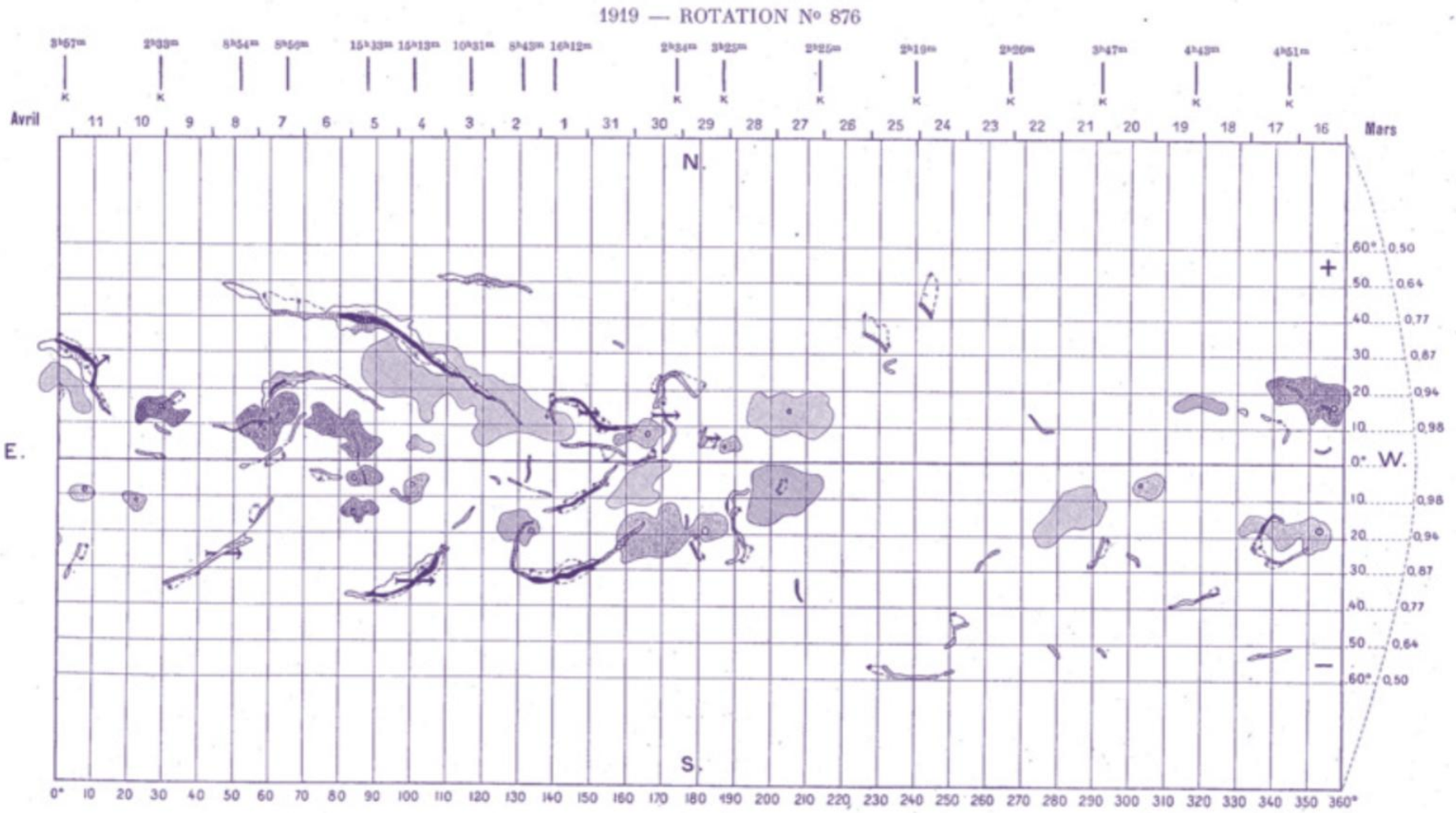

Figure 1.19: Carrington rotation 876 from Meudon Synoptics map archive. Image source:http://bass2000.obspm.fr/

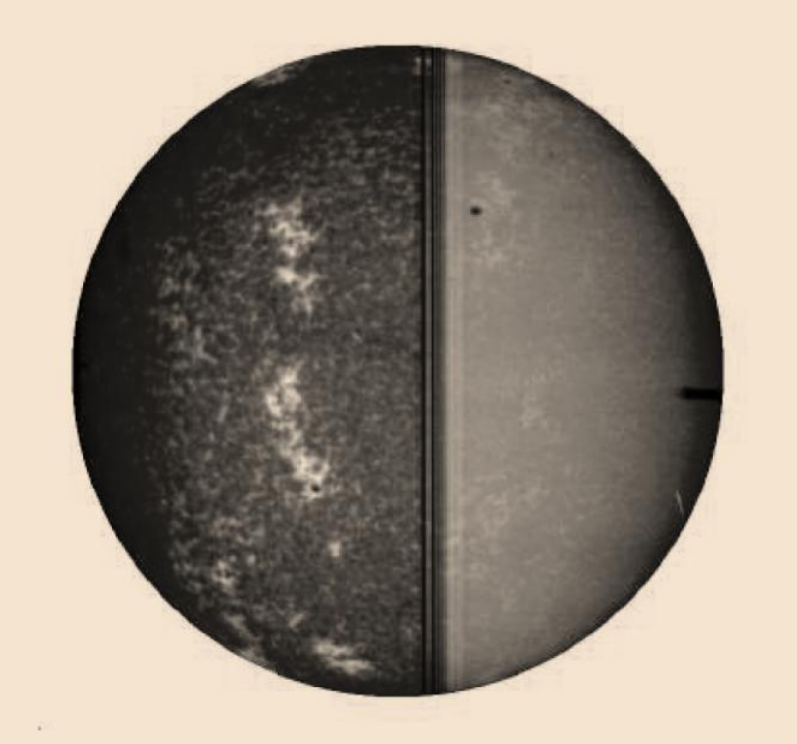

Figure 1.20: Effect of bandwidth on feature contrast. Figure shows MWO observation on June 28, 1979. The right half of the image was captured with a a broader bandwidth as compared to the left half.

recorded through photographic plates and films which were used by scientific community to make manual identification of different features such as sunspots, plages, filaments/prominences and study different related events. However to make a systematic long-term study of those feature avoiding human bias usage of automated computer codes are inevitable. This required the data in digital format. To cater to this necessity, a dedicated digitization setup was installed at Kodaikanal Observatory.

1.2.11 Digitization Setup

The digitisation setup at Kodaikanal Observatory consists of an labsphere/uniform illumination source, plate or film holder, an imaging lens and a 4096×4096 CCD sensor (Figure 1.23). The films/plates are illuminated through the labsphere and imaged onto the CCD sensor with proper magnification using the lens system. The CCD sensor is cooled at −100°C to minimise the thermal noise. Dark frames and flats, necessary for calibration, are captured during digitisation. The digitisation for all three datasets have been completed and are publicly available at http://kso.iiap.res.in.

Figure 1.21: Kodaikanal Solar Observatory established in 1899, located in Palani hills, Tamil Nadu, India. Image Source: https://www.iiap.res.in

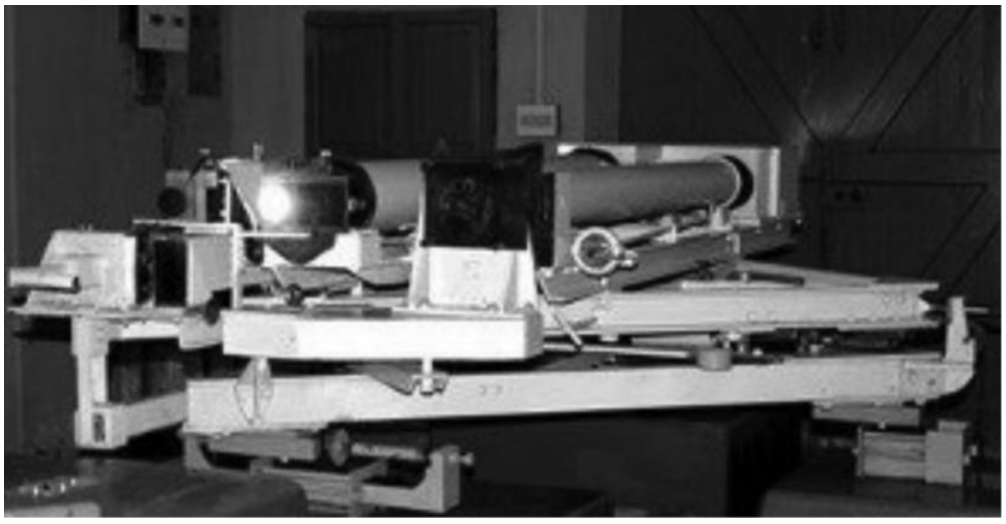

Figure 1.22: Twin full disc spectroheliographs at Kodaikanal Observatory capturing images in Ca II K and H_α. Image Source: https://www.iiap.res.in

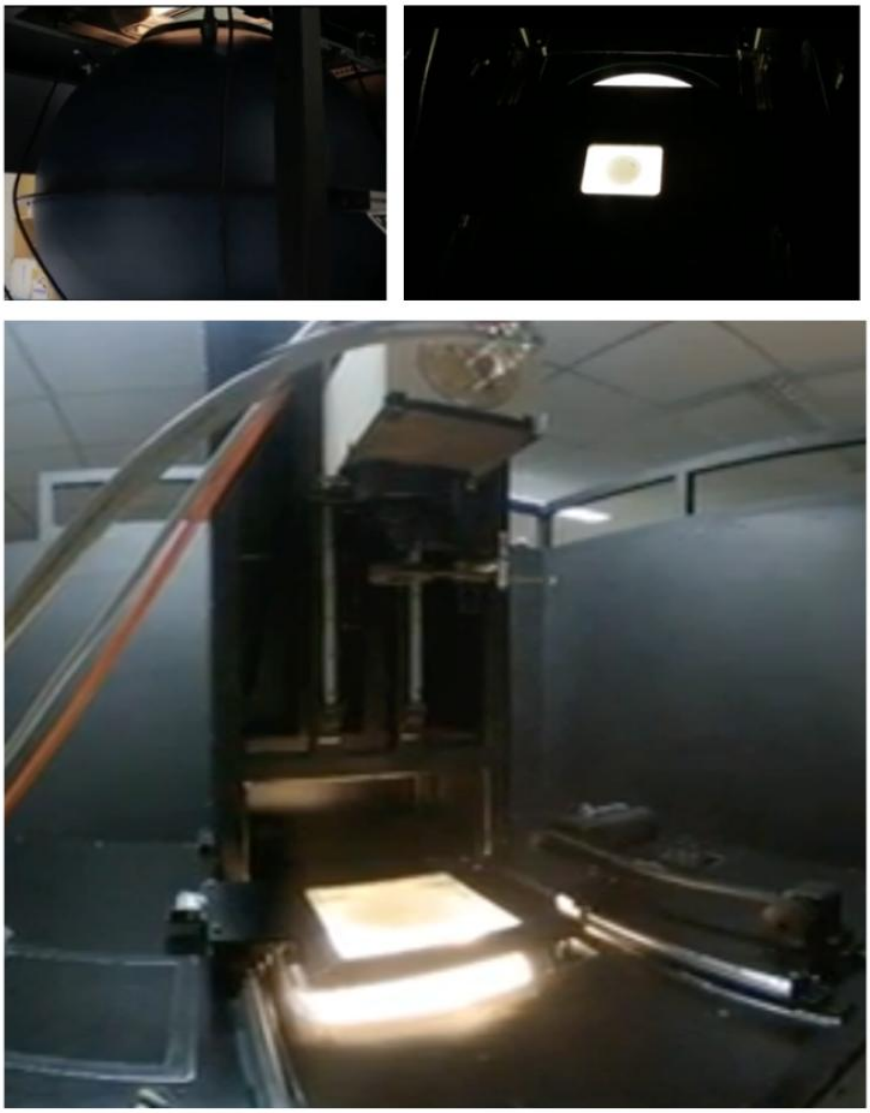

Figure 1.23: Digitisation setup at Kodaikanal Observatory. *Top Left panel* shows the integrating sphere creating uniform illumination. *Top Right panel* shows the photographic plate placed above 1m labsphere with exit port of 350 mm size. *Bottom panel* shows the full setup including the imaging lens and CCD camera. Image Source: https://www.iiap.res.in

1.2.12 Feature Detection from Long-term Datasets

Feature detection techniques can be broadly classified into three categories namely manual, semi-automated and automated. Manual detection involves human operators to mark features without help of any computer code. Semi-automated techniques involved code with human intervention at certain stage. Automated techniques entirely rely on computer algorithms. The main drawbacks of manual detections are their speed and inter-observer variability. It is natural that for any long-term data set containing thousands of images takes enormous amount of time for human beings to detect features. Now, if the process is parallelized involving several human operators, it is evident that the detections will lack consistency as all the eyes are not equally trained. Thus, for any long-term dataset it is extremely important to develop semi-automated/automated codes which enhance the speed hugely and also the consistency. Before starting to detect features from historical digitised solar images it is important to calibrate the images. Flat-fielding and bias correction are the initial steps to apply. However, those flats are obtained during digitisation and do not include the effect of vignetting due to telescope optics [Priyal et al. 2014b]. Scattered light or stray-light correction through deconvolution of instrument Point Spread Function allows to enhance the contrast of the image [Chatzistergos 2017]. The solar disc captured through photographic plates/films are often not centered. To detect features and find their physical coordinates it is necessary to know the disc centre and radius. Circle Hough Transform [Sonka et al. 2014] provides an effective way to detect the solar disc automatically where several features are present other than disc on the film. It is also vital to understand the solar rotation axis. As rotation axis of the sun is tilted with respect to ecliptic normal, the projected tilt of the rotation axis shows yearly modulation. Image rotation over the course of a day is often seen for historical images as they are traditionally captured though siderostats. Thus using instrument parameters and yearly p-angle modulation one can correct the image rotation and align them uniformly. After centering aligning the disc, it is important to estimate the limb-darkening profile, a line-of-sight effect. As most of the intensity thresholding techniques rely on a single threshold to be applied on entire solar disc, it is necessary to ensure that image contrast is uniform from disc centre to edge [Priyal et al. 2014b]. This is achieved

through division of original image with limb-darkening profile [Priyal et al. 2014b, Chatterjee et al. 2016]. Though limb darkening is ideally a rotationally symmetric, effect of atmosphere and instrument make it asymmetric. Several methods starting from median filter to fifth order polynomial fitting are used to estimate the asymmetric profile [Bertello et al. 2010, Priyal et al. 2014b, Chatterjee et al. 2016, Chatzistergos et al. 2018]. However, they have their own advantages and disadvantages. Morphological techniques such as top-hat transformation avoids limb darkening removal for feature detection and has been used for sunspot detection from historical dataset [Ravindra et al. 2013, Mandal et al. 2017]. A recent study also detects plages using morphological method [Barata et al. 2018]. Plage detection from long-term historical datasets have been accomplished by several methods in the past. Some of those rely on constant thresholds for the images [Priyal et al. 2014b] and some adjusts the threshold based on image contrast [Foukal 1998, Chatterjee et al. 2016]. The constant threshold techniques suffer from over-estimation or under-estimation of plage areas when background is not properly normalised. The adaptive threshold method based on multiplicative factor to disc standard deviation gets rid of this problem but has a tendency to be affected by solar cycle modulation [Chatzistergos 2017]. A method named 'plage index' avoids any thresholding and provides an estimate of plage occurrence though image histogram [Bertello et al. 2010]. There have been techniques to estimate supergranular scales from chromospheric images. Most common among them are auto-correlation technique and fast-fourier method [Sýkora 1970, Hagenaar et al. 1997, Muenzer et al. 1989]. However, It is not possible to detect individual supergranule features from auto-correlation and fast-fourier method. The watershed method has been seen to be appropriate in segmenting individual cellular structures [McIntosh et al. 2011, Chatterjee et al. 2017]. As filaments are fine hair-like structures , it often challenging to detect them from historical data. Though automated thresholding algorithms such as OTSU method work on recent data [Hao et al. 2015], the results become unreliable for historical images as they contain dark scratches. This is why filament detection from long-term data has been mostly manual [Xu et al. 2018]. However, semi-automated techniques for filament can improve the consistency and speed. There has also been study of automated detection of filaments using supervised machine learning [Zharkova & Schetinin 2003]. But for

training data for this requires manual marking as automated detection results do not provide any information on false positives.

1.3 Aims and Objectives

1.3.1 Aims

- To Characterize image quality of Solar Ultraviolet Imaging Telescope
- To perform Long-term study of Sun in relevant wavelengths

1.3.2 Objectives

1. Design optimization, ghost image analysis and tolerance analysis for Solar Ultraviolet Imaging Telescope (SUIT) considering requirements and constraints.
2. Scattering analysis to determine optical surface roughness, integration ambience requirement, and baffle design
3. Flat field generation and alignment plan
4. Plage detection, Carrington maps and long-term study from Kodaikanal Ca II K data
5. Supergranule detection and long-term study from Kodaikanal Ca II K data
6. Filament detection and long-term study from Kodaikanal H_α data
7. Prominence detection and long-term study from Kodaikanal Ca II K disc-blocked data

1.4 Structure of The Thesis

- **Chapter 1** introduces briefly about the Sun and its observational aspects. It then focuses the importance of solar observation in UV from the perspective of irradiance budgeting and space climate impact. Different existing space-based EUV

telescopes are discussed. Subsequently, the lack of NUV observation and its impact on Earth's climate dynamics allong with irradiance variability is illustrated. It then introduces the upcoming ADITYA-L1 mission and SUIT as a payload, which will observe in NUV. Some of the solar features to be observed by SUIT have importance in estimation of solar magnetic field. Those features have history of long-term observation from different ground based observatories. Kodaikanal Observatory is one among those recording solar images for more than 100 years in different wavelengths having relevance to NUV observations. Knowledge gained from such datasets will be useful in the context of SUIT and also the data pipeline can be benefited by different feature detection techniques developed, as applied to historical datasets.

- **Chapter 2** illustrated the the optical design of SUIT and its optimisation applying design requirements and constraints such as resolution, mass and dimension constraints. It further presents optimisation of filter tilts through ghost image analysis. This chapter also presents the SUIT optics manufacturing and alignment tolerances. The change of performance is depicted when simultaneous errors occur in different design parameters. Thermal tolerance is also illustrated through first order analysis under different temperature profiles across telescope tube.

- **Chapter 3** depicts another crucial analysis when imaging in Ultraviolet i.e. scattering analysis. This chapter illustrated sources of scattering, their modelling and effect on image quality. Design of baffles is also presented in this chapter. It also proposes a possible scheme to reduce the effect of scattering.

- **Chapter 4** presents the image calibration scheme for SUIT. It depicts the plan for flat field generation through LEDs and optimisation of the same. It also talks about the optical alignments and integration plan for SUIT.

- **Chapter 5** introduces the century-long Ca II K data from Kodaikanal Observatory. It shows how the plages were detected and synoptic maps were generated for the entire dataset. It also demonstrates the connection between plage and magnetic patches through locational correlation in overlapping times.

- **Chapter 6** illustrates the detection of supergranules, the chromospheric cellular structures depicting scales of horizontal Kinetic energy, from Kodaikanal Ca II K data. The chapter elaborates the the cyclic variation of supergranule parameters near and away from active regions showing different signs of correlation with sunspot cycles.

- **Chapter 7** introduces the long-term H_α dataset from Kodaikanal Observatory. This chapter majorly talks about the detection of an important magnetic neutral proxy called filaments through Carrington maps generated from this dataset.

- **Chapter 8** illustrated the detection of prominences, the off-limb counter parts of filaments majorly from Kodaikanal Ca II K disc blocked dataset through an automated method. It further demonstrated, how Kodaikanal data in later years were complemented with other recent ground-based prominence datasets, providing uniform detection of prominence locations and polar rush. The poleward migration rates provide important inputs for constraining meridional flow rates, an important parameter in solar dynamo modelling.

- **Chapter 9** Summary and future scope. Summarises work presented in the thesis, the limitations and scope of further improvement.

- **Chapter 10** Appendix.

Chapter 2

Optical Design Optimization and Tolerance Analysis of SUIT

2.1 Introduction

Solar Ultraviolet Imaging Telescope on-board ADITYA-L1 mission aims at imaging full disc of the Sun in near ultraviolet for the first time on regular basis. The desired imaging performance of the telescope required optimization of the optics [Ghosh et al. 2016, Tripathi et al. 2017]. SUIT optics is based on an off-axis Ritchey-Chretien configuration. It will consist of a thermal filter, two hyperbolic mirrors, science filters and a field correctors lens as shown in the schematic of Figure 2.1. This particular design is chosen to meet the dimension constraints and to minimize the scattering effects. The metal-dielectric thermal filter will reflect most of the solar flux outside near ultraviolet (NUV) band 200-400 nm and cut-down within band flux allowing only 1% of flux to enter the optical chamber of SUIT [Ghosh et al. 2016, Tripathi et al. 2017]. The mirrors made of Zerodur will be coated with aluminium, chromium and magnesium floride to achieve desired reflectivity in NUV. The optical system will allow full disc imaging of the Sun through 11 different filters in NUV. A combination of two filters in the beam path will be used to select the desired bandpass. Among 11 filters, 8 will be Narrow-band and 3 Broad-band. They will be mounted on two independent filter wheels each having eight filter slots (a total of sixteen slots). Other five slots will consist of four neutral density (ND) filters and an opaque block. Those ND filters will be combined with

the science filters to cut the solar flux and out of band light leaks. The details of the science filters and their science goals are elaborated in Table 2.1. The lens placed before image plane will ensure uniform image quality across the field of view (FoV) and will be placed on a linear stage aimed to compensate image degradation due to first order thermal effects. SUIT image plane will use a 4096 × 4096 CCD sensor with 12-micron pixels. In this work, section 2.2 will illustrate steps performed for SUIT optical design optimization followed by tolerance analysis in section 2.3 and thermal tolerance analysis in section 2.4. Finally, in section 2.5 the results are concluded along with necessary discussion.

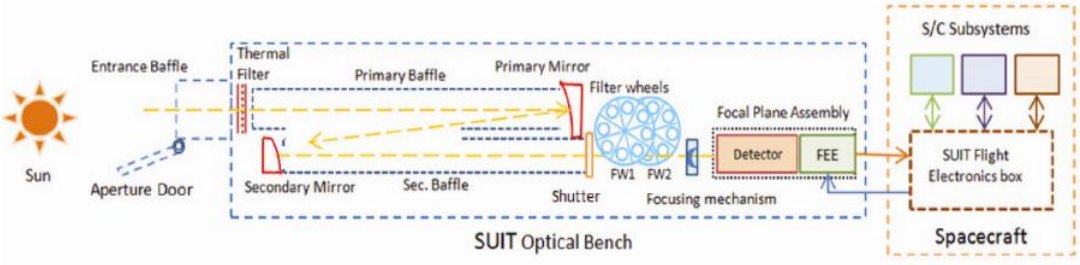

Figure 2.1: Functional diagram of SUIT.

2.2 Optimizing SUIT Optics: Adopted Steps

2.2.1 Design Requirement and Constraints

The required spatial resolution for SUIT was ≈ 1.4 $arcsec$. This requirement transformed to to pixel scale requirement of ≤ 0.7 $arcsec$. Now SUIT uses a 4096 × 4096 CCD sensor with pixel size of 12-microns. This gives a Field of View of 0.8°×0.8° and the focal length as the ratio of pixel linear size and angular size i.e. $\frac{12\times10^{-3}\ mm}{(\pi/180)\times(1/3600)\times0.7\ rad} \approx$ 3536 mm.To allow enough margin for aberration intrinsic and due to misalignment the primary diameter (D) was chosen such that the airy disc diameter (first minima) corresponds to an angular size of 1 $arcsec$ at wavelength of 280 nm. Thus upon equating

Table 2.1: Filter passbands that will be used by SUIT to map different atmospheric layers of the Sun and the corresponding science goals

Spectral Channels (nm)	Bandpass (nm)	Science
214	5	Dynamics of the magnetic bright points in the photosphere
274.7 Blue wing of Mg lines	0.4	Chromospheric and lower transition region dynamics, waves, shocks, filaments and prominences
279.6 Mg II h line	0.4	
280.3 Mg II k line	0.4	
283.2 Red wing of the Mg II lines	0.4	Sun-Earth climate connection
300	1	Sunspot
388	1	Monitoring the magnetic flux proxies
397.8	0.1	Chromosphere
200-242, O_2 Herzberg Continuum, O_3 Hartley Band	42	Sun-Earth climate connection: photodissociation of oxygen and ozone in the stratosphere
242-300, O_3 Hartley Band	58	
320-360 O_3 Hartley-Huggins bands	40	

we get, $(2.44\lambda/D) \times (180/\pi) \times 3600 = 1\ arcsec$. Putting $\lambda = 280\ nm$ primary diameter was derived as, $D = 141\ mm$. The mechanical constraints relevant to the design were namely length and weight of the optical system being limited by 1.1 meter and 35 kg respectively.

2.2.2 Optical Design Parameters and Their Initial Values

All optical surfaces are defined by the following parameters. As SUIT is an off-axis system, it is necessary to specify off-axis distance.

- **Radius of Curvature (RoC):** For the spherical surfaces such as lens the RoC will be constant everywhere. For conic surfaces, RoC is specified at the vertex.
- **Conic Constant:** This is defined as $K = -e^2$, where e is the eccentricity. For hyperbola $K < -1$.
- **Off-axis distance (OAD):** Distance of aperture center from vertex of parent hyperbola.

Before doing optimization in ZEMAX the initial values of the parameters were

calculation using the following formulas:

$$R_{M1} = \frac{-2df}{f-b}$$

$$R_{M2} = \frac{-2bd}{f-b-d}$$

$$m = \frac{f-b}{d}$$

$$K_{M1} = -1 - \frac{2b}{m^3 d}$$

$$K_{M2} = -1 - \frac{2}{(m-1)^3}[m(2m-1) + \frac{b}{d}]$$

Here, R_{M1} and R_{M2} are respectively the RoCs of primary (M1) and secondary mirror (M2) respectively. K_{M1} and K_{M2} represent the conic constants of M1 and M2 respectively. f, b and d are respectively the telescope effective focal length, M1 to M2 distance and M2 to telescope focus distance. Putting f = 3536 mm, d = 530 mm and b = 860 mm from dimension constraints the initial values of RoC and conic contants were acquired as $R_{M1} = -1400.660$ mm, $R_{M2} = -424.790$ mm, $K_{M1} = -1.0252$, $K_{M2} = -2.4329$.

2.2.3 Design Optimization Using Zemax Software

Zemax optimisation was performed using the initial Ritchey-Chretien configuration as described in previous section. The off-axis distances for M1 and M2 were chosen as 159 mm and 40 mm respectively using mechanical constraint on M1 to M2 aperture separation along the OAD direction. Before optimisation two filters and a field-corrector lens were put before CCD and component to component distances, conic constants and surface RoCs were made variable with the focal length constraint. The merit function to be minimised was RMS spot radius on image plane over different wavelengths and field points from field centre to edge. The spot diagram obtained in ZEMAX software on the image plane in depicted in Figure 2.2. The optimised optical design (in scale) is depicted in Figure 2.3 and design parameters are listed in Table 2.2. The optimised lens came out to be of negative meniscus type which provided near-uniform RMS spot-size across the FoV. Because of two-mirror off-axis design the dominant aberration is astigmatism,

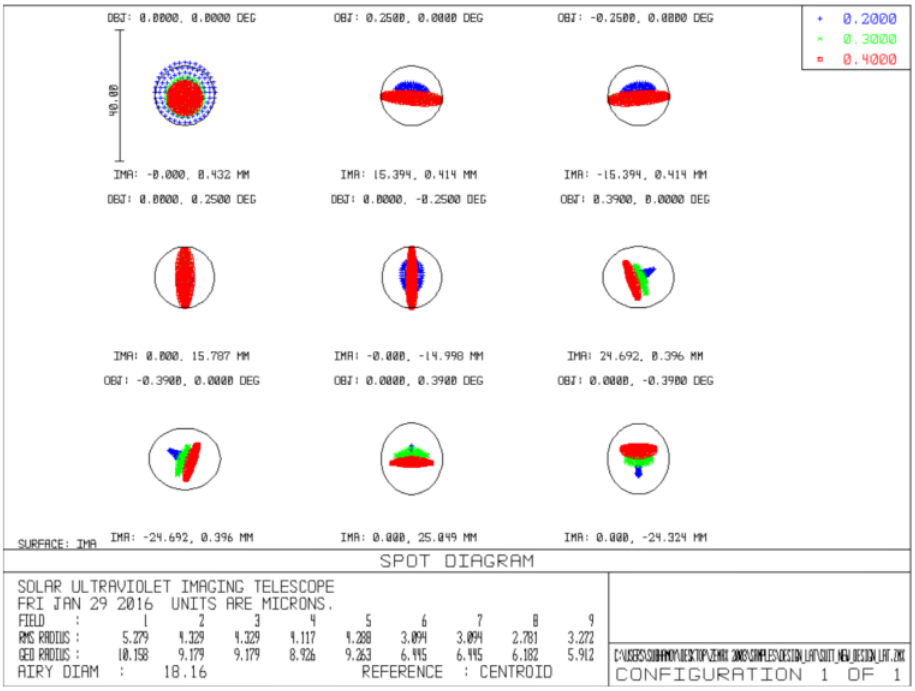

Figure 2.2: Image plane spot diagrams for nominal configuration.

where the spot falls within airy disc of mid-wavelength (300 nm). Though, this is not an achromatic design the lateral chromatic aberration is well within tolerance. It can be observed that science filters are tilted with respect to each other. However, the tilt of the filters do not have considerable effect on image quality. Those tilts were derived from ghost image analysis which is illustrated in the following section.

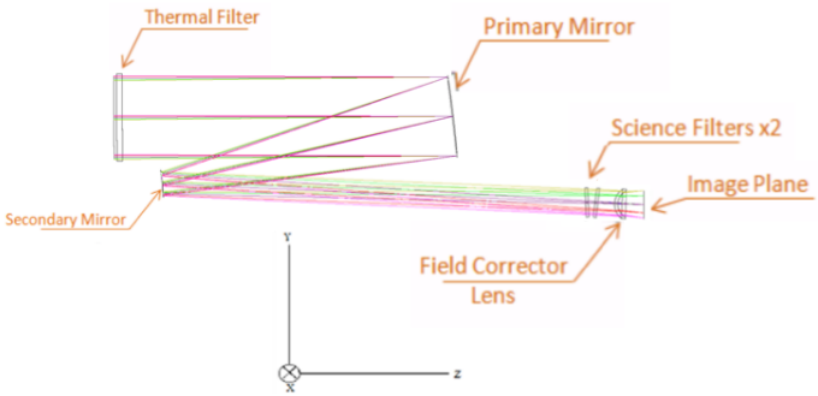

Figure 2.3: 2D Optical layout of SUIT with different components marked. Reference axes is also overlayed for definition of tilts.

Table 2.2: SUIT Optical Design parameters

Component(s)	Parameter description	Value
Thermal Filter	Clear Aperture	156 mm
	Thickness	10 mm
Thermal Filter and Primary Mirror	Separation (Z)	600.803 mm
Primary Mirror	Clear Aperture	141 mm
	Radius of Curvature	-1404.67 mm
	Conic Constant	-1.0255
	Off-Axis Distance	159 mm
Primary and Secondary Mirror	Separation (Z)	527.8067 mm
Secondary Mirror	Clear Aperture	44 mm
	Radius of Curvature	-438.252
	Conic Constant	-2.4867
	Off-Axis Distance	40 mm
Secondary Mirror and Filter1	Separation (Z)	760 mm
Filter1 and Filter2	Separation (Z)	7 mm
Filters	Clear Aperture	49 mm
	Thickness	5 mm
	Filter1 Tilt	-2.2432 degree (about X)
	Filter2 Tilt	7.2568 degree (about X)
Filter2 and Lens	Separation (Z)	30 mm
Lens	Clear Aperture	49 mm
	Thickness	6 mm
	Radius of Curvature (Front)	32.971 mm
	Radius of Curvature (Back)	28.0369 mm
	Tilt	2.3432 degree (about X)
Filters and Lens Glass	Fused Silica	n_d = 1.458464, V_d = 67.82
Lens and Image Plane	Separation (Z)	47 mm
Image Plane	Tilt (about X)	0.2092 degree

2.2.4 Ghost Image Analysis of SUIT

2.2.4.1 Origin of Ghost Patterns

Spurious patterns on the image plane apart from ideal image are called ghost images. They occur because of splitting of rays at each optical surface. So apart from rays following desired optical path, unwanted rays hit the image plane at different locations coming from repeated inter-reflection and refraction through the optics. Sometimes these unwanted rays get focused saturating the CCD which is termed as ghost focus.

But if these patterns are diffused in a manner they may not affect the image quality, they cause flux loss for the specular image. The flux loss needs to be estimated to understand if they are acceptable in terms of throughput requirement of a system. Also, knowing the spatial distribution of ghost flux may be useful to remove the same.

2.2.4.2 A Simple Model for Ghost Flux

Let there is G_0% of ghost flux on the CCD with respect to specular flux when there is no reflection from the CCD. Now if CCD reflects back a fraction $(1 - Q)$ towards lens and science filters specular flux becomes $100Q$ and ghost flux becomes G_0Q with the back-reflected flux as $(100 + G_0)(1 - Q)$. Now the reflection from lens and science filters again returns a flux fraction (Q') to the CCD. Process of such repeated reflection back-and-forth builds the ghost flux as $G_0Q + (100 + G_0)(1 - Q)Q'Q + (100 + G_0)(1 - Q)^2Q'^2Q + (100 + G_0)(1 - Q)^3Q'^3Q + ...$ Summing the infinite series we get Ghost Flux= $G_0Q + (100 + G_0)Q\frac{Q'(1-Q)}{1-Q'(1-Q)}$ whereas Specular Flux= $100Q$. Thus the ratio of ghost flux to specular flux becomes:

$\frac{Ghost\ Flux}{Specular\ Flux} = \frac{G_0Q+(100+G_0)Q\frac{Q'(1-Q)}{1-Q'(1-Q)}}{100Q} = \frac{G_0+(100+G_0)\frac{Q'(1-Q)}{1-Q'(1-Q)}}{100}$ Now, knowing G_0 and Q' for different filters, the flux ratio can be predicted from the model for any CCD coating i.e. the parameter Q. Setting $Q = 1$ from simulation we can easily find the value of G_0. Doing another simulation with $Q < 1$ for same filter we can determine the value of Q' as G_0 is known. This is to be noted that G_0 and Q' are unique for every filter. In the following two subsections, the method for estimation filter coating parameters for SUIT and simulation of ghost patterns in ZEMAX using those coating parameters are shown.

2.2.4.3 Extraction of Coating Reflection, Transmission and Absorption as Functions of Wavelength and Angle of Incidence (AoI)

Before a simulation of ghost patterns in ZEMAX, the coating informations of the filters were needed to be extracted through the limited set of parameters namely filter total transmission at normal incidence as a function of wavelength and the effective refractive index (n_e) provided by the filter manufacturer. It is shown below how a full dataset of total transmission, total reflection and absorption was generated as a functions of AoI

and wavelength. Fresenel reflection coefficients for s and p polarised light are given by:

$$R_p(\theta_i) = \left[\frac{\cos\theta_i - n_e\sqrt{1-(\sin\theta_i/n_e)^2}}{\cos\theta_i + n_e\sqrt{1-(\sin\theta_i/n_e)^2}}\right]^2$$

$$R_s(\theta_i) = \left[\frac{n_e\cos\theta_i - \sqrt{1-(\sin\theta_i/n_e)^2}}{n_e\cos\theta_i + \sqrt{1-(\sin\theta_i/n_e)^2}}\right]^2$$

At normal the reflection coefficient becomes-

$$R = R_p(0) = R_s(0) = \left[\frac{1-n_e}{1+n_e}\right]^2$$

Now total transmissivity (Figure 2.4) as a function wavelength at normal incidence can be expressed as-

$$T_{tot}(0,\lambda) = \frac{(1-R)^2\tau(0,\lambda)}{1-R^2\tau(0,\lambda)^2}$$

and total reflectivity (Figure 2.4) at normal incidence as-

$$R_{tot}(0,\lambda) = \frac{R+\tau(0,\lambda)^2R-2R^2\tau(0,\lambda)^2}{1-R^2\tau(0,\lambda)^2}$$

Where $\tau(0,\lambda)$ donates the internal tramissivity (Figure 2.4) over the thickness of the filter a normal incidence and wavelength λ. This is calculated from given data of $T_{tot}(0,\lambda)$ inverting the formula above as-

$$\tau(0,\lambda) = -\frac{(1-R)^2}{2R^2T_{tot}(0,\lambda)} + \sqrt{\frac{(1-R)^2}{4R^4T_{tot}(0,\lambda)}^2 + \frac{1}{R^2}}$$

τ can be scaled to nonzero AoIs as-

$$\tau(\theta_i,\lambda) = \tau(0,\lambda)^{1/\sqrt{1-(\sin\theta_i/n_e)^2}}$$

Using $\tau(\theta_i,\lambda)$ total Reflectivity and total Transmissivity as function of AoI and wavelength can be calculated for both s and p polarization as-

$$T^{s/p}_{tot}(\theta_i,\lambda) = \frac{\left[1-R_{s/p}(\theta_i)\right]^2\tau(\theta_i,\lambda)}{1-R_{s/p}(\theta_i)^2\tau(\theta_i,\lambda)^2}$$

$$R^{s/p}_{tot}(\theta_i,\lambda) = \frac{R_{s/p}(\theta_i)+\tau(\theta_i,\lambda)^2R_{s/p}(\theta_i)-2R_{s/p}(\theta_i)^2\tau(\theta_i,\lambda)^2}{1-R_{s/p}(\theta_i)^2\tau(\theta_i,\lambda)^2}$$

This gives rise to a total absorption (A) of-

$$A^{s/p}(\theta_i,\lambda) = 1 - T^{s/p}_{tot}(\theta_i,\lambda) - R^{s/p}_{tot}(\theta_i,\lambda)$$

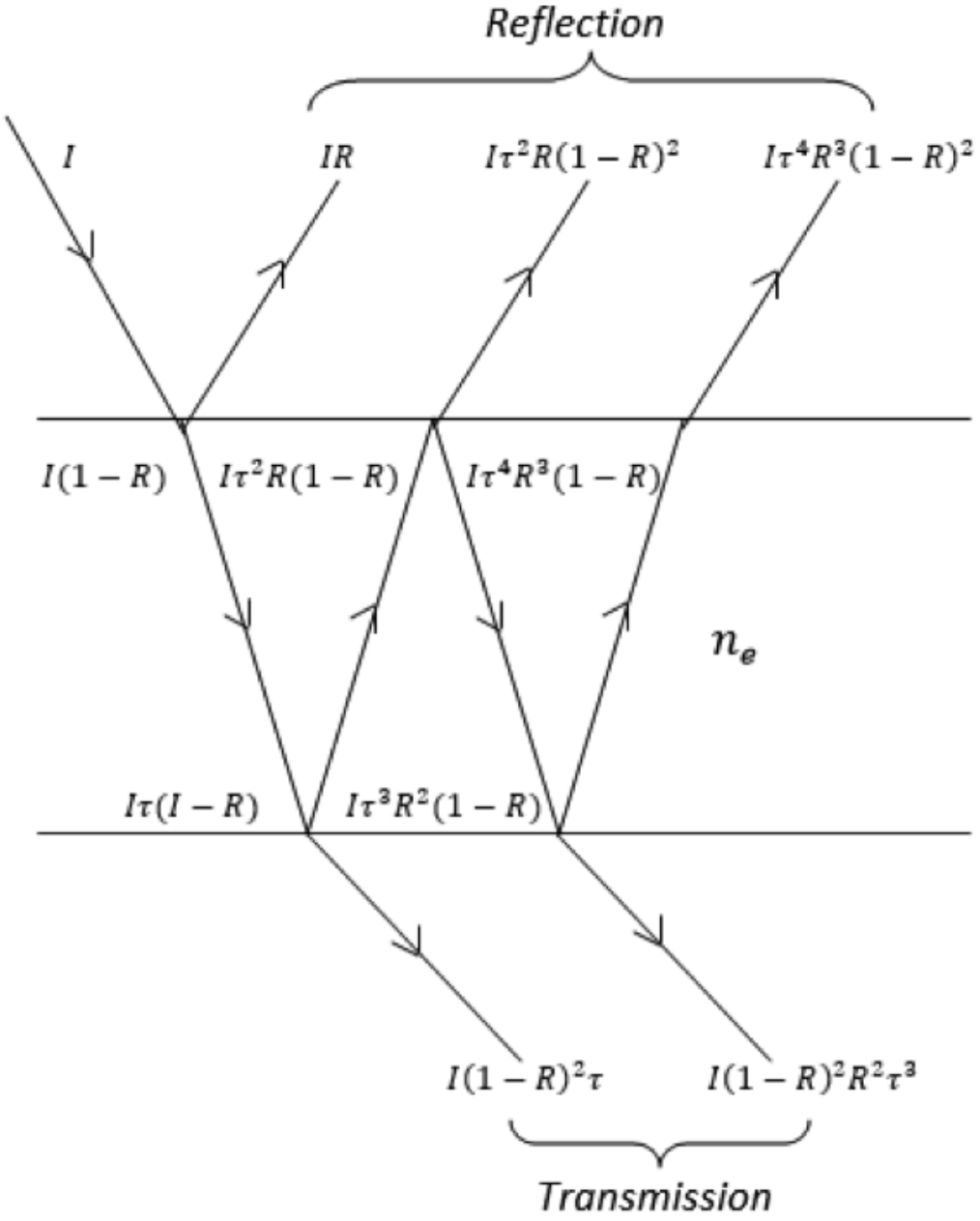

Figure 2.4: A schematic ray diagram showing total reflected and transmitted light through repeated transmission and reflection at interface with absorption from material thickness

2.2.4.4 Non-sequential Ghost Simulation in Zemax Software

The simulation was performed entirely in non-sequential setup of Zemax. Ray tracing was performed without and with splitting (Figure 2.5). 8 Point sources on every concentric ring were considered where the flux was scaled by the radius of the ring as shown in the Figure 2.5. The trace without split gave the location of specular light whereas the trace with split additionally gave the locations of ghost light. The measure used the estimate relative amount of ghost is given by-

$$Gost\ Measure = 100 \times \frac{Total\ Ghost\ flux\ within\ Disc}{Total\ Specular\ flux\ within\ Disc}$$

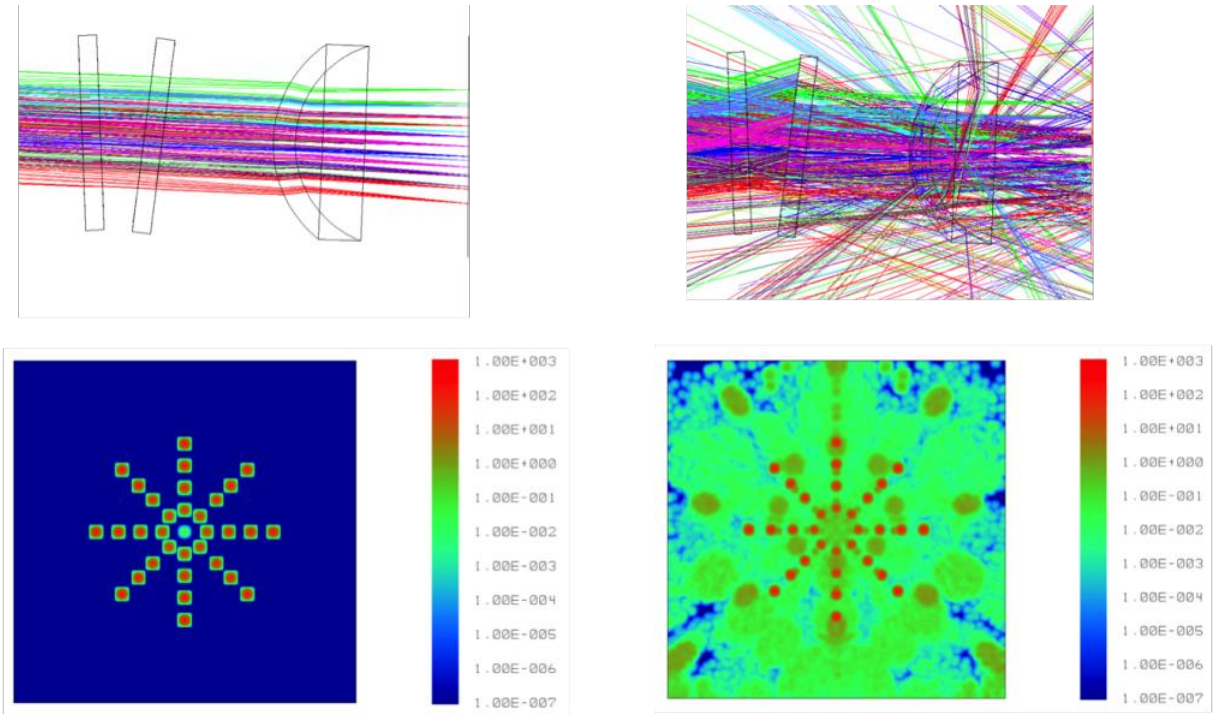

Figure 2.5: Result of non-sequential ghost simulation in ZEMAX. *top left* panel shows image formation corresponding to different field points without any splitting from filter and lens surfaces; *bottom left* depicts images of the grid of field points depicted in *top left*; *top right* panel shows image formation along with with ray spitting mimicking the real scenario; *bottom right* shows spurious patterns (Ghost) formed on the image plane apart formed specular field images from the ray tracing in *top right* figure.

2.2.4.5 Strategy of Ghost Reduction

For the parallel science filter configuration high value of ghost measure was obtained as depicted 'config1' of Table 2.3. This undesirable, as we opt for a ghost flux of the

Table 2.3: Gost Optimization

Filter (nm)	Ghost Measure				
	config1	config2	config3	config4	config5
274.7	14.01	13.03	15.17	a) 5.31, b) 5.43	3.11

order of photon noise (SNR=100 for dark regions). To reduce the ghost flux within FoV we opted for different filter arrangements as mentioned below:

- config1=Without additional filter tilt or Filter coating flip
- config2=filter coating flip
- config3=filter 1 and 2 swap with tilt in same direction
- config4=tilt in same direction
- config5=filters oppositely tilted at 9.5°

We thus found the 'config5' as the best arrangement. However, filter tilts cause blue-shift of central wavelengths and also change of bandwidth for converging beam.To accommodate these tilts, red-shift at normal incidence and bandwidth adjustments are needed which are currently under consideration.

2.2.4.6 Ghost Indices for Different Filters

Table 2.4 shows the ghost measures for all the filter bands and different options of CCD coatings with 'config5'. The 24 nm coating was found to give the most uniform results for all the filters.

2.3 Tolrance Analysis for SUIT

2.3.1 Need of Tolerance Analysis

Tolerance analysis is a vital part of any optical system design and analysis. This analysis specifies the tolerances of different parameter perturbations in the optical system during

Table 2.4: Gost Measure for tilted filter configuration

Filters (nm)	Ghost Measure for CCD coatings (nm)		
	18	24	30
320-360	1.06	1.03	0.53
200-242	5.20	6.32	7.04
242-300	4.54	4.20	4.50
214	4.16	5.07	5.70
274.7	2.95	2.52	3.11
279.6	2.93	2.45	2.80
280.3	3.09	2.50	2.77
283.2	2.92	2.29	2.40
300	4.83	4.02	3.80
388	3.34	3.01	2.54
397.8	4.85	4.60	4.30

fabrication and alignment according to acceptable performance criteria. The tolerances are found by studying how sensitive are difference design parameters in terms of imaging performance and also the feasibility of manufacturing process. Optical design softwares namely ZEMAX and CODE V are standard in performing tolerance analysis of optical systems. They offer immense flexibility in choosing performance criteria and tolerance operands.

2.3.2 Fabrication and Alignment Tolerance

To find the tolerance first the parameters, also called tolerance operands, were identified. Following subsections present the steps to achieve the set of tolerance values.

2.3.2.1 Optical Parameter Errors

SUIT manufacturing tolerances consider errors such as RoC (Radius of Curvature), Test plate fit, Conic Constant, Off Axis Distance, surface irregularity, thickness, glass refractive index, element wedge. Some of these are described below.

1. **Surface irregularity:** This is defined as the peak-to-valley low frequency surface height fluctuation expressed in terms of number of fringes.

2. **Test plate fit:** This is similar to RoC tolerance. It is generally used to define RoC error for flat surfaces in terms of number of fringes.

3. **Element wedge:** This measures the taper of any optical element which is the difference of upper and lower edge width. It is expressed in terms of angle which is the ratio of edge width difference and aperture diameter.

Alignment tolerances considered were typically element tilts, decenters and component-to-component distances.

2.3.2.2 Compensators

When tolerance analysis is done without using compensators, very tight tolerances are achieved. Those often challenge feasibility of manufacturing. Thus, commonly

compensators are used, which are parameters of the optical set-up such as component-to-component distances, element tilts etc. The compensators try to balance the image degradation caused by other parameter errors. The compensators used in SUIT tolerance study are the following-

1. M1 to M2 separartion
2. Lens to Image plane Separation
3. M2 x-decentre
4. M2 y-decentre
5. M2 x-tilt
6. M2 y-tilt

Individual tolerances were derived from inverse sensitivity analysis putting imaging performance upper limits and the compensators. The individual tolerances were then relaxed or tightened based on feasibility of manufacturing process. To estimate the cumulative effect of the individual errors on image quality Modulation Transfer Function (MTF) was used as performance descriptor and TOR simulation was done in CODE V as described in the following subsections.

2.3.2.3 MTF as Descriptor for Image Quality

To bring consistency in resolution estimation we have considered resolution as the separation between Point Spread Functions (PSF) for two point sources at the worst field which brings dip of the added pattern till $\approx 26\%$ less than peaks. Now for ease of calculation we tried to find the MTF value for a spatial frequency corresponding to the PSF separation mentioned. For aberration free circular entrance aperture (diameter=d) the PSF for wavelength λ and angle θ is given by:

$$PSF(\lambda, d, \theta) = \left[\frac{2J_1(\pi d \sin\theta/\lambda)}{\pi d \sin\theta/\lambda}\right]^2$$

Considering Rayleigh resolution limit [Born et al. 1999] of 1.22 λ/d as PSF separation added profile of two identical PSFs gives the dip at the middle with respect to peak as:

$$\frac{1+\left[\frac{2J_1(1.22\pi)}{1.22\pi}\right]^2-2\left[\frac{2J_1(0.61\pi)}{0.61\pi}\right]^2}{1+\left[\frac{2J_1(1.22\pi)}{1.22\pi}\right]^2}=26.54\%$$

Corresponding MTF at spatial frequency f follows the following expression:

$$MTF(f)=\frac{2}{\pi}\left[\cos^{-1}\frac{f}{f_c}-\frac{f}{f_c}\sqrt{1-(f/f_c)^2}\right]$$

for $f \leq f_c$

f_c is the cut-off frequency at which MTF becomes zero or in other words it corresponds to the PSF separation of Sparrow resolution limit i.e. $0.94\lambda/d$. Hence, $f_c = \frac{d}{0.94\lambda F}$ with F being the telescope focal length. For separation corresponding to Rayleigh resolution limit i.e. $f = \frac{d}{1.22\lambda F}$, MTF becomes 12.73%. The factor of 2 difference between PSF intersection dip and MTF for certain separation and corresponding spatial frequency respectively can be observed. As this analysis considers only an ideal case, we checked the same for SUIT PSFs at different fields and wavelengths.

Figure 2.6a shows PSF intersection for 200 nm at (0, 0) degree field with separation of 24 microns (2 pixel separation) and Figure 2.6b shows corresponding tangential and sagittal MTF variation till the spatial frequency equivalent to the PSF separation. It can be observed that the PSF intersection dip is 98% less compared to the peak whereas the MTF falls to 45% at 42 cyles/mm i.e. $\frac{1}{2\times12\mu m}$. For Figure 2.6c and Figure 2.6d the dip becomes 89% less compared to the peak whereas MTF falls to 36% at 42 cycles/mm. So, it can concluded from the analysis that if MTF is > 13% at certain spatial frequency the dip should be at least 26% less than peak for PSF intersection with separation corresponding to MTF spatial frequency.

2.3.2.4 Tolerance Simulation Method

Monte Carlo simulation is an effective way to estimate the tolerances. It is a method which iteratively evaluates a deterministic model using sets of random numbers as inputs. Each of inputs can follow different probability distributions. Others faster techniques are now being available to study the cumulative effect of different parameter perturbations on imaging performance. CODE V's primary tolerance analysis option, TOR, supports the following performance metrics-

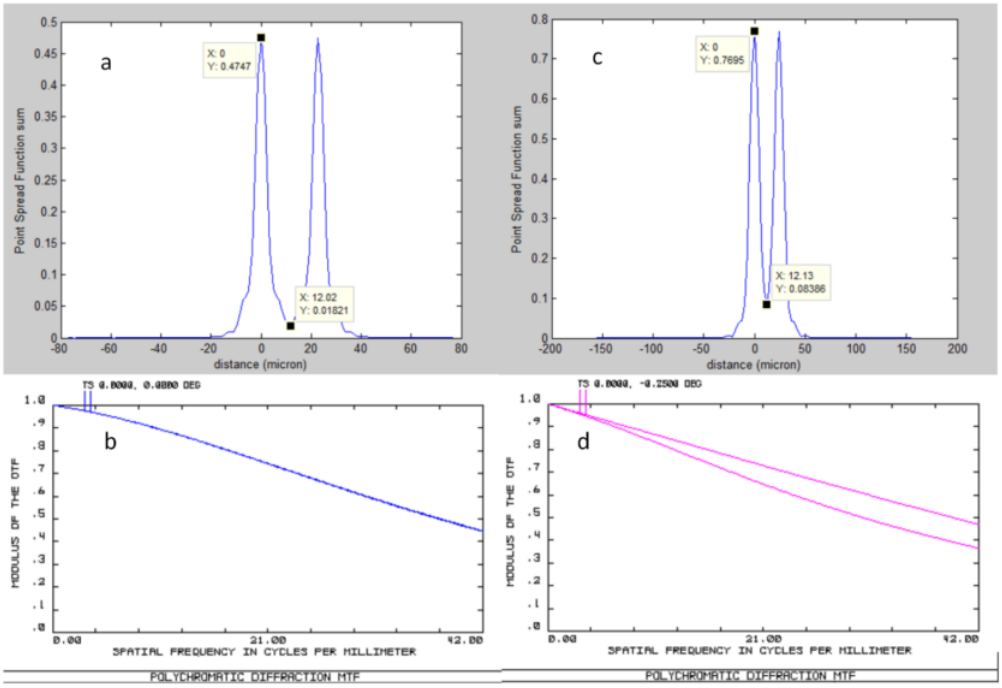

Figure 2.6: (a) Intersection of two identical PSFs at field (0,0) degree for 200 nm wavelength; (b) Tangential and Sagittal MTF at field (0,0) degree for 200 nm wavelength; Because of circular PSF cross-section for this field tangential and sagittal MTFs are not very different. (c) Intersection of two identical PSFs at field (0,-0.25) degree for 400 nm wavelength; (d) Tangential and Sagittal MTF at field (0,-0.25) degree for 400 nm wavelength. Because of elliptical PSF cross-section for this field tangential and sagittal MTFs differ.

1. Diffraction MTF

2. RMS Wavefront error

3. Fiber Coupling Efficiency

4. Polarization Dependent Loss

5. Zernike Wavefront Coefficients

TOR uses a Fast Wavefront Differential algorithm to determine the performance impact due to tolerances. Required information computed from a real ray trace of the nominal system. It includes simultaneous occurrence of different parameter perturbations. It can be 50 to 1000 times faster than Monte Carlo method.

As 2 pixel separation is the minimum that should be resolved by SUIT we used the MTF value at corresponding frequency i.e. $\frac{1}{2\times12\mu m} \approx 42$ cycles/mm as the image quality criteria and performed the TOR simulation in CODE V.

2.3.2.5 Simulation Result

From the simulation we find that all the cases of simultaneous errors provide an MTF greater that 30% at 42 cycles/mm for all the field angles (Figure 2.7). This is much higher than the minimum MTF requirement of 13%. The fabrication and alignment tolerances are presented in Table 2.5 and Table 2.6 respectively along with the probable compensator movements in Table 2.7. It should be noted that, when using some parameter as compensator, the tolerance on the same is nullified. The tolerance on different parameters are not relaxed more to allow some margin on MTF for other effects such as thermal degradation.

2.4 Thermal Tolerance Analysis

Thermal fluctuation on-board can degrade image quality of the telescope mainly because of change in component-to-component separation. Thus, there should be control

Table 2.5: Manufacturing Tolerance for SUIT optical components

Components	Parameters	Nominal	Min.	Max.	Units
Thermal Filter	Test plate fit	0	-3λ/2	3λ/2	λ=632 nm
	Surface irregularity (P-V)	0		λ/4	λ=632 nm
	Thickness	10	-0.05	0.05	mm
	Wedge	0	-10	10	arcsec
	nd	1.458464	-0.0005	0.0005	
	vd	67.82	-0.5%	0.5%	
Primary Mirror (M1)	RoC	-1404.66906	-2	2	mm
	Conic Constant	-1.0255	-0.001	0.001	
	OAD	159	-0.15	0.15	mm
	Surface irregularity (P-V)	0		λ/10	λ=632 nm
Secondary Mirror (M2)	RoC	-438.252	-0.6	0.6	mm
	Conic Constant	-2.4867	-0.002	0.002	
	OAD	40	-0.15	0.15	mm
	Surface irregularity(P-V)	0 0		λ/10	λ=632 nm
Science Filter1 (F1)	Test plate fit	0	-λ	λ	λ=632 nm
	Surface irregularity (P-V)	0		λ/6	λ=632 nm
	Thickness	5	-0.03	0.03	mm
	Wedge	0	-10	10	arcsec
	nd	1.458464	-0.0005	0.0005	
	vd	67.82	-0.5%	0.5%	
Science Filter2 (F2)	Test plate fit	0	-λ	λ	λ=632 nm
	Surface irregularity (P-V)	0		λ/6	λ=632 nm
	Thickness	5	-0.03	0.03	mm
	Wedge	0	-10	10	arcsec
	nd	1.458464	-0.0005	0.0005	
	vd	67.82	-0.5%	0.5%	
Lens (L)	RoC front	32.971	-0.01	0.01	mm
	RoC back	28.0369	-0.01	0.01	mm
	Surface irregularity(P-V)	0		λ/6	λ=632 nm
	Thickness	6	-0.02	0.02	mm
	Wedge	0	-10	10	arcsec
	nd	1.458464	-0.0005	0.0005	
	vd	67.82	-0.5%	0.5%	

Table 2.6: Alignment Tolerance for SUIT optical components

Components	Parameters	Nominal	Min.	Max.	Units
Thermal Filter	Tilt X	0	-61.92"	61.92"	Degree/arcsec
	Tilt Y	0	-61.92"	61.92"	Degree/arcsec
Primary Mirror (M1)	Decenter X	0	-0.05	0.05	mm
	Decenter Y	0	-0.05	0.05	mm
	Tilt X	0	-61.92"	61.92"	Degree/arcsec
	Tilt Y	0	-61.92"	61.92"	Degree/arcsec
	M1 to M2 distance	600.803	-0.2	0.2	mm
Secondary Mirror (M2)	Decenter X	0	-0.05	0.05	mm
	Decenter Y	0	-0.05	0.05	mm
	Tilt X	0	-61.92"	61.92"	Degree/arcsec
	Tilt Y	0	-61.92"	61.92"	Degree/arcsec
	M2 to F1 distance	527.8067	-0.1	0.1	mm
Science Filter1 (F1)	Decenter X	0	-0.02	0.02	mm
	Decenter Y	3.5	-0.02	0.02	mm
	Tilt X	-2.2432°	-61.92"	61.92"	Degree/arcsec
	Tilt Y	0	-61.92"	61.92"	Degree/arcsec
	F1 to F2 distance	12	-0.03	0.03	mm
Science Filter2 (F2)	Decenter X	0	-0.02	0.02	mm
	Decenter Y	3.5	-0.02	0.02	mm
	Tilt X	7.2568°	-61.92"	61.92âĂİ	Degree/arcsec
	Tilt Y	0	-61.92"	61.92"	Degree/arcsec
	F2 to L distance	30	-0.03	0.03	mm
Lens (L)	Decenter X	0	-0.02	0.02	mm
	Decenter Y	3.5	-0.02	0.02	mm
	Tilt X	2.3432°	-61.92"	61.92"	Degree/arcsec
	Tilt Y	0	-61.92"	61.92"	Degree/arcsec
	L to D distance	47	-0.02	0.02	mm
Detector (D)	Decenter X	0	-2	2	mm
	Decenter Y	3.5	-2	2	mm
	Tilt Y	0	-180"	180"	Degree/arcsec

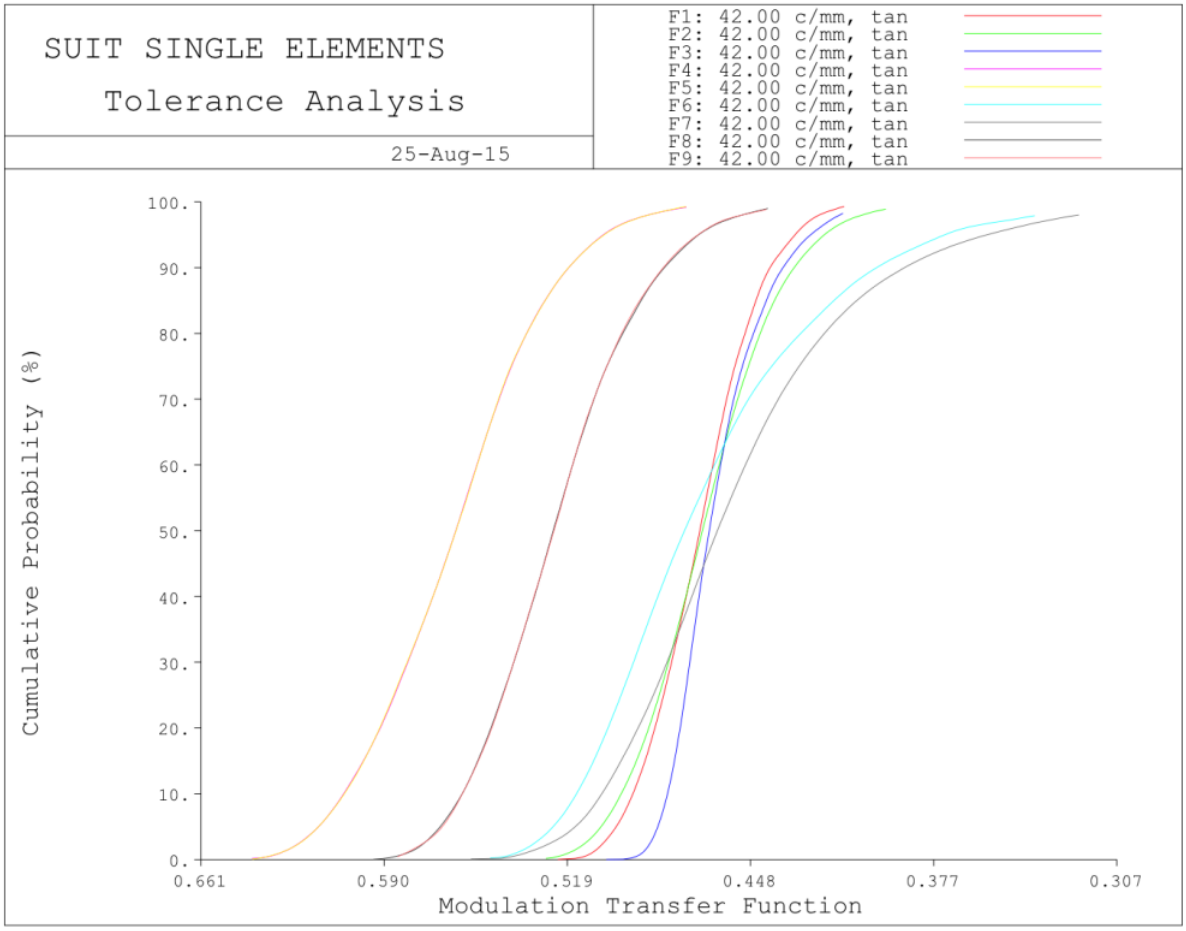

Figure 2.7: Cumulative probability plot for SUIT MTF value at the spatial frequency 42 cycles/mm after tolerancing in CODE V

of the temperature and proper requirement on that should be placed. The following subsections present the first order analyses made for placing the requirements on temperature control.

2.4.1 Thermal Expansion of Optical Base Plate

Effects of temperature fluctuation at space are namely thermal expansion of frame, RoC (Radius of curvature) change, filter thickness and refractive index change. $L(T1) - L(T) = \alpha(T1 - T)L(T)$ and $RoC(T1) - RoC(T) = \alpha(T1 - T)RoC(T)$ where α is the coefficient of thermal expansion (CTE synonymous to TCE). T and $T1$ are the initial and final temperatures respectively. $L(T)$ is the linear dimension at temperature T. Change in these parameters degrade image quality if proper compensator is not used.

Table 2.7: Probable compensator movements

M1 to M2 separartion	1.208836 mm
Lens to Image plane Separation	0.609211 mm
M2 x-decentre	0.243454 mm
M2 y-decentre	0.315480 mm
M2 x-tilt	0.057816 degree
M2 y-tilt	0.040618 degree

2.4.2 Thermal Compensation using Focusing Mechanism

Thermal expansion causes the distance between primary and secondary to change. This in turn cause a focus shift of the amount $\approx m^2\Delta z$ where m is magnification of the secondary mirror and Δz denotes the change the primary to secondary separation due to thermal expansion. A the field corrector lens is easier to move than the image plane, the lens is moved on a linear stage to compensate for the image degradation. In the following two subsections two scenarios for first order thermal effects are presented with lens movement as the compensator.

2.4.2.1 Uniform Temperature

Linear dimensions of any optical setup change according to thermal expansion coefficient of the material used. Zerodur will be the glass material used for SUIT mirrors having Coefficient of Thermal Expansion or TCE= $-0.08 \times 10^{-6}/°C$. Fused UV grade SILICA will be used for SUIT filters and lenses having TCE= $0.51 \times 10^{-6}/°C$. For SUIT baseplate Titanium alloy will be used having TCE= $8.8 \times 10^{-6}/°C$. Multi-configuration editor in ZEMAX was used to simulate SUIT system configuration at different temperatures as integrated effect of different material expansions. Modulation Transfer Function has been considered as the performance descriptor which is the absolute value of Fourier Transform of Point Spread Function (PSF). As PSF becomes broader MTF becomes narrower i.e. the contrast at different spatial frequencies reduces. Nyquist frequency for SUIT is given by $1/(2 \times pixelsize) = 1000/24(mm^{-1}) \approx 42$ cycles/mm.

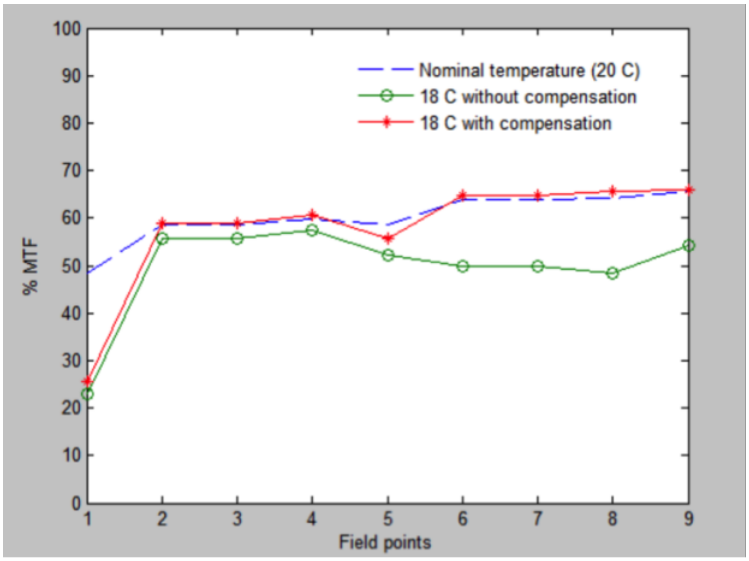

Figure 2.8: Improvement of image quality at different field points (depicted by columns of the table) with lens movement for 214 nm filter when temperature goes 2 C below operating one.

More than this critical frequency can not be resolved by SUIT. Minimum of tangential and sagittal MTF values are studies at mentioned spatial frequency for different filters when temperature change occurs. Tables 2.8,2.9,2.10 depict if the field corrector lens is allowed to move towards or away from image plane from its nominal position it can keep the MTF value at 42 cycles/mm more than the acceptable limit of 13% for all the filters and field points within a constant temperature excursion ±3°C about operating temperature. The improvement in image quality with lens movement can be observed from Figure 2.8. However, it could only marginally improve the image quality for central field. Also, the lens movement with temperature change was found to be linear.

2.4.2.2 Gradient Along Tube

In the previous section we presented the temperature change by a constant amount throughout the baseplate. In this section the effect of temperature gradient on image quality will be studied. It is assumed that temperature gradient is constant i.e. temperature varies linearly over optical path. $T(0)$ is the temperature of the baseplate region where operating temperature is maintained. $T(l)$ is the temperature of the baseplate at its ends with l being the distance from the point where temperature is $T(0)$.

$$T(x) = T(0) + \frac{T(l) - T(0)}{l} x$$

Table 2.8: Effect of +/- 1°C temperature excursion from Nominal on optical performance

Filter (nm)	Temperature (°C)	Minimum of tangential and sagittal MTF at 42 cycles/mm									Lens movement about its nominal position (mm)
		(0°,0°)	(0.25°,0°)	(-0.25°,0°)	(0°,0.25°)	(0°,-0.25°)	(0.39°,0°)	(-0.39°,0°)	(0°,0.39°)	(0°,-0.39°)	
214	Nominal	48.3326	58.7319	58.7319	59.8374	58.6972	63.8582	63.8582	64.1799	65.5333	0
	Nominal-1	37.1306	64.5243	64.5243	64.9619	64.2670	64.4045	64.4045	65.2057	65.7828	0.4792
	Nominal+1	57.8735	51.4879	51.4879	53.4821	51.8076	63.1548	63.1548	62.7096	65.1613	-0.4325
274.7	Nominal	53.0287	47.9745	47.9745	49.0130	47.8686	55.1238	55.1238	55.8931	56.2424	0
	Nominal-1	45.3482	53.5237	53.5237	53.9736	53.1896	55.2996	55.2996	56.2163	56.2211	0.4792
	Nominal+1	58.7302	41.5706	41.5706	43.3196	41.7749	54.5427	54.5427	53.3450	55.8073	-0.4325
279.6	Nominal	52.9587	47.3677	47.3677	48.3941	47.2585	54.4090	54.4090	55.1863	55.4993	0
	Nominal-1	45.5213	52.8396	52.8396	53.2879	52.5044	54.5741	54.5741	55.4844	55.4731	0.4792
	Nominal+1	58.4326	41.0692	41.0692	42.7916	41.2656	53.7905	53.7905	52.5962	55.0380	-0.4325
280.3	Nominal	52.9454	47.2831	47.2831	48.3077	47.1734	54.3066	54.3066	55.0847	55.3929	0
	Nominal-1	45.5421	52.7436	52.7436	53.1916	52.4082	54.4703	54.4703	55.3794	55.3663	0.4792
	Nominal+1	58.3877	40.9998	40.9998	42.7183	41.1950	53.6850	53.6850	52.4914	54.9300	-0.4325
283.2	Nominal	52.8821	46.9375	46.9375	47.9548	46.8260	53.8811	53.8811	54.6623	54.9516	0
	Nominal-1	45.6188	52.3503	52.3503	52.7972	52.0145	54.0396	54.0396	54.9438	54.9232	0.4792
	Nominal+1	58.1953	40.7176	40.7176	42.4202	40.9082	53.2524	53.2524	52.0626	54.4869	-0.4325
300	Nominal	52.2853	45.0679	45.0679	46.0422	44.9454	51.4093	51.4093	52.1920	52.3942	0
	Nominal-1	45.7847	50.1857	50.1857	50.6269	49.8480	51.5295	51.5295	52.3958	52.3476	0.4792
	Nominal+1	56.9153	39.2236	39.2236	40.8344	39.3869	50.8718	50.8718	49.7216	52.0416	-0.4325
388	Nominal	45.7329	37.5482	37.5482	38.2824	37.3971	38.7131	38.7131	39.2503	39.4054	0
	Nominal-1	42.1552	40.9850	40.9850	41.3777	40.6783	38.8645	38.8645	39.4005	39.4596	0.4792
	Nominal+1	48.0278	33.6535	33.6535	34.7981	33.7041	38.5112	38.5112	38.9457	39.3123	-0.4325
397.8	Nominal	44.7950	36.7781	36.7781	37.4858	36.6274	37.3618	37.3618	37.8672	38.0248	0
	Nominal-1	41.4567	40.0368	40.0368	40.4225	39.7369	37.5138	37.5138	38.0143	38.0853	0.4792
	Nominal+1	46.9172	33.0840	33.0840	34.1793	33.1263	37.1630	37.1630	37.5755	37.9287	-0.4325
200-242	Nominal	49.1403	57.1059	57.1059	58.2721	56.9612	62.5532	62.5532	62.0589	64.3529	0
	Nominal-1	38.3787	62.6254	62.6254	63.1692	62.2119	62.5976	62.5976	62.0966	64.5070	0.4792
	Nominal+1	58.0680	50.0892	50.0892	52.0859	50.3396	62.0985	62.0985	61.3127	63.8326	-0.4325
242-300	Nominal	52.7201	48.6249	48.6249	49.6401	48.5422	54.8790	54.8790	56.0914	55.3777	0
	Nominal-1	44.8017	54.2174	54.2174	54.6585	53.8850	55.4437	55.4437	56.6727	55.8880	0.4792
	Nominal+1	58.6198	42.1168	42.1168	43.8353	42.3647	54.0982	54.0982	54.1312	54.6834	-0.4325
320-360	Nominal	49.7680	41.3988	41.3988	42.2488	41.2733	45.3079	45.3079	46.0848	46.0467	0
	Nominal-1	44.7754	45.7562	45.7562	46.1647	45.4398	45.4958	45.4958	46.2900	46.1157	0.4792
	Nominal+1	53.1388	36.4559	36.4559	37.8325	36.5786	45.0350	45.0350	45.0926	45.9109	-0.4325

Table 2.9: Effect of +/- 2°C temperature excursion from Nominal on optical performance

Filter (nm)	Temperature (°C)	Minimum of tangential and sagittal MTF at 42 cycles/mm									Lens movement about its nominal position (mm)
		(0°,0°)	(0.25°,0°)	(-0.25°,0°)	(0°,0.25°)	(0°,-0.25°)	(0.39°,0°)	(-0.39°,0°)	(0°,0.39°)	(0°,-0.39°)	
214	Nominal	48.3326	58.7319	58.7319	59.8374	58.6972	63.8582	63.8582	64.1799	65.5333	0
	Nominal-2	25.5387	58.9625	58.9625	60.5348	55.8184	64.7413	64.7413	65.7002	65.9104	0.9256
	Nominal+2	65.1243	43.3534	43.3534	46.3371	44.0971	62.1757	62.1757	60.5979	63.4741	-0.8867
274.7	Nominal	53.0287	47.9745	47.9745	49.0130	47.8686	55.1238	55.1238	55.8931	56.2424	0
	Nominal-2	36.4065	58.0090	58.0090	58.0744	57.5647	55.4090	55.4090	56.2581	56.1972	0.9256
	Nominal+2	62.2113	34.7282	34.7282	37.2272	35.2789	50.1750	50.1750	48.2078	51.1020	-0.8867
279.6	Nominal	52.9587	47.3677	47.3677	48.3941	47.2585	54.4090	54.4090	55.1863	55.4993	0
	Nominal-2	36.8039	57.2837	57.2837	57.3514	56.8370	54.6783	54.6783	55.5145	55.4479	0.9256
	Nominal+2	61.7216	34.3484	34.3484	36.8048	34.8854	49.4638	49.4638	47.5197	50.3754	-0.8867
280.3	Nominal	52.9454	47.2831	47.2831	48.3077	47.1734	54.3066	54.3066	55.0847	55.3929	0
	Nominal-2	36.8566	57.1814	57.1814	57.2494	56.7344	54.5740	54.5740	55.4082	55.3411	0.9256
	Nominal+2	61.6502	34.2963	34.2963	36.7467	34.8314	49.3645	49.3645	47.4240	50.2739	-0.8867
283.2	Nominal	52.8821	46.9375	46.9375	47.9548	46.8260	53.8811	53.8811	54.6623	54.9516	0
	Nominal-2	37.0647	56.7607	56.7607	56.8301	56.3126	54.1413	54.1413	54.9671	54.8985	0.9256
	Nominal+2	61.3507	34.0861	34.0861	36.5114	34.6132	48.9590	48.9590	47.0337	49.8595	-0.8867
300	Nominal	52.2853	45.0679	45.0679	46.0422	44.9454	51.4093	51.4093	52.1920	52.3942	0
	Nominal-2	37.9697	54.4072	54.4072	54.4889	53.9557	51.6242	51.6242	52.3983	52.3287	0.9256
	Nominal+2	59.5223	33.0085	33.0085	35.2911	33.4895	46.7648	46.7648	44.9414	47.6129	-0.8867
388	Nominal	45.7329	37.5482	37.5482	38.2824	37.3971	38.7131	38.7131	39.2503	39.4054	0
	Nominal-2	37.5117	43.8936	43.8936	44.0485	43.4925	39.0060	39.0060	39.4653	39.5321	0.9256
	Nominal+2	49.0301	29.4915	29.4915	31.0819	29.7689	38.1082	38.1082	36.9604	38.7190	-0.8867
397.8	Nominal	44.7950	36.7781	36.7781	37.4858	36.6274	37.3618	37.3618	37.8672	38.0248	0
	Nominal-2	37.0958	42.7971	42.7971	42.9589	42.4059	37.6570	37.6570	38.0851	38.1636	0.9256
	Nominal+2	47.8197	29.1306	29.1306	30.6493	29.3907	36.9139	36.9139	36.1828	37.8046	-0.8867
200-242	Nominal	49.1403	57.1059	57.1059	58.2721	56.9612	62.5532	62.5532	62.0589	64.3529	0
	Nominal-2	27.0934	59.0855	59.0855	60.6829	56.2568	62.2236	62.2236	61.4223	64.3141	0.9256
	Nominal+2	64.7894	42.1476	42.1476	45.0685	42.8546	60.5769	60.5769	58.9588	61.8597	-0.8867
242-300	Nominal	52.7201	48.6249	48.6249	49.6401	48.5422	54.8790	54.8790	56.0914	55.3777	0
	Nominal-2	35.6778	58.6640	58.6640	58.7425	57.4985	55.8168	55.8168	56.8397	56.2672	0.9256
	Nominal+2	62.3423	35.1340	35.1340	37.5998	35.7445	50.8782	50.8782	48.9978	51.8947	-0.8867
320-360	Nominal	49.7680	41.3988	41.3988	42.2488	41.2733	45.3079	45.3079	46.0848	46.0467	0
	Nominal-2	38.5366	49.4088	49.4088	49.5132	48.9819	45.6520	45.6520	46.3389	46.1936	0.9256
	Nominal+2	54.8328	31.2014	31.2014	33.1392	31.5995	42.5146	42.5146	40.9988	43.2626	-0.8867

Table 2.10: Effect of +/- 3°C temperature excursion from Nominal on optical performance

Filter (nm)	Temperature (°C)	Minimum of tangential and sagittal MTF at 42 cycles/mm									Lens movement about its nominal position (mm)
		(0°,0°)	(0.25°,0°)	(-0.25°,0°)	(0°,0.25°)	(0°,-0.25°)	(0.39°,0°)	(-0.39°,0°)	(0°,0.39°)	(0°,-0.39°)	
214	Nominal	48.3326	58.7319	58.7319	59.8374	58.6972	63.8582	63.8582	64.1799	65.5333	0
	Nominal-3	14.6433	50.3976	50.3976	51.7457	46.0214	64.9864	64.9864	65.8654	63.9724	1.3767
	Nominal+3	69.7184	34.7984	34.7984	38.7467	35.9737	57.1810	57.1810	54.3427	57.7766	-1.3408
274.7	Nominal	53.0287	47.9745	47.9745	49.0130	47.8686	55.1238	55.1238	55.8931	56.2424	0
	Nominal-3	26.9526	54.4474	54.4474	55.3255	51.6530	55.4642	55.4642	56.0795	56.1482	1.3767
	Nominal+3	63.3884	27.7609	27.7609	30.9666	28.6521	45.1063	45.1063	42.3820	45.5154	-1.3408
279.6	Nominal	52.9587	47.3677	47.3677	48.3941	47.2585	54.4090	54.4090	55.1863	55.4993	0
	Nominal-3	27.5279	54.3236	54.3236	55.1726	51.6296	54.7303	54.7303	55.3311	55.3988	1.3767
	Nominal+3	62.7375	27.5079	27.5079	30.6567	28.3799	44.4627	44.4627	41.7818	44.8646	-1.3408
280.3	Nominal	52.9454	47.2831	47.2831	48.3077	47.1734	54.3066	54.3066	55.0847	55.3929	0
	Nominal-3	27.6062	54.3027	54.3027	55.1476	51.6228	54.6258	54.6258	55.2245	55.2922	1.3767
	Nominal+3	62.6442	27.4739	27.4739	30.6146	28.3432	44.3734	44.3734	41.6988	44.7743	-1.3408
283.2	Nominal	52.8821	46.9375	46.9375	47.9548	46.8260	53.8811	53.8811	54.6623	54.9516	0.01
	Nominal-3	27.9209	54.2081	54.2081	55.0365	51.5856	54.1924	54.1924	54.7824	54.8507	2.25
	Nominal+3	62.2572	27.3382	27.3382	30.4456	28.1963	44.0100	44.0100	41.3622	44.4068	-2.24
300	Nominal	52.2853	45.0679	45.0679	46.0422	44.9454	51.4093	51.4093	52.1920	52.3942	0
	Nominal-3	29.4525	53.4379	53.4379	54.1781	51.1223	51.6753	51.6753	52.2172	52.2910	1.3767
	Nominal+3	60.0056	26.6845	26.6845	29.6046	27.4791	42.0785	42.0785	39.5940	42.4534	-1.3408
388	Nominal	45.7329	37.5482	37.5482	38.2824	37.3971	38.7131	38.7131	39.2503	39.4054	0
	Nominal-3	32.0772	46.0850	46.0850	46.1310	44.9762	39.1282	39.1282	39.4397	39.5979	1.3767
	Nominal+3	48.6458	25.1936	25.1936	27.2303	25.7046	34.9389	34. 9389	33.3704	35.2460	-1.3408
397.8	Nominal	44.7950	36.7781	36.7781	37.4858	36.6274	37.3618	37.3618	37.8672	38.0248	0
	Nominal-3	31.9619	44.8838	44.8838	44.9424	44.0603	37.7833	37.7833	38.0734	38.2370	1.3767
	Nominal+3	47.4121	25.0388	25.0388	26.9842	25.5243	34.2532	34.2532	32.7772	34.5533	-1.3408
200-242	Nominal	49.1403	57.1059	57.1059	58.2721	56.9612	62.5532	62.5532	62.0589	64.3529	0
	Nominal-3	16.3309	51.0312	51.0312	52.4184	46.9595	61.5170	61.5170	60.1973	63.8079	1.3767
	Nominal+3	68.8925	33.7638	33.7638	37.5822	34.9234	55.4080	55.4080	52.7262	56.1388	-1.3408
242-300	Nominal	52.7201	48.6249	48.6249	49.6401	48.5422	54.8790	54.8790	56.0914	55.3777	0
	Nominal-3	26.1215	54.1298	54.1298	55.0948	51.2841	56.0286	56.0286	56.6675	56.5173	1.3767
	Nominal+3	63.7558	28.0167	28.0167	31.1881	28.9762	45.8024	45.8024	43.1372	46.2933	-1.3408
320-360	Nominal	49.7680	41.3988	41.3988	42.2488	41.2733	45.3079	45.3079	46.0848	46.0467	0
	Nominal-3	31.4868	50.5683	50.5683	51.1478	48.8402	45.7687	45.7687	46.2425	46.2509	1.3767
	Nominal+3	54.7468	25.8312	25.8312	28.3132	26.5049	38.5183	38.5183	36.4622	38.8708	-1.3408

Table 2.11: Effect of temperature gradient over optical path on image quality

Filter (nm)	Configuration	Minimum of tangential and sagittal MTF at 42 cycles/mm									Lens Movement (mm)
		0,0	0.25,0	-0.25,0	0,0.25	0,-0.25	0.39,0	-0.39,0	0,0.39	0,-0.39	
214	1	25.6387	59.0434	59.0434	60.6017	55.8937	64.7373	64.7373	65.6962	65.9090	0.9214
	2	65.0595	43.4239	43.4239	46.4222	44.1804	62.1931	62.1931	60.6411	63.5137	-0.8829
	3	36.3981	64.8853	64.8853	65.2668	63.2230	64.3783	64.3783	65.1676	65.7745	0.4930
	4	58.3289	51.0507	51.0507	53.1479	51.4248	63.0751	63.0751	62.5315	65.1108	-0.4647

$$\Delta L = \int_0^L \alpha \left[T(x) - T(0)\right] dx = \alpha \frac{T(l) - T(0)}{l} \int_0^L x dx = \alpha \frac{T(l) - T(0)}{2l} L^2$$

L is the position of any optical component from the reference position and ΔL corresponds to the change in position. Four configurations for the 214 nm filter were simulated as below.

1. -3°C to 0°C temperature change from telescope front to back with linear profile
2. +3°C to 0°C temperature change from telescope front to back with linear profile
3. -3°C to +3°C temperature change from telescope front to back with linear profile
4. +3°C to -3°C temperature change from telescope front to back with linear profile

This filter was chosen as all other filters provided better performance for constant temperature change over baseplate. Again the simulation results presented in Table 2.11 show all the MTFs to be well within the acceptable limit i.e. greater than 13%

2.5 Discussion and Conclusion

Optimization of optical system should be performed using appropriate design requirements, constraints and a ray tracing [Spencer & Murty 1962] simulation software to optimize the aberrations. Again, tolerance study of the design must be done to address uncertainty in manufacturing process [Ma 2013, Milby 2009]. This work thus performed optimization of SUIT optics generating an off-axis Ritchey-Cretien configuration with a negative meniscus field corrector lens (Figure 2.3). Optimization ensured a pixel limited spatial resolution of 1.4". In estimating ghost-to-specular flux ratio a mathematical model was developed, which could be used for different CCD reflectivities to chose appropriate coating (Table 2.4). Appropriate coating ensures uniform response across

a wavelength regime of interest [Kelt et al. 2006]. Minimization of ghost flux resulted in optimal tilt of the science filters. Tolerance analysis was performed simulating effect of simultaneous fabrication and alignment errors on image quality. MTF at 42 cycles/mm was used as the image quality descriptor [King 1969, Rimmer 1978]. All the cases simulated in tolerance study provided MTF values which were well within acceptable limits[Born et al. 1999] providing a set of fabrication and alignment tolerances. Next, thermal tolerances were analysed simulating optical base-plate expansion under constant temperature shift and gradient condition. Using, the field corrector lens as compensator, it was found that a temperature fluctuation ±3°C about nominal operating temperature can be tolerated with a temperature gradient from telescope tube front to back as high as 6°C. The field corrector lens movement could bring back the image quality close to nominal except for central field within the mention temperature excursion. Also, the movement was found to be linear with temperature change. However, it should be noted that only first order thermal effects [Jamieson 1981] are illustrated here. Effect of thermal change on higher order optical surface deformations and thus image quality is not presented.

Thus this study could present an optimised optical configuration of SUIT and analyse effect of different errors (viz. fabrication, alignment and thermal) in imaging performance of the telescope. Those analyses provided parameter tolerances within imaging performance limit. The analysis results will also help the calibration and alignment of SUIT optics.

Chapter 3

Scattering Analysis of SUIT

3.1 Introduction

Scattering is an inherent property of any optical system. It can cause considerable degradation in the image quality if not properly estimated and controlled. Scatter, in general, scales inversely with wavelength. So, when imaging in the low wavelength regime scatter requires serious consideration. Several factors in an optical system contribute to total scatter. Optical surfaces will unchangeably have height fluctuation in a very high spatial frequency on top of the surface figure which lies in the low frequency domain. The high frequency fluctuations are generally termed as roughness. This surface roughness causes light to spread around specular direction after reflection or refraction. This phenomena is termed as surface scatter. This causes light from one object field to mix with another object field in the image plane degrading the contrast and thereby image quality. Using Kirchoff's diffraction theory, formulation for angle resolved scatter has been derived [Stover et al. 2016]. They are functions of surface power spectral density (PSD), a spatial frequency domain representation of surface height fluctuations [Church & Takacs 1990, Harvey et al. 2014]. Scatter can become close to Lambertian or very directional depending on the nature of PSD [Church & Takacs 1995]. In most of the cases PSDs are seen to fall monotonically after certain spatial frequencies. Inverse of this frequency happens to give the correlation width, the spatial scale within which the surface height fluctuations are correlated. When this angle resolved scatter is integrated over a hemisphere about surface normal it gives estimate

of total scatter being a function of RMS value of surface roughness and also wavelength [Harvey et al. 2012]. But often only small parts of scattering angles are covered by image plane. Among two surfaces with same RMS roughness, more scatter is seen in the image plane due to the surface which has larger correlation width. This is because of the fact that surface with higher correlation width creates most of the scattered power within a small cone angle about specular. Other than surface roughness, different edges in the optical path also cause scatter most of which are of Lambertian type. To restrict these from reaching image plane, baffles are designed with vanes structure to restrict different orders of reflection of edge scattered light from reaching optical surfaces [Plesseria et al. 2003]. All these scatters are strongly dependant on wavelength. But another type scatter exists in the optical systems which is also time varying. This scatter is caused by the contamination of optical surfaces with particulates of sizes greater than wavelength of light. For different types of environments these contaminations are different functions of time. For space telescopes this kind of contamination majorly occur during payload testing and integration. The particulates cause Mie scattering and add to the scattering caused by surface roughness. It is worth mentioning that scatter due to particulate contamination is not a strong function of wavelength. But there should be strict requirements on the operating environments to control this kind of scatter. In this work, we report, scatter modelling and baffle design of Solar Ultraviolet Imaging Telescope (SUIT) on-board the upcoming solar mission ADITYA-L1 intended to image the Sun in Near UltraViolet (NUV) through different filters. The imaging being in ultraviolet needs careful analysis, estimation and control plans for scatter. Different types of scatter contributors and their effect are analyzed in the section 3.2 followed by baffle design in section 3.3 and effect of other ADITYA-L1 payload in section 3.4. In section 3.5, we propose a strategy for scattering reduction and finally conclude in section 3.6 along with necessary discussion.

3.2 Analyzing Scatter Contributors of SUIT

As the imaging is to be performed in near ultraviolet region of electromagnetic spectrum it is immensely important to understand how the imaging performance in terms

of resolution and contrast is going to be affected by scattering. Now, there can various factors causing the scatter. For SUIT, the scattering is majorly contributed by optical surface micro-roughness and particulate contamination. In the following two subsections 3.2.1 and 3.2.2 we will discuss those in detail.

3.2.1 Optical Surface Micro-roughness

It is known that optical surface micro-roughness , the high frequency height fluctuations, contribute significantly to scattered power distributing light in a uniform or directional way about specular direction. Now, when this scattered power over different directions is integrated over the hemisphere about surface normal and divided with the total power including the specular, it is termed as Total Integrated Scatter (TIS) which is inversely related to the wavelength (λ) and dependant on RMS surface micro-roughness (σ) and angle of incidence (θ_i) as the following-

$$TIS = \frac{S}{S+R} \approx (2\pi\Delta n\sigma \cos\theta_i/\lambda)^2$$

when $2\pi\Delta n\sigma \ll \lambda$ and S, R represent scattered power, specular power respectively. Δn stands for the difference in refractive indices between incoming and outgoing light media. For reflective surfaces $\Delta n = 2$. The angular distribution of the scatter defines the directionality or uniformity. This distribution is named as Bidirectional Scattering Distribution Function (BSDF) and TIS can be expressed as integral of the BSDF. It is very intuitive that BSDF has relation with power spectra of the surface spatial frequencies named as Power Spectral Density (PSD). We used the experimental x and y averaged PSD data of polished coupons and fitted the average of them to one dimensional K-correlation PSD form expressed by-

$$S_1(f_x) = \frac{A}{2(1+B^2 f_x^2)^{\frac{c}{2}}}$$

where f_x is the spatial frequency along x and B is the correlation width. $B = 2\pi l_c$ with l_c being surface correlation length, a length scale within which surface height fluctuations are correlated. Experimental fit gave the best fit parameters c and B as 2.0237 and 31.7μm respectively (Figure 3.1). Now, one dimensional and two dimensional PSDs (S_2) are related [Church et al. 1990] by the following-

$$S_1(f_x) = \int_{-\infty}^{\infty} S_2(f_x, f_y) df_y$$

Assumption of rotational symmetry gives-

$$S_2(f_x, f_y) = \frac{AB\Gamma(\frac{c+1}{2})}{2\sqrt{\pi}\Gamma(c/2)(1 + B^2 f_x^2 + B^2 f_y^2)^{\frac{c+1}{2}}}$$

And also, $\sigma^2(\lambda) = 2\pi \int_{1/L}^{1/\lambda} S_2(f) f df$ where $f = \sqrt{f_x^2 + f_y^2}$. $\sigma(\lambda)$ is the wavelength dependent RMS surface micro-roughness and L is the dimension of the test surface which dictates the lowest spatial frequency which can be observed in the PSD. Using the fitted parameters we found $\sigma(\lambda)$ approximately as 15.27Åat $\lambda = 200$ nm. When this 2D PSD is converted to BSDF is takes the form as follows:

$$BSDF(s \neq 2) = \frac{2\pi \Delta n^2 R B^2 \sigma^2(\lambda)(s-2)\cos\theta_i \cos\theta_s}{\lambda^4 [1 - (1 + B^2/\lambda^2)^{1-\frac{s}{2}}](1 + \beta^2 B^2/\lambda^2)^{s/2}}$$

where $s = c + 1$ and $\beta = \sqrt{\sin^2\theta_i + \sin^2\theta_s - 2\sin\theta_i \sin\theta_s \cos\phi}$ with ϕ being the azimuthal angle of the scatter ray with respect to the plane of incidence, R is the surface reflectivity. θ_i and θ_s are angle of incidence and angle of scattered ray with respect to surface normal respectively. Wavelength scaling [Dittman 2006] of RMS surface micro-roughness is given by-

$$\frac{\sigma^2(\lambda_2)}{\sigma^2(\lambda_1)} = \frac{(1 + B^2/L^2)^{1-\frac{s}{2}} - (1 + B^2/\lambda_2^2)^{1-\frac{s}{2}}}{(1 + B^2/L^2)^{1-\frac{s}{2}} - (1 + B^2/\lambda_1^2)^{1-\frac{s}{2}}}$$

We performed a full scattering simulation in ASAP using K-correlation BSDF functionality and feeding the fitted model parameters (Figure 3.2) to each optical surface at three different wavelengths namely 200 nm, 300 nm and 400 nm. The results are shown in Table 3.1. We find the aggregate scatter as the sum of scatter contributions from all the optical surfaces. This is because of the linearity of the system with respect to scattered and specular flux. It can also be observed that the scatter is dominated by secondary mirror (M2) followed by primary mirror (M1), science filters, lens and thermal filter. We also performed diffraction simulation to estimate the effect of scatter on PSF (Figure 3.3). Figure 3.3 right panel depicts square root of scattered power is less than 25% of peak which means bell-shaped wing due to scatter is less than or equal (1/16) times of PSF peak. Though this wing broadening is not enough to degrade SUIT resolution, it can certainly affect the contrast.

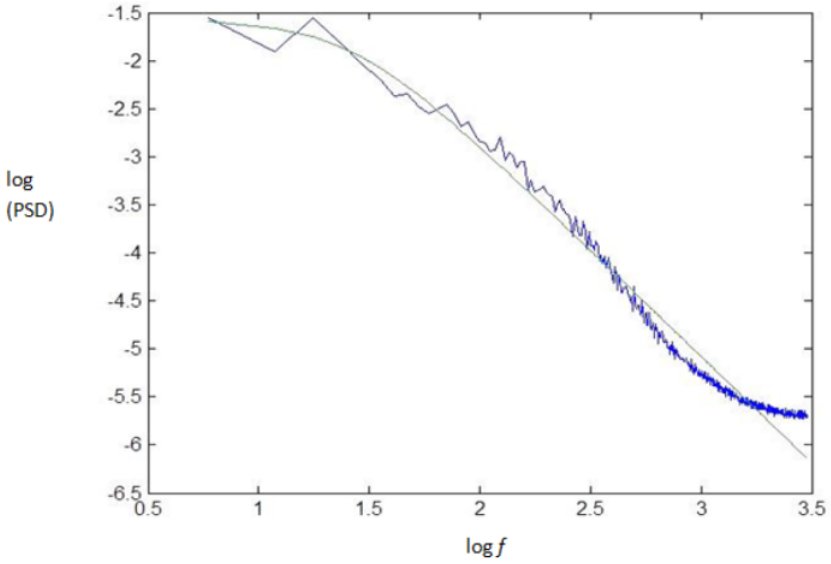

Figure 3.1: PSD fit; Blue curve depicts experimental data and the green one is the least square fitted curve for 1D PSD

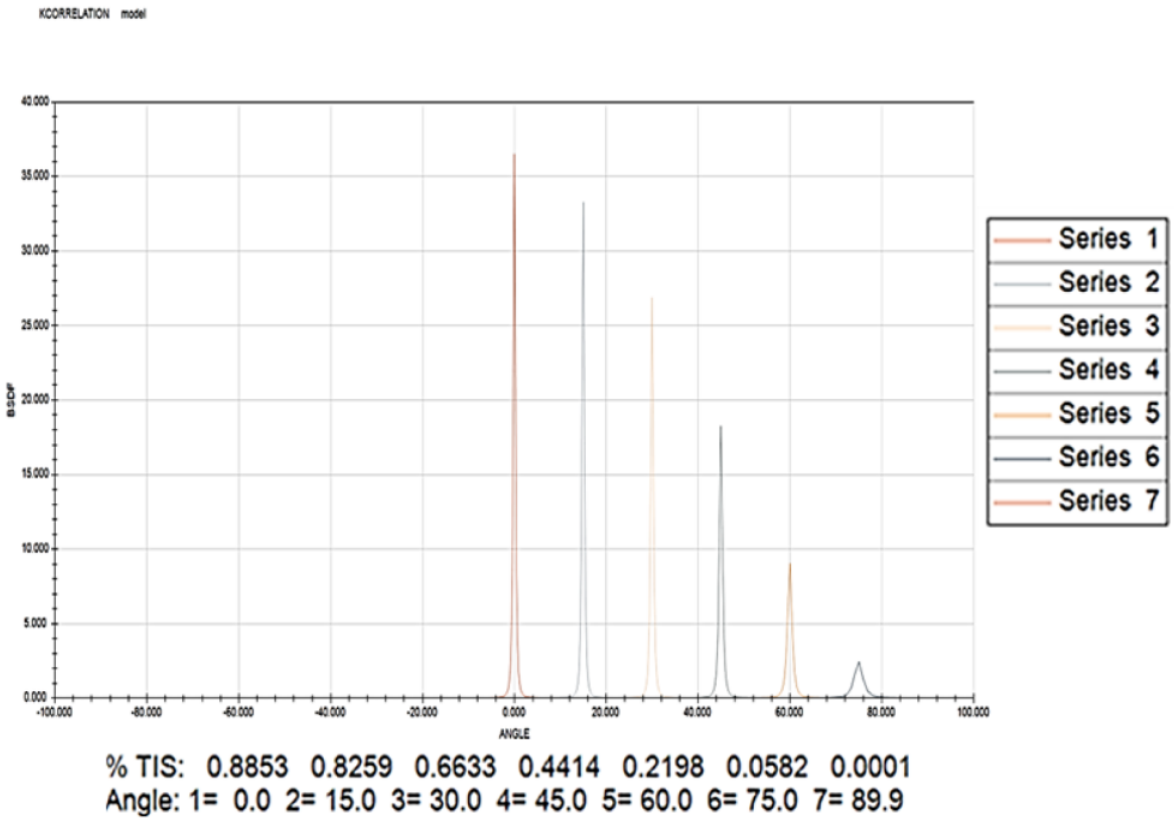

Figure 3.2: Fitted BSDFs at different angles of incidence for $\lambda = 200$ nm.

Table 3.1: Component wise scattering contribution.

Components	within disc scatter to specular ratio in %		
	$\lambda = 200nm$	$\lambda = 300nm$	$\lambda = 400nm$
Thermal filter	0.0309	0.0063	0.0019
M1	0.2655	0.0695	0.0241
M2	0.6698	0.2514	0.1141
Science filter 1	0.1470	0.0455	0.0235
Science filter 2	0.1427	0.0492	0.0236
Lens	0.1288	0.0414	0.0221
Aggregate	1.3942	0.4636	0.2095

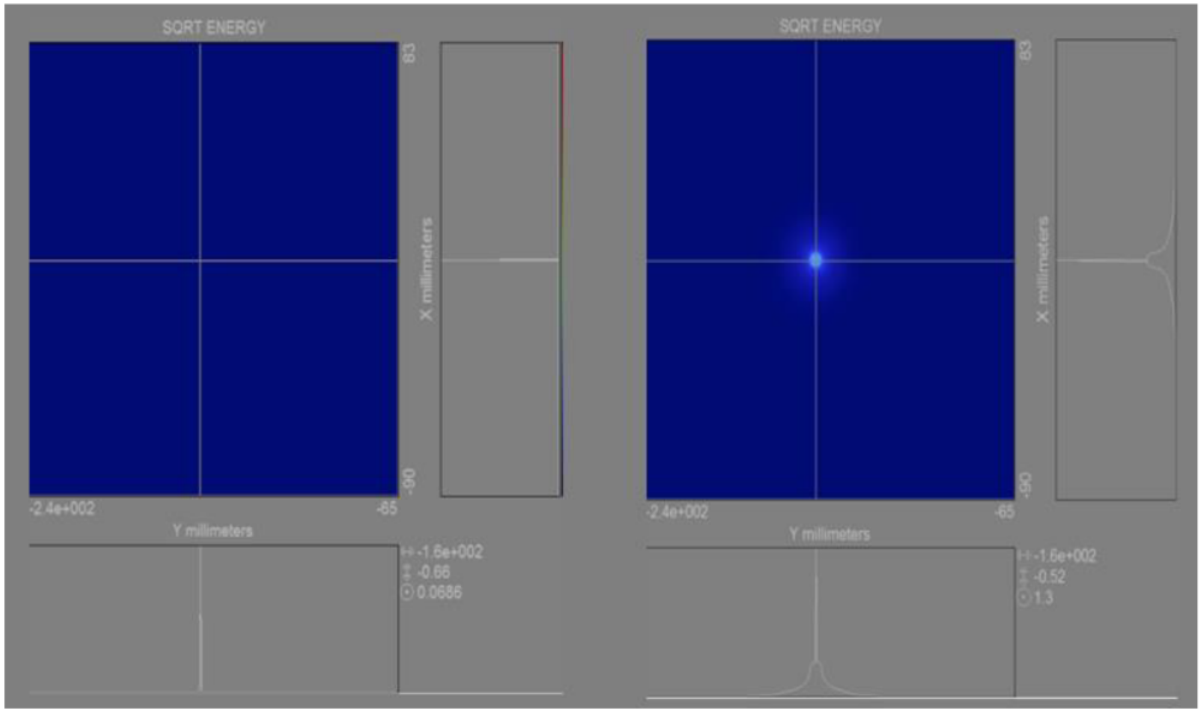

Figure 3.3: PSF wing broadening due to scatter at 200 nm for axial field. *Left Panel* shows PSF without scatter contribution. *Right Panel* shows PSF with scatter contribution.

3.2.2 Particulate Contamination

During manufacturing and assembly the particulate concentration in the telescope optical cavity contaminates the optical surfaces and gives rise to Mie scattering. The patitculate size distribution according to MIL-1246C [Tribble et al. 1996] can be expressed as-

$$\log N(X) = 0.926[\log^2 X_1 - \log^2 x] + \log(\log X_1 / \log x)$$

where x is the particle diameter in μm, $N(x)$ is the number of particles per squrae foot having size $\geq x$. $X1$, named as surface cleanliness level, is the particle size in micron above which there can be ≈ 1 particle per squre foot. Mie scattering simulation was performed in ASAP assuming all optical surfaces of SUIT to have same cleanliness level. Scatter (I_{scat}) to specular flux (I_{spec}) ratio was plotted as a function of surface cleanliness level as in Figure 3.4. Also an equation was fitted to the discrete simulation points using least square fit given by-

$$100 \times \frac{I_{scat}}{I_{spec}} = e^{0.3461 \log^2 X_1 + 0.8133 \log X_1 - 17.3306}$$

Surface obscuration (Percentage area coverage=PAC=100*total particle cross-section area/optical surface area) due to particulate contamination is related to surface cleanliness level as-

$$PAC = \frac{9.5 \times 10^{-12} \times 22}{erfc(\ln X_1 / 11.5768)}$$

The equation which depicts time evolution of surface cleanliness level X_1 for different cleanroom classes N_c (number of particles per cubit foot of size $\geq 0.5\mu$m) is given by-

$$\log((0.02)cpN_c^{0.773}t) = 0.926[\log^2 X_1 / \log^2 5] + \log(\log X_1 / \log 5)$$

The time evolution of scatter to specular ratio in SUIT was estimated for different cleanroom environments (given by their FED STD 209E Class) in both horizontal and vertical optical surface orientations. The critical level of contamination that causes within disc scatter to specular ratio of 0.1% at SUIT image plane was also calculated for various these clean room environments. It was found that the time taken for reaching critical levels of contamination is 21 days for horizontally exposed surface (Figure 3.5) and 211 days for vertically exposed surface (Figure 3.6) in FED Class 1000 environment.

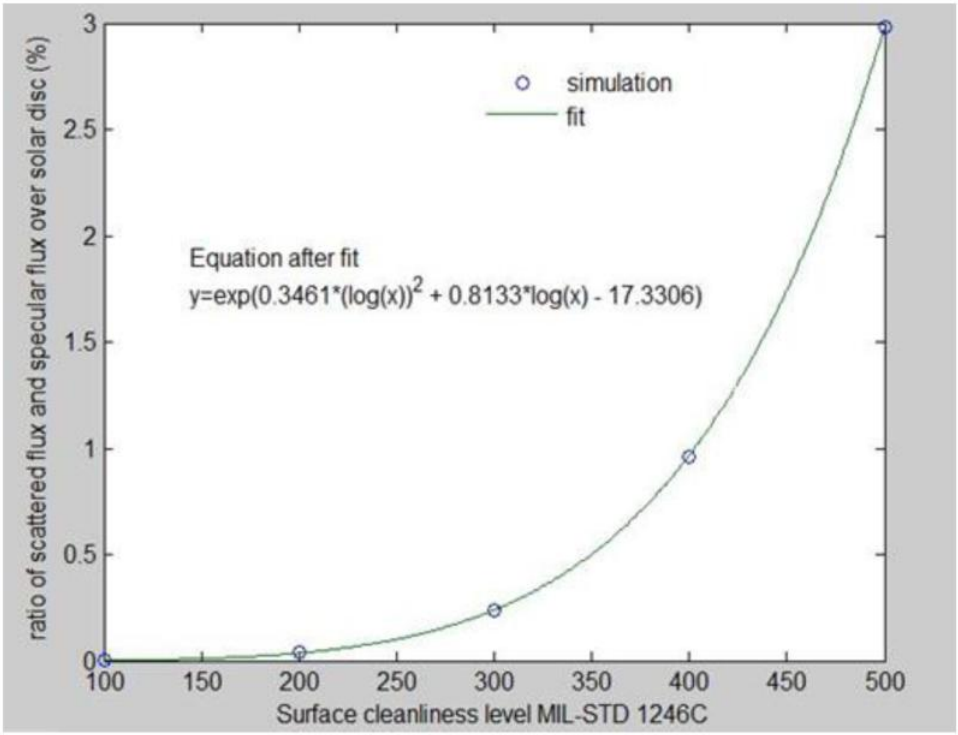

Figure 3.4: SUIT scatter as a function of cleanliness level.

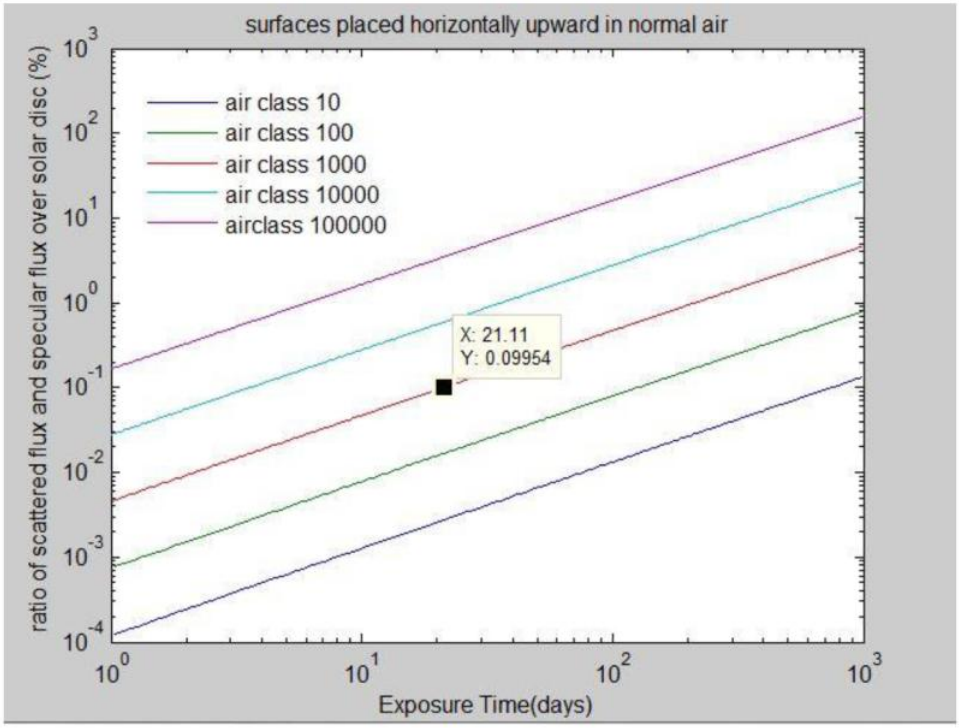

Figure 3.5: SUIT scatter due to particulate contamination as a function of time for horizontal surface orientation.

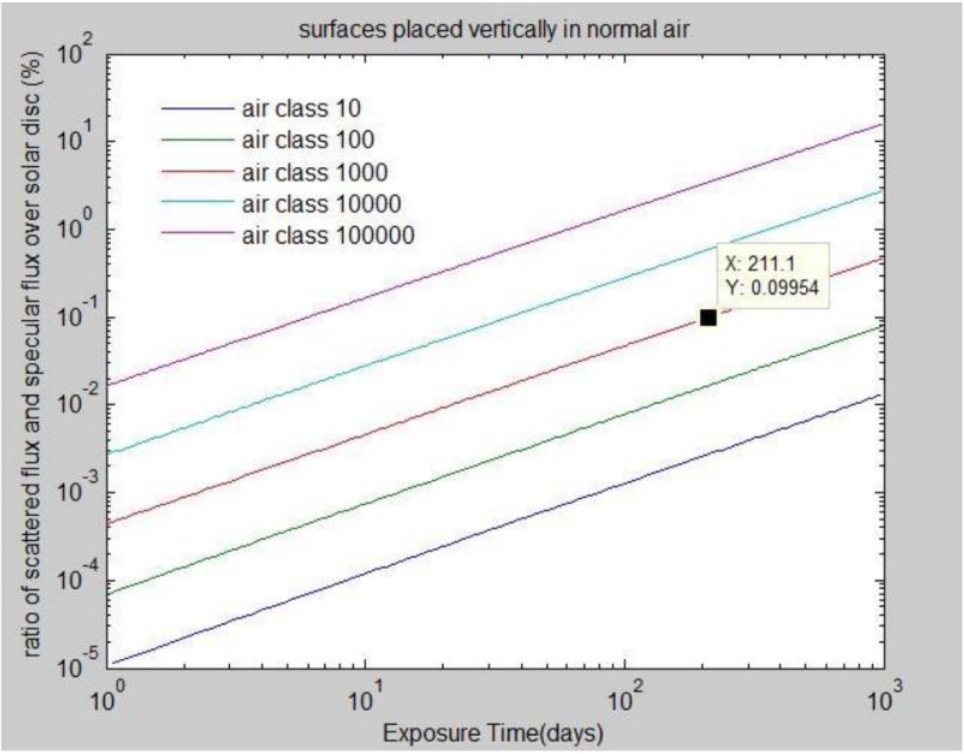

Figure 3.6: SUIT scatter due to particulate contamination as a function of time for vertical surface orientation.

3.3 Baffle Design for SUIT

To design vane structures one should decide between diffuse reflections and specular reflections [Freniere 1981, Nejad et al. 2013]. As SUIT baffle inner surfaces Airoglaze Z306 blaick paint which has absorption > 90%, scattered light from those surfaces will carry negligible energy to the image plane. We thus opted for baffle vane design to block specular reflections from baffle inner walls.

3.3.1 Primary Baffle

Here we designed vanes to ensure no first order reflection of scattered light from SUIT entrance edge reaches primary mirror. $x_0 = 0$ and $y_0 = r - r_0$
For $0 \leq n \leq 1$,

$$x_{n+1} = x_0 + d_{n+1} + d'_{n+1}$$

$$y_{n+1} = x_{n+1} \tan \beta$$

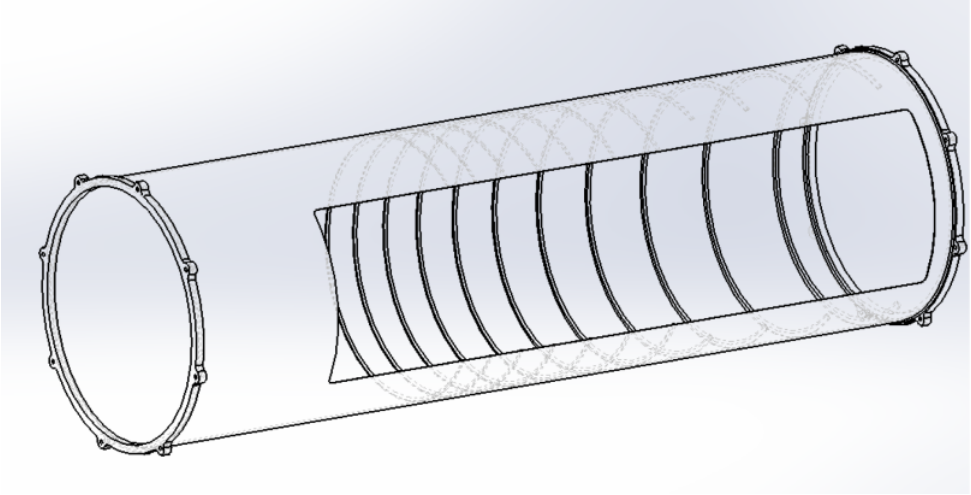

Figure 3.7: SUIT primary baffle with internal vane structures.

For $n \geq 2$,

$$x_{n+1} = x_n + d_{n+1} + d'_{n+1}$$

$$y_{n+1} = y_0 + x_{n+1} \tan\beta$$

$d_1 = 0$; $d'_1 = \frac{y_0}{\frac{r+a}{l} - \tan\beta}$; $d_2 = \frac{2rl}{3r+a}$; $d'_2 = \frac{d_2 \tan\beta + r - r_0}{\frac{3r+a}{l} - \tan\beta}$ and
$d_{n+1} = \frac{x_n y_n}{2r - y_n}$; $d'_{n+1} = \frac{y_n d_{n+1} + d^2_{n+1} \tan\beta}{y_n - d_{n+1} \tan\beta}$ for $n \geq 2$
where $\tan\beta = \frac{r_0 - a}{l}$ and $\beta = \frac{FoV}{2}$

l is tube length, a stands for primary mirror radius and r is baffle tube inner radius x_n is the position of n^{th} vane with respect to entrance aperture and y_n represents the depth of n^{th} vane ($n \geq 1$). The primary baffle with internal vane arrangement is shown in Figure 3.7

3.3.2 Secondary Baffle

Let the height of entrance window and optical component edges with respect to baffle wall be H and h respectively in horizontal cross-section. d is the maximum gap between baffle wall and the beam in horizontal cross-section. $\beta 1$ is the half divergence angle of the beam from secondary mirror. l is the distance between entrance aperture edge and optical component edge along baffle tube. Then position of n^{th} vane x_n is with respect to entrance window is given by- $x_1 = d_1 + d'_1$ and $y_1 = d - x_1 \tan\beta 1$
For $n \geq 1$,

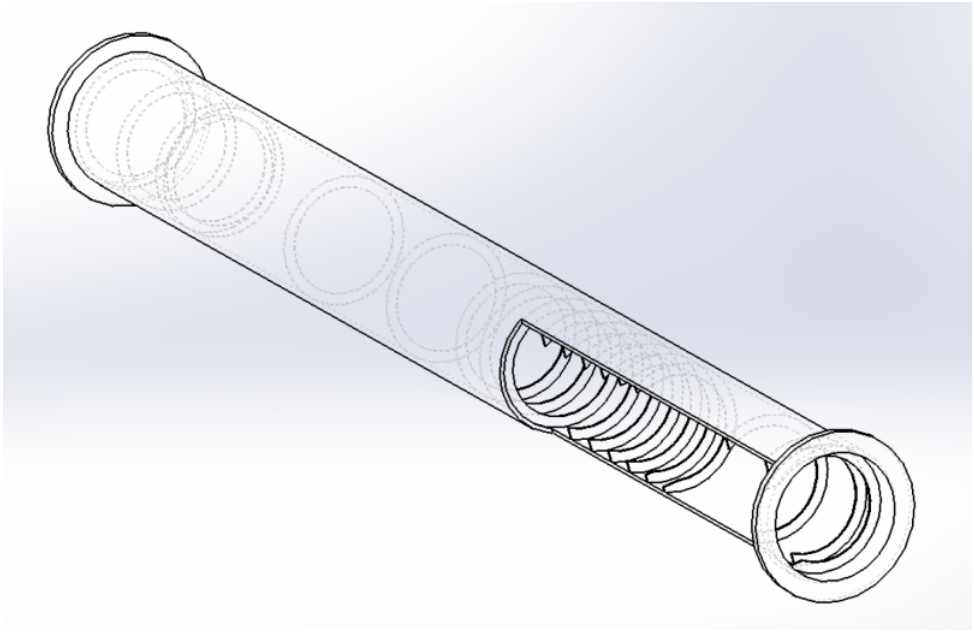

Figure 3.8: SUIT secondary baffle with internal vane structures.

$$x_{n+1} = x_n + d_{n+1} + d'_{n+1}$$

$$y_{n+1} = d - x_{n+1} \tan \beta 1$$

where $d_1 = \frac{Hl}{H+h'}$; $d'_1 = \frac{d - d_1 \tan \beta 1}{\frac{H+h}{l} + \tan \beta 1} and d$
$d_{n+1} = \frac{x_n y_n}{H - y_n}$;$d'_{n+1} = \frac{y_n d_{n+1} - d^2_{n+1} \tan \beta 1}{y_n + d_{n+1} \tan \beta 1}$ The secondary baffle with internal vane arrangement is shown in Figure 3.8. Figure 3.9 depicts the SUIT optical arrangement with primary and secondary baffles.

3.3.3 Scatter from Baffles

Putting the baffle vane structures we performed a scattering simulation using polynomial BSDF for Airoglaze Z306 paint. We also turned off all the scattering due optical surface micro-roughness during this simulation. We found a negligible scattered flux to specular flux ratio of 0.008% originating from 2nd or higher-order reflections of entrance aperture scattered light at baffle inner surfaces.

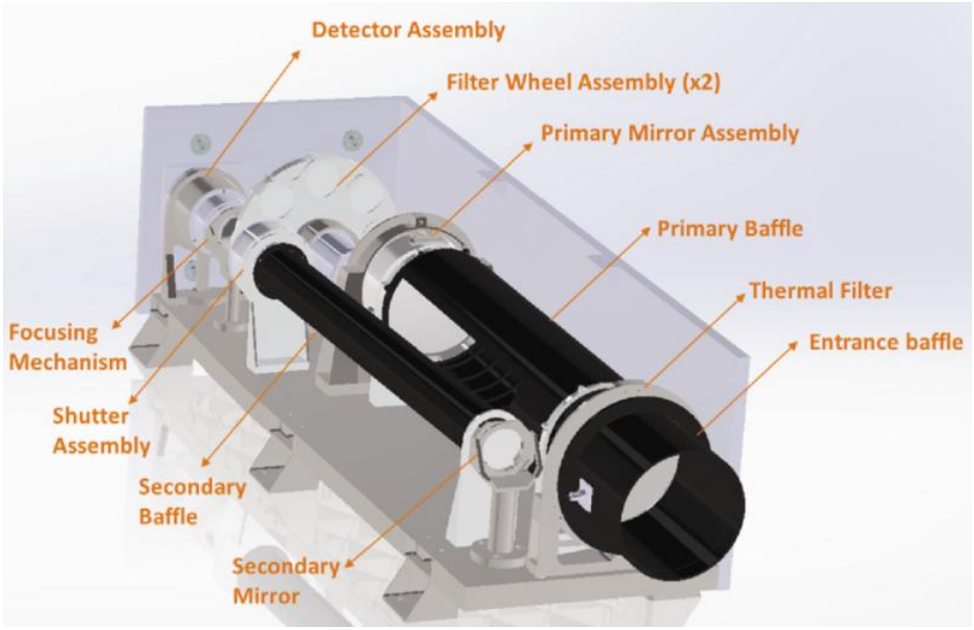

Figure 3.9: SUIT optics assembly with baffles.

3.4 Analyzing Effect of Scattering from VELC Package on SUIT

We have used ASAP to simulate the effect of reflection from rough MLI (reflectivity 30% from 200-400 nm) coated VELC surfaces ahead of SUIT (Figure 3.10). The roughness has been generated by applying random distribution of macroscopic heights (Gaussian) and surface normals (uniform). RMS macroscopic roughness and slope (or surface normal) have been taken as 100 microns and 0.2 radians. This essentially created hills and valleys of varied spatial scales. On top of these macroscopic height fluctuations we have used K-correlation scatter model with RMS microroughness as 100 angstrom and correlation length of 400 microns. For the simulation we have used light sources in front of SUIT and VELC with same ray density having angular divergence of 0.25 degree. We created a detector plane at SUIT entrance aperture to check the VELC (reflected+scattered) flux with respect to SUIT specular flux for solar imaging. Figure 3.11 shows the spatial distribution of VELC MLI reflection on SUIT entrance. This is biased towards positive X as the VELC components are shifted to positive X with respect to SUIT. The total VELC (reflected+scattered) flux was found to be only 0.082% of SUIT specular light. The same ratio in the biased side of the detector increases to 0.271% presenting the worst

case scenario. Now, we know only 1.4% of the specular light at 200 nm is scattered due to SUIT optical surface micro-roughnesses. So, another 1.4% of the 0.082% VELC (reflected+scattered) light will add negligibly to the original SUIT scatter. It can be noted that none of the VELC (reflected+scattered) specular light can reach SUIT CCD because of high field angle. It can only reach through scatter or multiple reflections on SUIT inner baffle walls again being attenuated to several orders with respect to specular flux. So, the aggregate scatter will be 1.4 + 0.082×(1.4/100) % =1.40115% [worst case=(1.4 + 0.2710 × (1.4/100))% = 1.40379%] of specular.

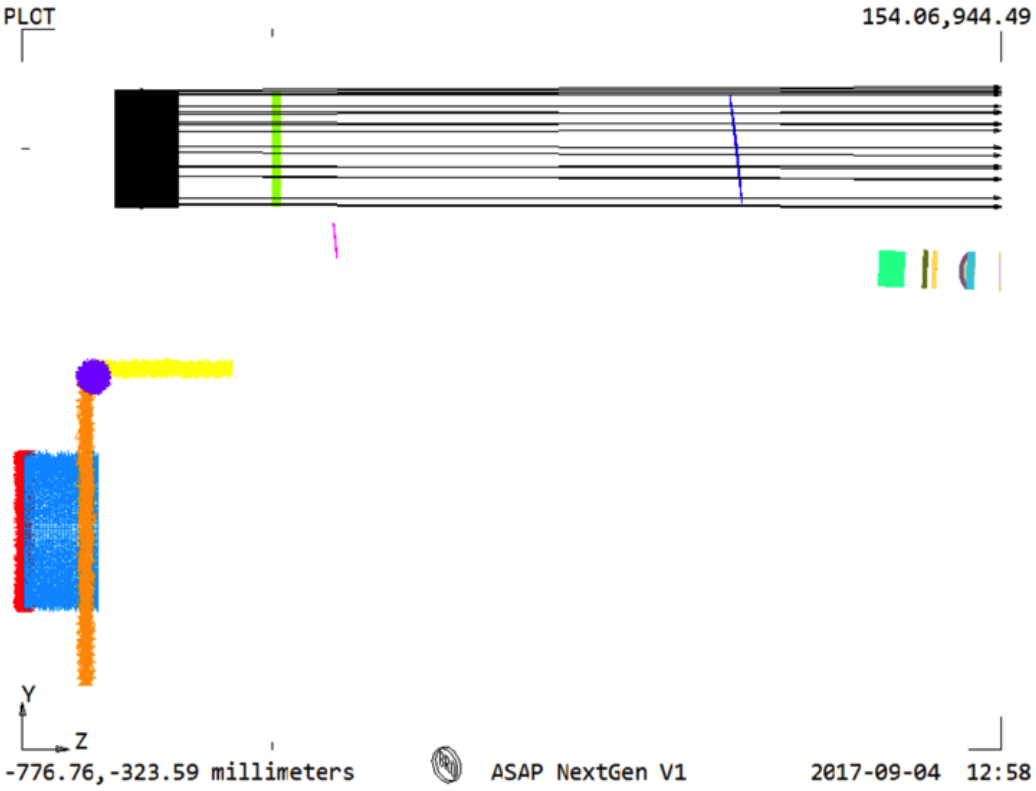

Figure 3.10: VELC MLI coated rough looking components ahead of SUIT optics.

3.5 Proposed Strategy for Scatter Reduction

The ratio of scattered light to specular light (mean disc light) within FoV, being worse than requirement i.e. 0.036% for dark regions and 0.11% for bright regions [Ghosh et al. 2016], needs removal through better polishing or post processing. Keeping PSD nature the same, if the RMS mircro-roughness of the primary mirror is brought down

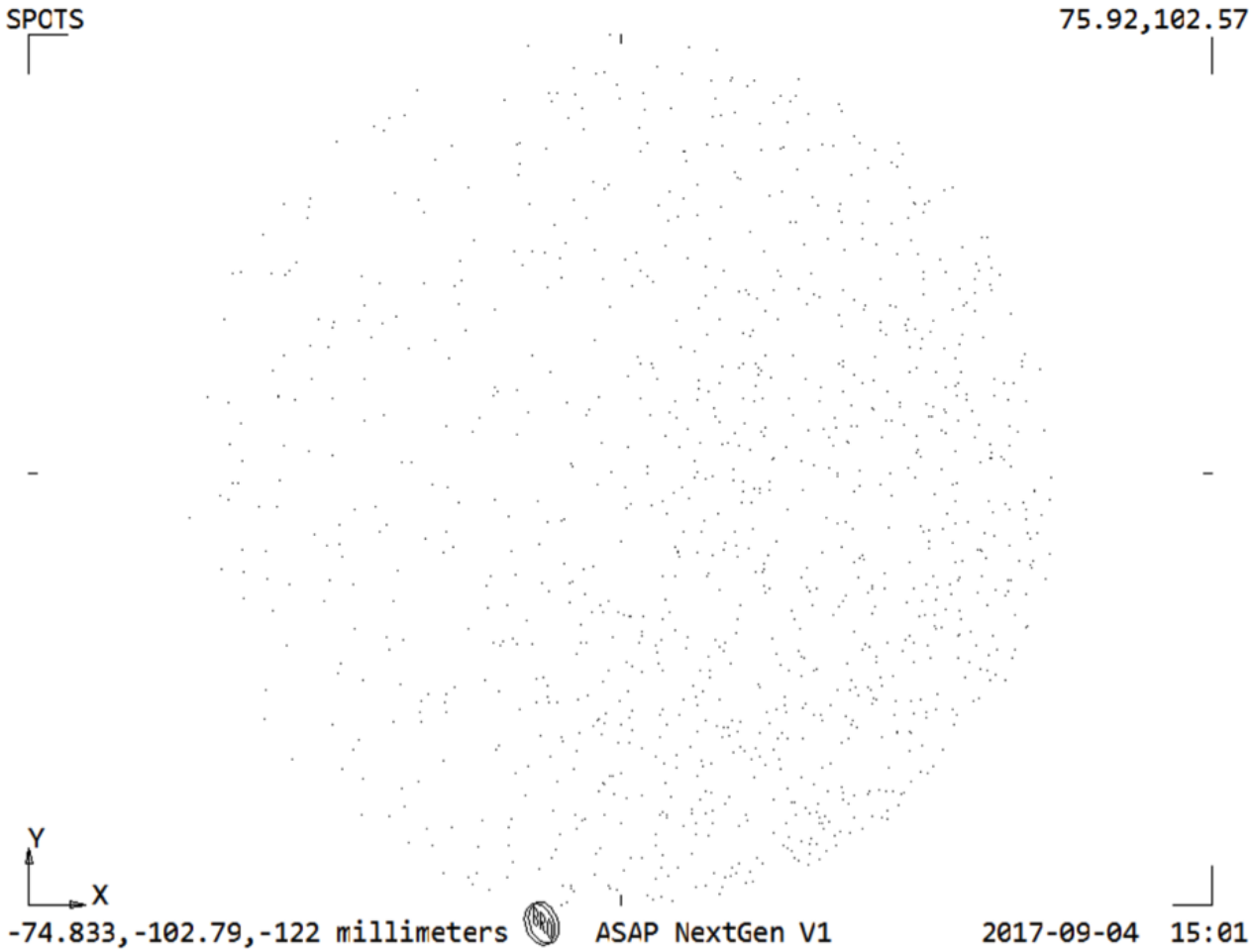

Figure 3.11: Spot distribution at SUIT entrance due to VELC MLI reflection and scatter.

to 10 Å and secondary mirror to 5 Å with all other surfaces close to image plane to 7 Å , the aggregate scatter to specular ration becomes ≈ 0.31% at 200 nm which is less than 1/4 times of the same for originally considered micro-roughness values. Now, the narrow-angle scatter for our case is only expected to affect the image contrast due to PSF wing broadening as depicted before in subsection 3.2.1. Thus, we propose a PSF deconvolution strategy to partially enhance the contrast [Seibert & Boone 1988]. This requires assumption of linearity and shift-invariance [Seibert & Boone 1988]. But, as PSF changes over FoV, the deconvolution might be done diving the entire FoV into smaller subfields. The estimation of PSF wing-broadening can be made from the off-limb profile of disc as in Figure 3.12. The representative example from Kodaikanal Observatory Ca II K historical dataset shows diffuse light outside the solar disc through

the middle of left panel of Figure 3.12 in purple. The distribution of the off-limb pixel value resembles broadened PSF wing as depicted in Figure 3.3. It should be noted that, the historical solar images were recorded through photographic plates/films. Thus, pixel values in those represent photographic emulsion density which scales logarithmically with solar irradiance. Also, the off-limb diffuse light here might have contribution from Earth's atmosphere apart from optical surface micro-roughness. But, such off-limb diffuse intensity distribution for SUIT will necessarily represent effect of surface scattering.

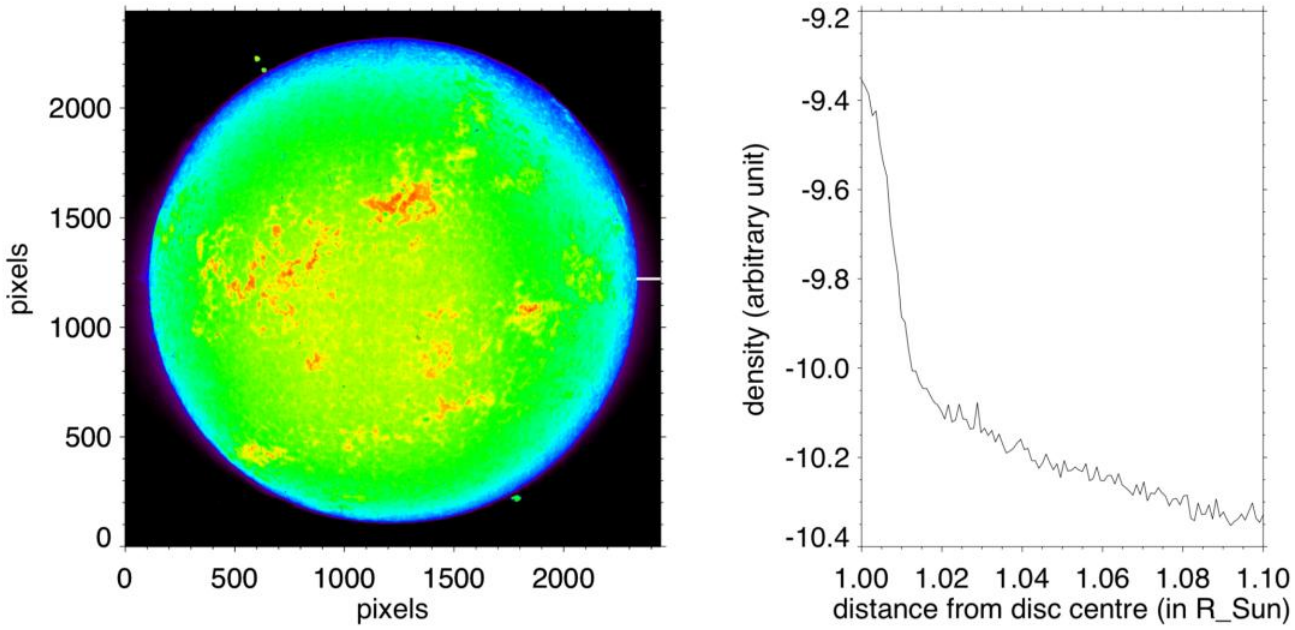

Figure 3.12: Scattered light and solar off-limb intensity profile. *Left panel* shows digitised density (as captured by Photographic films/plates historically) image in Ca II K (3933.67 Å; bandwidth 0.5 Å) from Kodaikanal Solar Observatory captured on Nov 11, 1957 at IST 09:23. *Right panel* shows the density profile corresponding to the off-limb position marked by white straight line in left panel. This can be due PSF wing-broadening as a result of surface scatter from disc light.

3.6 Discussion and Conclusion

Scattering analysis is crucial for UV imaging as it scales inversely with wavelengths [Harvey et al. 2012, Stover et al. 2016]. Sun being an extended source, spatially resolved solar imaging requires understanding of the angular distribution of scatter [Harvey

et al. 2012]. Contextually, this work identifies the sources of scattering for SUIT. It was found that optical-surface micro-roughness dominates the scattering. Among all optical components secondary mirror was seen to have the highest contribution (Table 3.1). This is because of the fact that there are no reflecting surfaces after M2. Scattered rays aimed to image plane from M2 can directly reach detector without much deflection whereas specular reflection of the scattered rays from M1 makes many of the them to go out of the beams not reaching the detector. The thermal filter being the the farthest element from detector along optical path contributes negligibly to the total scatter (Table 3.1). The BSDF generated from experimental PSD, produced narrow-angle scatter causing PSF wing-broadening. However, it was found that the the wing-broadening can not disturb the SUIT spatial resolution. It can only reduce the contrast.

Effect of particulate contamination for horizontal and vertically exposed SUIT surfaces were explored. An empirical function was found depicting SUIT scatter as a function of surface cleanliness level. Using that function, time evolution of scatter for both horizontally and vertically exposed surfaces were evaluated. Vertically exposed surface was seen to provide higher integration time for same clean room class as compared to horizontally exposed surfaces.

Design of baffles was performed with internal vane structures and its scattering effect was evaluated. The effect was found to be negligible. Finally, effect of MLI coated VELC package on SUIT in terms of reflection and scattering was simulated. The effect was found to be again negligible as compared to surface-microroughness.

The aggregate scatter depicted is higher than the requirement i.e. it exceeds the photon noise. To bring scatter to a fraction of photon noise we need better polishing of the optical surfaces, more strict contamination control strategies or post-processing. If PSD is scaled smaller RMS micro-roughness, we get smaller scatter to specular ratio. However, in reality better polish may not generate same distribution of spatial frequencies. If PSD can be shaped to generate a wide-angle scatter using different polishing tool, it may reduce the scatter within FoV [Church & Takacs 1995]. Finally, to validate the scatter a test setup should be built for probing BSDF of the optical surface [Filip et al. 2017]. Those profiles can then be put in the simulation software to generate

a scatter which should match more closely with the reality.

Thus, this study provided an integrated analysis of different sources of scattering, their effect on SUIT image quality and possible remedies to control those. The knowledge gained from this analysis, will possibly allow image enhancement through post-processing in SUIT data pipeline.

Chapter 4

Calibration and Alignment Plan for SUIT

4.1 Introduction

It is necessary to decouple the contribution of astronomical source and the effect of instrument for making data recorded through any astronomical telescope usable . The data recorded through the CCD will have contributions from filters, mirrors and lens because of their reflectivity and transmissivity as a function of wavelength. To remove those effects photometric calibration is necessary which uses astronomical sources of known flux as calibrator. Also, the CCD quantum efficiency non-uniformity modulates the recorded spatial information. Thus CCD calibration is also unavoidable. This is achieved through flat-fielding using an illumination of known uniformity. Photometric calibration is out of the scope of this thesis. Only flat-fielding plan for SUIT will be illustrated in this chapter. Before launch of telescope it is also necessary to ensure that the optical setup is adequately aligned and optical axis is known with respect to the satellite pointing direction. Taking these into consideration, an alignment plan has been devised for SUIT which will be presented in this chapter. This chapter illustrates the flat-field generation plan in section 4.2 followed by alignment plan in section 4.3 finally concluding in section 4.4 along with necessary discussion.

4.2 Flat-Fielding Plan

Generation of flat-field is an integral part of any astronomical imaging dealing with Charged Coupled Devices (CCDs). flat-field is created by providing an uniform illumination all-over the CCD pixels. This captures the variation of pixel-to-pixel sensitivity/quantum efficiency (QE). This spatial pattern representing CCD response to a nearly constant illumination is commonly termed as flat-field and is used for the image calibration. Dividing the science image with flat-field helps to get rid of artefact coming from the CCD. In the next two subsections 4.2.1 and 4.2.2 we discuss the flat-field generation plan for SUIT and related modelling respectively.

4.2.1 LED Arrangements

8 Light Emitting Diodes (LEDs) in groups of 2 will be mounted circumferentially 45° apart from each other before the filter wheels on the periphery of shutter mount. Within each group, 2 LEDs will be from two different wavelength having peak at 242 nm and 340 nm. At a time 4 equispaced LEDs (at 0, 90, 180, 270 degrees) of one wavelength will be turned on (Figure 4.1) İn next lap other 4 LEDs at (45, 135, 225, 315 degrees) will be turned on. Combining these two the uniform model flat field will be created. The ideal pattern is simulated by constructing a model. The experimental illumination pattern will be divided by the model pattern to generate the flat-field giving an idea about CCD pixel-to-pixel non-uniformity. Next section illustrates the developed mathematical model.

with respect to

4.2.2 Model for Flat-field Generation

Angular distribution of the LED optical o/p power was fitted to the expression $I(\theta_X, \theta_Y) \propto \exp[\frac{2\theta_X^{2n}+2\theta_Y^{2n}}{\alpha^{2n}}]$ where θ_X, θ_Y are angles in x and y respectively. From the fit, n was found to be 2 and considering the LED angle Full Width Half Maxima (FWHM) to be 120°, α was found to be $\approx 78.2°$ from the expression $\alpha = \frac{FWHM}{2}(2/\ln 2)^{\frac{1}{2n}}$ The model depicting flux at a point (x, y) on the detector with 4 equally spaced LEDs turned on simultaneously was framed as $D(x, y) = \sum_{\lambda_{low}}^{\lambda_{high}} \sum_{k=1}^{4} I_{LED}(\theta_X^{(k)}, \theta_Y^{(k)}, \lambda) \times T_{Filter1}(\beta_X^{(k)}, \beta_Y^{(k)}, \lambda) \times$

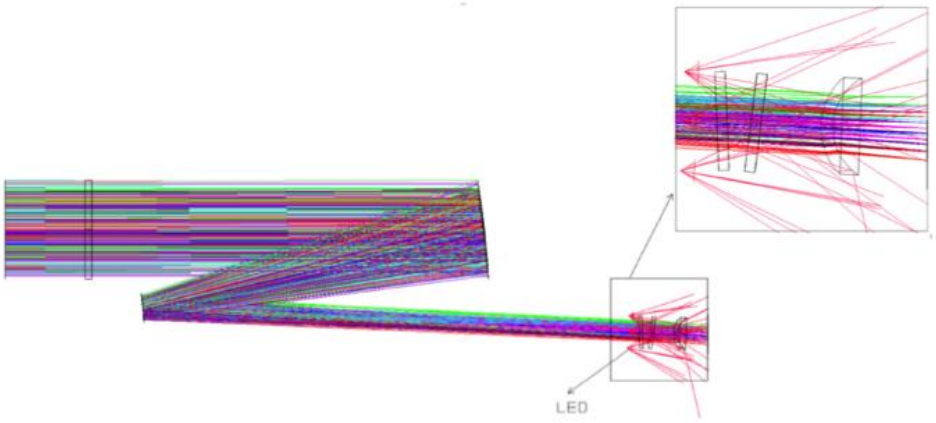

Figure 4.1: LED arrangement in SUIT for flat-field generation

$T_{Filter2}(\beta_X^{(k)}, \beta 1_Y^{(k)}, \lambda) \times T_{lens}(\alpha_X^{(k)}, \alpha_Y^{(k)}, \lambda) \times [1 - R_{CCD}(\gamma_X^{(k)}, \gamma_Y^{(k)}, \lambda)]\delta\theta_X \delta\theta_Y \delta\lambda$. Here $\mid \beta_Y^{(k)} - \beta 1_Y^{(k)} \mid = 9.5°$ as the filters are tilted with respect to each other by 9.5°. D stands for the flux at detector, I denotes LED irradiance and T stands for transmission and R for reflection. It can be noted that $\beta_X^{(k)}/\beta_Y^{(k)}$, $\beta_X^{(k)}/\beta 1_Y^{(k)}$, $\alpha_X^{(k)}/\alpha_Y^{(k)}$, $\gamma_X^{(k)}/\gamma_Y^{(k)}$ are x/y components of the angle of incidence of the ray at the 1st surfaces of filter1, filter2, lens and CCD respectively starting from k^{th} LED and reaching pixel (x, y) of the detector. $\theta_X^{(k)}/\theta_Y^{(k)}$ are x/y components of the same ray angle with respect to the k^{th} LED orientation. $\delta\theta_X, \delta\theta_Y$ are angles covered by pixel (x, y) of the CCD and $\delta\lambda$ represents the wavelength step. $I_{LED}(\theta_X, \theta_Y, \lambda)$ was chosen is such a way that $\iint I_{LED}(\theta_X, \theta_Y, \lambda)\, d\theta_X\, d\theta_Y = I_{LED}(\lambda)$ and $\int I_{LED}(\lambda) d\lambda = I_{LED}$. $I_{LED}(\lambda)$ follows a Gaussian pattern. Knowing the LED optical output power (I_{LED}) as 20 μW and 190 μW at peak wavelengths 242 nm and 340 nm respectively with FWHMs of 12 nm and 15 nm, $I_{LED}(\lambda)$ was derived.

4.2.3 Optimization of LED Positions

The LEDs will be mounted on a ring placed before science filters as depicted in Figure 4.2. The radial distance of LED from ring center is denoted by r and distance from distance as d. Figure 4.2 also shows the consequence of the limiting aperture where the filters block all the LED light from reaching detector for the combinations where r is high and d is small.Out of the all combinations the one with maximum d and minimum r gives the highest coverage of uniform illumination (Figure 4.3). Any point on the detector can be illuminated by maximum 2 LEDs when four are turned on.Combined

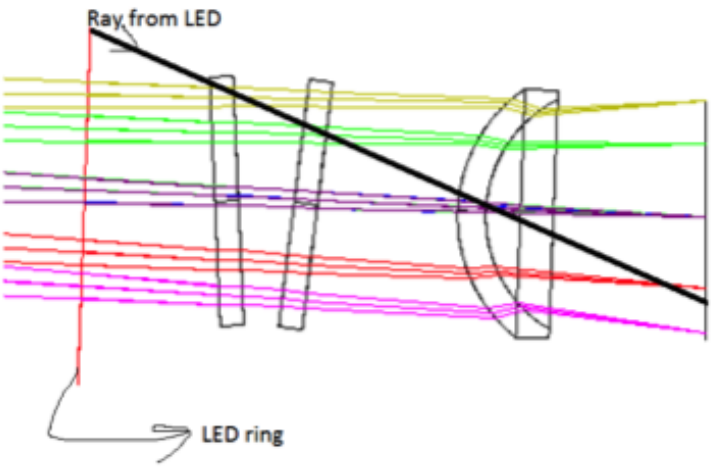

Figure 4.2: Effect of limiting aperture on CCD illumination through LEDs

flat is generated from maximum of two flats at every pixel (Figure 4.4).Center-to-edge contrast achieved is 17.7% which is well within the requirement of 25%.

4.3 Alignment Plan

Solar Ultraviolet Imaging Telescope (SUIT) is an off-axis RC telescope containing two hyperbolic mirrors of radii of curvature 1404.669 mm, 438.252 mm respectively and a field corrector lens. Despite having advantages with respect to scattering and thermal stability, any off-axis system presents more varieties of optical component perturbations compared to an axially symmetric one. The telescope is expected to have a resolution of 1.4 arcsec limited by the pixel size. To attain the same, accurate alignment on ground as well as proper measures should be taken to ensure stability onboard. In the following sections different levels of alignment and the alignment procedure will be discussed.

4.3.1 Levels of Alignment

The alignment of the optical setup and assembly will be performed in step-wise manner. The levels of alignment will be namely-

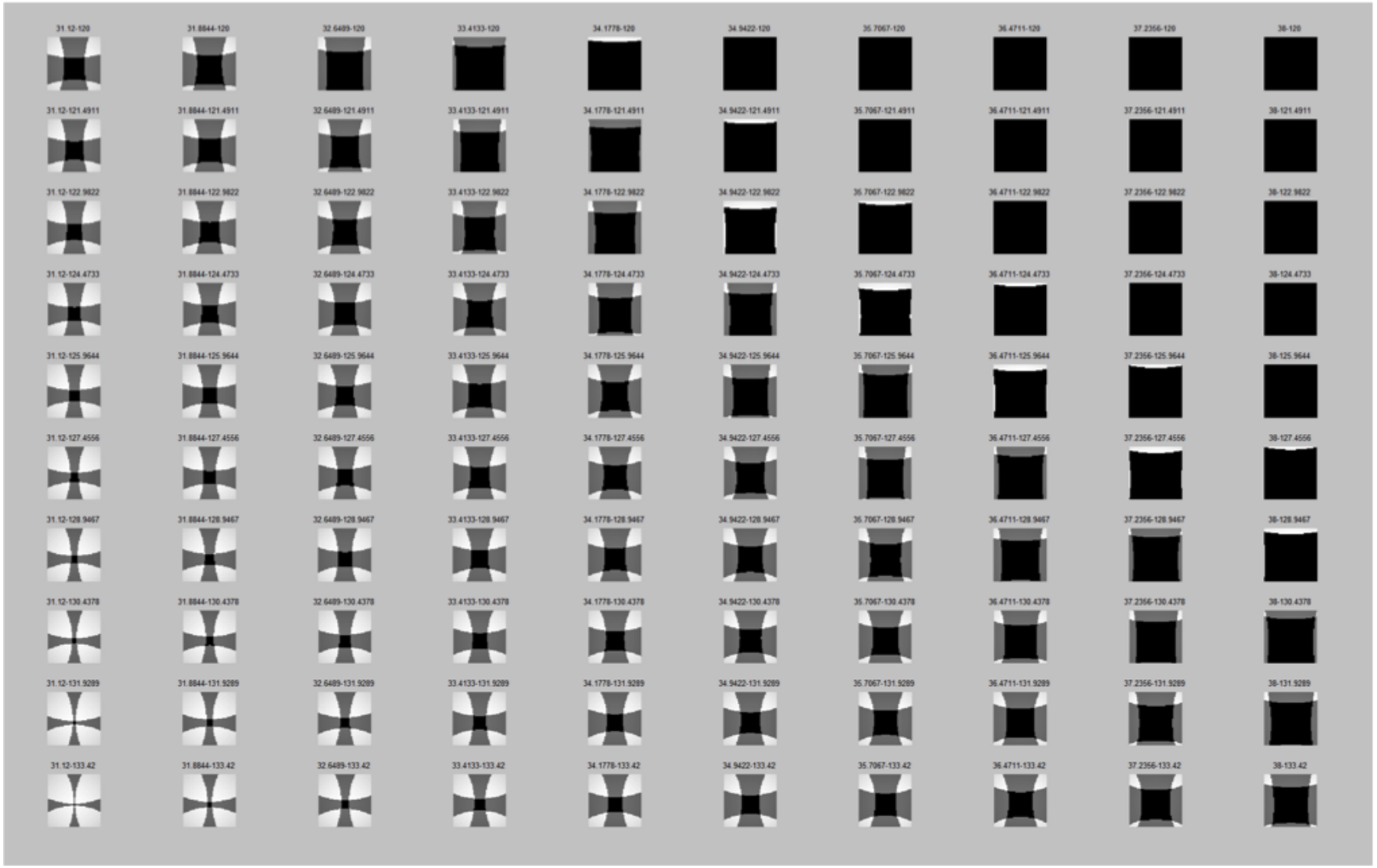

Figure 4.3: Optimizing LED positing though uniformity and continuity of generated flats.

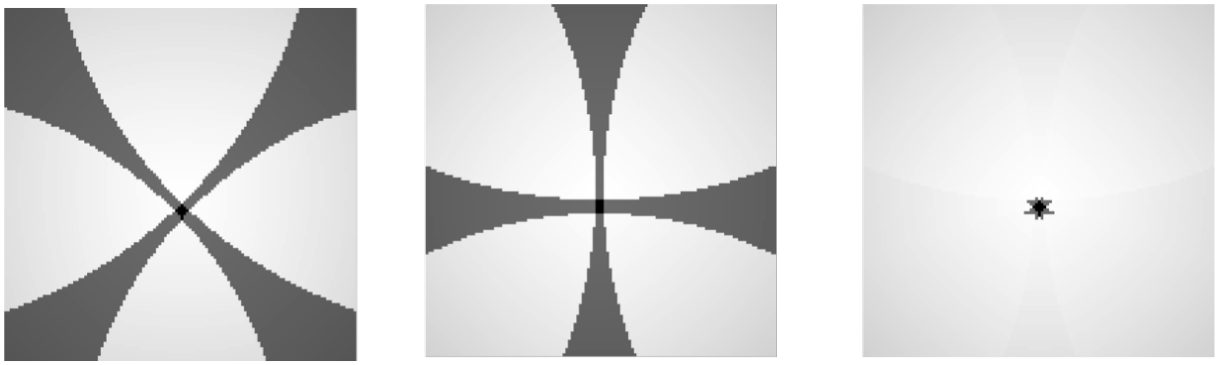

Figure 4.4: Combining two flats to generate a more filled flat. *left panel* shows flat generated from LEDS at 45, 135, 225 and 315 degree position; *middle panel* shows flat generated from LEDS at 0, 90, 180 and 270 degree position; *right panel* depicts the combined flat generated from maximum of *left panel* and *middle panel* flats at every pixel.

- **Test and alignment for individual components:** Every optical components will have their intrinsic errors such as radius of curvature error, figure error etc. Each will contribute to the image quality and the wavefront errors will add in quadrature. So, it ideal to test each of them separately to quantify the errors and checking whether those are within tolerance limit, finding their optical axes orientations.

- **Integrated Alignment:** After testing the optical components individually all of them will be placed in the respective positions and aligned to provide an optimal imaging performance.

  - Internal coarse alignment to align the optical components with respect to each other bringing the error below certain threshold. Theodolite is primarily used for this purpose to quantify the angular differences. Adjustments are done mechanically.

  - Internal fine alignment to align the optics very accurately estimating exact values of misalignments. Interferometry is widely used for this purpose. Fine adjustments are done mechanically.

- **Alignment of primary and secondary baffles:** Baffles are aligned with the optics so that vane edges define the beam envelopes.

- **External alignment** to align telescope package and alignment cube with optical axis

4.3.2 Alignment Procedure

4.3.2.1 Test and Alignment Plan for Individual Components

- **Test and alignment plan for primary**
  - On an optical table primary mirror will be placed with mount, reference flat and alignment cube for an interferometric test as in Figure 4.5.
  - Tip and tilt of the mirror will be adjusted to bring beam with interferometer creating fringe pattern.
  - The interferometer will be moved to the focal plane of primary for removing defocus component from the interferogram.
  - The horizontal misalignments will cause the interferograms to look like rotated about a symmetry line.
  - Tip (in-plane rotation if tip is not possible) adjustment of the mirror will cause the interferogram to derotate and make the symmetry line horizontal.
  - To remove the vertical misalignment the mirror will be tilted to make vertical fringes.
  - Every tip and tilt should also be followed by the reference flat.
  - Figure 4.5 also shows an alignment cube mounted on the side of primary the orientation of which will be performed optimizing the interference pattern seen at a small region at one end of the bigger interference pattern.
  - Three axes of the alignment cube will define optical axis, axis of bilateral symmetry and another perpendicular to both. Cube surface orthogonality is within ±5 arcsecs.

- **Test and alignment plan for secondary**
  - On an optical table secondary mirror will be placed with mount, reference flat and alignment cube for an interferometric test as in Figure 4.6.

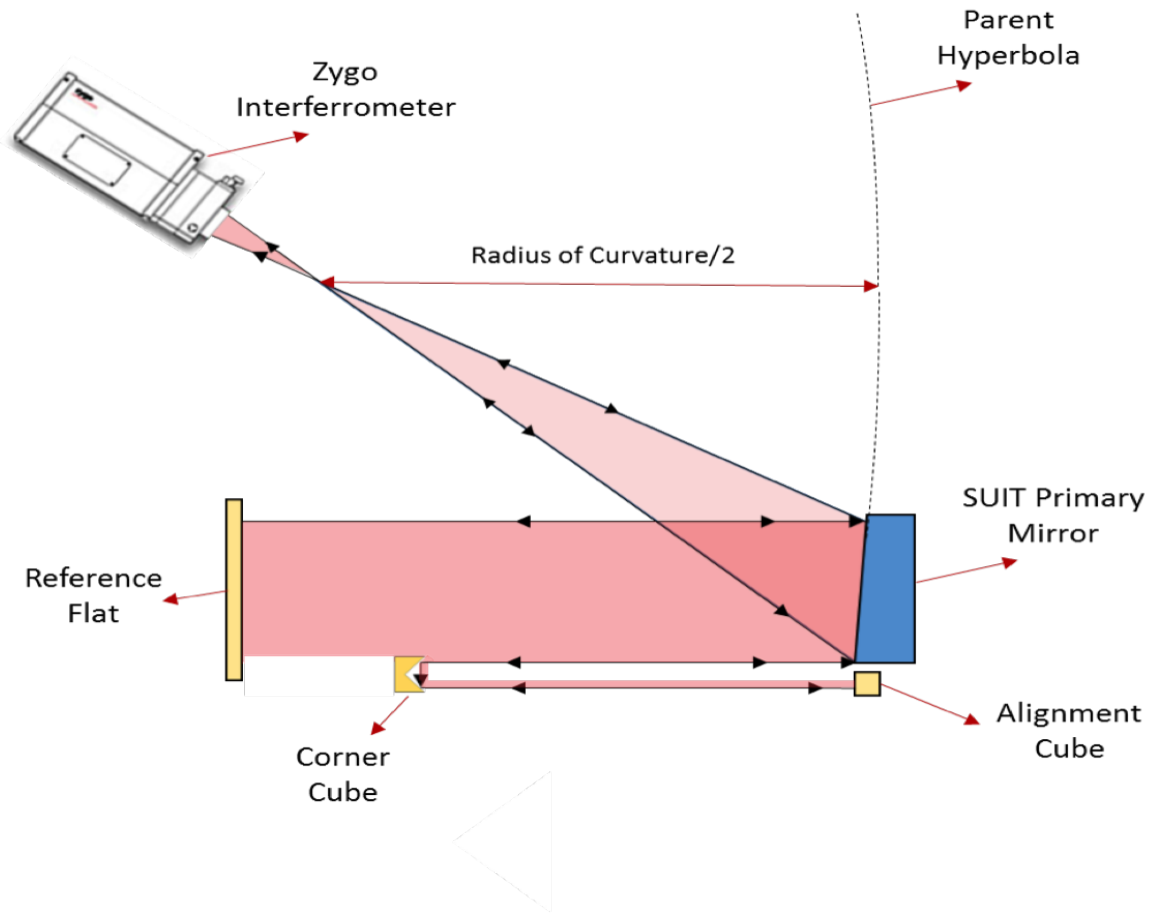

Figure 4.5: Finding optical axis of primary mirror. Interferometer converging beam is created combining transmission sphere and null lens to create proper collimated beam from primary mirror.

- Tip and tilt of the mirror will be adjusted to bring beam with interferometer creating fringe pattern.
- The interferometer will be moved so that the converging beam from the transmission sphere of the interferometer meets at the focal plane of secondary for removing defocus component from the interferogram.
- The horizontal misalignments will cause the inferograms to look like rotated about a symmetry line.
- Tip adjustment of the mirror will cause the interoferogram to derotate and make the symmetry line horizontal.
- To remove the vertical misalignment the mirror will be tilted to make vertical fringes.
- Every tip and tilt should also be followed by the reference flat.
- Figure 4.6 also shows an alignment cube mounted on the side of secondary the orientation of which will be performed optimizing the interference pattern seen at a small region at one end of the bigger interference pattern.
- Three axes of the alignment cube will define optical axis, axis of bilateral symmetry and another perpendicular to both. Cube surface orthogonality is within ±5 arcsecs.

- **Aligning science filters relative to filter wheels**
  - A reference flat will be first made perpendicular to filter wheel with theodolite.
  - Verification of the filter angles with respect to filter wheels plane will be done using interferometry with another a beam splitter and the reference flat perpendicular to filter wheel.
  - If a filter angle deviates from the tolerance of ±1degree it will be taken out of the slot and the mount will be readjusted mechanically

- **Test for the field corrector lens**

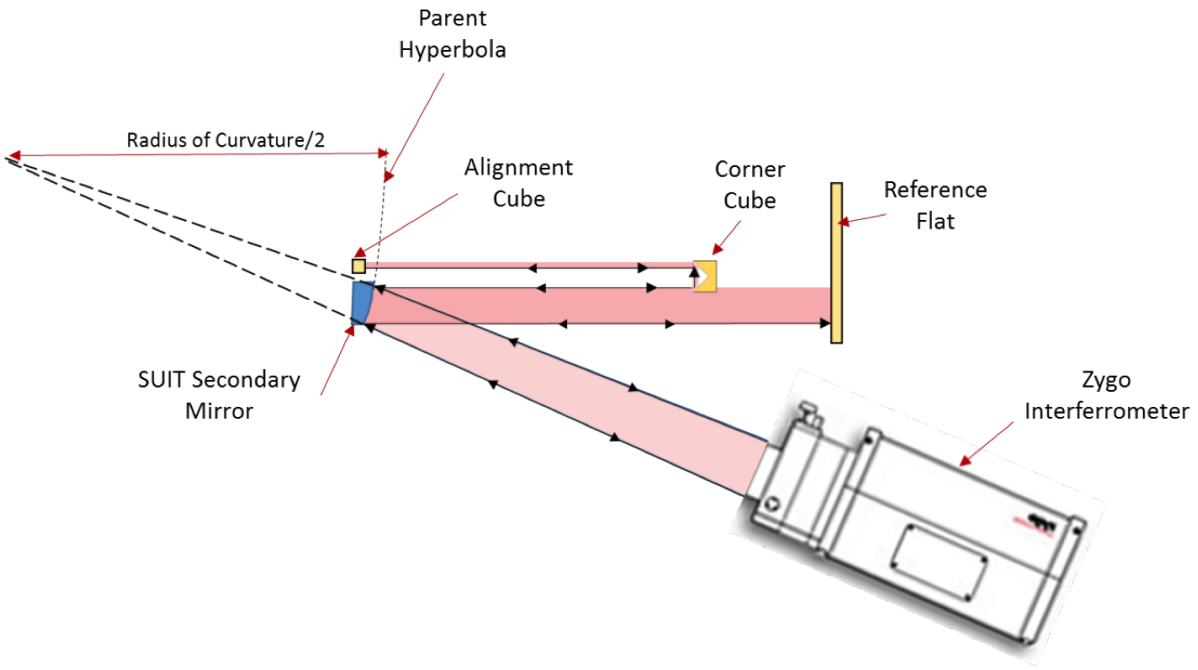

Figure 4.6: Finding optical axis of secondary mirror. Interferometer converging beam is created combining transmission sphere and null lens to create proper collimated beam from secondary mirror.

- A reference flat will be placed before the lens.
- Zygo interferometer focus will be placed at the focus of the lens and the wave aberration coefficients will be calculated.
- Apart from tip and tilt other terms will give the value of Codington shape variable
- Using lens power and coddington shape variable value we will find out approximately the radius of curvature of two surfaces.

4.3.2.2 Integrated Alignment Plan

- **Coarse Alignment**
  - Both primary and secondary mirrors will be placed on SUIT baseplate at respective positions (Figure 4.7).
  - Primary optical axis from its alignment cube will be aligned by measuring its deviations from a common telescope pointing reference flat.

- Three faces of secondary alignment cube will be aligned with those of the primary alignment cube using theodolite measurement and mechanical adjustment less than 1 arcmin (half of the relative tilt tolerance).
- Again Zygo focus will be placed at the best focus position of primary-secondary integrated setup.

- **Fine Alignement**
  - Using Zygo interferometer interferogram, wavefront error will be estimated due to fine misalignment between primary and secondary mirror.
  - From the wavefront error map, five Zernike coefficients Z5, Z6, Z7, Z8 and Z9 will be calculated.
  - Formulation presented in Zhang et al. [2016], will be used to find out primary and secondary relative alignment errors from mentioned Zernike coefficients. This uses Nodal Aberration Theory (NAT) equations. Relative decenters will embed in plane rotation of the mirrors.
  - Using those exact values shims will be used to the mounts for minimizing errors. With 10 micron shims each of the relative tilts can be minimized to +/- 40 arcsecs.
  - Putting the residual errors and optimizing in Zemax will give the optimal position of lens and image plane for fixed focal length 3500 mm.
  - Clear filters and lens will be placed in the optical path (Figure 4.7).
  - Lens tilt will be calibrated through two centering targets and a reference flat placed using theodolite.
  - Lens will be moved slightly in all directions keeping the tilt intact to remove the defocus wavefront error estimated from interferogram.
  - Again the Zygo will be moved laterally to find best direction for optimizing over different fields.
  - Detector will be placed along that plane.

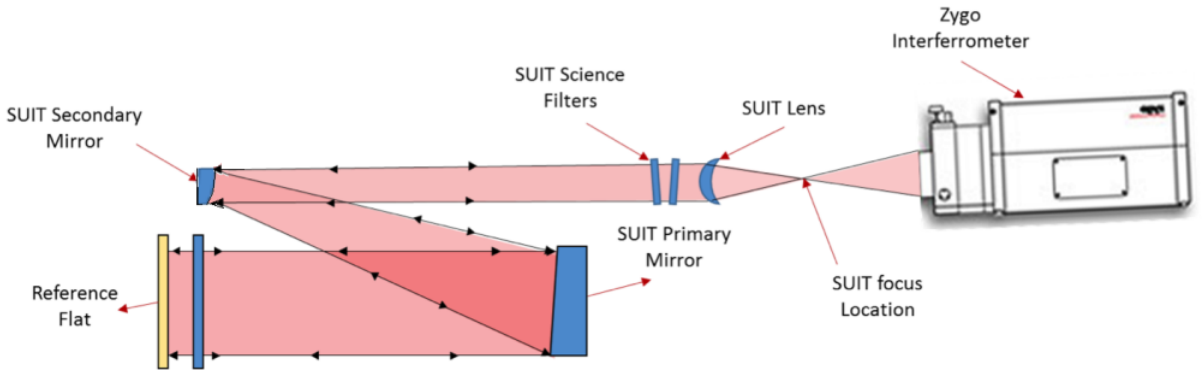

Figure 4.7: Alignment of optical components using Zygo interferometer.

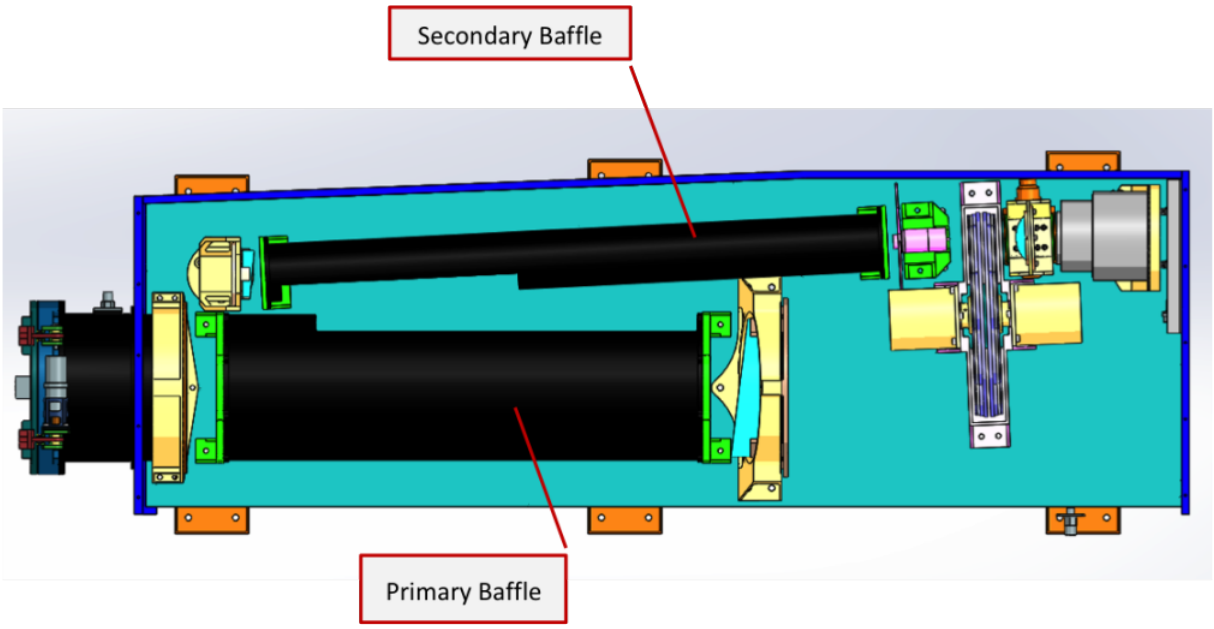

Figure 4.8: Alignment of SUIT baffles.

4.3.2.3 Baffle Alignment

- Baffles will be metrologically tested to ensure the design tolerance on vanes.
- Using cross-hairs and centering targets the baffle axes are planned to be aligned with the primary and secondary mirrors.
- The primary and secondary baffle axes are tilted by 2.88 degree in the horizontal plane (Figure 4.8). The baffle alignment scheme presented here is at initial phase and will be further advanced.

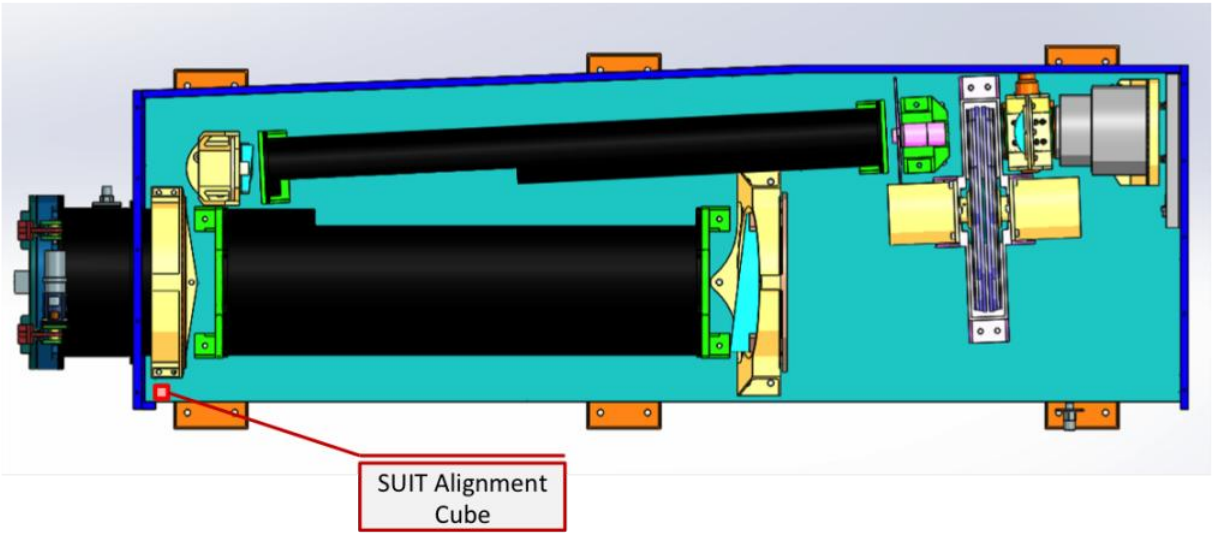

Figure 4.9: Alignment cube for SUIT package.

4.3.2.4 External Alignment

- An alignment cube (SUIT alignment cube) will be placed on the side of optical base plate close to the thermal filter (Figure 4.9).
- Using theodolite the angles between primary mirror alignment cube and SUIT alignment cube axes will be measured. They will be aligned better that 20 arcsec.
- The axes of these relative to the optical axes will be known. So the telescope pointing direction will be transferred to the field angles for SUIT.

4.4 Discussion and Conclusion

As a crucial step of detector calibration flat-fields should be generated for astronomical telscopes. As the Sun is an extended source it is vital to understand non-uniformity of detector pixels [Chae 2004, Xu et al. 2016]. In this regard, present chapter depicts a plan of flat-field generation for SUIT and provides a mathematical model to simulate the flat-field pattern using LEDs of known power and angular distribution of flux density. Usage of LEDs allow flexibility in terms of wavelength, long life and lower cost [Marshall & DePoy 2013]. Knowing the model flat-field, non-uniformity of the CCD pixels can be easily found from experimental flat-field. As the flat-field is generated

using simultaneous illumination of 4 LEDs, which don't intersect over entire detector (Figure 4.4), the LED malfunction can be determined from the symmetry of the flat-fields. Also, usage of LEDs at two wavelengths may allow reconstruction of flats at other wavelengths. As the LEDs are mounted just before science filters, flats will not incorporate the effect of entire SUIT optics. Thus, degradation of SUIT optics can not be nullified through current plan.

Space-based telescopes requires precise calibration of optical axis and alignment to ensure desired performance on ground. The SUIT alignment plan presented in this chapter, used Zygo interferometer, transmission sphere, alignment cubes and reference flats (Figure 4.5). Interferometry indicates misalignments precisely through patterns in the interferograms [Robert H. Barkhouser 1999]. It may be noted that usage of null lenses in conjunction with transmission spheres to generate proper collimated beam out of primary and secondary hyperbolic mirrors reaching alignment cubes and reference flats [Robert H. Barkhouser 1999]. Usage of the nodal aberration theory equations [Zhang et al. 2016] expressing Zernike coefficients as functions of alignment errors and known telescope parameters will allow us to achieve fine alignment. This will thus provide performance better than worst case of tolerance analysis.

Thus, the calibration and the alignment plan will allow us to decouple solar data from CCD effects, characterise the image quality and help telescope pointing. However, inter-payload misalignment should be minimised to allow solar disc pointing correction.

Chapter 5

Plage Detection and Carrington Maps from Century-Long Ca II K Spectroheliograms of Kodaikanal Observatory [1]

5.1 Introduction

Astronomical objects like stars are embedded with self organising system behaviour which is expressed in different scales and modes over time. Multimodal long duration data may assist in gaining insight about such complex system dynamics. Being a part of the solar system it is of particular interest for us to study the evolution of spatially resolved features on the Sun. In this regard, long term data available from different ground based observatories provide valuable informations at different wavelengths. Ca II K (3933.67 Å), line of singly ionised calcium, is one such study wavelength. This absorption line extends facts about solar chromosphere [Stix 2004]. Intensities observed through this line are dependent on magnetic field strength. Locations of

[1] *Results of this chapter are published in Chatterjee et al. [2016]*

higher magnetic fields are correlated with bright regions in Ca II K solar intensity images [Sheeley et al. 2011, Harvey & Worden 1998]. Thus the Ca II K line emission provides a good proxy for line of sight magnetic field fluxes, particularly for a historical period where regular direct magnetic field measurements are not available [Skumanich et al. 1975, Schrijver et al. 1989]. The Kodaikanal Solar Observatory (KoSO) has archived full disc Ca II K spectroheliograms for more than a century (1906 to mid 2007), using photographic plates as recorded through a telescope having a 30 cm objective with f-ratio of f/21 [Priyal et al. 2014b]. The effective spatial resolution was about 2 arcsec for majority of the documentation time. Recently, 16 bit digitisation has been performed on those plates through a CCD sensor (pixel size 15 micron cooled at -100^{o}C) to generate 4096×4096 raw images. This data provides a significant temporal window [Foukal et al. 2009] to study the evolution of solar activity while studying the variation of disc structures, namely plages, filaments, sunspots [Zharkova et al. 2005]. While comparing the quality of different Ca II K images as recorded from Arcetri, Kodaikanal, and Mount Wilson observatories Ermolli et al. [2009] concluded that KoSO provides a homogeneous and the longest series. Note that this comparison was made based on earlier low resolution scanned images (as obtained from KoSO) and the need for higher resolution digitisation was pointed out by Ermolli et al. [2009]. First results from the new digitisation process was reported in Priyal et al. [2014b] using KoSO data on Ca II K for the period 1955-1985. We have recalibrated the data for the full 100 years and are presenting the first results from the new time series. The extracted data through this study is also being made available to the scientific community for further processing. The digitised data is available through `https://kso.iiap.res.in/data`.

Few earlier studies have reported identification of chromospheric features, to generate time series for the understanding the long term variation of their sizes and location. But none of them used century-long data, which allows us to study several solar cycles and inter-cycle variation and this may help in our understanding of the the solar dynamo model [Jin & Wang 2015]. In the context of data processing, detection methods typically rely on intensity contrast and size of target features. However, contrast may differ between images causing mis-detection of structures. Also, such techniques suffer from fragmentation of segmented features resulting in centroid detection error

[Zharkova et al. 2005]. In the present work we used newly digitised higher resolution century-long KoSO Ca II K data for automated plage detection. This generated a number of time series (viz. area cycle, butterfly diagram and their combination) to facilitate the study of solar activity variation keeping in mind the limitations and constraints. Section 5.2 illustrates the image statistics, calibration, enhancement and processing techniques. The data was also exploited to generate synoptic Carrington Rotation (CR) maps. Section 5.3 depicts plage area cycle, butterfly diagrams and positional correlation of some Ca II K CR maps with the same generated from line of sight magnetograms. The CR maps corresponding to the 100 years data are available online (supplementary material). Relevance of our results are summarized and concluded in Section 5.4 along with necessary discussion.

5.2 Processing and Analysis of Ca II K Spectroheliograms

The digitised full disc century-long (1907 to mid 2007) 4096×4096 Ca II K solar images ($\approx$ 0.8 arcsec/pixel) from KoSO (Figures 5.1a-b) used in the study were recorded through a telescope having 30 cm objective with f-ratio of f/21 [Priyal et al. 2014b] and spatial resolution about 2 arcsec. We employed few calibration steps before the feature detection was performed. They were namely flat fielding, disc detection and centring, north-south rotation correction, intensity inversion and limb darkening correction. Hough circle transform [Sonka et al. 2014] was applied on edge detected raw images to efficiently identify the disc centre and radius in contrast to manual method described in earlier work by Priyal et al. [2014b]. The radius varied by some number of pixels systematically over time due to change in sun-earth distance during each revolution. All the disc centred images were rescaled to one fixed size ($N \times N$) having uniform disc radius (R) (Figure 5.2a).

5.2.1 Limb Darkening Correction

Limb darkening is a systematic large scale variation of solar intensity from its centre to limb due to line of sight effect. This should ideally be a radially symmetric function but due to atmospheric and instrumental effects it loses the symmetry. In contrast to the

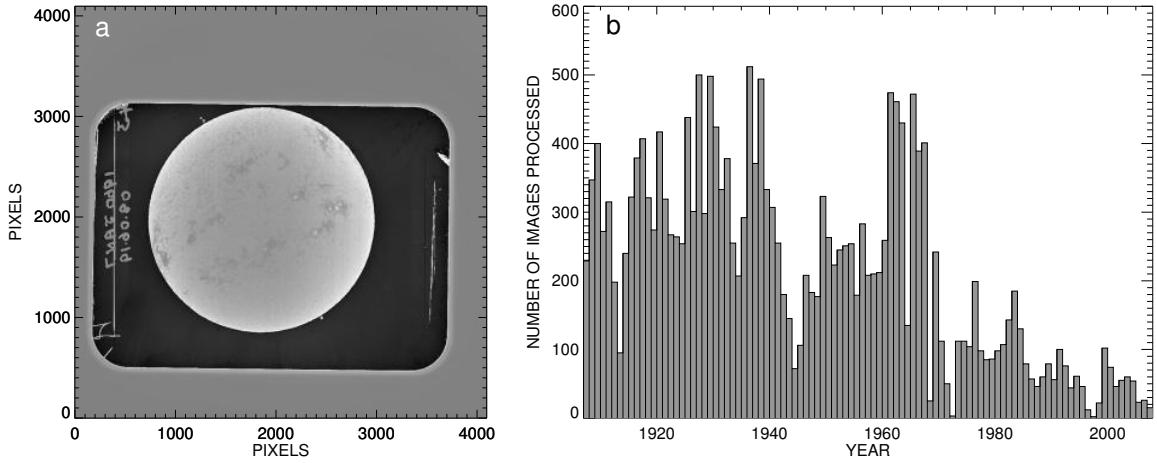

Figure 5.1: Input for the processing. a) One representative Ca II K spectroheliogram raw image from KoSO; b) Ca II K image histogram showing number of images considered for processing year wise

radially symmetric polynomial method of limb darkening estimation for KoSO data as presented in Priyal et al. [2014b], current study captured the variation applying a 40 × 40 2D median filter [Zharkova et al. 2005, Bertello et al. 2010] on the resized 512 × 512 disc centred images. This essentially performed blurring to represent large scale intensity variation (Figures 5.2b-c). Subsequently, the filtered image was again resized to original 4096 × 4096 size and was used to correct for limb darkening in the original image (Figure 5.2d).

5.2.2 Plage Detection

Histogram equalisation was applied on the limb darkening corrected images (LDC) to bring uniformity in intensity contrast throughout the study time and to enhance the target features with respect to background. There was no absolute intensity calibration or full disc flux measurement [Foukal & Lean 1988] unlike Ermolli et al. [2009]. The objective was only to detect plages. Global thresholds were then applied on the histogram equalised images to generate binary images (BW) with segmented regions of interest. Enhanced limb darkening corrected images were characterised by disc region intensity median ($\text{median}_{\text{Disc}}$) and standard deviation (σ_{Disc}). The disc region was described by pixels (i, j) satisfying $\sqrt{(i - \frac{N}{2})^2 + (j - \frac{N}{2})^2} \leq R$. The segmentation scheme was as

follows-

$$BW_{ij} = 1 \quad \text{when } LDC^{\text{HistEqual}}{}_{ij} > \text{median}_{\text{Disc}} + \sigma_{\text{Disc}}$$
$$= 0 \quad \text{otherwise}$$

After segmentation an area threshold of 0.25 arcmin^2 pixels was applied to discard unwanted regions. Subsequently, morph closing (a mathematical morphology operation consisting of dilation followed by erosion) [Sonka et al. 2014] was applied with a 3×3 (cross) structuring function to get rid of fragmentation in structures of interest (Figures 5.2e-f).

5.2.3 Plage Index Calculation

Plage index is an established metric, reflecting the occurrence of plage regions in Ca II K image. Following the description about plage index calculation as in Bertello et al. [2010], from the mean normalised intensity histrogram of solar disc with a bin-width of 0.01, 35 bins were selected above and below the mode. Within this range a Gaussian was fitted to calculate mean (μ) and variance (σ). Within $\mu - 2\sigma$ and $\mu + 7\sigma$, 30 bins were selected and another Gaussian ($f(x) = ke^{-\frac{(x-A)^2}{B}} + C$ where $(\mu - 2\sigma) \leq x \leq (\mu + 7\sigma)$) was fitted to it (Figure 5.3a). The constant term (C) of the Gaussian is named as plage index indicating the asymmetry in the histogram wings due to occurrence of high intensity regions called plages. For further validation the correlation of plage index with fractional plage area acquired from plage detection is also presented (Figure 5.3b). Hereafter for solar cycle variation studies we will use the fractional plage area, the fraction of solar disc area covered by plages, as a most favoured proxy. The 12 month running average smoothing was performed on monthly averaged plage area cycle and compared with same for Mount Wilson Observatory (MWO) in Figure 5.4.

5.2.4 Plage Centroid Detection and Butterfly Diagram

After morph closing operation on binary plage detected images the individual connected structures were identified through giving certain labels to the pixels falling in same region. Subsequently, centroid latitudes for all those regions were calculated

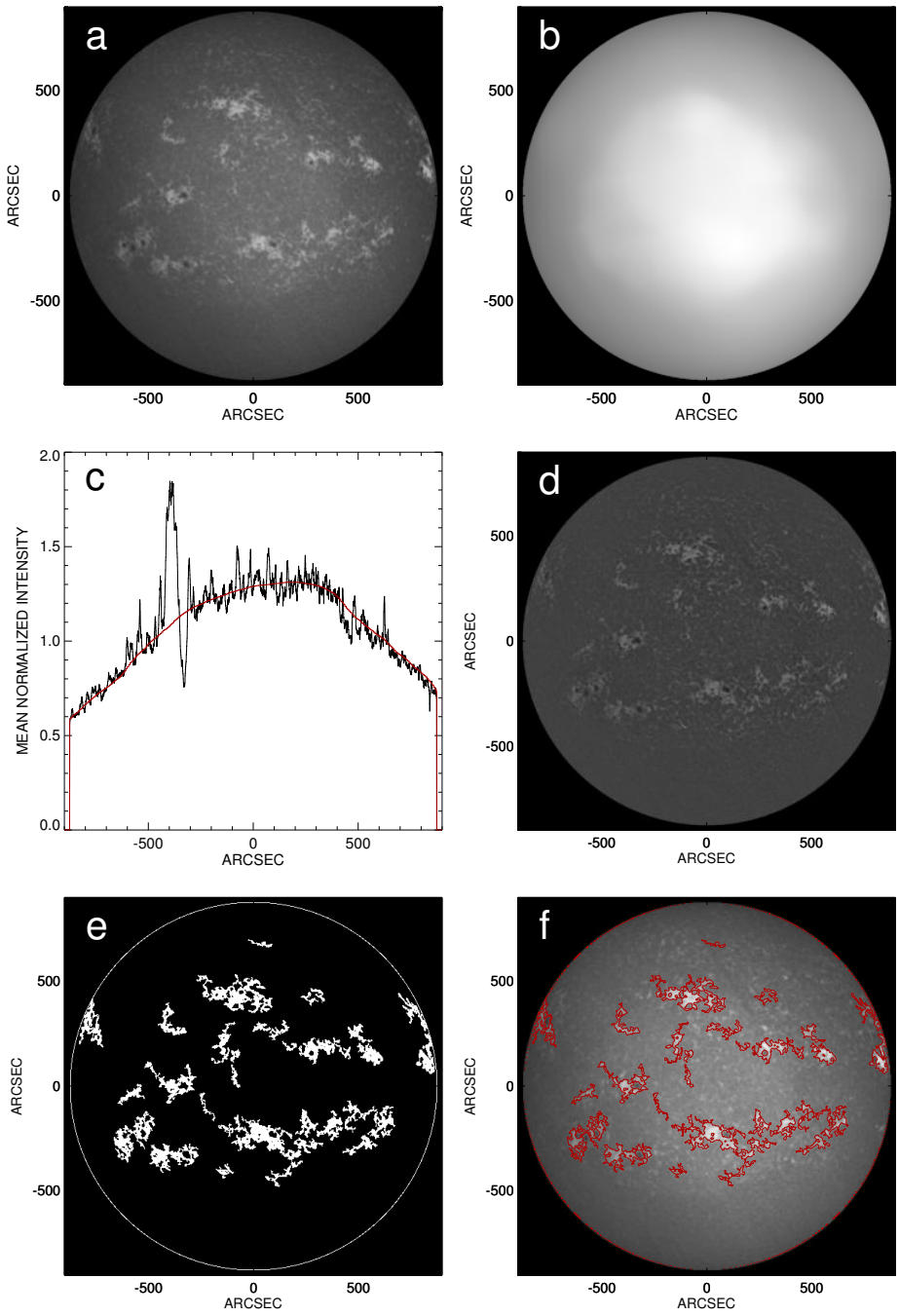

Figure 5.2: Processing steps involved for a representative KoSO Ca II K image to detect plages. a) Ca II K disc centred image; b) Blurred image applying large window median filtering on (a) to understand centre to limb intensity variation; c) x-profile overplotted through centre of (a) and (b); d) Limb darkening corrected image; e) Plage segmented image through row wise thresholding; f) Plage contour overplotted on (a)

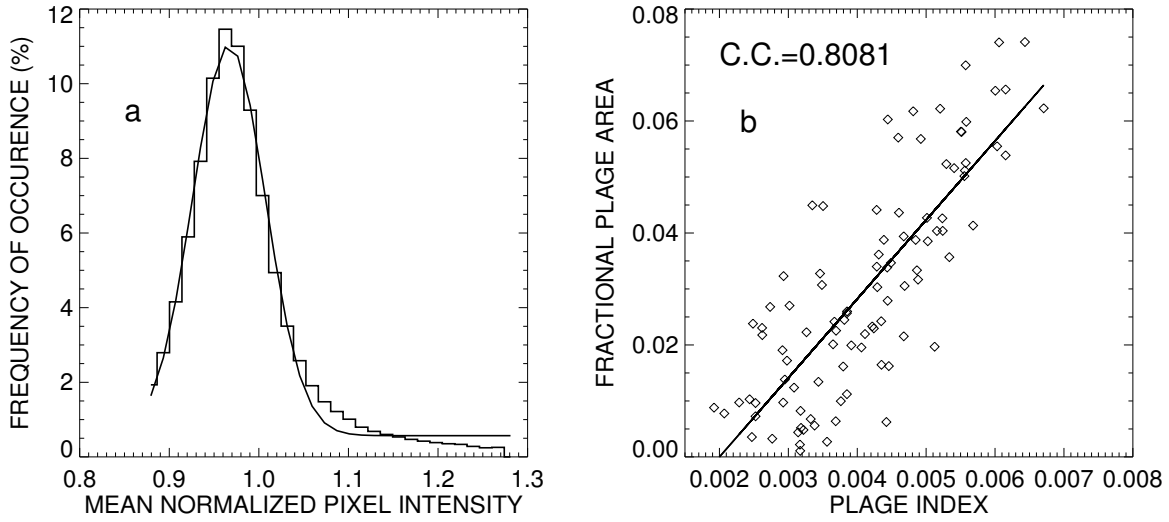

Figure 5.3: Validation of the current detection strategy. a) Intensity histogram of a Ca II K image disc region and its Gaussian fit; b) Correlation of fractional plage area and plage index with least square linear fit is given by, Fractional Plage Area $= -2.82 \times 10^{-2} + 14.1133 \times$ Plage Index

for each image and were stacked over time to generate butterfly diagram with four area thresholds for the plage regions 1 arcmin^2, 4 arcmin^2, 7 arcmin^2 and 10 arcmin^2 (Figure 5.6).

5.2.5 Carrington Map Generation

Carrington map is the Mercator projection of the spherical sun mostly generated from daily observation for one solar rotation. In this study, 60 longitude bands across the limb darkening corrected full disc Ca II K images were selected, B_0 angle corrected and stretched in form of a rectangle with a weightage of fourth power of cosine [Sheeley et al. 2011, Harvey & Worden 1998] over each longitude with respect to the central meridian. These slices were shifted and added according to date and time for 27.2753 days to generate a full 360 degree map of sun. A similar 360 degree map was obtained from rectangular binary slices called streak map [Sheeley et al. 2011]. The overlap of same Carrington longitudes was removed through division of the original 360 degree map with streak map to form an image called Carrington map or Synoptic map (Figures 5.5a-d). Carrington maps were also generated from few MDI LOS full disc magnetograms available after 1996. Binary Carrington maps were generated for Ca II K and MDI

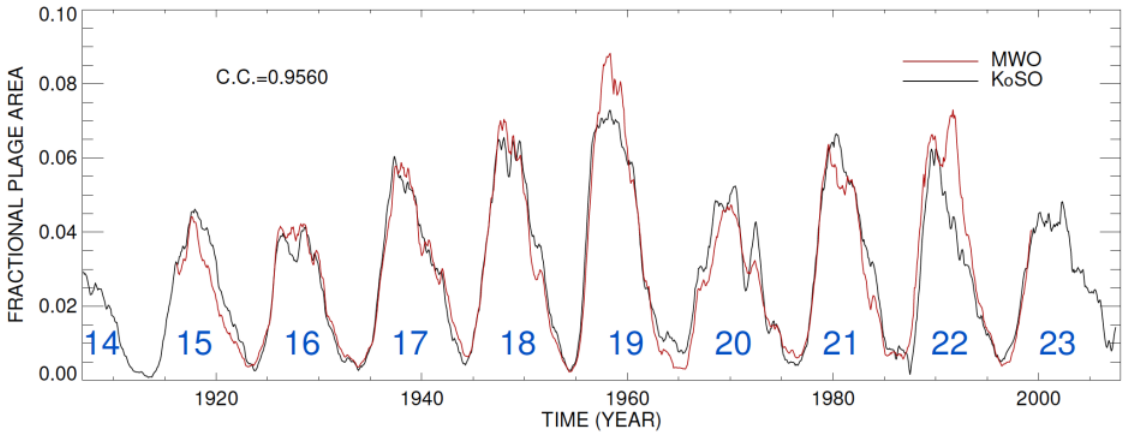

Figure 5.4: Ca II K plage area cycle depicting 12 months running averaging applied over monthly average plage area. Black curve corresponds to the Kodaikanal Ca II K archival data and the red curve corresponds Mount Wilson Observatory. Least square linear fit for the overlapping region (1915-2000) is give by, $\text{Plage Fraction}_{\text{MWO}} = -0.0009 + 1.0252 \times \text{Plage Fraction}_{\text{KoSO}}$. Cycle numbers are marked in blue.It should be noted that the plage series in red has contribution from other observatories after 1985 as MWO series ends in 1985. MWO, being the primary source, this series has been marked as MWO.

using mean $+\,\sigma$ and mean $\pm\,\sigma$ thresholds respectively. These maps were further blurred using Gaussian filter to account for the feature boundary uncertainty and were cross-correlated for different relative x-y shifts.

5.3 Results on Detected Plages and Carrington Maps

For the study of the century-long magnetic activity of the Sun, the Ca II K plage structures (Figure 5.2), with projected area ≥ 1 arcmin^2, have been used as the primary building block for magnetic proxy. Their segmentation endorsed the area threshold as 0.25 arcmin^2 to minimise loss of fragmented plage structures before morphological closing operation. This enabled us to deal with a good number of plage structures and to achieve desired statistics for the study of solar cycle variation. Histogram equalisation on individual limb darkening corrected solar images resulted in uniformity in image contrast. This also allowed us to detect the features automatically without any human bias of selection by visual inspection. The area cycle, a temporal evolution of fractional disc area covered by plages, showed a good correlation (95.6%) with the same from MWO for the overlapping time period (Figure 5.4). This is an improvement over the

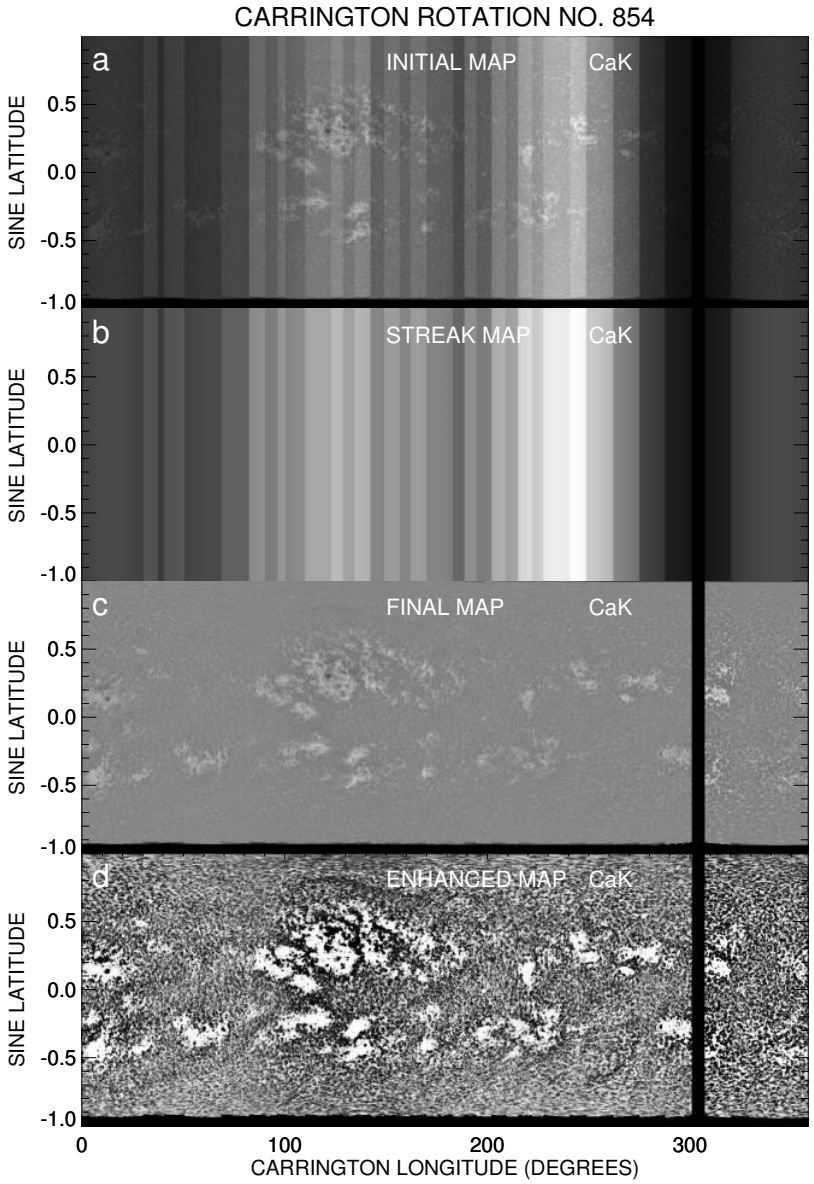

Figure 5.5: Carrington maps generated from Kodaikanal observatory Ca II K full disc spectroheliograms starting at 23rd July,1917. a) Carrington map before overlap correction; b) Streak map to determine overlaps; c) Corrected map by division of (a) by (b); d) Intensity enhanced map through histogram equalization.

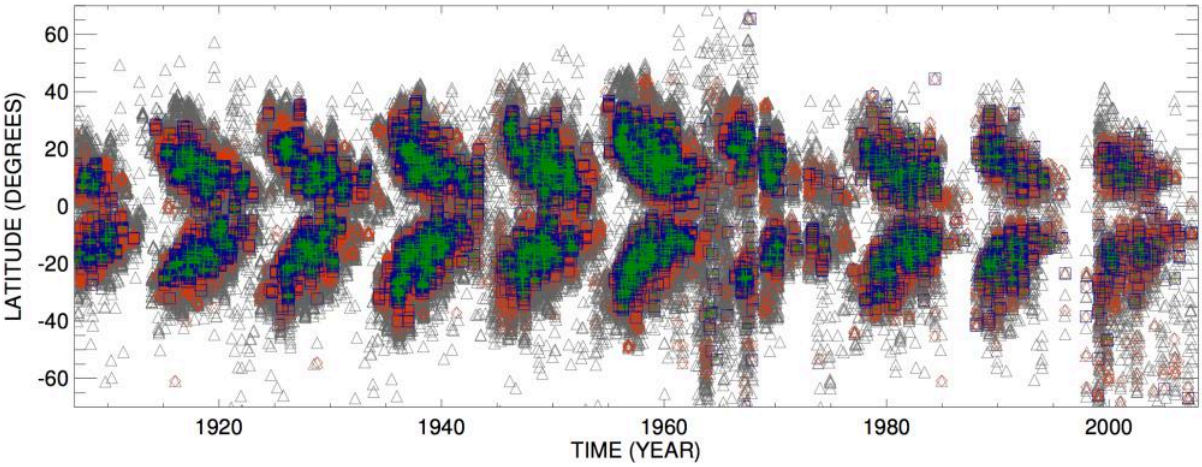

Figure 5.6: Ca II K butterfly diagram. Grey triangles depict centroids of plages having area ≥ 1 arcmin^2. Red, blue and green symbols depict centroids of plages having area ≥ 4 arcmin^2, ≥ 7 arcmin^2 and ≥ 10 arcmin^2 respectively.

earlier report by Priyal et al. [2014b] on KoSO Ca II K data for the period 1955-1985 in which the correlation was shown to be 89%. It further revealed the cycle 19 as the strongest one (Figure 5.4) and evidenced the double peak behaviour in some of the cycles. Some unreal spikes were also observed at the cycle minima after 1975 due to less availability and inferior quality of images being correlated with the occurrence of outlier points in the butterfly diagram for some study period after 1985 (≈2 years) and 1994 (≈1 year). Those data points were removed using a criteria involving the maximum latitude of plage appearance at a certain phase of a cycle.

To explore the change in latitudinal distribution of enhanced Ca II K emission with time we have produced the butterfly diagram. The centroids of plages have been used for the generation of this diagram, in contrast to Sheeley et al. [2011] who used the Carrington maps for the same. Butterfly diagram with three area thresholds (Figure 5.6) reveals that higher plage areas are more concentrated to the equator with a spatial correlation with active regions [Stix 2004]. In order to have a better visualisation of the latitudinal variation of different sizes with time a 3D version of the butterfly diagram was created, adding individual projected plage area as the third dimension (Figure 5.7). An animated figure has also been created to demonstrate how the time-latitude distribution changes with variation of plage size. This dynamic illustration has been provided as a supplementary material in the link ftp://ftp.iiap.

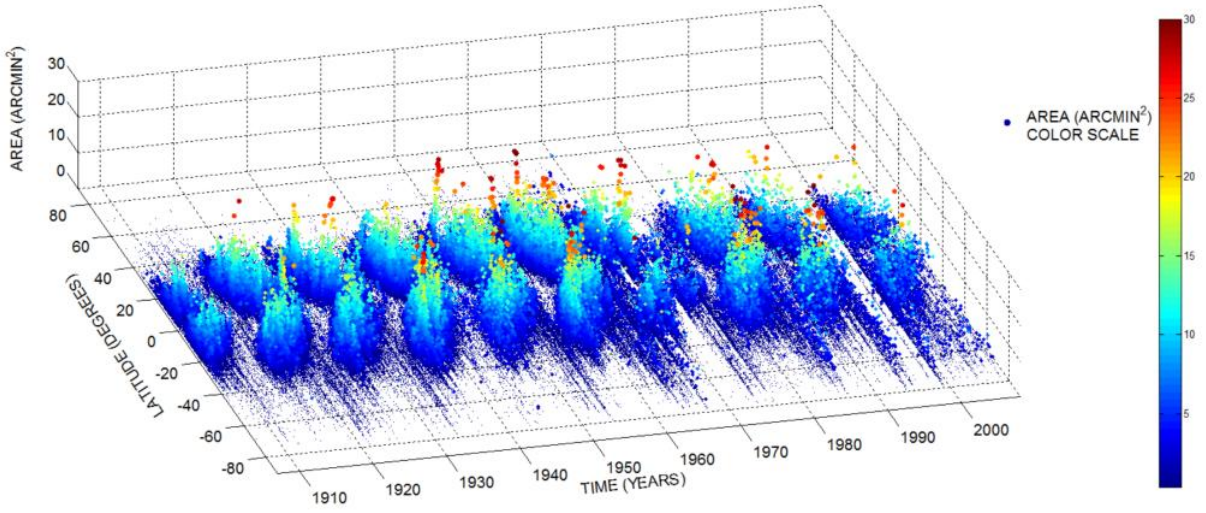

Figure 5.7: 3 dimensional visualisation of butterfly diagram with area of individual plages as the z-axis. Minimum to maximum plage area range is defined by dark blue to dark red through green, yellow and orange as indicated by the color scale. (A dynamic version of this figure in the form of an animated movie is available online).

res.in/subhamoy/cak_carrington_maps_kodaikanal/butterfly_cak_3d.gif and is available online. Figures 5.6 & 5.7 can be readily compared with well known butterfly diagrams as generated from sunspot areas showing higher latitude to equatorward occurrence of plage structures for each cycle. It should be noted that because of area thresholding the smallest features like network bright points are not detected in the current analysis and the poleward migration is not observed [Priyal et al. 2014a].

It has been pointed out earlier that the enhanced emission in Ca II K relates well with the magnetic field concentrations. Thus the Carrington maps do indicate the magnetic flux distribution over a solar rotation. In this article we presented Synoptic or Carrington maps (Figures 5.8a-c) incorporating plage evolutions for different solar rotations over the past 100 years. These maps will be particularly useful for the period when line of sight magnetograms are not available. Similar maps were generated by Sheeley et al. [2011] from MWO Ca II K data. First we will compare few representative cases of newly generated Carrington map from KoSO data and that of MWO. Figures 5.8 a,b,c can be compared with upper panel of Figure 4, lower panel of Figure 7 and lower panel of Figure 10 of Sheeley et al. [2011] respectively. The close resemblance of these maps provides a good validation of calibration, map generation and portray the quality of

Kodaikanal data. The longitude band selected for each full disc image to generate the map was result of a trade off between feature sharpness and data gap (Figure 5.8b). However, apart from geometrical similarity a difference in contrast and visibility of network structures can be observed between the maps from KoSO and MWO. This might have occurred because of the difference in digitisation and preprocessing of full disc images. In Figures 5.9 a, b, c and Figures 5.10 a, b, c we show few more examples of CR maps corresponding to different phases of a solar cycle as generated from Kodaikanal spectroheliograms without any data gaps. Enhanced Ca II K Carrington maps at later times (after 1990) show bright tilted periodic artefacts because of higher occurrence of scratches in the spectroheliograms.

Next we compare our Ca II K Carrington maps with Carrington maps of photospheric magnetic fields generated from full disc LOS magnetograms of MDI on SoHO. Cross-correlation of all sample Carrington maps from Ca II K (KoSO) and MDI showed maximum overlap at a relative x-shift and y-shift of about 5 pixels and 9 pixels respectively where size of the maps was 1571×500. This study reveals good spatial correlation ($\geq 75\%$) between magnetic patches and plage structures (Figures 5.11,5.12,5.13,5.14). Carrington maps from 1907 till mid 2007 have been provided as supplementary material (also available at `ftp://ftp.iiap.res.in/subhamoy/cak_carrington_maps_kodaikanal/`). We also provide a time lapsed movie which includes all these maps for the period of 100 years in the link `ftp://ftp.iiap.res.in/subhamoy/cak_carrington_maps_kodaikanal/cak_video_1907_2007.gif` (available online).

5.4 Discussion and Conclusion

We have used Ca II K line images, recorded in the KoSO, digitised and calibrated by our group, to construct Carrington maps and butterfly diagrams corresponding to the period of 1907-2007. The KoSO data allows us to study the cyclic activity of the solar magnetic fields for longer duration (>100 years) in contrast to that from MWO which is for about 85 years [Bertello et al. 2010]. Sheeley et al. [2011] studied Carrington maps from 1915 till 1985 from the MWO archive, whereas the current study generated

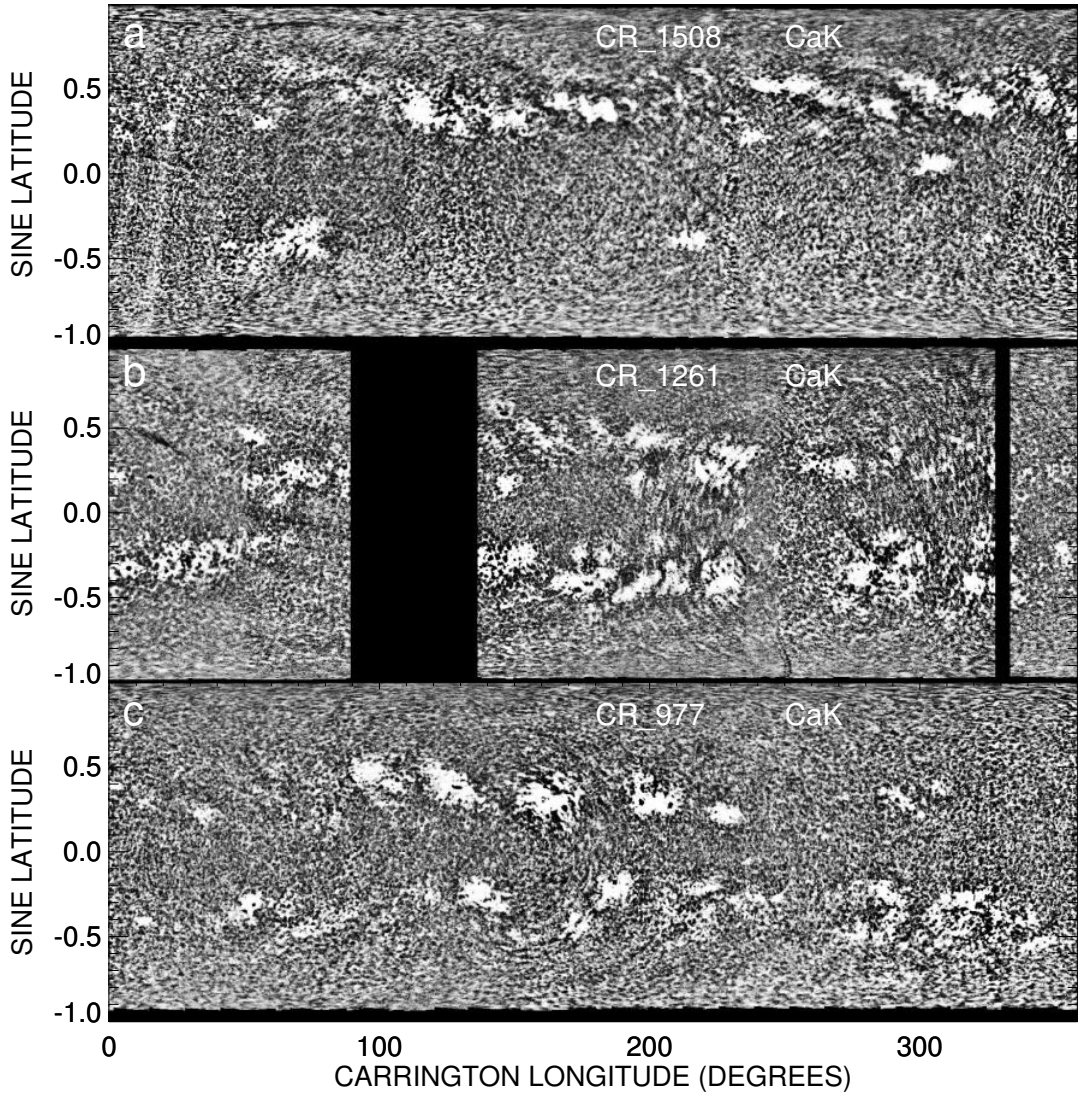

Figure 5.8: Carrington maps generated from Kodaikanal observatory Ca II K full disc spectroheliograms. a) Carrington map starting at 25th May, 1966; b) Carrington map starting at 14th December, 1947; c) Carrington map starting at 29th September, 1926.

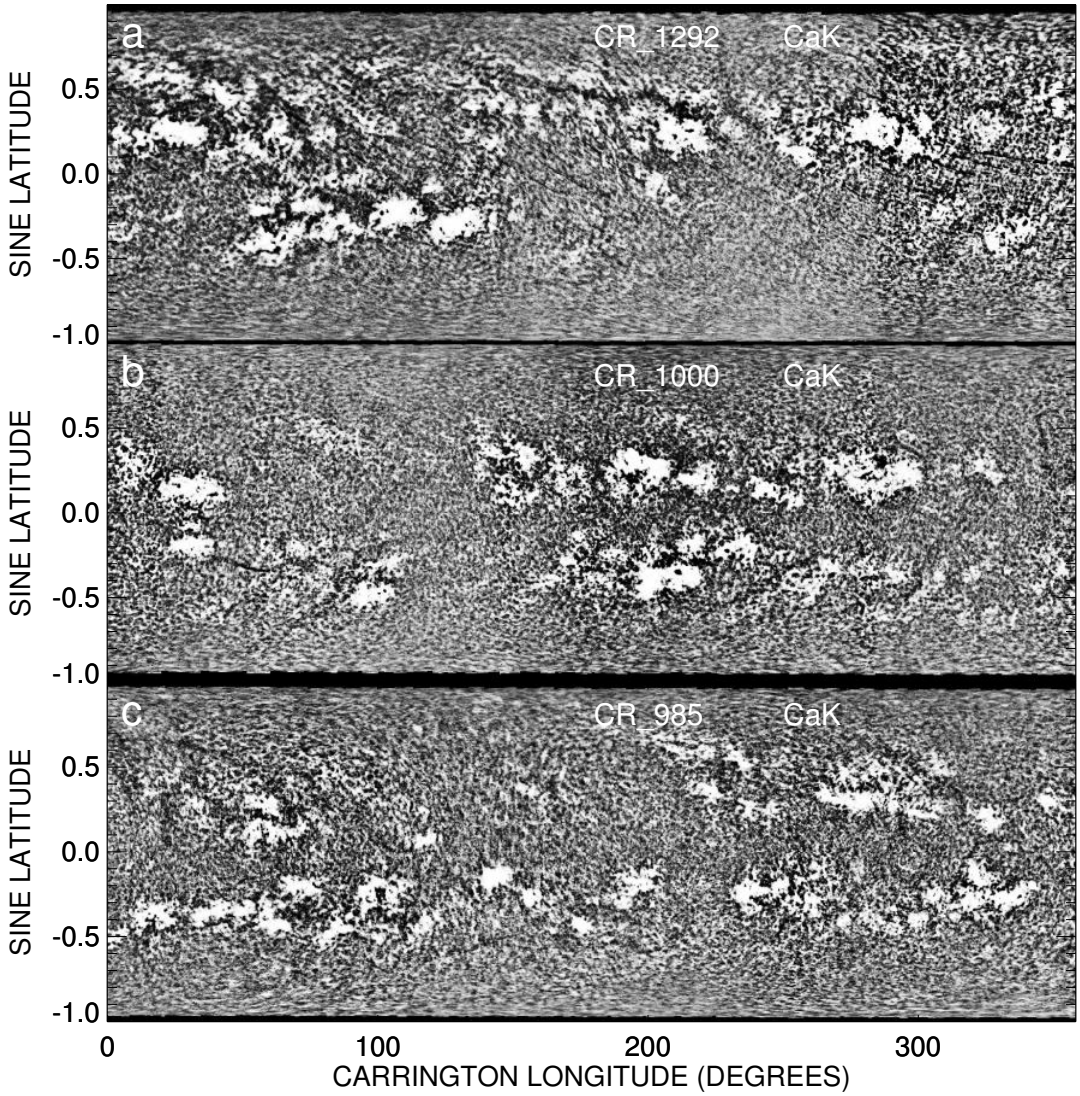

Figure 5.9: Carrington maps generated from Kodaikanal observatory Ca II K full disc spectroheliograms. a) Carrington map starting at 8th April, 1950; b) Carrington map starting at 17th June, 1928; c) Carrington map starting at 5th May, 1927.

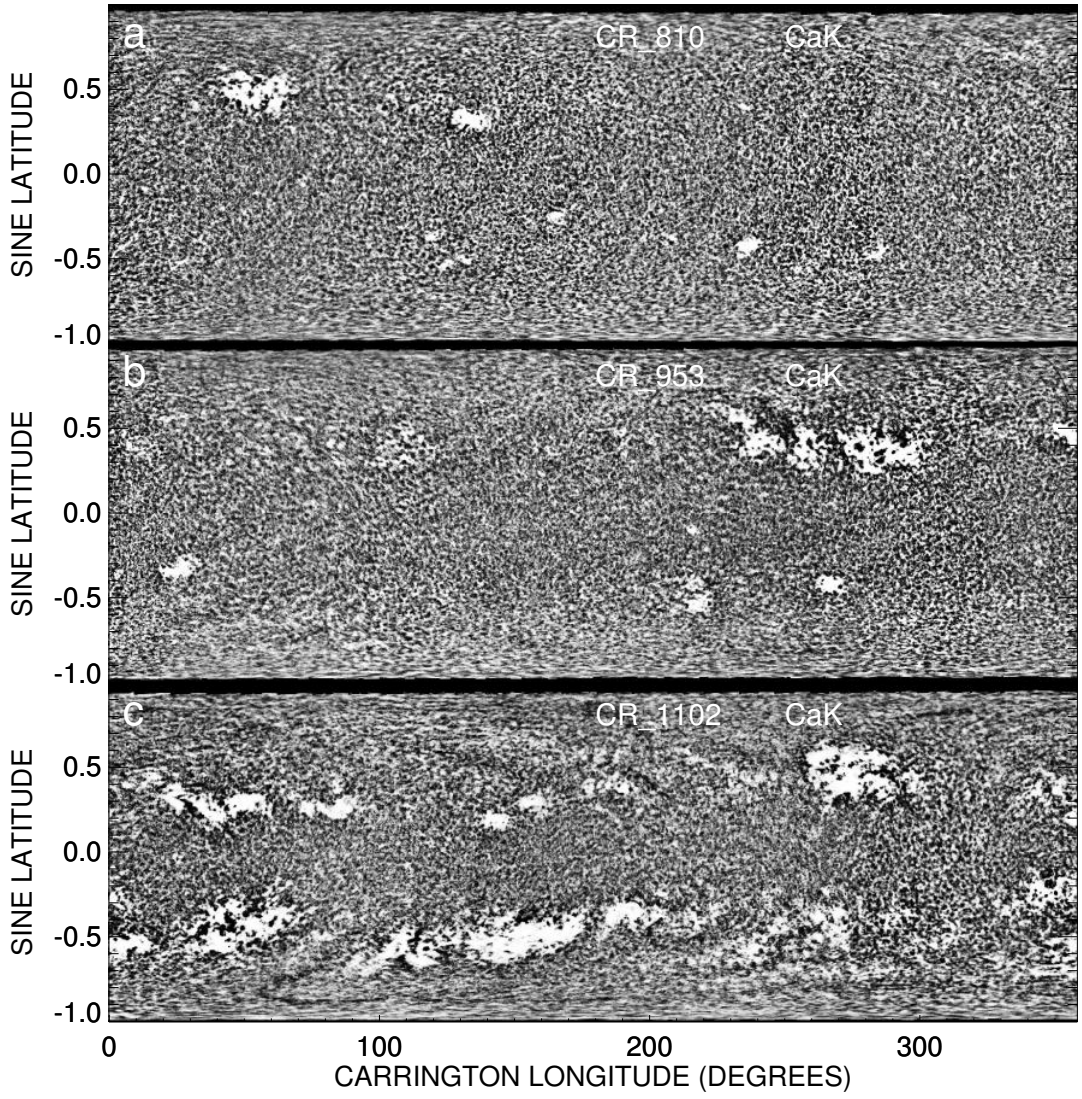

Figure 5.10: Carrington maps generated from Kodaikanal observatory Ca II K full disc spectroheliograms. a) Carrington map starting at 10th April, 1914 which is at the minimum phase between cycle 14 and 15; b) Carrington map starting at 13th December, 1924 which is at the minimum phase between cycle 15 and 16; c) Carrington map starting at 30th January, 1936 which is at the beginning of rising phase of cycle 17. For all these three maps plages are mostly at higher latitudes $\approx 30^o$.

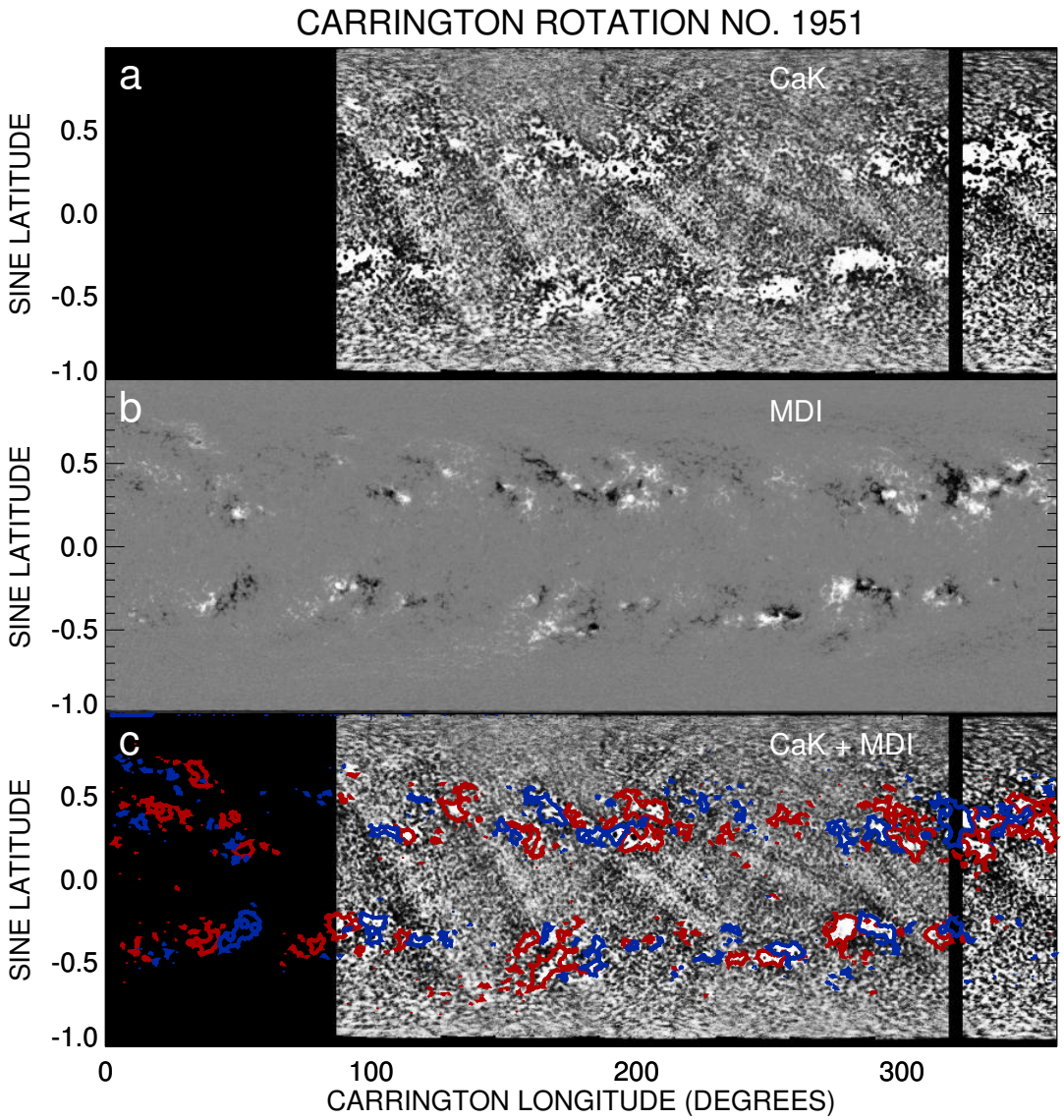

Figure 5.11: Overlap of plage structures and magnetic patches for Carrington rotation 1951. a) Carrington map starting at 24th June, 1999 generated from Kodaikanal Observatory Ca II K full disc spectroheliograms; b) Carrington map generated from MDI full disc LOS magnetograms for the same rotation as that for Ca II K; c) Contours of large magnetic patches overplotted on (a). Red and blue depict towards and opposite to LOS direction. Positional correlation ≈ 86.3%.

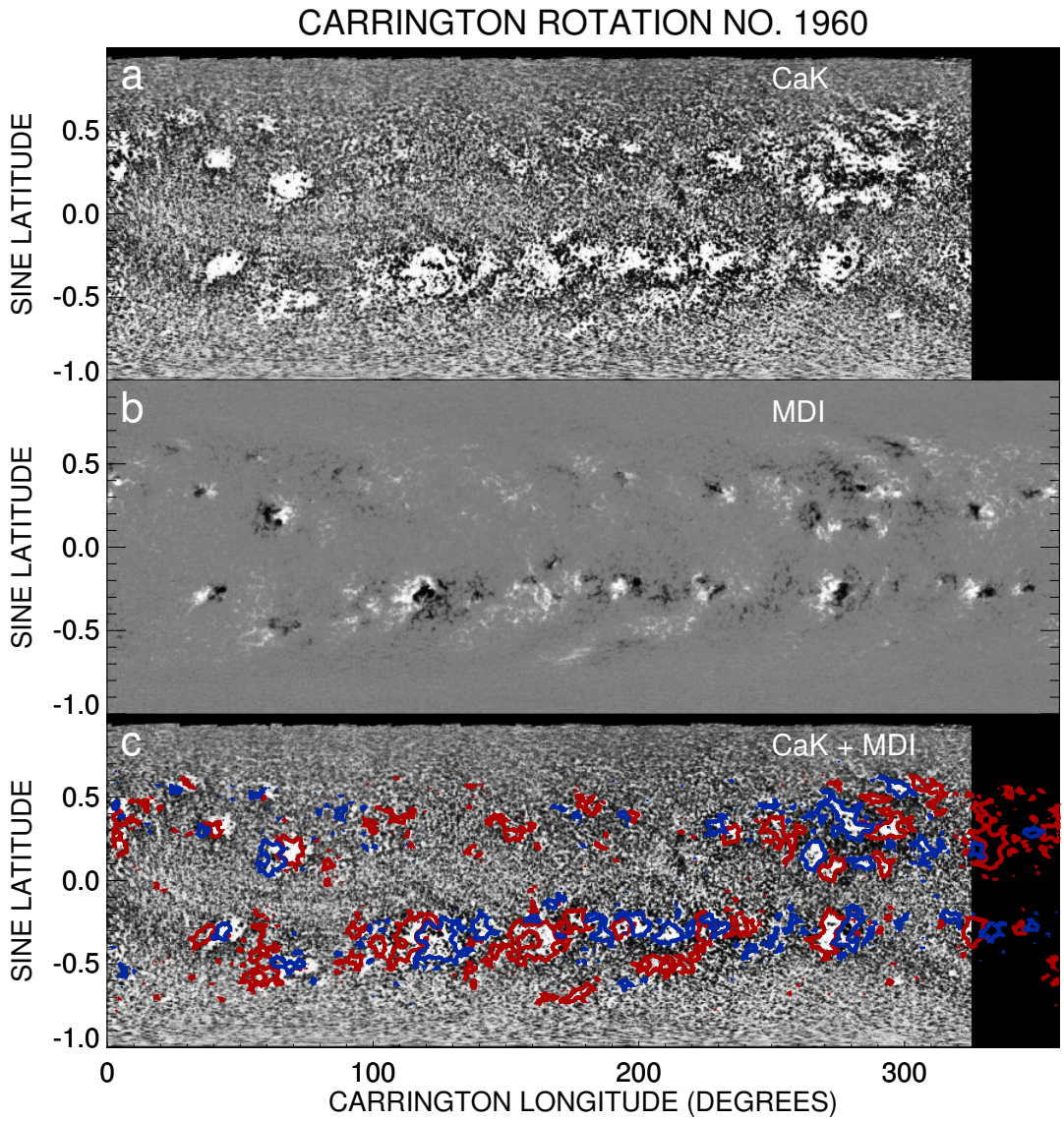

Figure 5.12: Overlap of plage structures and magnetic patches for Carrington rotation 1960. a) Carrington map starting at 25th February, 2000 generated from Kodaikanal Observatory Ca II K full disc spectroheliograms; b) Carrington map generated from MDI full disc LOS magnetograms for the same rotation as that for Ca II K; c) Contours of large magnetic patches overplotted on (a). Red and blue depict towards and opposite to LOS direction. Positional correlation ≈ 85.5%.

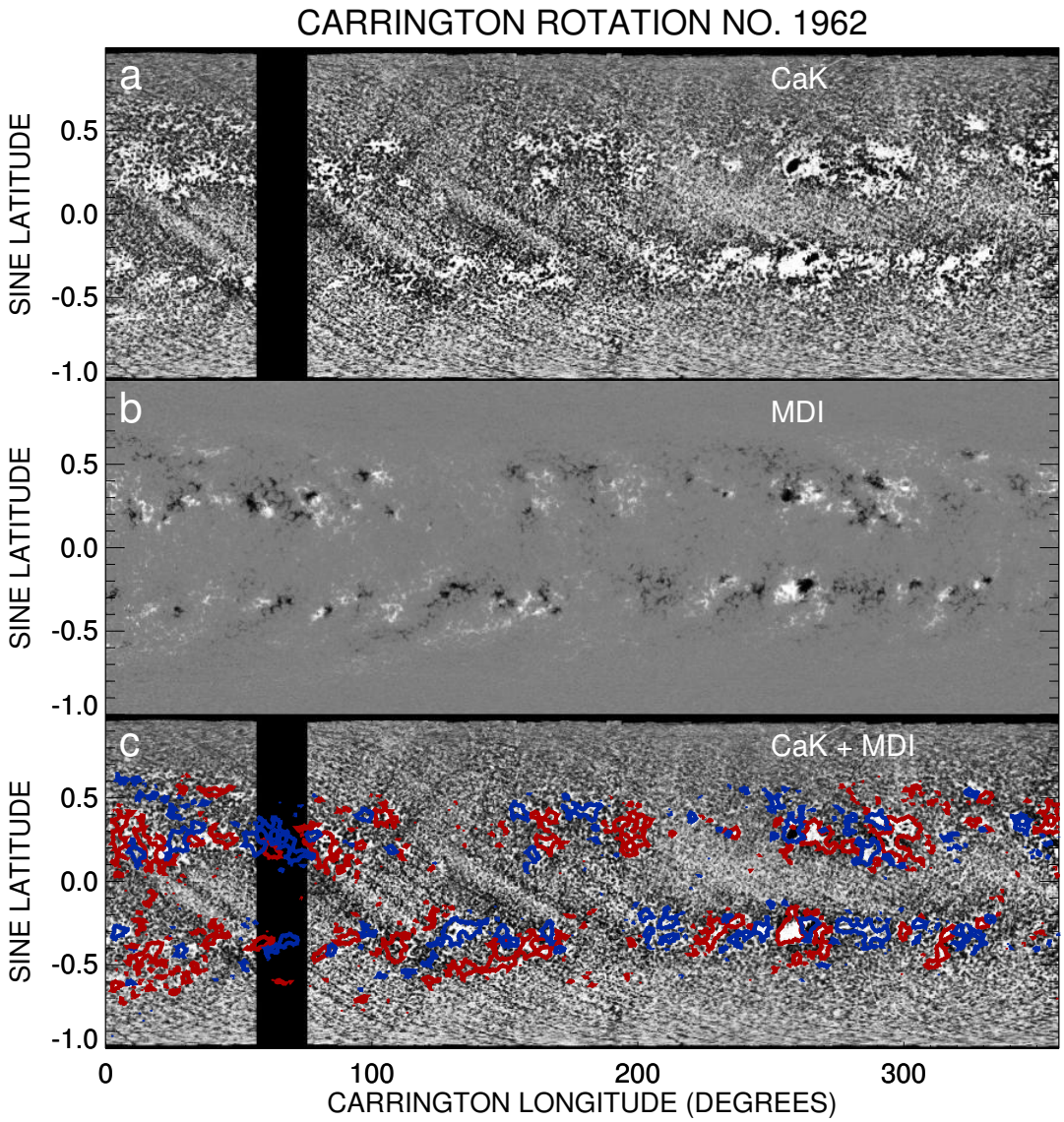

Figure 5.13: Overlap of plage structures and magnetic patches for Carrington rotation 1962. a) Carrington map starting at 19th April, 2000 generated from Kodaikanal Observatory Ca II K full disc spectroheliograms; b) Carrington map generated from MDI full disc LOS magnetograms for the same rotation as that for Ca II K; c) Contours of large magnetic patches overplotted on (a). Red and blue depict towards and opposite to LOS direction. Positional correlation ≈ 75.1%.

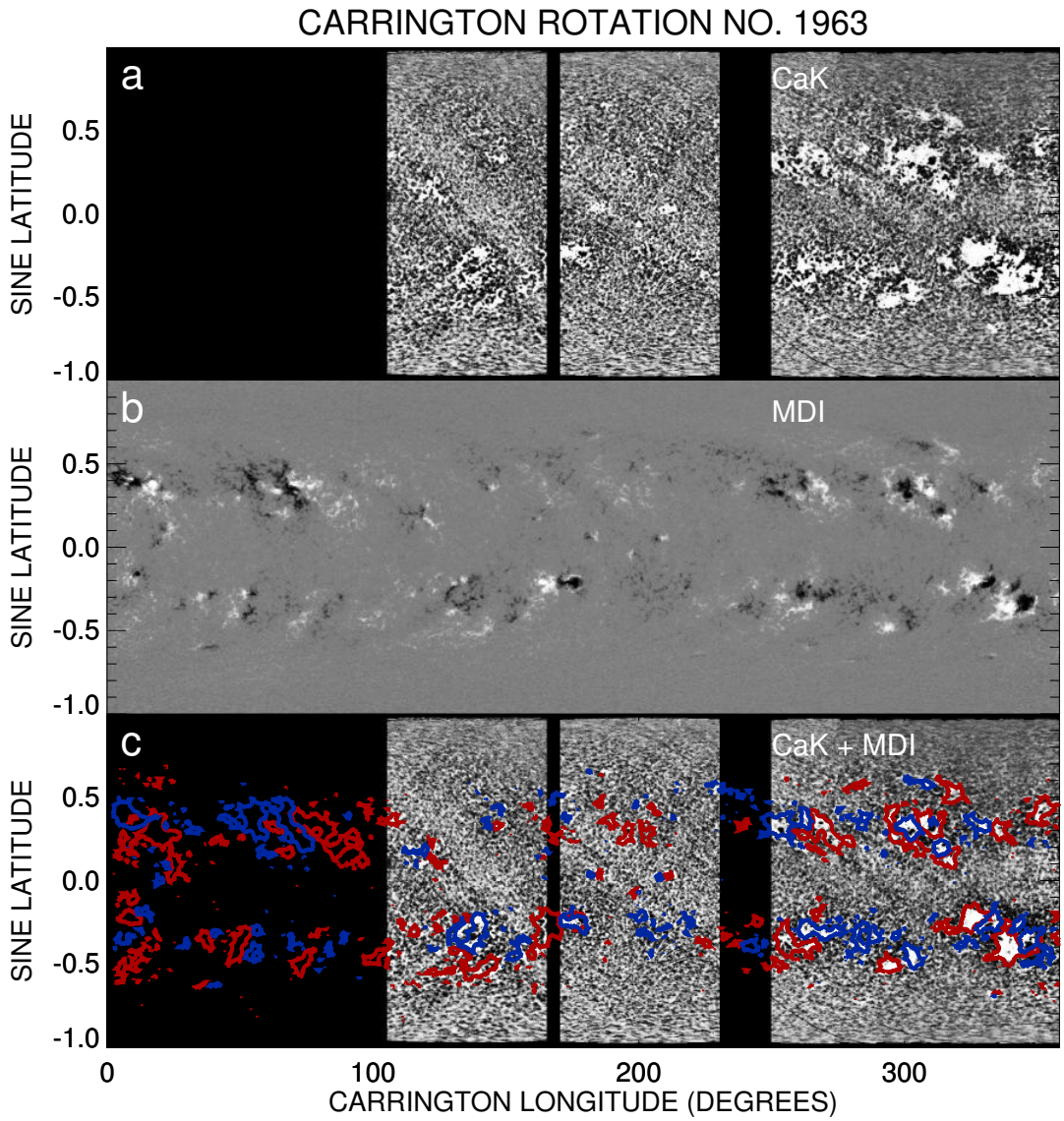

Figure 5.14: Overlap of plage structures and magnetic patches for Carrington rotation 1963. a) Carrington map starting at 17th May, 2000 generated from Kodaikanal Observatory Ca II K full disc spectroheliograms; b) Carrington map generated from MDI full disc LOS magnetograms for the same rotation as that for Ca II K; c) Contours of large magnetic patches overplotted on (a). Red and blue depict towards and opposite to LOS direction. Positional correlation ≈ 92.3%.

Carrington maps from 1907 to mid 2007 using images which were recorded at the KoSO. These maps provide ways of tracking magnetic field distributions all the way back to 1907, a period from which direct magnetic field synoptic observations are not available. In the context of long term evolution of features on Sun at specific wavelength present study segmented plage structures, generated area cycle and butterfly diagram from 100 years Ca II K KoSO data. Derived century-long Ca II K synoptic maps further elaborated correlation with the same generated from space based magnetograms for an overlapping study period and confirmed their physical connection [Stix 2004, Sheeley et al. 2011].

Figure 5.7 illustrated cyclic behaviour of the projected area for individual plages at different latitude bands. It also gives hint about the relative delay in attaining cycle peak for individual plage area between different latitudes. So, this area scaled butterfly diagram gives some additional information for a greater time span (1907-2007) in contrast to the super synoptic map presented in Sheeley et al. [2011] with study period between 1915-1985. Location overlap between plage structures and magnetic patches in turn validated the theoretical expectation of higher field strength correlated with less Ca II K absorption [Pevtsov et al. 2016]. Therefore the century-long Ca II K data can act as a proxy for understanding the locational evolution of magnetic patches.

This study essentially demonstrated the importance of century-long Ca II K spectroheliograms to delineate evolutionary features from different perspectives and their possible correspondence. Observations about latitude dependent plage area variation can add some more insight to the conventional area cycle, being an aggregate. Along with the study of long term evolution some smaller time scale phenomena can also be analysed from this huge data. Rotation rate variation for different latitudes can be analysed from plage areas over 100 years [Kiepenheuer 2012, Singh & Prabhu 1985]. Machine learning techniques can be applied on and validated through this huge data giving confidence about the prediction for future cycle characteristics [Colak & Qahwaji 2009]. We propose to address some of these aspects in our future studies.

We hope that the result presented here and Carrington maps published online (ftp://ftp.iiap.res.in/subhamoy/cak_carrington_maps_kodaikanal/) will also help the global community to study different features at a greater depth and the new database

available at https://kso.iiap.res.in/data will act as a valuable resource. Recently Pevtsov et al. [2016] have attempted to create a homogeneous, long term series of pseudo-magnetograms using a combination of Ca II K line images and sunspot polarity measurements. We hope to pursue the same in near future from our KoSO data. We further propose to combine the MWO and KoSO data sets to produce a single improved set. This will also enable to fill up the data gaps in the two independent datasets. This cross-calibration and comparison will yield a data series with uniform quality. We would like to mention that further refinements, improvements in the calibration process and cross-calibration between different data series will be released time to time through our web portal at https://kso.iiap.res.in/data with marked versions and data products.

Chapter 6

Variation of Supergranule Parameters with Solar Cycles Observed from Century-Long Kodaikanal Digitized Ca II K Data [1]

6.1 Introduction

Sun, a magnetically active star, has an atmosphere which varies widely with height in density and temperature. The lower most layer of the atmosphere is known as photosphere where we observe the signature of solar convection, the granules (characteristic scale of the granules is few Mm). There are patterns on the solar surface which are larger (~30 Mm) than the granular scales. These are known as supergranules. Supergranules appear with different shapes and sizes. The boundaries of these structures are the host of the magnetic fluxes and dispersal of such flux is believed to be governed by the diffusion caused by evolution of supergranules [Rast 2003, Crouch et al. 2007].

The origin of the supergranulation is not fully understood. It can be due to convection (like granules) or can be a dynamic instability also. The study of the supergranules is important from the fact that it reveals the intrinsic scale of physical mechanism which

[1] *Results of this chapter are published in Chatterjee et al. [2017]*

drives these structures. Also one can investigate the effect of strong magnetic field by studying the supergranular properties separately for active and quite regions. There have been a few studies in the past on the detection and calculation of different properties of the supergranules. Using a auto-correlation curve technique Sýkora [1970], Hagenaar et al. [1997] have detected the supergranular structures whereas Muenzer et al. [1989] have estimated the latitudinal dependence of the supergranule sizes, by using Ca II images, through a Fast Fourier Transform (FFT) analysis for both the active and quiet regions. These automated methods are useful in determining the aggregate properties of supergranules but they fail to record the parameters of individual structures. In an another work, Berrilli et al. [1999] have used an automated skeleton detection method and have shown the temporal variation of the quiet region region cell size for one year data set. Hagenaar et al. [1997] showed the invariance of supergranule scale distribution at different spatial smoothing. They have also studied the distribution of supergranule scales and found similarity of the same with Voronoi tessellation. A similar work has been done by Srikanth et al. [2000] where these authors have quantified the distribution using skewness and kurtosis parameters. In a recent work, McIntosh et al. [2011] have explored the variation of the supergranular parameters from five independent sources using the 'watershed segmentation' method to detect the supergranules from the images. From their results (for a period of 33 years, 1944-1976) they found imprints of the solar cycle variation in the supergranule parameters. Thus we see that a study of the supergranule parameters for several solar cycles is necessary to find out their relation with the large scale solar variation.

Using the Kodaikanal digitized Ca II K data, we present, for the first time, the variation of the supergranular parameters for a period of 100 years (1907-2007) in this work . Kodaikanal Solar Observatory (KoSO) has archived 100 years (cycle 14-23) of chromospheric images in Ca II K (3933.67 Å) through an unchanged *f/21* optics with a 30 cm objective. This gives an enormous opportunity to study the synoptic variation of supergranular cell sizes over many solar cycles and also to understand their correspondence with the solar activity. This work is organized as follows: After presenting a brief data description in Section 6.2, we define the detection method and various parameters associated with supergranlues in Section 6.3. Results from the

KoSO are discussed in Section 6.4 whereas in Section 6.5 we present the results using the data from other observatories. Finally, Section 6.6 concludes along with necessary discussion.

6.2 Data Description

The primary data used in this study are taken from the digitized archive of the Kodaikanal Ca II K observations [2] [Priyal et al. 2014b, Chatterjee et al. 2016]. Apart from that we have also used data from Precision Solar Photometric Telescope (PSPT) [Ermolli et al. 1998]. The details of each data set are given in Table 6.1.

We have used, for comparison, the V2.0 daily sunspot number data from SIDC (Solar Influences Data Analysis Center) which is available at http://www.sidc.be/silso/datafiles.

Table 6.1: Details of the different datasets used in this study

Data Source	Wavelngth (passband) (Å)	Duration	Pixel Scale
KoSO Ca II K	3933.67 (0.5)	1907-2007	0.8"
PSPT-ITALY	3934.00 (2.5)	1996-2016	1″
PSPT-USA	3934.00 (1.0)	2005-2015	1″

6.3 Definitions and Methods

6.3.1 Detection of Supergranules

Supergranules refer to the large scale velocity structures with a spatial extent of ~30 Mm and a typical lifetime of 25 hours [Rieutord & Rincon 2010]. These structures also have a strong horizontal flow of $\approx 400\,\mathrm{m\,s^{-1}}$. Now, in the intensity images taken through a chromospheric line such as Ca II K, we notice a boundary like pattern also known as 'chromospheric network'. These networks actually outline the supergranular cells

[2] https://kso.iiap.res.in/data

and can be used as a proxy for supergranular shape and size measurements [Simon & Leighton 1964]. We follow this convention thoughout the work. In order to identify these structures, we first select a rectangular region ['region of interest', ROI] at the disc center with sides equal to 60% of solar disc diameter. Such selection is made in order to minimize the errors due to the projection effect. Different steps, involved in detecting the supergranules from KoSO and PSPT intensity images, are shown in different panels of Figure 6.1. We highlight the ROIs with the rectangles as shown in panels 6.1.a's and the full view of the ROIs are shown in panels 6.1.b's. Next, these regions were histogram equalized and smoothed with a median filter to reduce noise (panels 6.1.c's).

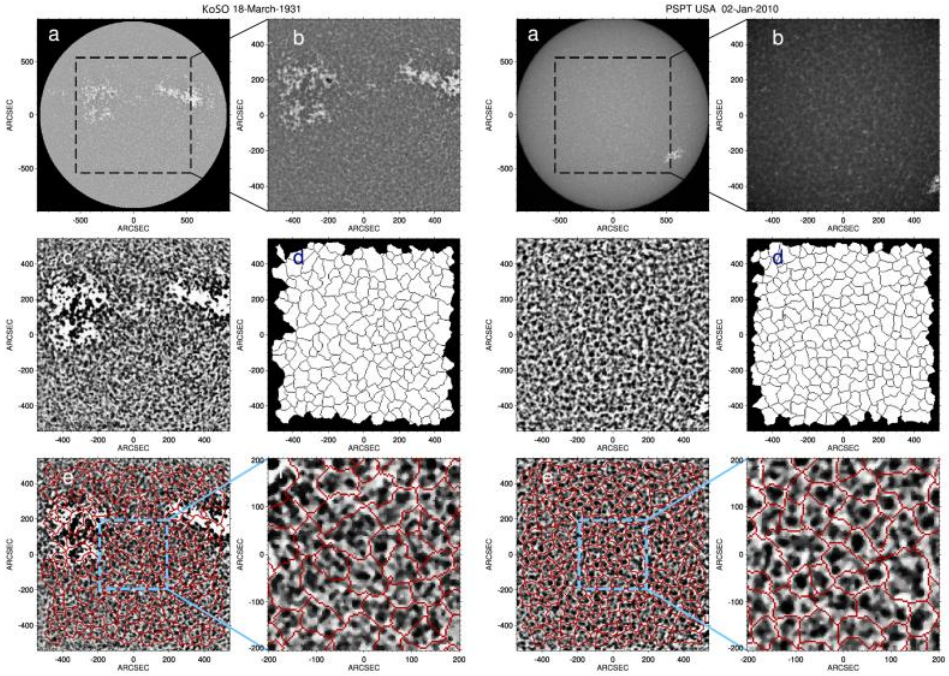

Figure 6.1: Different processing steps to detect supergranules. a) Ca II K disc centered image; b) A central window [as highlighted by the rectangle in (a)] used for further processing; c) Limb darkening corrected, intensity enhanced and smoothed version of (b); d) Detected supergranules using the Watershed transform [supergranule boundaries are shown in black]; e) Supergranule boundaries from (d) overplotted on (c); f) Magnified view of panel (e) having FoV of 400"x400".

We have used the morphological closing and subsequently Watershed transform [Vincent & Soille 1991, Lin et al. 2003, McIntosh et al. 2011] on those ROI images to detect the supergranules. The basic principle behind the watershed transformation is as follows: If an image is visualized as a topographic surface with gray-levels as heights, watershed segmentation divides the same into catchment basins. All pixels

corresponding to a basin is connected to a local minimum falling within the same through a pixel-path of steadily decreasing intensity height [Sonka et al. 2014]. Now, the rationale behind the usage of morphological closing was to avoid over segmentation into smaller scales through watershed method. The results of the watershed transformation on the ROI images are shown in panels 6.1.d's. To check for the detection accuracy visually, we have over-plotted the detected supergranular boundaries on top of the histogram equalized images as shown in panels 6.1.e's and find a very good match between the two. We also provided magnified 400"×400" views of panels 6.1.e's in panels 6.1.f's to depict the overlap of network with watershed boundaries (shown in dark blue double lines). After detecting the supergranules from every image using the above described method, we now define some of the parameters associated with it in the next section.

6.3.2 Scale, Cricularity and Fractal Dimension of Supergranules

All the detected supergranules, from every single image, have been isolated using the region labelling method [Sonka et al. 2014]. To calculate the 'supergranulation scale' (characteristics scale of these structures), we equate each supergranule area to the area of a circle and the radius of this circle is defined as the 'supergranule scale'. We take average of these radii for each image to find a number named as 'Average Supergranule Scale'.

Next, we define the circularity of each supergranule by the expression $4\pi A/P^2$ where A and P denotes area and perimeter of each supergranule [Srikanth et al. 2000]. In the digital domain, circularity shows some dependence on the size of the structures. This arises because the feature boundaries get exaggerated when size decreases (due to the fixed pixel resolution). To correct for this dependency, we first calculate a trend of circularity versus scale, for each image, by fitting a 2^{nd} degree polynomial (Figure 6.2.a) and then the data points are divided by the fitted curve to correct for the trend (Figure 6.2.b). As larger areas are assumed to have correct (scale independent) circularity, we have multiplied the normalized circularity values by minimum of the polynomial curve.

One of the other important parameter associated with a supergranule, is the fractal

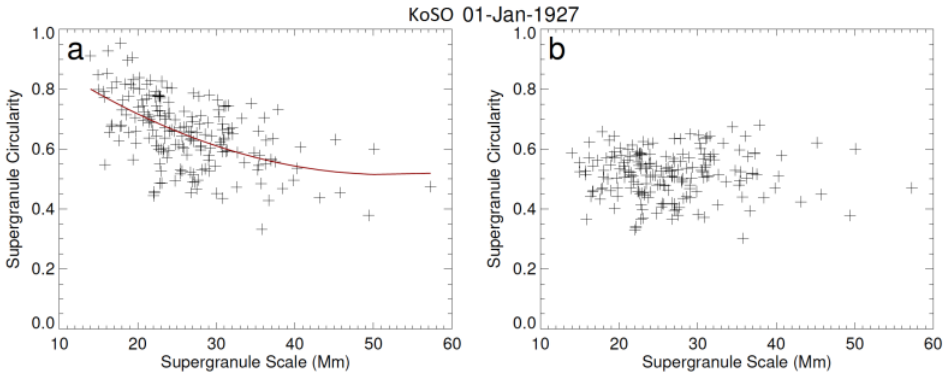

Figure 6.2: a) Dependence of supergranule circularity with the scale. The solid red line is the fitted 2^{nd} degree polynomial on the observed trend ; b) Same as previous only after removing the trend.

dimension which is a measure of complexity and self-similarity of a structure [Mandelbrot 1982]. It is also termed as fractional dimension and it captures the dependance of structure details on scale. Now, the fractal dimension (D) is estimated from the area (A) and perimeter (P) of a given structure, via the relation $P \propto A^{\frac{D}{2}}$ [Muller & Roudier 1994]. Thus, twice the slope of the area vs perimeter plot, in a log-log scale, will be equal to the fractal dimension [Paniveni et al. 2010].

6.4 Results from KoSO

6.4.1 Full ROI; The Aggregate

As mentioned in the previous section, we have calculated different supergranule parameters like scale, circularity and the fractal dimension within a selected ROI (we call it 'aggregate' hereafter) from each of the KoSO Ca II K images. Figure 6.3 shows the variation of average supergranule scale over 9 cycles (cycle 14 to cycle 22) studied in this work. The green dots correspond to average scales determined from individual images and the solid black curve represents smoothed version of the same. We have additionally plotted spline smoothed first and third quartile curves with blue and red dashes respectively in Figure 6.3 and it shows that scatter in the data is less than the temporal variation of the parameter.

All the smoothed curves presented in this work are generated using the CRAN package named 'cobs' of the statistical analysis software R (details about this can be

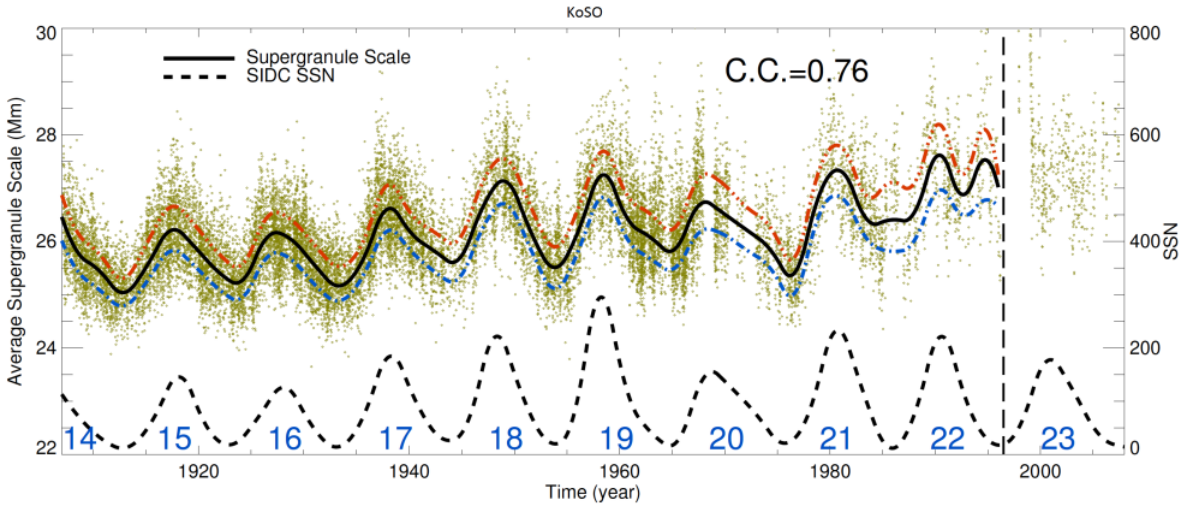

Figure 6.3: Cyclic variation of mean supergranule scale for 9 cycles. Green points correspond to data from KoSO. The black solid curve is smoothed average supergranule scale. Blue and red dashed curves depict spline smoothing for first and third quartiles respectively. The black dashed curve depicts temporal variation of smoothed sunspot number (SSN). Cycle numbers are marked in blue.

found in Feigelson & Babu [2012]). This smoothing technique is based on basis splines [Reinsch 1967] and allows manual input features such as constraints and knot points. For this study we have used a quadratic spline with the penalty parameter λ [Hastie & Tibshirani 1990] set to 1. This method takes care of the temporal variation of the data spread (or sudden discontinuities) and is effective in avoiding the 'artificial' jitters as opposed to the conventional running average technique. Moreover, to compare the two methods (spline smoothing and the running averaging) we have repeated all of the presented analysis with a running averaged data and the results are presented in Appendix.

The vertical dashed line in Figure 6.3 indicates that the KoSO image quality degraded substantially after this period (1997 onwards/cycle 23 onwards). Though we have detected and calculated all the supergranule parameters using the images from this time period also (1997 onwards, as shown in the plots), but all the correlation values (with the SSN) have been calculated for a period 1907-1996. To extend our analysis beyond 1996, we used the PSPT-Italy (1996-2016), PSPT-USA (2005-2015) data to cover the rest period and the results from them are discussed in subsequent sections.

Now from the curve we immediately notice that it has sunspot cycle like periodicity

of ~11 years. To understand its connection with the solar cycle more clearly, we have over-plotted the smoothed sunspot number (SSN) data in the same panel (dashed curve). A positive correlation value of 0.76 confirm the in-phase variation of the average supergranule scale with the sunspot number. The calculated scale values (Figure 6.3) vary from 24 Mm (during the cycle minima) to 28-30 Mm (during the cycle maxima) with an average around 26 Mm. These estimated scale values from the KoSO data match closely with the same presented in McIntosh et al. [2011] where the authors have used Mount Wilson Solar Observatory (MWO) historical data for three cycles (1944-1976). It must be emphasized here that McIntosh et al. [2011] could not get a clear trend of the in-phase variation of supergranule radius with the SSN in all the three cycles they analyzed. In our analysis, if we look for the same period as presented in McIntosh et al. [2011] i.e from 1944 to 1976, we notice that the in-phase variation signature is prominently visible for all of the cycles. In fact, the one to one correlation with the SSN is clearly demonstrated for all the cycles (cycle 14-22) investigated in this study. Thus, we conclude that the long-term data availability at KoSO has enabled us to establish the in-phase variation of the radius parameter with SSN over much greater span of time than any other previous studies.

6.4.2 Active and Quiet Regions

Since the major magnetic activities are concentrated on the active regions (ARs), it would be interesting to investigate the effect of the same on the different properties of supergranules in ARs and on the rest of the Sun, the quite regions (QRs).

Though there have been attempts to divide the solar images into ARs and QRs and study the changes in supergranule scale, all of them were for a very short span of time, at most for one solar cycle [Muenzer et al. 1989, Berrilli et al. 1999, Meunier et al. 2008]. In this study we have recorded the supergranule parameters, separately for AR and QR, for more than 9 cycles with a fully-automated method. To identify the locations of the ARs from the Ca II K images, we have used the plage locations as proxies for the magnetic field [Sheeley et al. 2011]. All the full disc limb darkening corrected KoSO Ca II K images were used to detect plages with a fully-automated method as described in Chatterjee et al. [2016]. Next we used a rectangular mask, around each of the detected

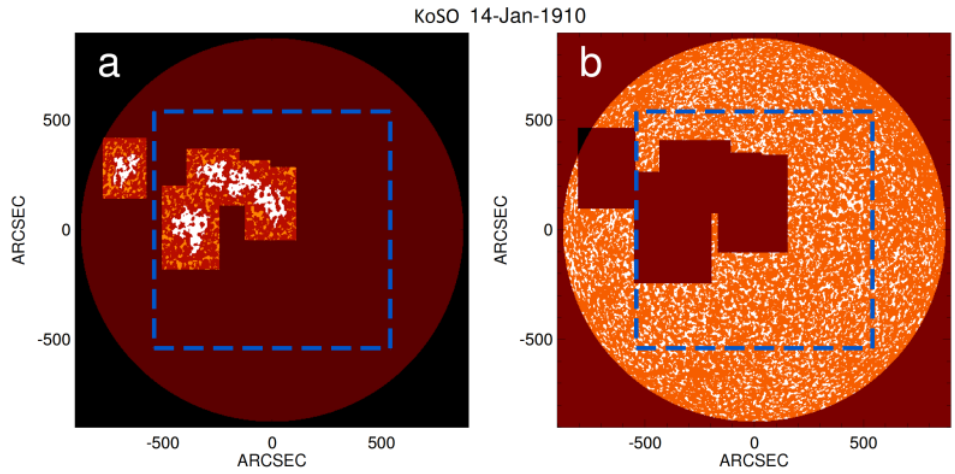

Figure 6.4: Separation of active and quiet region supergranules. a) Rectangular regions with white plage structures are defined as Active Regions (ARs); b) Regions away from plage structures (outside the rectangular patches and inside the disc) are considered as Quiet Regions (QRs). Dashed rectangles, in both the panels, show the regions within which supergranule detection is performed (this is same as the ROI).

plage, with sides 3 times the maximum distances of plage structure coordinates from centroid along X and Y. We define such rectangular regions as ARs. This procedure is shown, for a representative KoSO image, in Figure 6.4.a. We keep a margin of 0.5 times of those X and Y distances and region beyond that margin is considered as QR (Figure 6.4.b). Supergranule detection was performed within a rectangular region about the disc center as shown in Figures 6.1, 6.4.

Figure 6.5 shows the temporal variation of AR and QR supergranule scales with solar cycles. The AR supergranular scale varies coherently with the SSN (plotted as black dashed curve). The correlation coefficient between the two equals to 0.90. Apart from this in-phase variation with the sunspot cycle, we notice that the average AR scale, in this case, is around 25 Mm (we obtained similar number from the aggregate case as shown in Figure 6.3). The temporal variation of QR supergranule average scale is illustrated in Figure 6.5.b. Interestingly, for the QR case we find a strong anticorrelation between the mean scale and the SSN cycle. The correlation coefficient is -0.86. For both the AR and the QR, we find substantial cases when the scale values have comparatively low numbers (≈22 Mm).

We have also calculated the scale normalised average circularity, separately for AR

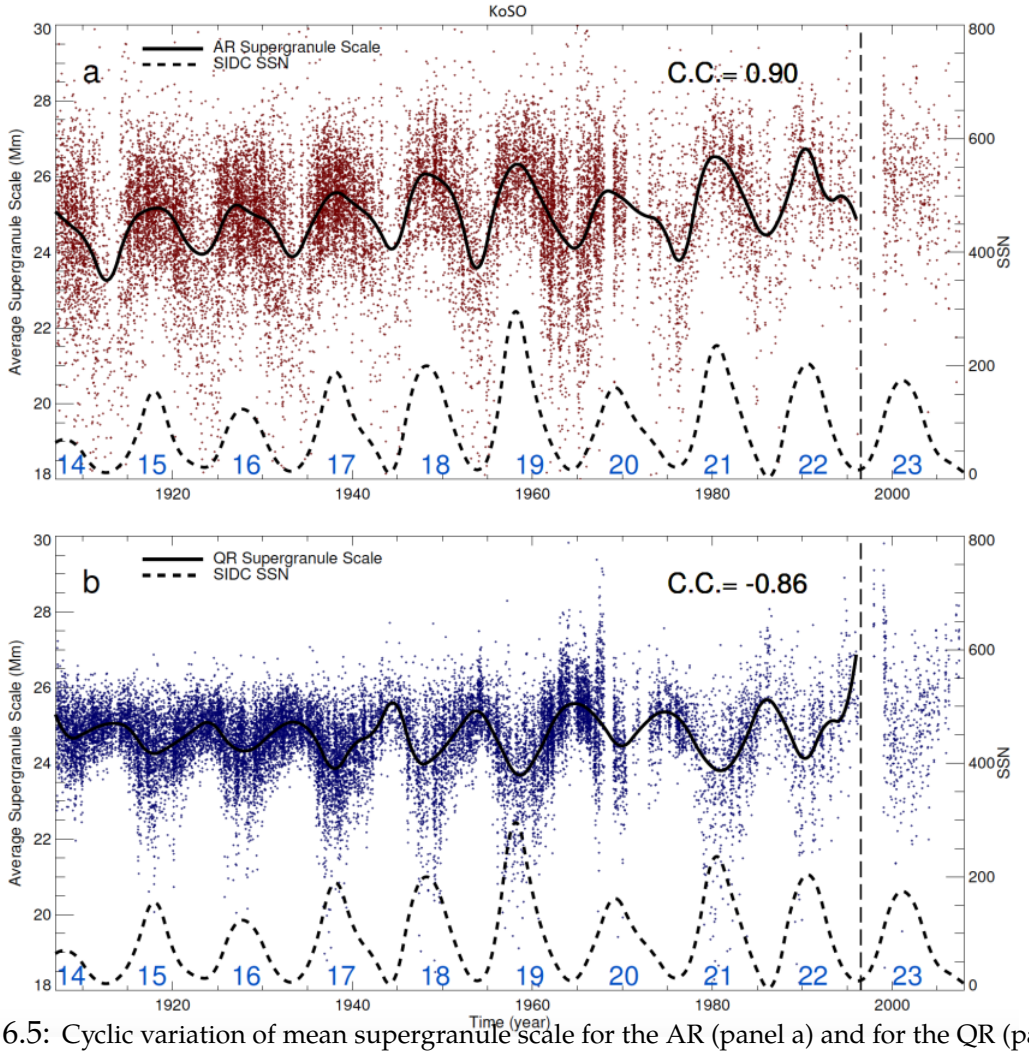

Figure 6.5: Cyclic variation of mean supergranule scale for the AR (panel a) and for the QR (panel b). Dots correspond to the measured mean scale values from individual images whereas the solid curves represent the smoothed versions of the same. The SSN cycle is shown with a dashed curve. Individual Cycle numbers are marked in blue. The color theme i.e. results from ARs in red and results from QRs in blue, is followed throughout this work.

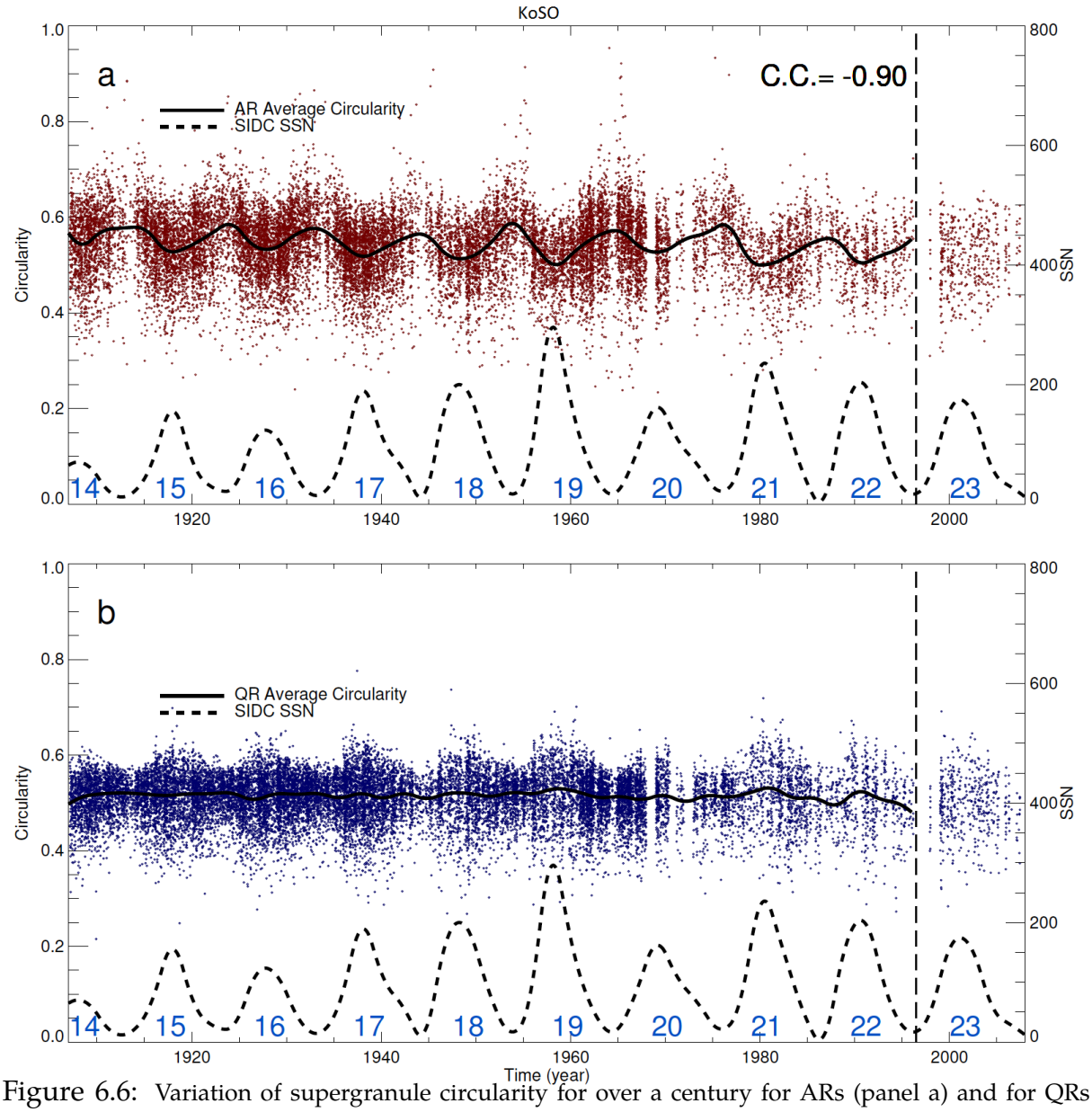

Figure 6.6: Variation of supergranule circularity for over a century for ARs (panel a) and for QRs (panel b). Dots correspond to circularity values obtained from individual images whereas the solid curves represent their smoothed version. The SSN cycle is also plotted at the bottom of each panel.

and QR, and the results are shown in panels a and b of Figure 6.6, respectively. From the evolution of the AR circularity, we observe that the supergranules are more circular during the solar minima as opposed to the solar maxima. A correlation coefficient of -0.90 confirms the same. For the QR (panel 6.6.b), it becomes interesting as the circularity parameter shows no apparent correlation with the sunspot cycle.

Next we calculate the fractal dimension for the ARs and the QRs. As defined in Section 6.3.2, the fractal dimension is equal to the twice of the slope of log-log area vs perimeter plot. Different panels of Figure 6.7 show the calculation of the fractal dimension for the AR and the QR from a single KoSO image. Previously, Paniveni et al. [2010] have quantified the AR and QR fractal dimension of supergranules (identified manually) from KoSO Ca II K filtergrams for period of 1.5 years between 2001 and 2002. In this study we have recorded the same for a much longer period and also using a fully automated method.

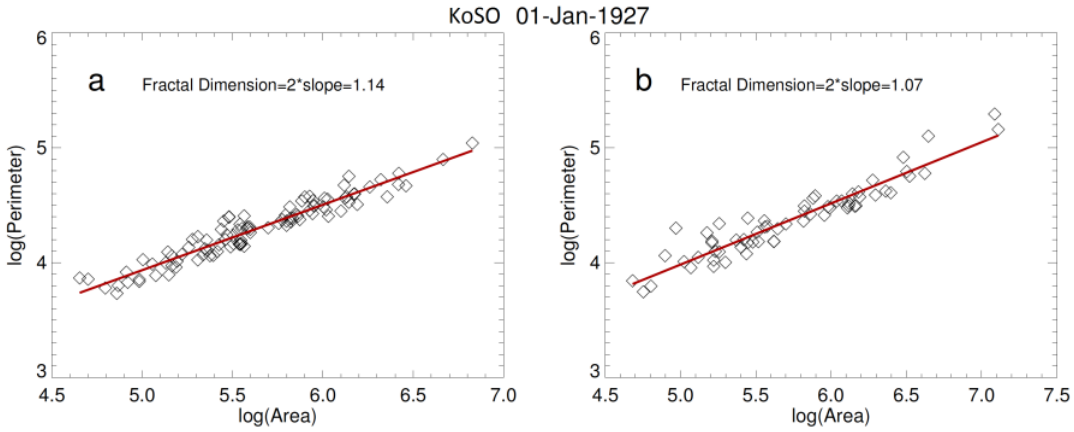

Figure 6.7: Calculation of fractal dimension of supergranules. a) Fractal dimension of supergranules in QRs; b) Fractal dimension of supergranules in ARs.

Figure 6.8 shows the temporal variation of the fractal dimension for the two regions as obtained from the KoSO data. For the AR fractal dimension we observe a good correlation (with correlation coefficient 0.80) with the solar cycle. For the QR, it is exactly opposite i.e the QR fractal dimension has a strong anti-correlation (with correlation coefficient -0.93) with the solar cycle. Additionally we notice that fractal dimension for active regions is lower than the same for quiet regions on an average as the smoothed pale-blue curve goes rarely below smoothed red curve (in accordance with Paniveni

et al. [2010]).

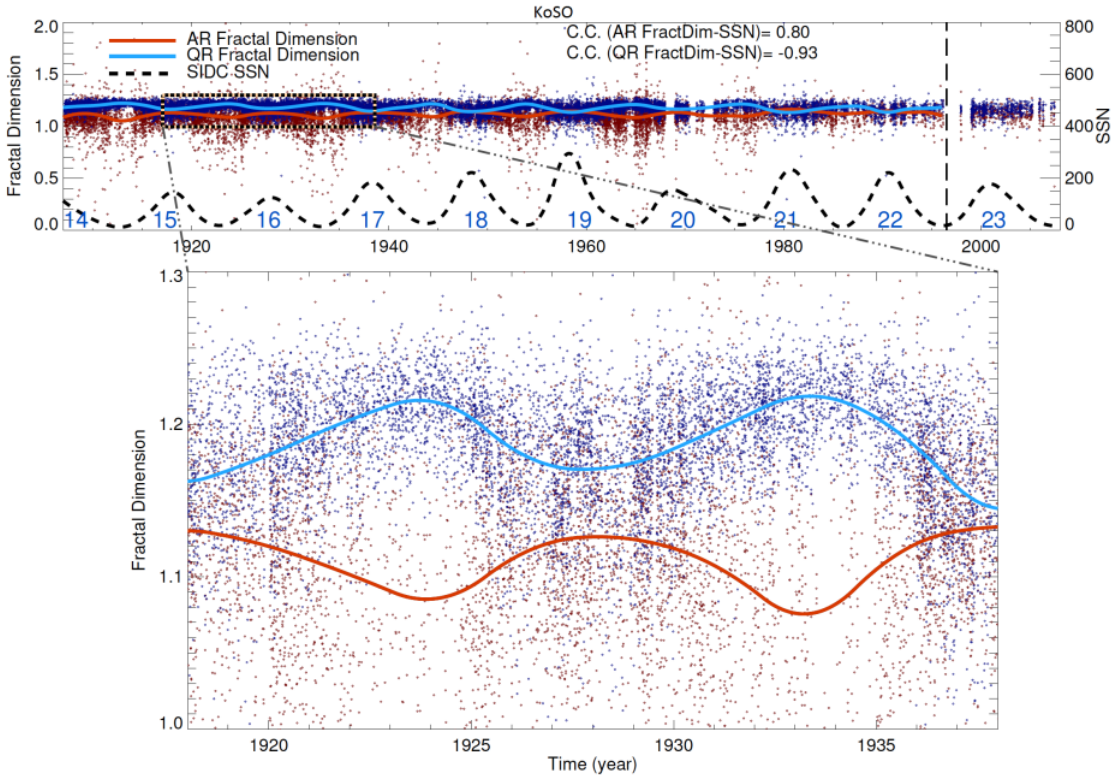

Figure 6.8: Variation of supergranule fractal dimensions corresponding to individual images in ARs (red dots) and QRs (blue dots). Smoothed curves for the two are shown in solid red and pale-blue curves respectively. Bottom panel presents the magnified view of the region enclosed by dotted rectangle in the top panel.

6.5 Results from PSPT

As mentioned in the previous section, the KoSO data quality degraded after 1996 and thus the calculated supergranule parameters have more scatter, less data points and large discontinuities.

We, have thus used the same technique (of supergranule detection) on the PSPT-Italy and PSPT-USA images. Results from these data sets are shown in different panels of Figure 6.9. From the plot we note that the average supergranule scales from two observations match well with each other. In fact, they are also close to the value obtained from the KoSO data (Figure 6.3). Upon careful observation of the plot we

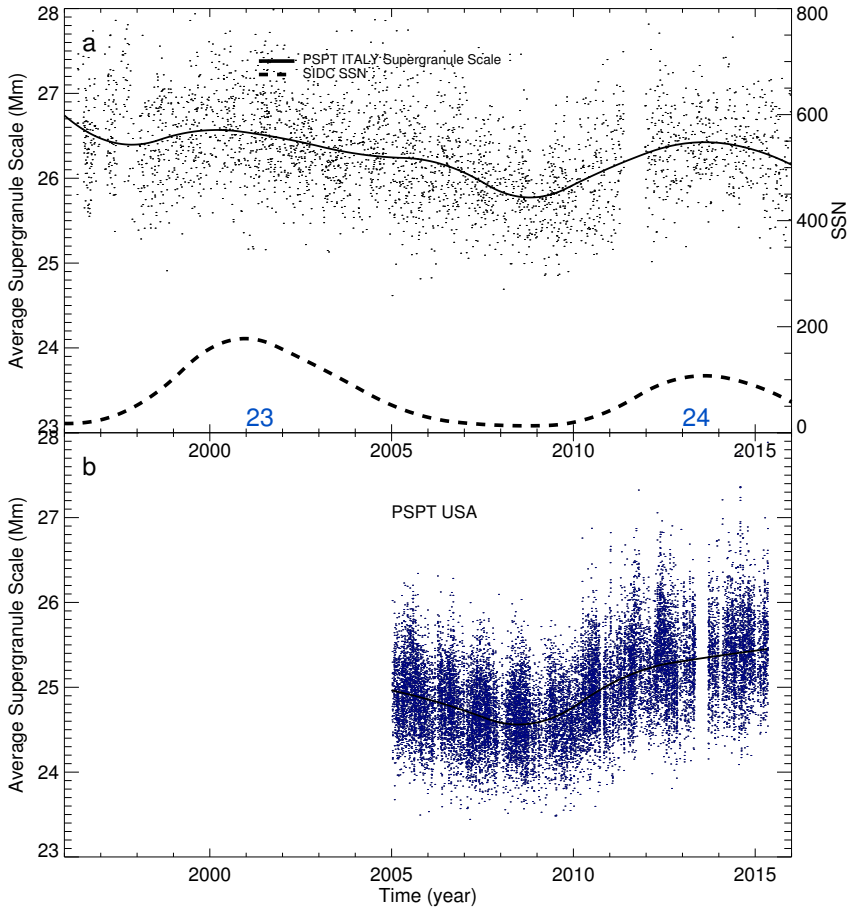

Figure 6.9: Cyclic variation of mean supergranule scale for 1996-2016 from various observatories.

find some differences though. The plot reveals that the there is a constant shift in the measured supergranule scale values (≈1 Mm) between the PSPT-Italy and PSPT-USA data. The reason behind this may be the fact the PSPT Italy data are available in 'JPEG' format which introduces some compression in the original image whereas PSPT-USA data are available in standard astronomical FITS format without any compression.

In panel 6.9.a we notice that the change in the mean scale value , from PSPT-Italy, does not show a clear in-phase variation with the cycle 23 (1996-2008). In the next cycle, cycle 24 (2008 onwards), we revive the solar cycle like variation. For PSPT-USA (panels 6.9.b), we do find an in-phase variation of the same with solar cycle. Thus we conclude that the results from the PSPT-Italy is not due to an detection artefact but rather related to the image quality (or continuity) of the telescope.

6.6 Discussion and Conclusion

In this study, we have used. for the first time, the calibrated Ca II K images recorded from KoSO to identify different supergranule parameters such as mean radius, circularity, fractal dimension for a century (1907-2007). This has been the longest time series till date for the supergranule geometrical parameters. The main findings are listed below:

• We have implemented a fully automated algorithm to detect the supergranules from the intensity images. Using this automated segmentation method we find the mean supergranule scale to vary between a range of 22 Mm to 28 Mm which is similar to the one presented in McIntosh et al. [2011].

• To isolate the effect of strong, large-scale magnetic field on the derived supergranule parameters, we segregate the ARs and QRs from every intensity image using the plages as proxies for the magnetic locations. Analysis shows that the AR supergranule mean scale varies in phase with the solar cycle whereas for the QR supergranule mean scale it is the opposite. AR supergranule scale fluctuation about mean is more than that of QR values. So, though QR scale is anticorrelated with SSN, AR scale dominates to make aggregate scale in phase with SSN. We conjecture that, AR scale fluctuation is influenced by the spatial extent of magnetic field. It other words, bigger active regions during solar maxima might be causing the AR supergranules to become bigger. Net-

work magnetic elements have shrinking effect on supergranules as hinted by Meunier et al. [2008]. During minima those reduce and might cause larger QR supergranules .

• The circularity parameter is found to behave differently for the two regions (ARs and QRs). AR circularity shows a strong anti-correlation with the sunspot cycle whereas the QR circularity shows no dependence. It may be that the 'random walk' associated with network magnetic element causes the active region supergranules to distort and become less circular during cycle maxima.

• Fractal dimension, the measure of the boundary irregularity, also has different evolution for the two regions. In this case, the AR fractal dimension has a positive correlation with the sunspot cycle whereas the QR has a negative correlation.

• We also used our detection technique on different data sets from different observatories. The similar parameter values clearly depicts the robustness of the technique used in this work.

In conclusion, we have used a unique data set to study the variation of the supergranular parameters with the solar cycle. The variation of supergranule parameters also have an effect on the 'total solar irradiance' [McIntosh et al. 2011]. In our future work we would like to explore further on this topic using data from different observatories. Now, active regions are the locations of strong large-scale magnetic fields (mostly the sunspot fields) which are believed to be generated by the global solar dynamo [Charbonneau 2010] whereas the small scale quiet Sun magnetic field is believed to be governed by a local dynamo [Stenflo 2012]. The different nature of the correlations for AR and QR supergranules thus, reflect this inherent difference in the nature of the magnetic fields. It is not clear how magnetic field is influencing scale variability but our results of segregating the AR and QR do provide new constraints that we hope future magneto convection models will be able to explain.

6.7 Additional Information

As mentioned earlier, we have re-computed all the correlation coefficients with running averaged curves in order to check for the robustness of the obtained results. Two of such plots have been shown in Figure 6.10. The top and the bottom panels in this

plot are similar to the Figures 6.3 and 6.8 with the smoothing technique being running averaging. Comparing the respective plots, we observe that the running averaging generates are much jittery curves compared to the spline smoothed ones. Such jitters actually results in a slightly lower correlation coefficient (C.C.) values. However, the improvement in correlations are mostly marginal except for one case (SSN vs AR fractal dimension). The C.C.s obtained from these two methods are listed in Table 6.2. Thus, the closeness of the correlation values confirm the fact that the physical interpretations are not affected by the smoothing methods.

Table 6.2: Comparison of correlation coefficients (C.C.) for two different smoothing techniques

	C.C.	
Correlated Data pair	Running average	Spline smoothing
SSN - Aggregate scale	0.73	0.76
SSN - AR scale	0.86	0.90
SSN - QR scale	-0.81	-0.86
SSN - AR circularity	-0.82	-0.90
SSN - AR fractal dimension	0.45	0.80
SSN - QR fractal dimension	-0.89	-0.93

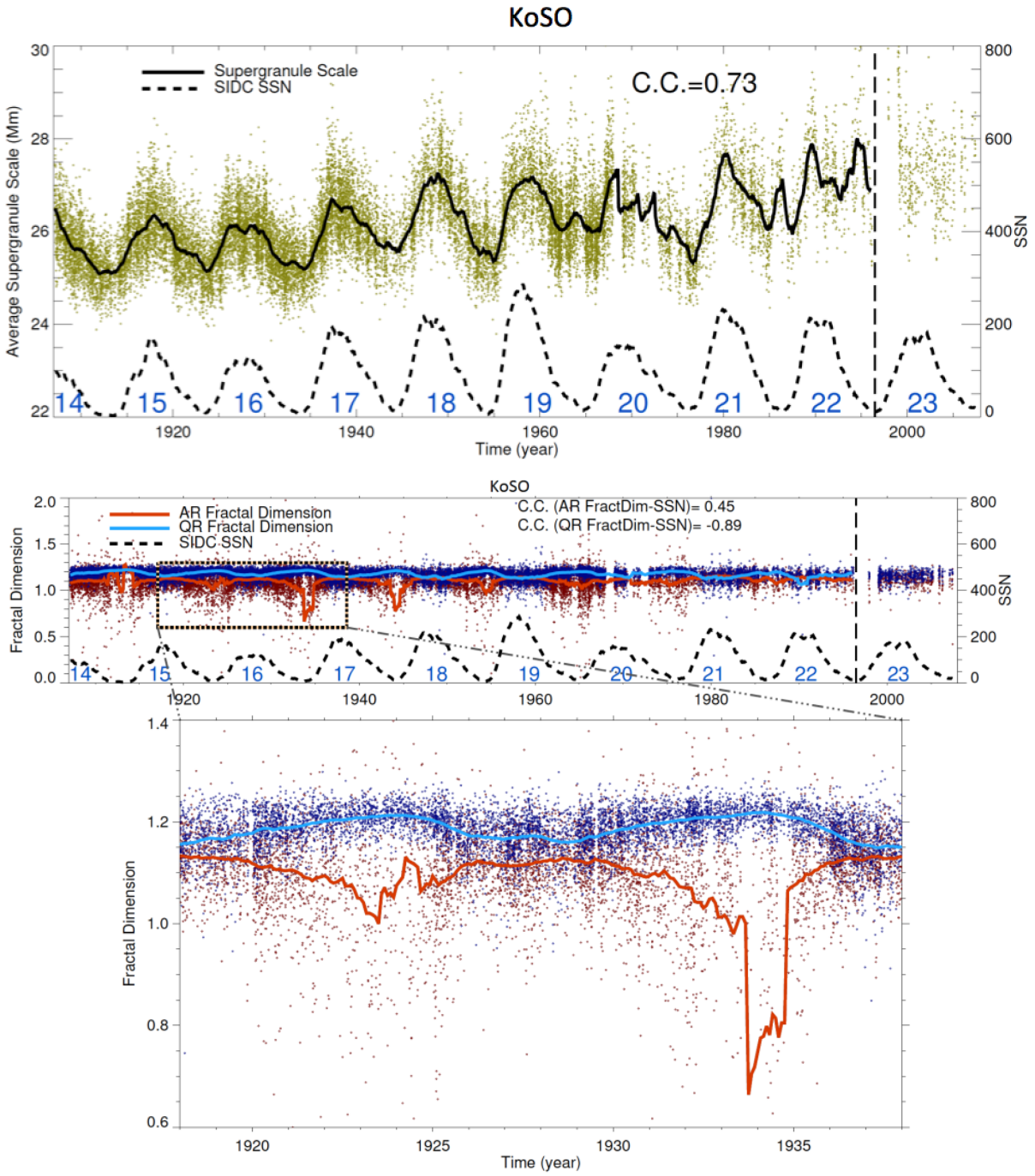

Figure 6.10: Cyclic variation of supergranule parameters for 9 cycles. The upper panel shows aggregate scale variation and the bottom panel shows cyclic variation of fractal dimension for AR and QR. These figures are same as Figure 6.3 and Figure 6.8 except the smoothing approach being running averaging.

Chapter 7

Long-term Study of the Solar Filaments from the Synoptic Maps as Derived from H_α Spectroheliograms of Kodaikanal Observatory[1]

7.1 Introduction

Sun is a star which is highly heterogeneous both temporally and spatially. It is crucial to study the long term evolution of the magnetic field, which is believed to be the major driver for this heterogeneity. Before 1970s regular magnetic field measurements were not available and thus long term study of proxies of solar magnetic field has been an important subject area. Solar filament has served as one such proxy [McIntosh 1972] for understanding the magnetic activity of the Sun. They are clouds of ionized gas projected against the solar disk which are cooler and denser than the plasma underneath. In H_α ($\approx$ 656.28 nm line center) observations they appear as dark, elongated, thin hairy structures. Filaments are formed along the polarity inversion line between opposite magnetic polarities [Martin 1998]. When filament becomes unstable due to magnetohydrodynamic instability, it erupts. Filament eruption is often associated with

[1] *Results of this chapter are published in Chatterjee et al. [2017]*

flare and coronal mass ejections (CMEs), which are the sources of geomagnetic storms [Gopalswamy et al. 2000, Gilbert et al. 2000, Gopalswamy et al. 2003, Chen et al. 2008, Zhang et al. 2012].

Solar filaments are seen at all latitudes on the solar disk from equator to pole during all phases of the solar cycle and outline the boundary between different magnetic field polarities. This makes them ideal candidate for the study of large scale concentrations of weaker magnetic field on the sun [McIntosh 1972, Low 1982, Makarov & Sivaraman 1983]. Thus, long term filament data can be efficiently used as a proxy for magnetic activity of the sun. Additionally, study of the occurrence of filaments give useful insight to distribution of these fields on the solar surface, their evolution and to understand the nature of sun's magnetic field [Mouradian & Soru-Escaut 1994]. Detection of filaments from the archival images is the first step for such a study. There have been many attempts to detect filaments in automated way from full disk H_α images. The methods range from modified Otsu thresholding [Hao et al. 2015] to application of artificial neural networks [Zharkova & Schetinin 2003]. But, most of these methods were applied only on good quality digital images of few recent solar cycles. Historical digitized data present itself with many inherent artefacts which can not be corrected by flat fielding [Zharkova et al. 2005]. Application of most automated methods on such data mostly result in under-estimation or over-detection of filaments. So, a careful detection of such features are necessary and it may require manual intervention. Detection of filaments from Carrington/synoptic maps of historical data have generated promising results as reported by few recent studies. Li et al. [2007] used synoptic charts of filament archive from Meudon observatory to study long term variation of solar filaments. Using the same data set, Li [2010] studied latitude migration of filaments at low latitudes (less than 50°) and found latitudinal drift of filaments differs from that of sunspot groups. Hao et al. [2015] utilized Big Bear Solar Observatory (BBSO) data from 1988 – 2013 to extract variation of filament area, spine length, tilt angle and barb number with respect to calendar year and latitude. The study also included North – South asymmetry of filament number. Tlatov et al. [2016a,b] using synoptic charts from Meudon observatory and Kislovodsk Mountain Astronomical station studied variation of filament tilt angle and classified filaments with different tilt angle viz., active region filaments, quiescent

filaments and polar filaments. There have been some works from Kodaikanal historical data on prominences [Ananthakrishnan 1952, Evershed 1907, 1908, Rausaria et al. 1993a], flares [Rausaria et al. 1993b, Sundara Raman et al. 1994, 2001]. Most of these earlier studies were for shorter period of time. Ananthakrishnan [1952] used Ca II K disk blocked plates to study the evolution of prominences till 1954 and Makarov & Sivaraman [1983] used kodaikanal Ca II K and H_α plates till 1919 to study poleward migration of magnetic neutral lines. In this work we present for the first time, the newly digitized unique data set of H_α filaments from Kodaikanal Solar Observatory (KoSO) and study solar activity variation for 9 solar cycles. To our knowledge this is the oldest digitised archive of H_α. In section 7.2, we present the description of the data. Method of analysis, and representative results are presented in sections 7.3 and 7.4 respectively. Finally in section 7.5 results are concluded along with necessary discussion.

7.2 Data Description

Systematic H_α observations were carried out at KoSO since 1914 with a telescope (spectroheliograph) having 30 cm objective and f-ratio of 21. The spectroheliograms (656.3 nm) were consistently recorded in photographic plates until 1978 and subsequently in films on daily basis. These plates/films have recently been digitised by the help of a uniform illumination source and a 4096 × 4096 CCD cooled at -100°C. We used those digitized full disk 4096 × 4096 KoSO H_α density images from 1914 to 2007 (≈ 0.86 arcsec /pixel) in our current study. The seeing limited resolution has been ≈ 2 arcsec for majority of observing period. Figure 7.1a shows the number of images available in the archive (used in this work) and Figure 7.1b shows the time span over which the KoSO digitized images are available along with other major data sources. Observation for time duration close to Kodaikanal has been by the Meudon Observatory, France (since 1919) (Figure 7.1b). Recent studies with this data has been performed by Tlatov et al. [2016a,b] combining H_α observation of Kislovodsk Mountain Astronomical Station, Pulkovo Astronomical Observatory, the Russian Academy of Sciences after 1959.

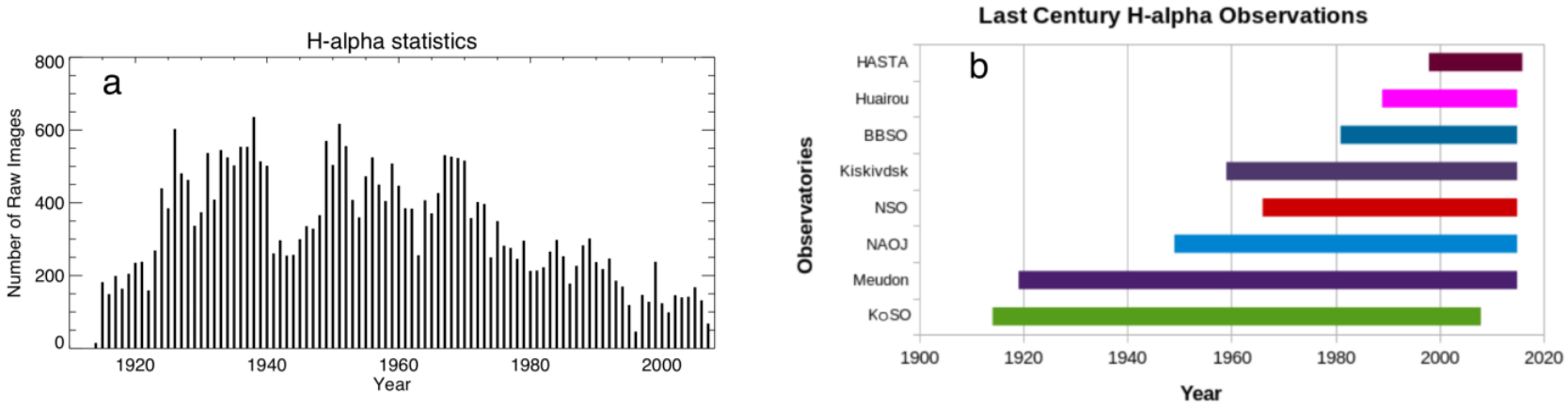

Figure 7.1: Availability of H_α images. a) Yearly histogram of KoSO H_α data; b) Availability of H_α dataset across the globe. Different sources are marked with abbreviations along y-axis.

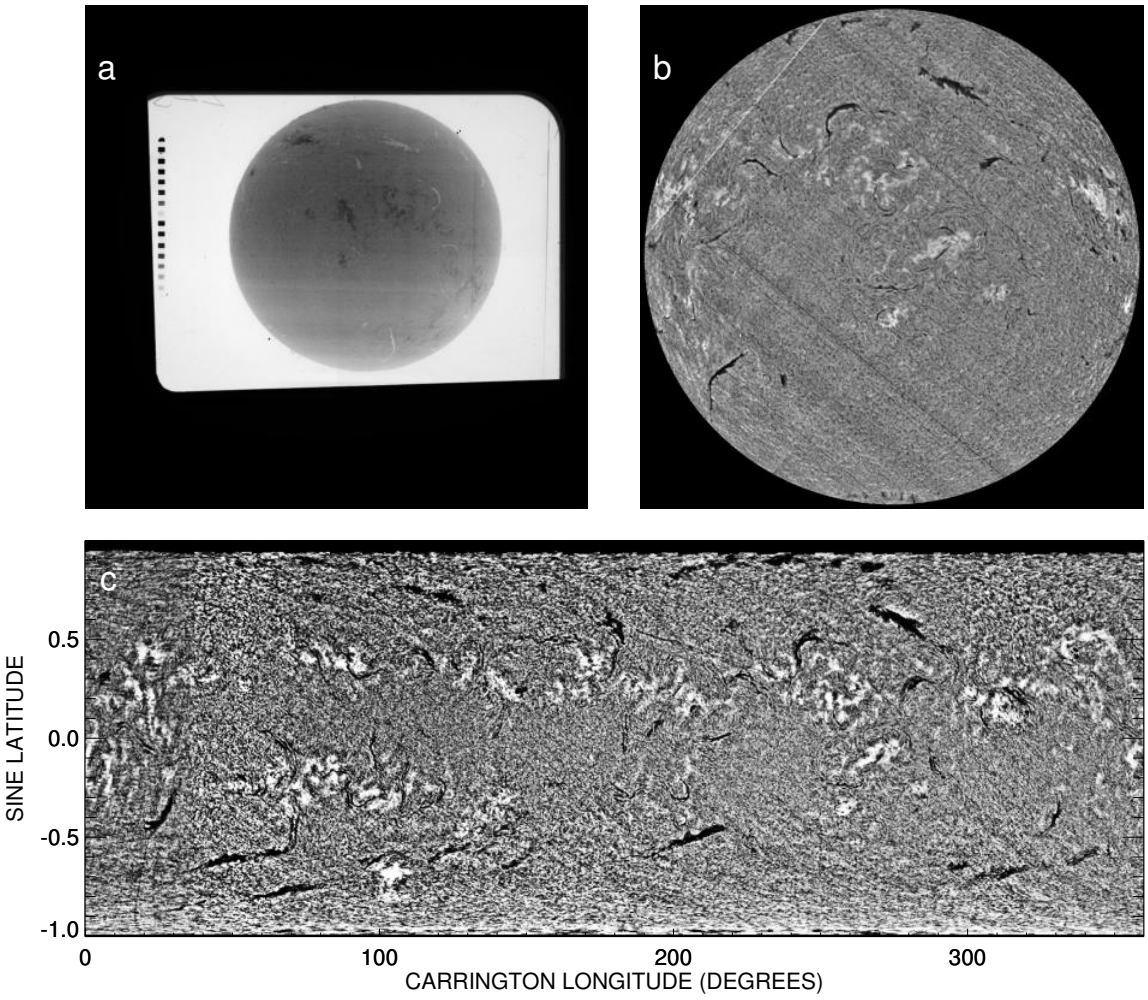

Figure 7.2: KoSO H_α data calibration and filament detection. a) H_α RAW image taken on March 16, 1981; b) Limb darkening corrected and disk centered image; c) Carrington map for rotation number 1706 starting on March 8, 1981.

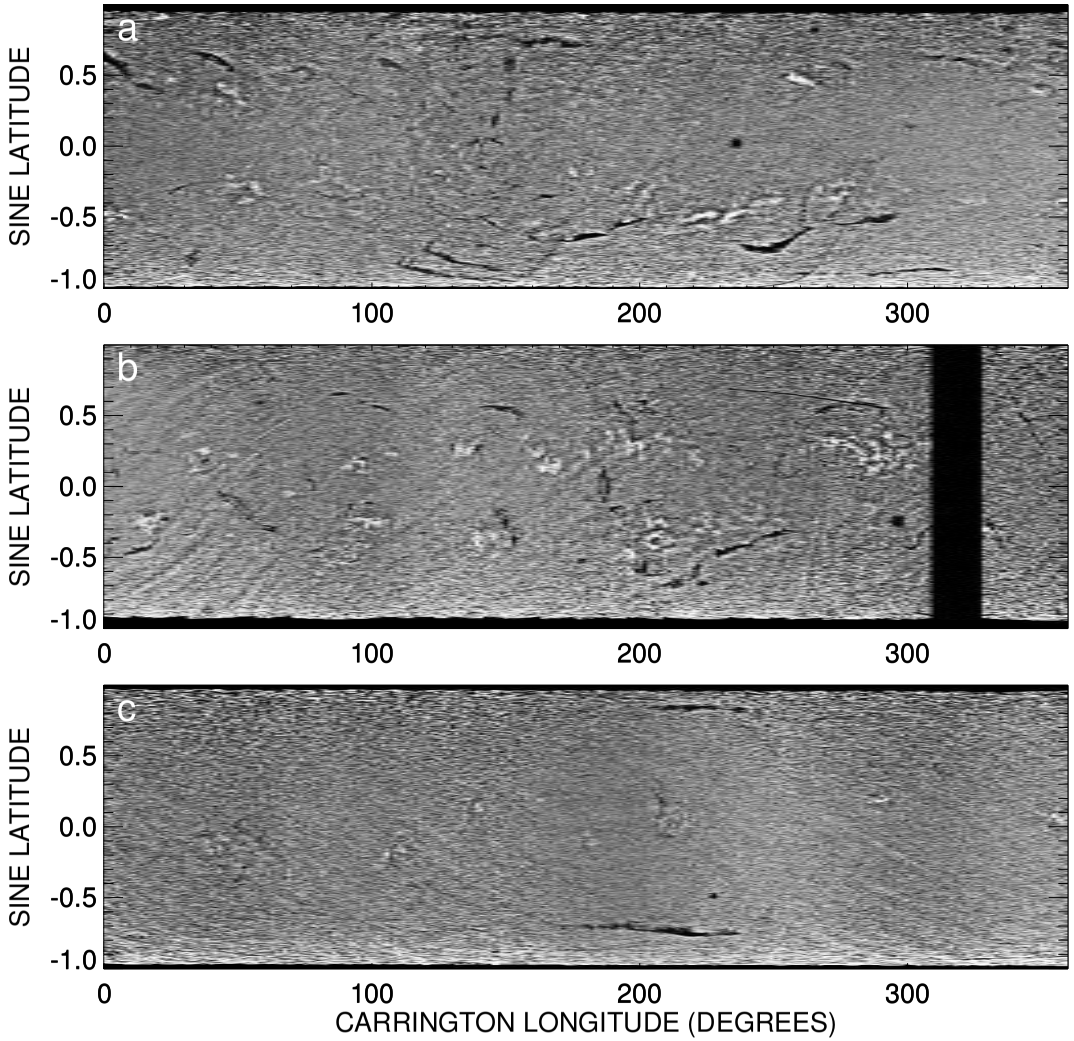

Figure 7.3: KoSO H_α maps for different phases of solar cycles. a) Carrington rotation 970 depicting a representative filament distribution at the rising phase of cycle 16; b) Carrington rotation 1001 depicting a representative filament distribution at the maxima of cycle 16; c) Carrington rotation 1641 depicting a representative filament distribution at the minima of cycle 20.

7.3 H_α Data Calibration and Filament Detection Technique

7.3.1 Calibration

The calibration includes several steps. First the RAW images (Figure 7.2a) were inverted in grey scale. Edge detection operators were applied to produce a binary edge detected image. Circle Hough transform [Sonka et al. 2014] was applied on that binary image to find the center and radius of disk. After disk centering the images were resized to a smaller version and were median filtered to obtain the asymmetric limb darkening profile combining effects of line of sight and imaging instrument. This step was applied to reduce the time complexity of the automated calibration per image as the limb darkening profile captures only the large scale intensity variation. The profile was again blown up to original size and original image was divided with the same to generate limb darkening corrected images as shown in Figure 7.2b.

7.3.2 Carrington Map Generation

Carrington map is a type of Mercator projection of the spherical sun generated from synoptic observation corresponding to one solar rotation. In this study, 60° longitude bands (-30° to 30° heliographic longitude) in the limb darkening corrected full disk H_α images were selected. Those were B_0 angle corrected and mapped to the Carrington longitude-latitude grid in form of a rectangle with a weightage of cosine 4th power [Sheeley et al. 2011] over each heliographic longitude. These rectangular slices were shifted and added according to date and time for 27.2753 days to generate a full 360 degree map of sun. A similar 360 degree map was obtained from rectangular binary slices called streak map [Sheeley et al. 2011, Chatterjee et al. 2016]. The overlap of same Carrington longitudes was removed through division of the original solar 360 degree map with streak map to form an image called Carrington map or Synoptic map. One representative Carrington map is shown in Figure 7.2c. A total of 1185 Carrington maps from rotation 817 to 2062 are posted on this portal (ftp://ftp.iiap.res.in/subhamoy/halpha_carrington_maps_kodaikanal/). Figure 7.3 depicts three

representative Carrington maps for three different phases of solar cycles. Figures 7.3a, 7.3b and 7.3c present respectively rising phase, maxima of cycle 16 and minima of cycle 20. It can be observed from the maps that polar filaments are dominantly present during rising phase and minima of the solar cycles whereas low latitudes filaments dominantly occur in-between i.e. around cycle maxima. It should be noted that bright and dark ridge like structures in the Carrington maps are not of solar origin. Scratch lines present in the RAW images are responsible for those and they manifest as curved shape in the carrington maps due to north-south rotation correction.

7.3.3 Filament Detection and Parameter Extraction

Figure 7.4a shows the Carrington rotation 1823 with many filaments and an artefact mimicking a filament marked with red arrow. If a fully automated filament detection algorithm is used the artefact will be detected as filament. This was the reason we went for semi-automated technique. The Carrington maps were first intensity enhanced through histogram equalization. Seed points (shown with '+' in Figure 7.4) were selected manually on the dark filaments. 8-neighbourhood region growing [Sonka et al. 2014, Bonnin et al. 2013] was performed to detect filament for each selected seed point. A similar method for filament extraction from full disc Meudon data of the year 2002 has been used by Bonnin et al. [2013]. The region grows by including neighbour pixels about the seed point satisfying intensity threshold. This process is repeated for each new neighbour pixel until pixels go totally outside intensity threshold and a connected region is produced. As we see in Figure 7.4a some filaments need multiple seed point selection for sudden jumps of intensity above the threshold selected for region growing. Subsequently, binary filament detected Carrington maps are generated. Contour of the produced binary map for rotation 1823 is overplotted in green on the gray scale Carrington map in Figure 7.4b. Because of image contrast, data gaps and temporal evolution naturally Carrington maps depict unnatural fragmentation in filaments. As the polar filament (latitude $> 50^{\circ}$) are longer, their lengths are affected more. Morphological closing operations with different kernel sizes are performed for higher latitude filaments to examine change in number of polar filaments. Parameters such as centroid longitude, latitude and filament tilts are generated. In Figure 7.5a we show the Ca

II K carrington map as generated from the KoSO data to compare the correspondence between the bright plage locations in Ca II K (Figure 7.5a) and their traces in H_α (Figure 7.5b) corresponding to the rotation 1706. To make correspondences between filaments and active regions more evident, we plotted the filament skeletons on the Ca II K as shown in Figure 7.5c. Using Michelson Doppler Imager (MDI) on-board SoHO line-of-sight magnetograms available after the year 1996 we generated Carrington maps and Figure 7.6 includes one such MDI map for inspecting the location of filaments in terms of distribution of magnetic fields. Carrington rotation 1962 has been compared from Ca II K, H_α and MDI in Figures 7.6a, 7.6b and 7.6c respectively. Formation of filaments along magnetic neutral lines can be observed at different locations and one such example is shown in the zoomed inset of Figure 7.6 d.

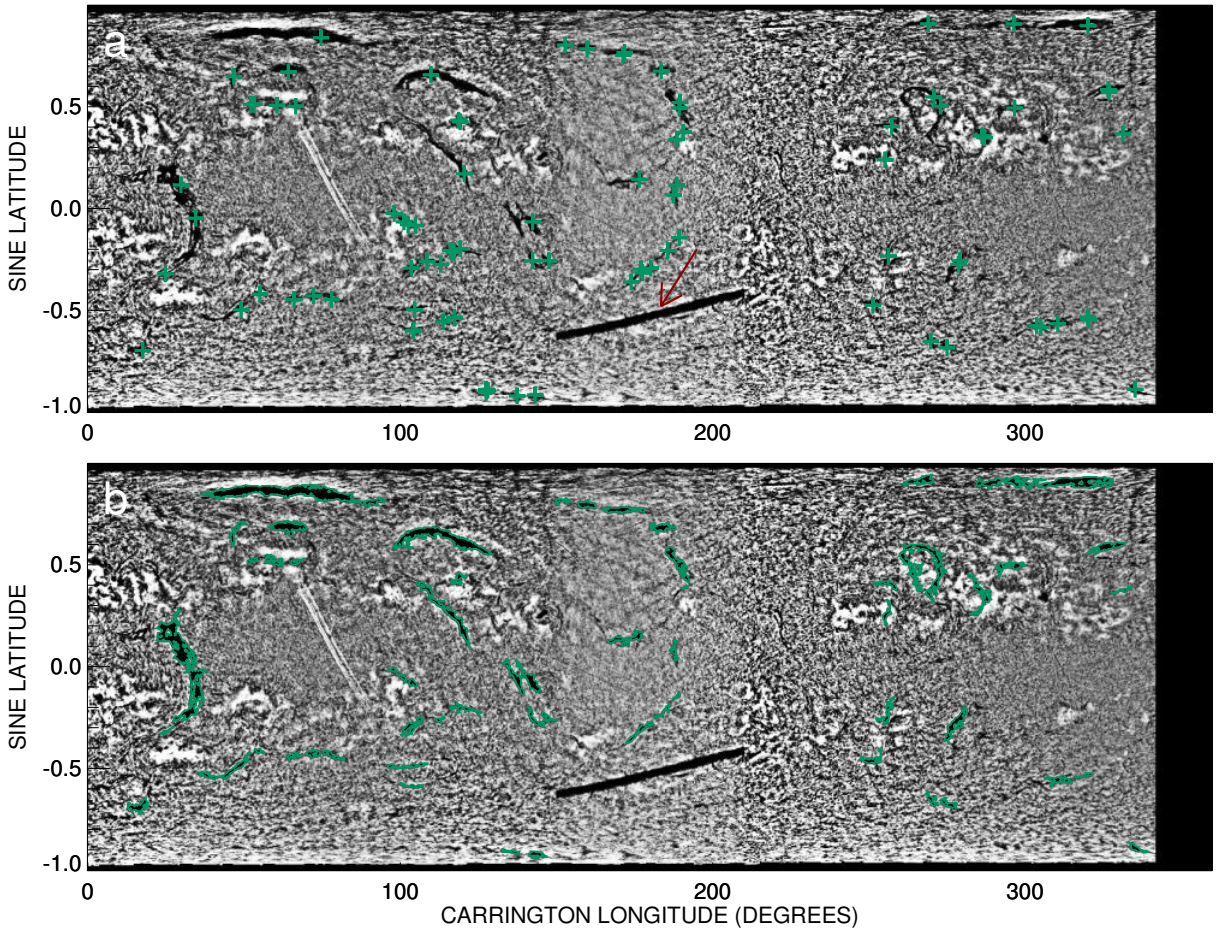

Figure 7.4: Region growing for KoSO H_α filament detection. a) H_α Carrington rotation 1823 with seed points marked with green '+' symbols. Scratch line resembling a filament is marked with red arrow; b) Green contours depict filament boundaries detected through region growing about the manually selected contours.

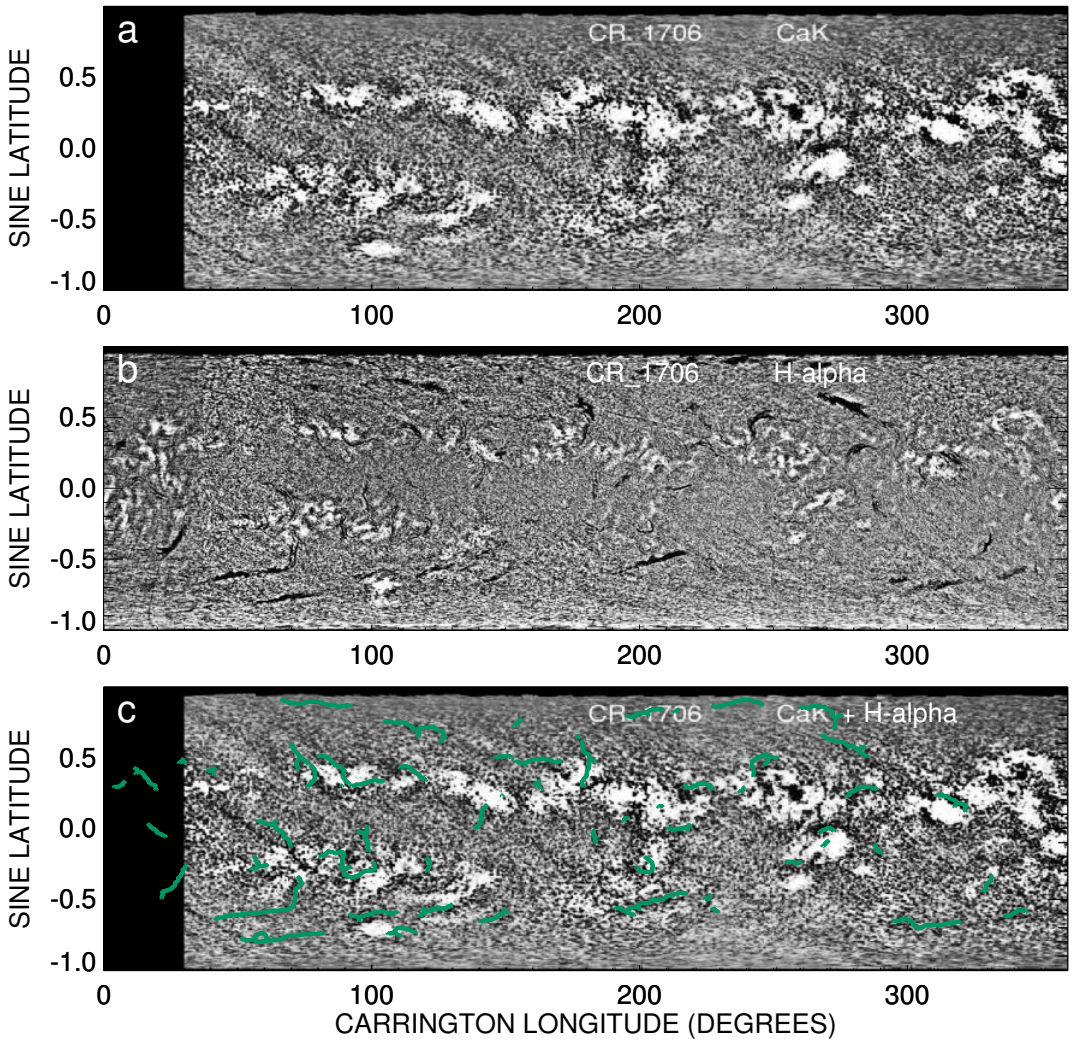

Figure 7.5: Correspondence between KoSO Ca II K and H_α maps. a) KoSO Ca II K Carrington rotation 1706; b) KoSO H_α Carrington rotation 1706; c) Filament spine in green from (b) over plotted on (a).

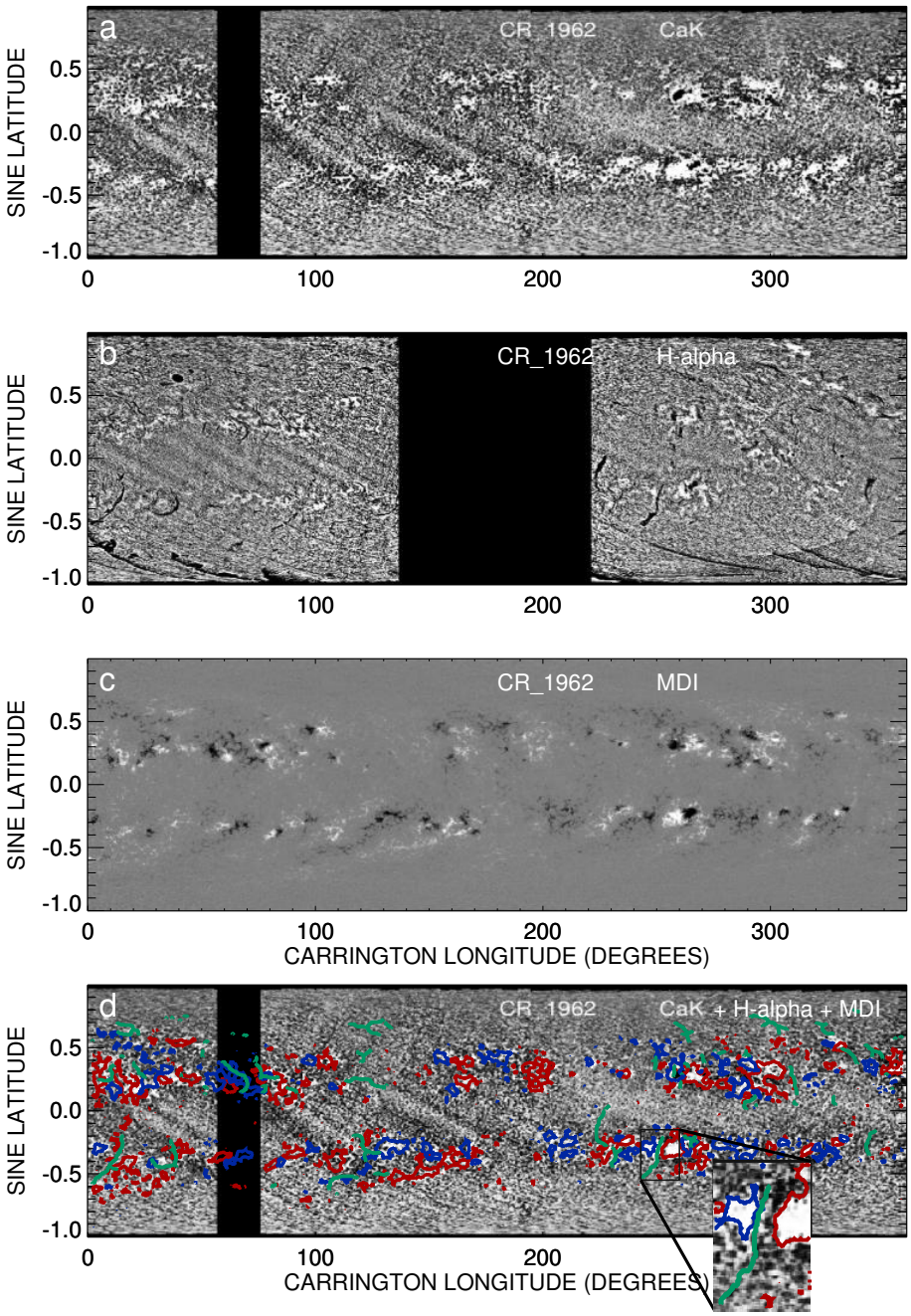

Figure 7.6: Correspondence between KoSO Ca II K, H_α and MDI magnetogram maps. a) KoSO Ca II K Carrington rotation 1962; b) KoSO H_α Carrington rotation 1706; c) Carrington map generated from MDI/SoHO full disc LOS magnetograms for rotation 1962; d) Filament spine in green from (b) over plotted on (a) with positive (red) and negative (blue) magnetic field contours of rotation 1962 from MDI/SoHO. This panel also shows a magnified view of small window within the Carrington map depicting a filament lying in between two magnetic patches of opposite polarity.

7.4 Results

Figure 7.7a shows temporal evolution of the filament centroid latitudes over 9 cycles. This plot illustrates how the filaments are distributed at all latitudes and also reveals (like sunspots) that filaments also migrate towards equator (butterfly diagram) but from a higher latitude. Along with the butterfly diagram like nature, signature of poleward migration is observed in the plot. One such example is highlighted by a red circle with an arrow. Corresponding to cycles 15, 17, 20, 21 and 23, in southern hemisphere rush to the pole is clearly seen. Similarly, in northern hemisphere, cycles 15,16, 20, 21 and 23 show this behaviour. Though there are traces, poleward rush is not very clear for cycles 18, 19, 22. The observed polar rush can be compared with the same from Ca II K prominence results as presented in Ananthakrishnan [1952]. Though we don't observe the rush till pole because of projection effects on the on-disk feature, we find the early phases for most of the cycles. Now we focus our attention to the polar filaments. Figure 7.7b shows the temporal variation of the number of polar filaments (centroid latitude > 50°) overplotted on smoothed sunspot number (SSN) from Solar Influences Data Center (SIDC; http://www.sidc.be/silso/datafiles). We must point out here that we find some cases of fragmentation in filaments during detection and at this point we don't have a method to estimate the correct length for such cases. Thus we concentrate on number density of filament rather than exact length estimates. We apply Morph close operations on the detected filaments with disc kernels of radii 22 and 30 pixels named as kernel 1 and kernel 2 respectively in Figure 7.7b. The target Carrington maps are of sizes $1570(x) \times 500(y)$ with x-axis or longitude spanning from 0° to 360° and y-axis or sine latitude spanning over -1 to 1. In this exercise we explore whether the temporal location of polar filament number maxima changes varying the kernel sizes. Figure 7.7b illustrates the natural reduction of filament number with higher kernel size though there is no apparent change in the epoch of maxima. Both the time series clearly present 11 year periodicity with same delay between their peaks and SSN maxima. Based on Wilcox Solar Observatory polar field data (taken from http://wso.stanford.edu/) we plot the SSN-polar filament maxima delay vs SSN maxima-pole reversal delay in Figure 7.8 from three cycles namely 21, 22 and 23. For

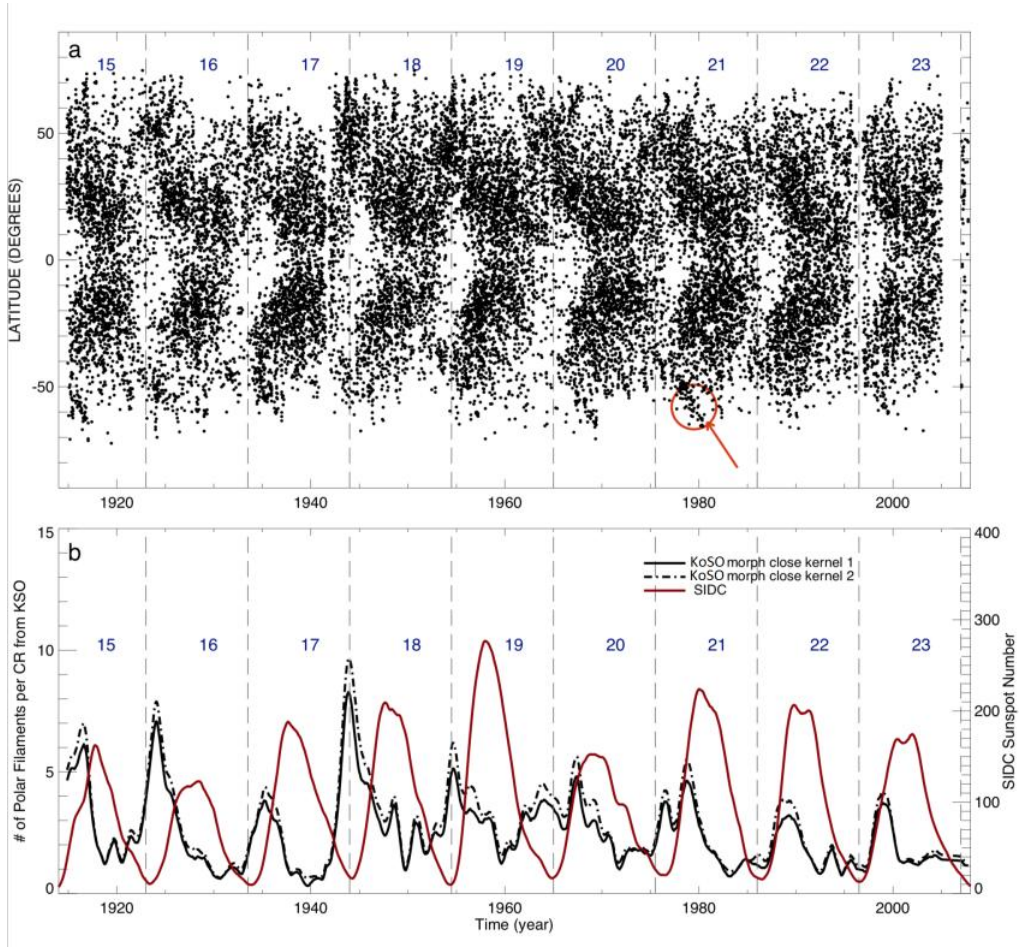

Figure 7.7: Distribution of filaments. a) Time-latitude distribution (1914 – 2007) of solar filaments as detected from KoSO Carrington maps. A representative signature of poleward migration is marked by a red circle and arrow. Cycle numbers are printed in blue with dashed vertical lines marking the cycle minima; b) Temporal variation (19014 – 2007) of number of polar filaments as recorded from KoSO and its comparison with SIDC sunspot number. The solid black curve and dot-dash correspond to filaments morphologically closed by a disc kernel of radius 22 pixels and 30 pixels respectively. It is worth noting that temporal locations of filament number maxima do not change with different sizes of closing operation except for the relative change in number of filaments.

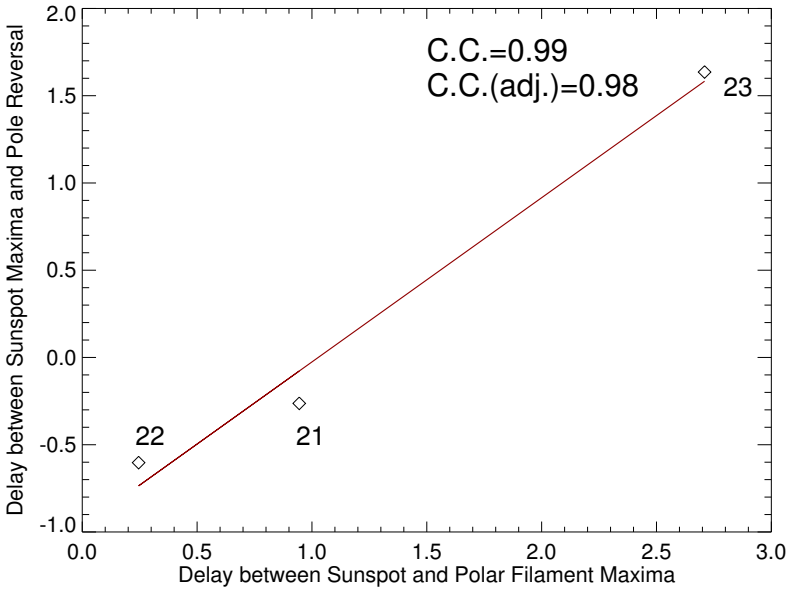

Figure 7.8: Correlation of the sunspot-polar filament number maxima delay and sunspot number maxima-pole reversal delay for last three cycles. As number of data points is only 3, adjusted correlation coefficient is also shown.

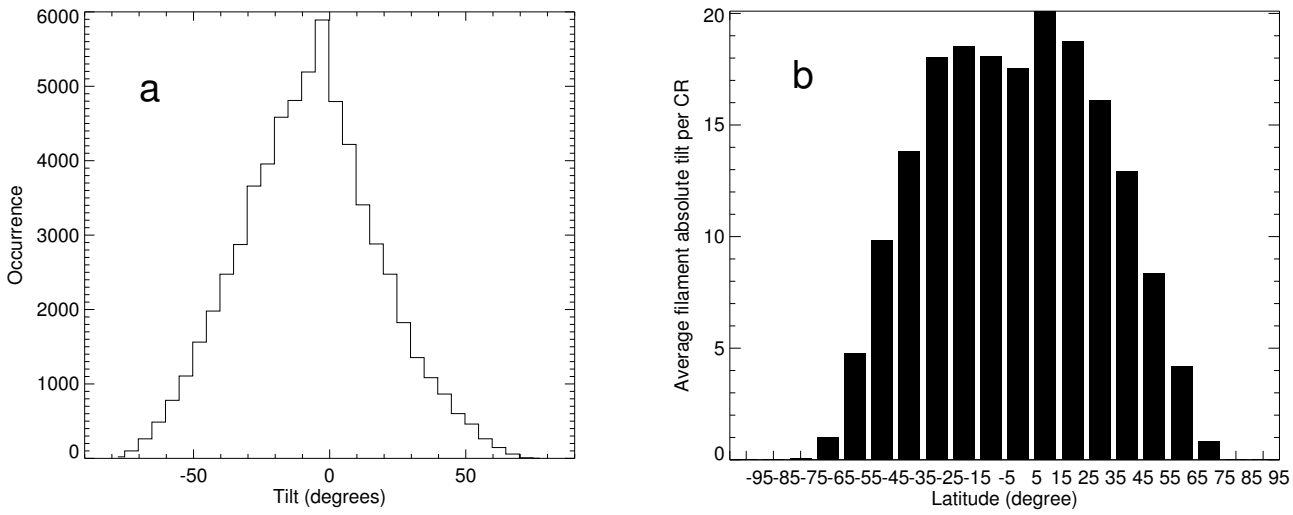

Figure 7.9: Filament tilt attributes. a) Histogram of filament tilt angle with respect to equator; b) Latitudinal distribution of solar filament tilts.

understanding the epoch of pole reversal (North-South)/2 curve is considered. They show a linear correlation (r) of 0.99. As the number of data points are limited, we also

calculate the 'Adjusted Pearson Correlation Coefficient' defined by the expression,

$$r^2_{\text{adjusted}} = 1 - (1 - r^2)\frac{n-1}{n-p-1}$$

where, n is the number of data points which is 3 in our case and p is the number of independent variables which is 1 here. We find the adjusted coefficient to be 0.98 which still remains pretty high confirming the association between epoch of number of polar filament peak and pole reversal with respect to sunspot maxima. This emphasises the role of polar filaments in polarity reversals. Faster the polar filaments migrate to poles, earlier will be the pole reversal. To our understanding this is a very important finding and demands a detailed study, which we plan to do in near future.

Now we will look at the tilt angle distribution. Fig 7.9a illustrates histogram of solar filament tilt angle with respect to equator. It shows an asymmetric nature consistent with the findings of Tlatov et al. [2016b]. We also take average of tilt angle absolute values for different latitude bands. This latitudinal distribution is plotted in Fig 7.9b. It is consistent with the Joy's law for sunspot pairs. Though we don't estimate the exact length of the filaments we believe that the average tilt of the fragmented filaments (a fraction of the total sample) are more or less the same as the fitted straight line slope of the whole filament and thus this plot should not change much due to filament fragmentation. As the filaments are expected to be oriented along neutral lines, they become more parallel to the equator at higher latitudes where the sunspot pairs (appearing till $\approx 40°$) become more tilted. It is worth mentioning that filaments appear allover the disk reaching much higher in latitudes compared to sunspot pairs and they maintain the trend of declining tilt with respect to equator. Thus the filament distribution may provide much detailed insight on the distribution of magnetic field at all latitudes rather than the sunspot locations alone.

7.5 Discussion and Conclusion

In this work, we present the calibration (no density to intensity calibration has been performed yet) and processing of RAW H_α dataset (1914 – 2007) from the Kodaikanal Solar Observatory. We have generated Carrington maps from the calibrated and processed daily spectroheliograms for the whole study period. To our knowledge for the

first time we have been able to produce Carrington maps of H_α spanning for almost 100 years from digitized images taken from one single observatory. Thus this could be the most uniform and longest database for the statistical studies on H_α. A semi-automated algorithm relying on seed selection and region growing has been used to consistently detect filaments from the Carrington maps. From, the detected maps we have generated parameters such as filament centroid latitude and tilt angle with respect to the equator. Salient features of the new findings are listed here.

- We have generated the time-latitude distribution of filaments giving a clear signature of polar rush for several cycles along with butterfly diagram like pattern. It is worth noting that Cycle 23 shows a comparable signature of polar rush as that presented in Figure 5 of Hao et al. [2015].

- We segregated polar filaments with centroid latitude greater than 50° and plotted their number for all the Carrington maps over time. The plot depicted similar 11 year periodicity as normally observed for sunspot number cycle with delays. We measured those delays between polar filament and sunspot number maxima. We could also get the epochs of polar magnetic field reversal from Wilcox Solar Observatory data for last three cycles. Those have have been used to correlate the sunspot number-polar filament delay and sunspot number-pole reversal delay. With limited study points, we found out very high correlation indicating the role of polar filaments in polar reversal. This new result along with the rate of drift of filaments towards the pole may shed new light on the polar reversal.

- We found out asymmetry in the histogram of filament tilts consistent with the finding of Tlatov et al. [2016b]. Also, we could get the behaviour similar to Joy's law in the latitudinal distribution of filament tilts. It is believed that the tilt angle of sunspots and bipolar groups determines the conversion efficiency of the toroidal field into the poloidal magnetic field Tlatov et al. [2016b]. As filaments lie along polarity inversion lines, measurement of their tilt angle help us to understand the distribution of the solar magnetic field across the solar disk. In contrast to sunspots, filaments are distributed at all latitudes, so the long term variation of the distribution of poloidal and toroidal components of magnetic fields may be

better studied if we follow the filament distribution.

In this work we announce the availability of the longest digitized archive of H_α dataset (1914 – 2007) from the Kodaikanal Solar Observatory. The data will be made public through its portal at http://kso.iiap.res.in/data. We also show representative results from this archive to prove the potential of such an archive which demands further detailed investigations. In our subsequent studies on filaments, we want to combine multi-wavelength analysis of the historical data from KoSO as hinted in this work. This can lead to the classification of filaments into active region filaments, quiescent filaments. We also want to explore the hemispheric differences in filament behaviours and find more proxies to predict the future cycles. As a next step, we will employ different techniques for getting rid of filament fragmentation to estimate the filament lengths correctly. The length determination may prove to be vital in terms of its correlation to different statistical studies related to filament eruption and CMEs [Ruzmaikin et al. 2011, Filippov & Koutchmy 2008]. We plan to carry out a work similar to Ipson et al. [2005] which will include magnetic neutral line detection from MDI Carrington maps and cross-calibration with KoSO filament maps of intersecting dates to predict polar inversion line locations in the past. We hope that this KoSO archive and some of the new results as presented here will provide new momentum for the long-term study of H_α.

Chapter 8

Time-Latitude Distribution of Prominences for 10 Solar Cycles: A study using Kodaikanal, Meudon and Kanzelhohe Data

8.1 Introduction

Magnetic field is responsible for the heterogeneity as observed on the Sun in different temporal and spatial scales. Continuous monitoring of the solar magnetic field has been possible only in recent past with the launch of space-borne telescopes like Michelson Doppler Imager (MDI, on the Solar Heliospheric Observatory, SoHO, [Hoeksema et al. 1997]) and more recently Helioseismic and Magnetic Imager (HMI, on the Solar Dynamics Observatory, SDO [Fleck et al. 2012]). Before that magnetic field measurements in low resolution was initiated by ground-based observatories like Mount Wilson and most prominently by Wilcox Solar Observatory since the year 1976 [Bogart et al. 1992, Murdin 2000] and KittPeak/National Solar Observatory(NSO) since 1970 [Livingston & Harvey 1971, Minarovjech et al. 2011]. These data sources have been extensively used for solar cycle studies [Harvey & Munoz-Jaramillo 2015]. To trace back the solar magnetic field activity before 1976 different proxies have been used. Some of the prominent

features serving as proxies are sunspots, plages and filaments/prominences.

Prominences are structures formed in the solar atmosphere following magnetic neutral lines. They are formed in the chromosphere by cool dense (hundred times cooler and denser than the coronal material) plasma held in place by solar magnetic fields. At the limb they appear as bright features when observed in few optical, EUV lines such as H_α, Ca II K, He II 304 Å. They appear as dark elongated hairlike features on the disk for example in H_α 6562.8 Å or in He II 304 Å (named as filaments). Prominences present themselves in different morphology, lifetime and complexity in magnetic field environments. Thus long term study of prominences over several cycles and at different phases of solar cycle can give valuable insight on the physics of the solar atmosphere. There have been several studies to correlate prominence distributions and coronal mass ejections (CMEs) [Gilbert et al. 2000, Chatterjee et al. 2016, Schrijver et al. 2008]. Lockyer [1908, 1922, 1931] using coronal drawings and photographs obtained during the total solar eclipse suggested that there is an intimate connection between the distribution of prominences around the solar limb and the forms of corona. Though prominences form all over the Sun, their latitudinal distribution changes significantly with time being correlated with global properties of large scale magnetic fields on solar surface.

As pointed out earlier, prominences were first seen during total solar eclipses. Early history of prominence observations can be found in Tandberg-Hanssen [1974, 1998]. Zone of polar prominences and its pole-ward migration was discovered by Secchi [1872]. To probe the change in time-latitude distribution of prominences and its heterogeneity for the understanding and predicting solar magnetic fields over longer time scales, one needs long-term, homogeneous datasets. Along with the observations of on-disc filaments with spectroheliograph, systematic prominence observations were also carried out. Daily prominence observation at the Kodaikanal Solar Observatory (KoSO hereafter) started before the observational set-up for H_α was ready. This is because of the fact that the prominences were observed in Ca II K at KoSO above the solar limb by blocking the disk. So, full-disk and disk blocked observation started simultaneously at KoSO in Ca II K wavelength using spectroheliograph. Meudon observatory started prominence observation in H_α consistently after KoSO since 1919. Lomnicky Peak Observatory also recorded solar prominences in H_α from 1967 [Rušin

et al. 1988, Bumba et al. 1990, Rusin et al. 1994, Minarovjech et al. 1998a] until 2009. It is worth mentioning that Kislovodsk solar station in Russia started observing the Sun in H_α since 1957 and recorded filaments, prominences in the form of synoptic charts [Makarov et al. 2001a,b, 2003]. The observatory continues to make this observations till today. Recently, ground based disc-blocked prominence observation in H_α has been initiated at Kanzelhoehe Solar Observatory since 2009.

There have been several works reported in past using these historical data on prominences. From such datasets both pole-ward and equator-ward migration were shown by Abetti [1957]. Waldmeier [1973] established 3 narrow zones, which show different latitudinal behaviour in the 11-year cycle, namely sunspot prominences, stable long-lived prominences and polar zone prominences forming at latitudes around 45° at minimum and migrating towards poles around solar maximum gaining a velocity of 10 – 25 ms^{-1}. The change of migration rates from lower latitudes to near poles was pointed out by Makarov et al. [2001b]. D'Azambuja & D'Azambuja [1948] made a large number of measurements on filaments and prominences during the period of 1919 – 1930 and found on an average that all prominences have a low pole-ward drift in both the hemispheres. Verma [2000] studied the distribution and asymmetry of Solar Active Prominences (SAP) for the period of 1957 – 1998 (solar cycles 19 – 23) and found that E – W asymmetry of SAP events is not significant. He reported that N – S asymmetry of SAP events is significant and it has no relation with the solar maximum or solar minimum during solar cycles. Another study on asymmetry of SAP spatial distribution was made by Joshi et al. [2009]. Liu et al. [2012] using Solar LImb Prominence CAtcher and Tracker (SLIPCAT), studied prominences during the period 2007 – 2009. Shimojo [2013] using Nobeyama Radioheliograph reported the unusual migration of prominences producing region of activities in the southern hemisphere and interpreted the anomalies from the distribution of the photospheric magnetic field during the cycles 23 – 24. Parenti [2014] reviewed characteristic properties of prominences and filaments as derived from observations. Other studies were made to quantify the time-latitude distribution of prominence [Bumba et al. 1990, Minarovjech et al. 1998a] and correlated them with other solar cycle indices [Makarov et al. 2001b] for making cycle prediction [Makarov et al. 2003].

Most of the aforementioned works focused on temporal variation in spatial distribution of prominences. This requires a uniform dataset. Combined data from different observatories require cross calibration, otherwise detection techniques with same parameters but as applied to different data are not comparable. Rybák et al. [2011] cross calibrated data from Lomnicky Peak Observatory (1967 – 2009) and Kanzelhoehe Solar Observatory (2009 – 2010) before detection of prominences. In this context, it is worth mentioning that KoSO recorded prominence observations from 1906 until 2002 on daily basis with an instrument of unchanged optics. This ensured uniformity in the KoSO prominence data quality making it advantageous for feature detection. Prominence data from Kodaikanal for the period 1904 – 1914 is discussed by Evershed & Evershed [1917] and by Moss [1946] for the period 1905 – 1928. Half-yearly summaries of prominence observations were published in the Bulletin of the Kodaikanal Observatory. Using this data, prominence eruption was also reported in Evershed [1917]. But the notable study from KoSO prominence data was made by Ananthakrishnan [1952]. He performed manual identification of prominences during the period 1905 – 1950 and found a relationship between prominence activity and sunspot cycle. General review and discussion about the prominence data collected at Kodaikanal observatory was summarised by Ananthakrishnan [1954]. KoSO photographic plates have been recently digitised for the entire duration of observations. In modern times it is important to identify and detect structures such as prominences using computer codes for avoiding human bias and increasing speed. Rybák et al. [2011] have used the digitized Lomnicky Peak Observatory and Kanzelhohe Solar Observatory data to detect the prominence structures through semi-automated codes. Later, they have cross-calibrated these two data-sets as well.

Our objective is to detect prominence locations from the digitized KoSO data in a fully automated manner. In the present study to improve the statistics and to make the detection up-to-date, we also included the full disc H_α data from Meudon (1980-2002) and Kanzelhohe Observatory (2000-2018) blocking the disc and bringing them to equal footing as KoSO data. In this article we present an automated technique to identify the prominence latitudes from combined (KoSO-Meudon-kanzelhohe) disc-blocked dataset without being largely affected by artifacts. We describe the data in Section 8.2

followed by methods in Section 8.3 encompassing calibration and prominence detection techniques. We finally illustrate the results of the study in Section 8.4, discuss the results in Section 8.5 and conclude in Section 8.6.

8.2 Data Description

In following three subsections we discuss the three datasets used in our study for prominence detection.

8.2.1 Kodaikanal Dataset

The Ca II K line is very broad in wavelength coverage with 3 prominent positions such as K_1, K_2 and K_3 on the line profile. The K_3 region (3633.7Å), is where we see filaments and prominences similar to those seen in H_α but with much less contrast and less well defined boundaries. Photographic observations of solar prominences in Ca II K line (central wavelength 3633.7Å, passband 0.5Å) using spectroheliograph were started at Kodaikanal during 1905 [Ananthakrishnan 1954]. With weather permitting (when the sky and seeing conditions were good), the routine solar observations with the prominence spectroscope and the spectroheliograph were made between 02:00 to 04:30 UT, at KoSO. Due to the unavailability of pole marking on the images taken before 1906 we use the data starting from 1906. The spectroheliograph was used for generating the Ca II K images. This is the same instrument used to make the Ca II K spectroheliograms as well. In order to get the contrast for the prominences, the chromosphere was mechanically blocked by a circular mask of same size before capturing the image on photographic plates/films. The telescope used for this had an optics with a 30 cm objective, with f-ratio of f/21 [Priyal et al. 2014b]. This optics was unchanged throughout study time ensuring uniformity in quality. The disc blocked images were digitized recently through a 16-bit digitizer unit at KoSO consisting of an uniform illumination source, imaging optics for proper magnification and a 4096×4096 CCD cooled at −100°C. The digitized images from 1906 until 2002 (Table 8.1) used in our

study were in all '.fits' format and of size 4096×4096 with a pixel size of ≈ 0.88 arcsec /pixel. Figure 8.1a shows the typical digitized disk-occulted chromospheric image. The date and time of the observations is written in each of the plate on one corner of the plate, opposite to the side of emulsion. The white line on the right bottom corner is the occulter stick. Double and single dots outside the occulter represents the North and South pole of the sun. Lots of prominences could be seen in the digitized image on the limb. Figure 8.2a depict the number of days of observational data available per year for different years. On an average ≈ 269 observing days are available each year for the analysis before 1975. But, after 1975 the number of days of available data per year is ≈ 143. Other data sources, as mentioned in Table 8.1, were used to complement Kodaikanal data in later years and complete the analysis till date.

8.2.2 Meudon Dataset

Digitised full-disc H_α spectroheliograms (Figure 8.1c) from Meudon Observatory [Demarcq et al. 1985] starting from the year 1980 till May, 2002 were used in our study (Table 8.1). The image sizes varied from 928×942 to 1007×1003. Yearly histogram of observing days is depicted in Figure 8.2b. The average number of images available per year over the study period for Meudon is ≈ 254.

8.2.3 Kanzelhohe Dataset

Kanzelhohe Solar observatory (KSO) full-disc H_α images (Figure 8.1c) starting from the year 2000 till April, 2018 were used in this study (Table 8.1). KSO comes under Global H_α Network [Pötzi et al. 2013]. These filtergrams were captured through two different CCDs before and after the year 2008. Because of that, the images are of size 2032×2032 (before 2008) and 2048×2048 (since mid January, 2008). Yearly histogram of observing days is depicted in Figure 8.2c. The average number of images available per year over the study duration for KSO is ≈ 260.

[1] https://kso.iiap.res.in/new/Ca_K
[2] ftp://ftpbass2.obspm.fr/
[3] http://cesar.kso.ac.at/

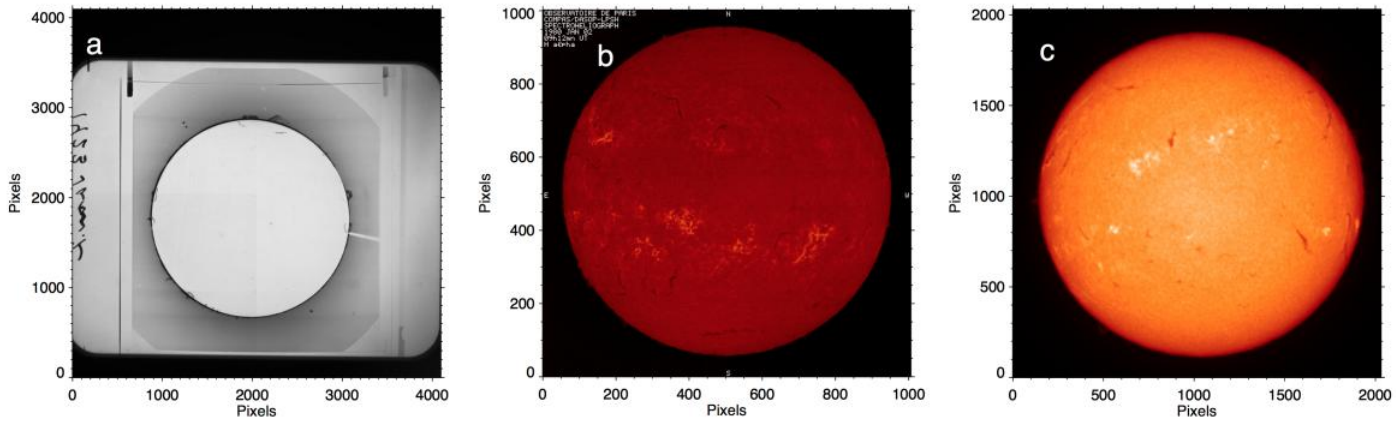

Figure 8.1: Raw datasets used for prominence detection. a) Representative raw KoSO Ca II K disc blocked spectroheliogram captured on January 02, 1923; b) Representative raw Meudon H_α full disc spectroheliogram captured on January 02, 1980; c) Representative raw Kanzelhohe H_α full disc filtergram captured on January 21, 2003.

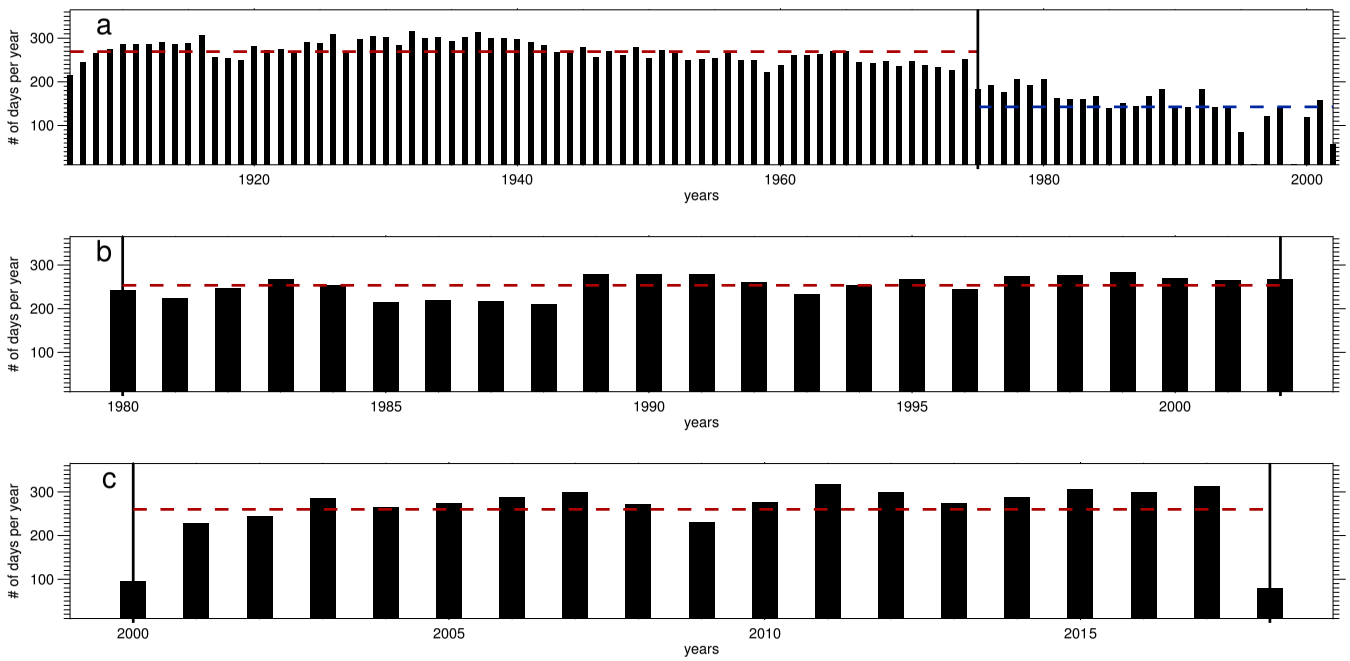

Figure 8.2: Histograms of observing days during the time period studied for KoSO, Meudon and KSO. a) Yearly histogram of available days in KoSO Ca II K disc blocked dataset. The red and blue dashed lines indicate the yearly mean before and after 1975 respectively; b) Yearly histogram of available days in Meudon H_α full disc dataset. The red dashed line indicates the mean yearly observing days for entire study period; c) Yearly histogram of available days in KSO H_α full disc dataset. The red dashed line indicates the mean yearly observing days for entire study period.

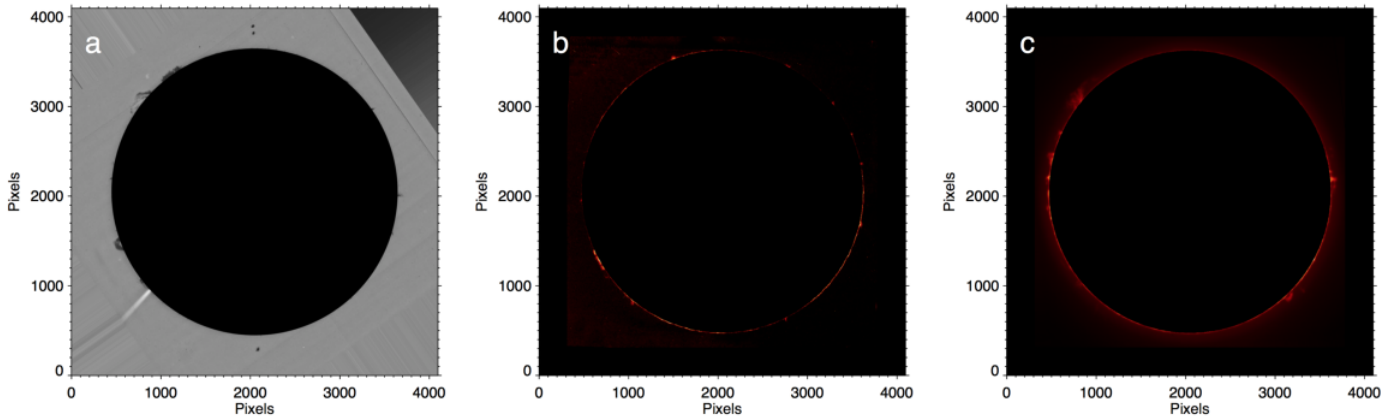

Figure 8.3: Calibrated disc-blocked images. a) Disc centered and radius normalised version of Figure 8.1a; b) Disc blocked, centered and radius normalised version of Figure 8.1b; c) Disc blocked, centered and radius normalised version of Figure 8.1c.

Table 8.1: Datasets used for prominence detection

Observatory	Data Type	Time span
Kodaikanal	Ca II K disc blocked	1906–2002 [1]
Meudon	H_α full disc	1980–2002 [2]
Kanzelhohe	H_α full disc	2000–2018 [3]

8.3 Data Calibration, Prominence Detection and Fitting Techniques

8.3.1 Calibration

Before detection of prominence locations, the digitised images had to go through few calibration steps. In the following two subsections we introduce the steps to calibrate both Kodaikanal Ca II K disc-blocked images and Meudon, Kanzelhohe H_α full-disc images in detail to make them ready for automated detection of prominence location using a single algorithm.

8.3.1.1 Calibration of Kodaikanal Ca II K Disc-blocked Images

All the digitized 4096×4096 raw images were initially binned to a size of 512×512 and 'Prewitt' [Sonka et al. 2014] edge detection operator was applied on the same to highlight the solar disc edge. Subsequently the edge detected image was thresholded to convert it to a binary form. The resulting binary image showed different edge features prominent in the photographic film in addition to the solar disc. To separate the disc out of all the features in the image, we used Circle Hough Transform [Sonka et al. 2014, Chatterjee et al. 2016]. For reducing the time and complexity we imparted a small search range about a nominal radius. This nominal radius value in pixel was obtained by dividing the disc angular size in arcsec, varying over a year, with the image pixel scale in arcsec. This gave precise values of disc center coordinates and its radius.

To find the large scale intensity variation outside the solar disc, resized 512×512 images were blurred using 2D median filter of size 15×15 pixels and the filtered image was subsequently resized to original size of 4096×4096. This method has been commonly used to estimate asymmetric center-to-limb variation of intensity in full disc solar Ca II K images [Bertello et al. 2010, Chatterjee et al. 2016]. The raw image was thereafter divided with the median filtered image to generate a normalized image of minimal near-limb intensity fluctuation. Using the informations obtained from Hough transform, we generated disc centered normalized images with a margin of 30% of the disc radii (r, in pixels) on both sides of solar disc to have provision of detecting large prominences. All the disc centered images of size $(2\lfloor 1.3r \rceil + 1) \times (2\lfloor 1.3r \rceil + 1)$ ($\lfloor . \rceil$ stands for the nearest integer function or the rounding operation) were converted to images of size 4096×4096. This step made disc radii constant throughout the study time. Because of the change of Sun-Earth distance over a year the radial extent of the images ($1.3r$ or 2048 pixels) varies between 1226 arcsec and 1265 arcsec. Also, in term of image scale this variation is within $\approx 0.6 - 0.62$ arcsec/pixel. It can be seen from Figure 8.1a that the raw images have north-south pole marking denoted by double and single dots outside solar disc for north and south poles respectively. By detecting those we found the exact angle by which the image has to be rotated so that the North pole will be located right in upward direction. The region within a radius of 1600 pixels was removed to get rid of any effect due to any misalignment of blocking disc in the instrument and the actual solar disc. It is worth mentioning that the misalignment causes a stretch of solar limb to be connected to the actual prominences causing over-detection. A representative calibrated image from the raw image depicted in Figure 8.1a is shown in Figure 8.3a.

8.3.1.2 Calibration of Meudon and Kanzelhohe H_α Images

Full-disc images from Meudon and Kanzelhohe observatory (Figures 8.1b,c) were first smoothed using median filter and subsequently edge detection was performed to detect the disc edges. This is to be noted that the sizes of the both Meudon images and Kanzelhohe images were not constant over time. So, the size of the smoothing kernels were varied accordingly. On the binary image containing limb, Circle Hough transform was applied to find the disc center and radius. Using those information disc centering

was performed and the centered image was rotated for p-angle compensation. The disc portion of centered and rotation corrected image was then blocked using a circular mask. The disc-blocked image depicts the prominences (Figures 8.3b,c). Before applying the detection algorithm all these disc blocked images were brought to the size of 4096×4096 (same as Kodaikanal) keeping 30% margin outside limb.

8.3.2 Detection of Prominence Locations

The calibrated images (I_{cal}), described in the last section, with image-center coordinates (c_x, c_y) were first converted to polar form (I_{polar}) using the following expression,

$$I_{polar}(R,\theta) = \begin{cases} I_{cal}(\lfloor c_x + R\cos\theta \rceil, \lfloor c_y + R\sin\theta \rceil), & \text{if } \lfloor c_x + |R\cos\theta| \rceil < 4096 \\ & \text{and} \lfloor c_y + |R\sin\theta| \rceil < 4096 \\ 0, & \text{otherwise} \end{cases} \quad (8.1)$$

with $c_x = 2048$, $c_y = 2048$, $0 \leq R < \lfloor 2048\sqrt{2} \rceil$ and $0° \leq \theta < 360°$. Rounding operation ($\lfloor . \rceil$) has been used to get integral pixel coordinates. Subsequently, polar images of size 2896 pixels ×360 pixels (Figure 8.4) were produced from disc centered calibrated images of size 4096×4096 (Figure 8.3). For the polar maps pixel scale values obtained along R and θ are $\approx 0.6 - 0.62$ arcsec and 1° respectively.

The periodic curved patterns in the polar image I_{pol} stand for the four straight sides of I_{cal} and the regions above the curved portion are dark due to no data outside square I_{cal}. It can be seen that the curved edges in I_{pol} starts appearing for $R > 2048$ for obvious reasons. So, for segregating the prominences we considered I_{pol} pixels only for $1600 < R < 2000$. Within this region we calculated median (med_{pol}) and standard deviation (σ_{pol}) of pixel intensity. Thereafter we produced binary image (BW_{polar}) applying a threshold of (med_{pol}-σ_{pol}) to KoSO polar images making all the pixel intensity below that threshold as 1 and rest as 0. For Meudon and Kanzelhohe polar images, binary version was produced by making all pixel intensities above (med_{pol}+σ_{pol}) as 1 and rest as 0. This difference was introduced considering whether prominence grey level is brighter or dimmer compared to background. Figure 8.4b depicts the binary image contours overplotted in red on the polar image shown in Figure 8.4a. This prominence

segmented binary image presents itself with several problems. Firstly, it captures small scale intensity fluctuations in the background. Secondly, near the limb sudden jump of intensity occurs as a result of median filtering which connects the prominence structures making disjoint regions to appear as single connected region. Finally, the thresholding captures curved artefacts which are manifestations of scratches in the original images. As the background small scale non-uniformity in intensity has no relation with θ, count of thresholded pixels along R should follow the prominence height fluctuations. To partially get rid of background non-solar features, all the detected regions not connected to solar limb were removed. This step is demonstrated through Figures 8.4b,c. From the resulting binary image with reduced noise, we generated prominence radial pixel count curves as function of θ expressed by-

$$c(\theta) = \sum_{R} BW_{polar}(R, \theta)$$

$c(\theta)$ corresponding to Figure 8.4c is shown in Figure 8.4d.

It was obvious that local maxima of prominence heights are good representatives of prominence locations. So, we calculated the locations of local maxima $\{\theta_M\}$ of $c(\theta)$. This process can be described as,

$$\{\theta_M\} = \underset{0^\circ \le \theta < 360^\circ}{\arg} \{\frac{dc(\theta)}{d\theta} = 0 \text{ and } \frac{d^{2n}c(\theta)}{d\theta^{2n}} < 0\}$$

We refined these maxima locations by putting a threshold as function of mean (m) and standard deviation (σ) over $c(\theta_M)$. Finally we described the prominence locations as $\Theta = \theta_M(\underset{k}{\arg}\{c(\theta_M(k)) > m + 0.7\sigma\})$. The coefficient of σ was selected by several iterations to select prominence locations efficiently. Count maxima at the locations Θ corresponding to Figure 8.4a are marked with red symbols on the count curve $c(\theta)$ in Figure 8.4b. Including the $B_\circ$ angle correction, Θ was converted to prominence latitudes (L_{promin}) in the range $[-90^\circ, 90^\circ]$ using eq.(8.2).

$$L_{promin} = \sin^{-1}(\cos(B_\circ)\sin(\Theta)) \tag{8.2}$$

Along with the latitudes we also recorded the counts i.e. $c(\Theta)$. Figure 8.4c depicts the prominence locations with red symbols plotted above the prominences. It can be

observed that the north and south pole markings did not get detected as prominences as they are detached from the limb.

Thus, between KoSO and Meudon/KSO data the basic difference in calibration lies in the fact Meudon/KSO are full-disc H_α images and thus their disc regions are artificially blocked using computer coded mask to make them equivalent to mechanically disc-blocked Ca II K spectroheliograms of KoSO. After blocking the disc and bringing resulting images to equal size with constant disc radius in terms of pixel, all subsequent operations are similar for all three datasets. As a first step to identify prominence locations bright and dark limb connected pixels were thresholded for KoSO and Meudon/KSO calibrated images respectively.

8.3.3 Polar Rush Fitting

Before fitting polar branches of prominence time-latitude diagram, we combined the three datasets namely KoSO, Meudon and Kanzelhohe. Subsequently, histogram prominence locations for each latitude bin of 1° and time bin of 0.1 years. Using the histogram density values the time-latitude plot was converted to an image. That image was thresholded to generate the binary version. For every latitudinal step, the mean temporal locations and standard error of the same were found for all the polar branches. Now, to fit the branches for extraction of migration rates we adapted two approaches. At first, we fitted the the latitudes (θ) and mean temporal locations (t) to the form $t = p_0 + p_1\theta + p_2\theta^2$ for $\theta \geq 50°$. By supplying the standard errors of mean temporal locations we found the uncertainties in the coefficients denoted by $\Delta p_0, \Delta p_1, \Delta p_2$. Now, taking derivative of the mentioned function we found the rate in °/year as $r = \frac{1}{p_1+2p_2\theta}$. The uncertainty in the rate (Δr) was calculated using $\Delta r^2 = (\partial r/\partial p_1)^2\Delta {p_1}^2 + (\partial r/\partial p_2)^2\Delta {p_2}^2 = \frac{1}{(p_1+2p_2\theta)^4}(\Delta {p_1}^2 + 4\theta^2\Delta {p_2}^2)$. Now, the rate uncertainty is a function of latitude which can be avoided by fitting a linear function of the form $t = p_0 + p_1\theta$. As a second approach we fitted a piecewise linear function defined by eq.(8.3).

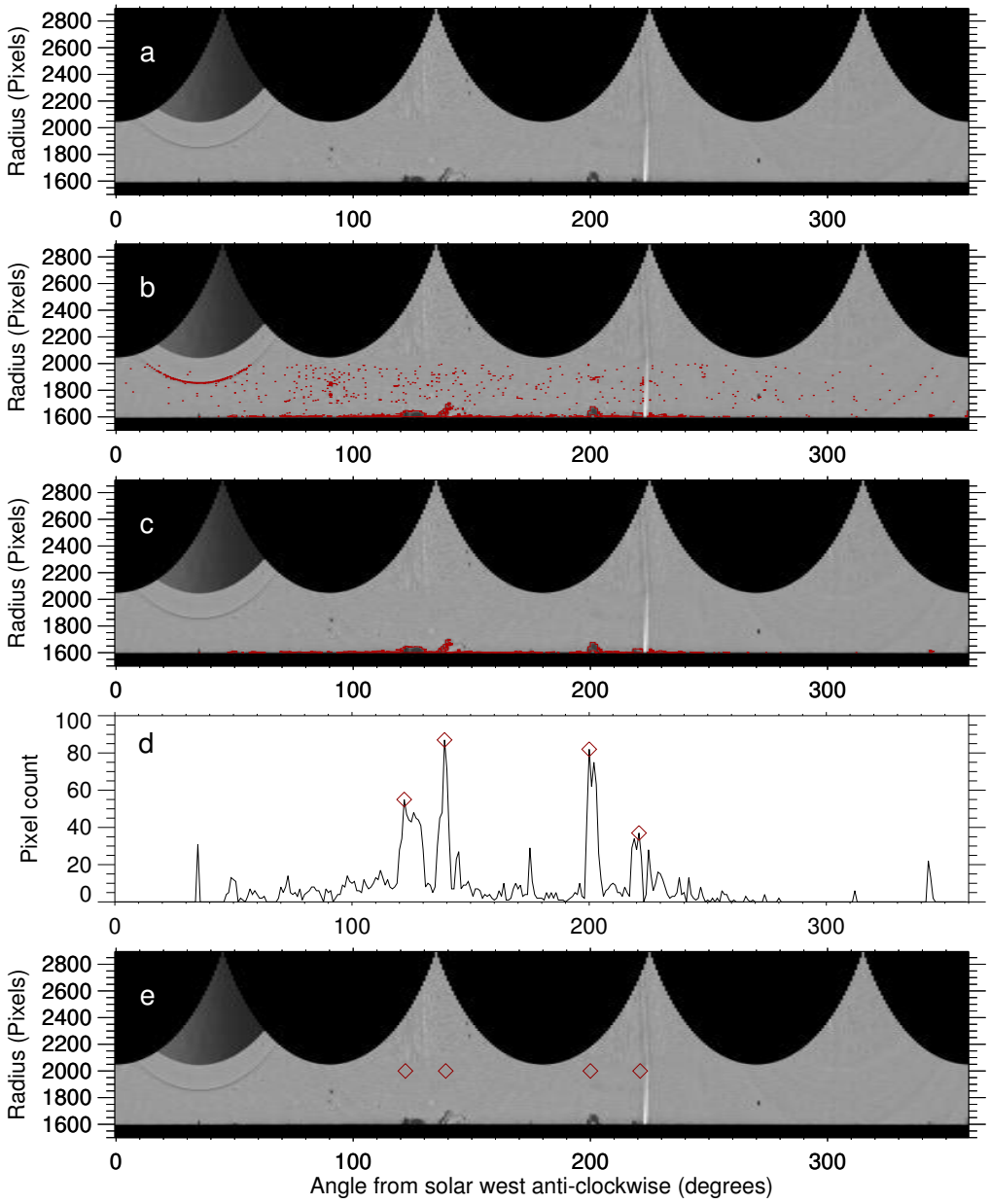

Figure 8.4: Steps for detection of prominence locations. a) Polar map generated from Figure 8.3a; b) Red contours correspond to the segmented regions after intensity thresholding of the polar map; c) Contours obtained after removing regions not connected to limb from (b); d) Counts of detected pixels along radius (c) for each angle w.r.t. solar equator is plotted and local maxima with higher counts in red symbols are considered to be locations of prominence structures; c) Prominence locations identified in (d) over plotted on (a).

$$t = \begin{cases} p_0^{(1)} + p_1^{(1)}\theta, & \text{if } 50^\circ \leq \theta < \theta_{sep} \text{ (Low Polar Zone)} \\ p_0^{(2)} + p_1^{(2)}\theta, & \text{if } \theta \geq \theta_{sep} \text{ (High Polar Zone)} \end{cases} \tag{8.3}$$

The separator latitude θ_{sep} was varied such that the fitting error is minimised. In this case two zones of poleward migration are created with rates $1/p_1^{(1)}, 1/p_1^{(2)}$. The rate errors for those are given by $\Delta p_1^{(1)}/(p_1^{(1)})^2, \Delta p_1^{(2)}/(p_1^{(2)})^2$. Hereafter we use LPZ and HPZ as abbreviations for 'Low Polar Zone' and 'High Polar Zone' respectively.

8.4 Results on Detected Prominences and Poleward Migration

From the detection of prominence locations as described in the last section we obtained time latitude diagrams for prominences for Kodaikanal, Meudon and Kanzelhohe Observatory. Figure 8.5 depicts time-latitude distribution and fitted polar branches of prominences from 1906 till April, 2018. Time-latitude pattern of prominences detected using KoSO dataset is shown in Figure 8.5a. From this diagram we immediately notice the clear signature of poleward migration till the close vicinity of poles from 15 through 21 both in northern and southern hemispheres. The nature of polar rush from cycle 15 until cycle 18 can be directly compared with the time-latitude plots depicted in Ananthakrishnan [1952, 1954]. Polar branch remains clear for northern hemisphere in cycle 22 whereas that in the southern hemisphere does not show clear trend. This is the effect of diminishing number of observing days after cycle 21. The same algorithm applied on Meudon and Kanzelhohe H_α images manages to provide clear depiction of poleward migration from cycle 22 through cycle 24 (till mid of cycle 23 for Meudon in red and mid cycle 23 till cycle 24 for Kanzelhohe in Blue) in both hemispheres (Figure 8.5b). Polar rush fits on the combined dataset using 2nd degree polynomial and piecewise linear function, as described in section 8.3, are depicted in Figure 8.5c and Figure 8.5d respectively. Figure 8.5e depicts the 13-month running averaged monthly sunspot area variation in north and south from Greenwich dataset [4].

[4] http://solarscience.msfc.nasa.gov/greenwch.shtml

As pointed in several studies [Ananthakrishnan 1954, Bumba et al. 1990, Minarovjech et al. 1998a], after sunspot minimum prominence activity begins to develop in the high latitude zones between $40^\circ - 50^\circ$ latitudes and with progress in sunspot activity, the prominence activity shifts towards pole with a rapid rush near sunspot maximum. Very similar phenomena can be noted from in the time-latitude plots (Figures 8.5a-d) when compared with epochs sunspot area cycle maxima (Figures 8.5e) for both the hemispheres. The mean of absolute differences between epoch of sunspot maxima and epoch of prominences reaching pole over all cycles comes about ≈ 1.5 years in north and ≈ 0.8 year in south from our detection. Also, near minima there is consistent decrease in prominence counts in low latitudes for all the cycles. Cycle 23/24 minima shows a clear depiction of this and also that the prominences are created $\approx 50^\circ$ latitude (Figure 8.5b). We segregated the polar prominences for every cycle with latitude $\gtrapprox 50^\circ$. The change of migration rate from near 50° latitude to near poles are clearly demonstrated through the fits in the Figures 8.5c,d.

To validate our prominence detection, we compared our results with the available filament and prominence catalogues from Meudon H_α synoptic maps and LSO/KSO cross calibrated [Rybák et al. 2011] H_α series respectively (Figures 8.6a,b). To accomplish this, we first converted our detected prominence butterfly diagram and also available catalogues to 2-dimensional histograms with temporal binning of 0.1 year and spatial binning of 1° latitude. As our results primarily focus on polar-rush, we segregated the polar branches satisfying $|latitude| > 55^\circ$. For every cycle, we smoothed those polar branches with a kernel of dimension 1 year$\times$ 10° (Figures 8.7a-h). For every cycle, we correlated those smoothed histogram density images from our detection and the catalogues. The results of correlation for both north and south analysis are presented in Table 8.2. It can be observed that all the correlations vary within a range of $\approx 0.6 - 0.9$ confirming a good match. It can be observed from the histogram images (Figures 8.7a-d) that for older cycles, where KSO data is not available, KoSO prominence data have an advantage over Meudon filament catalogue in depicting polar rush to higher latitudes with better data density and continuity. Poor data density in polar branch is also responsible for lower correlation coefficient. The good visual match between our detection and LSO/KSO catalogue for cycle-24 (Figures 8.7e-h) is

also reflected in high correlation coefficients of Table 8.2.

Following the method described in section 8.3, the instantaneous rates with error-bars have been calculated at three different latitudes ($55°, 65°, 75°$) from nonlinear fits have been documented in Table 8.3 and Figures 8.8a-c. At 55°, the rates are seen to vary between 2.09 ± 0.48 m/s and 3.99 ± 2.52 m/s (Table 8.3). Though at higher latitude (75°) there is indication of rate reaching ≈ 10 m/s, the rates get affected by very large error-bars making it difficult to observe cycle to cycle and also to confirm the increase of rate gradually to pole (Table 8.3, Figure 8.8c). With piece-wise linear fit method, we could find migration rates at two different latitude zones above 50° latitude with much smaller error bars (Table 8.4 and Figures 8.9a, b). At LPZ the rates were seen to vary between 2.03 ± 0.13 m/s and 10.09 ± 1.0 m/s (Table 8.4 and Figure 8.9a). Clear increase of rate was seen in HPZ on an average as the rates were seen to vary between 1.31 ± 0.07 m/s and 19.48 ± 5.71 m/s (Table 8.4 and Figure 8.9b). Cycle 19 was seen to dominate the migration rates in LPZ north and south. Also, rate in HPZ north was seen to be dominated by cycle 19. Because of higher error bars, same cannot be said for HPZ south. The average separator latitudes automatically found by the piece-wise linear fit came to be 67.5° and 69.2° for north and south respectively.

Following the idea as presented in a recent study by Petrovay et al. [2017] on coronal green line data, we calculated the rate of polar rush r_i derived from linear fits for both northern and southern hemispheres during every cycle (i) starting from 15 till 23. We used the rate for HPZ as it represents migration close to pole. Using the HPZ rate r_i (°/year) we also found the epochs where polar branches reach pole (TP_i). Using the Greenwich sunspot area data[5] we also extracted the epochs of sunspot area maxima (TS_i) for both north and south. From the mentioned two epochs we calculated the delay Δt_i as $TS_{i+1} - TP_i$. Subsequently, we checked the linear correlation between Δt_i and r_i for north and south separately. We find a linear Pearson correlation of 0.54, for north, which has a significance level of 0.13 (Figure 8.10) and a correlation of 0.44 for south with a significance of 0.24. All the correlation coefficients are corrected for the attenuation effect [Matzke et al. 2017] considering the uncertainties in the poleward migration rates. The rate versus delay correlations are not as high the one found by Petrovay et al. [2017]

[5] http://solarscience.msfc.nasa.gov/greenwch.shtml

between same parameters with i ranging from 18 until 23. Our correlations do not show high statistical significance which is an effect of less data points due to treating north and south separately. Treating north and south together enhances the correlation to 0.56 with a significance of 0.02 (Figure 8.11). To find the linear relation between variable pairs we performed Bayesian analysis and acquired posterior probability distribution of regression line slope, intercept [Carroll et al. 1999, Kelly 2007]. While doing the analysis we also fed uncertainties in the migration rates. From the analysis with i ranging from 15 until 23, we found the linear relation with posterior median as $\Delta t_i = 0.24 r_i + 4.88$ (Figure 8.10a) and $\Delta t_i = 0.06 r_i + 8.89$ (Figure 8.10b) for north and south respectively. For north we found [0.04, 0.44] years^2/degree and [1.34, 8.54] years as 95% posterior probability intervals for slope and intercept respectively. Similarly for south intervals containing 95% posterior probability were found as [-0.15, 0.29] years^2/degree and [4.04, 13.40] years for slope and intercept respectively. When north and south were treated together (Figure 8.11) the 95% posterior probability intervals were found to be [0.06, 0.36] years^2/degree and [3.11, 8.46] years respectively.

On correlating we found sunspot area cycle amplitude (S_i in μHem) for cycle-i to have statistically significant correlation of 0.74 with poleward migration rate r_i for northern hemisphere (Figure 8.10c). Apparently, southern hemisphere showed no significant correlation (0.17) between S_i and r_i (Figure 8.10d). Upon performing the same Bayesian analysis as before, we found the linear relation between r_i and S_i (i ranging from 15 to 24) acquired from posterior median as $S_i = 37.80 r_i + 520.34$ (Figure 8.10c) and $S_i = 19.83 r_i + 778.29$ (Figure 8.10d) for north and south respectively. [-13.44, 87.56] and [-380.66, 1462.18] were derived as 95% posterior probability intervals for slope and intercept respectively in the north. In south, [-37.45, 78.71] and [-373.40, 1932.06] were found as 95% posterior probability intervals for slope and intercept respectively.

Following the index suggested in [Makarov et al. 2001b] we correlated SS_i (μHem), the sum of yearly averaged sunspot area from cycle $(i-1)/i$ minima to the epoch when first pole branch reaches the pole, with r_i forth both north (Figure 8.10e) and south (Figure 8.10f) . Significant improvement in the correlation (0.61) for south can be observed from the case when only cycle amplitude was correlated with r_i (0.17

Table 8.2: Correlation of polar branches from our detection and available catalogues

Cycle	Our detection vs Meudon catalogue		Our detection vs LSO/KSO catalogue	
	North	South	North	South
16	0.64	0.61	-	-
17	0.81	0.73	-	-
18	0.61	0.79	-	-
19	0.74	0.61	-	-
20	0.88	0.81	-	-
21	0.65	0.63	0.79	0.80
22	0.82	0.61	0.70	0.67
23	-	-	0.78	0.73
24	-	-	0.86	0.94

in Figure 8.10d). Linear relationships between SS_i and r_i using posterior medians from Bayesian analysis were found as $SS_i = 54.26r_i + 2262.93$ (Figure 8.10d) and $SS_i = 57.57r_i + 1958.44$ (Figure 8.10e) for north and south respectively. The intervals [-35.49, 143.63] and [636.31, 3866.03] represented 95% posterior probability for slope and intercept respectively in the north. In south, [-32.18, 156.90] and [-1.76, 3829.96] were found as 95% posterior probability intervals for slope and intercept respectively. Regions within dashed curves filled with grey vertical lines (Figure 8.10 a-f) depict 95% posterior probability of linear relations, between variable pairs, derived from Bayesian analysis.

To decode the correlation coefficients between the variable pairs we performed Bayesian analysis [Gelman et al. 2013, Lee & Wagenmakers 2014] scanning through bivariate normal distributions with different population correlations (ρ). The derived posterior probability distributions of ρ (depicted as histograms in every panel of Figure 8.10) showed higher probability ($\geq$ 81 %) of positive correlation in every case (Table 8.5).

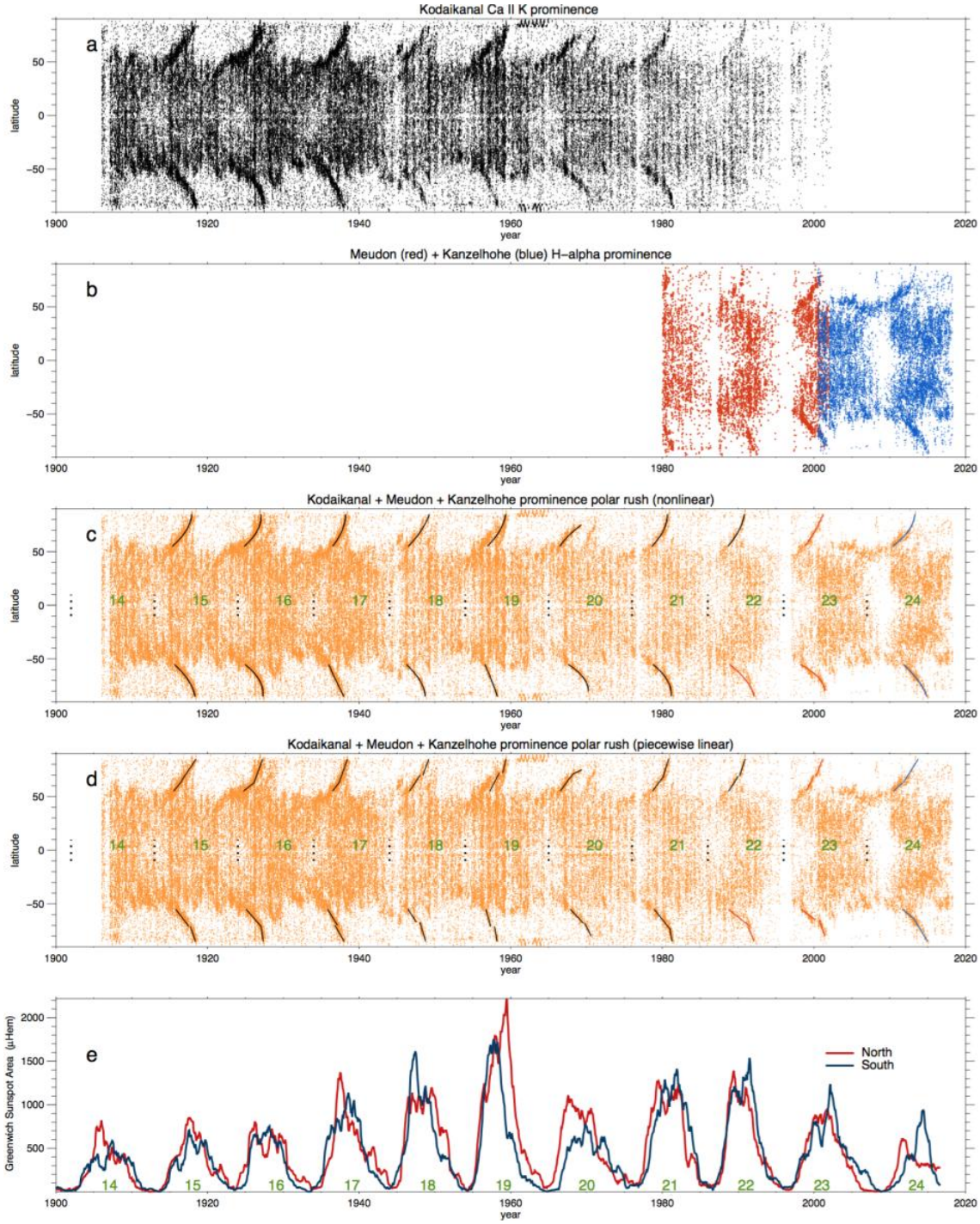

Figure 8.5: Prominence locations from 1906 until April, 2018. a) Time-latitude distribution of the KoSO prominences clearly depicting polar rush till latitudes close to 90° for cycles 15-21 in both northern and southern hemispheres; b) Detected prominence locations using same algorithm on Meudon and Kanzelhohe H_α data.; c) Extracted poleward drift by fitting 2^{nd} degree polynomial for prominences of latitude $\geq 50°$. Black, red and blue curves are generated respectively from KoSO, Meudon and Kanzelhohe data. Combined time-latitude distribution of prominences have been put in background with orange dots; d) Piecewise linear fits to the polar branches depicting the latitudes from which migration rate changes; e) 13-month running average smoothed Greenwich sunspot area cycle till 2016 for north and south.

Table 8.3: Poleward migration rates at different latitudes through nonlinear fit

Observatory	Cycle	rate in °/year (m/s)					
		55°N	65°N	75°N	55°S	65°S	75°S
Kodaikanal Ca II K	15	6.11±1.20	8.94±2.75	16.62±10.17	6.26±1.59	8.72±3.31	14.42±9.67
		(2.35±0.46)	(3.44±1.06)	(6.40±3.91)	(2.41±0.61)	(3.36±1.27)	(5.55±3.72)
	16	6.27±1.37	9.77±3.55	22.09±19.39	5.64±1.28	9.00±3.49	22.16±22.68
		(2.42±0.53)	(3.76±1.37)	(8.50±7.46)	(2.17±0.49)	(3.46±1.34)	(8.53±8.73)
	17	8.94±3.04	13.21±7.11	25.24±27.85	16.63±7.33	15.39±6.72	14.32±6.23
		(3.44±1.17)	(5.08±2.74)	(9.72±10.72)	(6.40±2.82)	(5.92±2.59)	(5.51±2.40)
	18	7.30±3.70	9.32±6.49	12.92±13.40	6.39±2.22	9.24±4.98	16.68±17.42
		(2.81±1.42)	(3.59±2.50)	(4.97±5.16)	(2.46±0.85)	(3.56±1.92)	(6.42±6.70)
	19	7.07±2.17	9.91±4.55	16.54±13.56	15.55±8.34	16.99±10.67	18.72±13.89
		(2.72±0.84)	(3.81±1.75)	(6.37±5.22)	(5.99±3.21)	(6.54±4.11)	(7.21±5.35)
	20	10.37±6.55	7.03±3.23	5.32±1.99	4.69±0.68	7.83±2.01	23.59±19.49
		(3.99±2.52)	(2.71±1.25)	(2.05±0.77)	(1.81±0.26)	(3.01±0.77)	(9.08±7.50)
	21	7.39±1.96	11.04±4.69	21.79±19.58	5.65±1.15	8.90±3.06	20.91±18.09
		(2.84±0.76)	(4.25±1.80)	(8.39±7.54)	(2.18±0.44)	(3.43±1.18)	(8.05±6.96)
	22	8.31±1.96	11.28±3.87	17.56±10.05			
		(3.20±0.75)	(4.34±1.49)	(6.76±3.87)			
Meudon H_α	22				5.41±1.16	7.4±2.32	11.71±6.21
					(2.08±0.45)	(2.85±0.89)	(4.51±2.39))
	23	9.73±4.56	11.41±6.72	13.78±10.53	3.82±0.69	6.41±2.08	19.88±21.5
		(3.75±1.75)	(4.39±2.59)	(5.30±4.05)	(1.47±0.26)	(2.47±0.80)	(7.65±8.28)
Kanzelhohe H_α	24	5.42±1.24	7.93±2.83	14.77±10.52	6.67±1.72	8.42±2.93	11.42±5.77
		(2.09±0.48)	(3.05±1.09)	(5.68±4.05)	(2.57±0.66)	(3.24±1.13)	(4.40±2.22)

Table 8.4: Poleward migration rates at different latitudes through piecewise linear fit

Observatory	Cycle	rate in °/year (m/s)				separator latitude	
		LPZN	HPZN	LPZS	HPZS	N	S
Kodaikanal Ca II K	15	8.69±0.84	10.44±0.430	9.24±0.51	20.62±2.79	65°	71°
		(3.35±0.32)	(4.02±0.16)	(3.56±0.20)	(7.94±1.07)		
	16	5.56±0.48	19.34±1.46	8.09±0.42	50.62±14.83	63°	71°
		(2.14±0.18)	(7.44±0.56)	(3.11±0.16)	(19.48±5.71)		
	17	9.26±1.01	19.67±1.33	11.52±0.62	12.15±0.460	64°	70°
		(3.57±0.39)	(7.57±0.51)	(4.43±0.24)	(4.67±0.18)		
	18	10.78±0.79	19.65±3.23	11±1.02	23.62±2.56	70°	67°
		(4.15±0.31)	(7.56±1.24)	(4.23±0.39)	(9.09±0.98)		
	19	13.52±1.40	31.84±7.48	26.21±2.59	40.59±10.61	72°	71°
		(5.21±0.54)	(12.26±2.88)	(10.09±1.0)	(15.62±4.08)		
	20	9.60±0.57	3.40±0.170	7.46±0.49	14.09±2.21	71°	68°
		(3.69±0.22)	(1.31±0.07)	(2.87±0.19)	(5.42±0.85)		
	21	9.32±0.57	22.14±2.17	8.95±0.34	37.51±12.45	69°	74°
		(3.59±0.22)	(8.52±0.83)	(3.45±0.13)	(14.44±4.79)		
	22	11.33±0.62	21.42±2.45			69°	
		(4.36±0.24)	(8.25±0.94)				
Meudon H_α	22			5.62±0.22	16.58±1.53		71°
				(2.16±0.08)	(6.38±0.59)		
	23	14.11±1.19	18.29±1.65	5.27±0.34	22.51±2.23	69°	65°
		(5.43±0.46)	(7.04±0.64)	(2.03±0.13)	(8.66±0.86)		
Kanzelhohe H_α	24	6.69±0.87	11.15±0.680	5.94±0.49	11.67±0.48	63°	64°
		(2.58±0.34)	(4.29±0.26)	(2.29±0.19)	(4.49±0.18)		

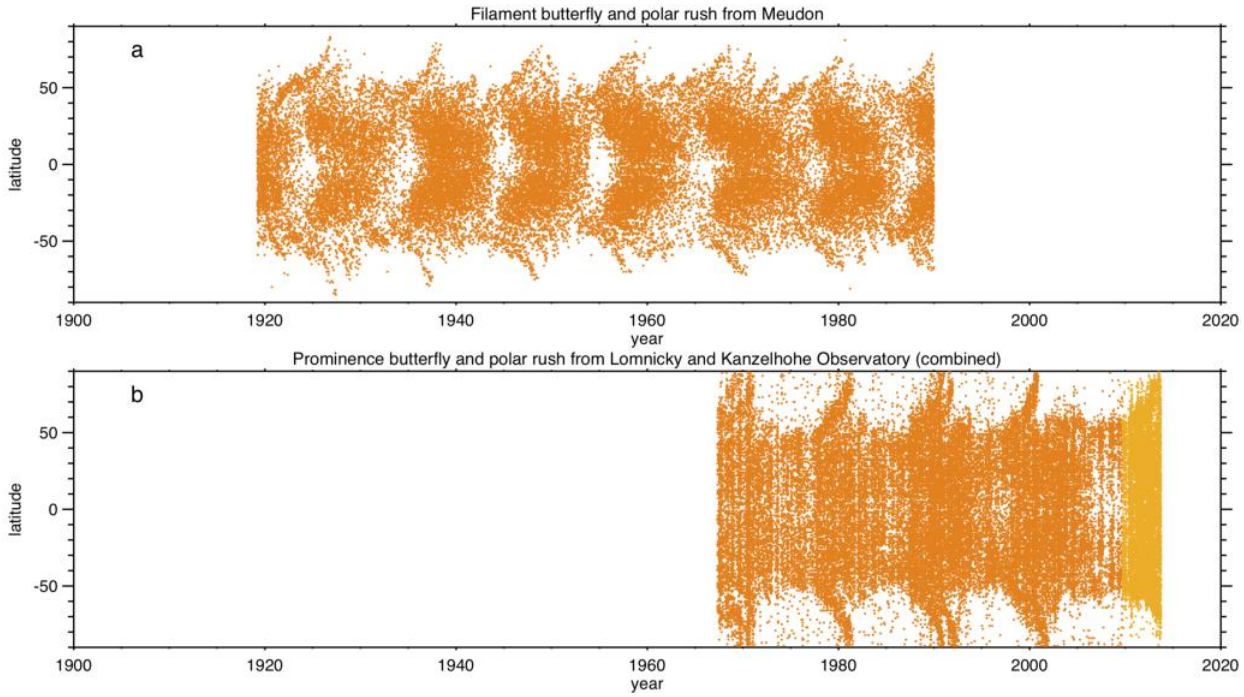

Figure 8.6: Available filament and prominence catalogues. a) Time-latitude distribution of on-disc filament centers from Meudon H_α synoptic map catalogue; b) Time-latitude distribution of H_α prominences from Lomnicky (orange) and Kanzelhohe (yellow) catalogue.

Table 8.5: Posterior probability distribution of Pearson correlation coefficient ρ

Variable Pairs	Probability ($\rho > 0$)	Median ρ
r_i (HPZ) vs Δt_i North	0.98	0.74
r_i (HPZ) vs Δt_i South	0.83	0.36
r_i (HPZ) vs Δt_i North+South	0.99	0.66
r_i (HPZ) vs S_i North	0.96	0.56
r_i (HPZ) vs S_i South	0.81	0.30
r_i (HPZ) vs SS_i North	0.91	0.43
r_i (HPZ) vs SS_i South	0.92	0.44

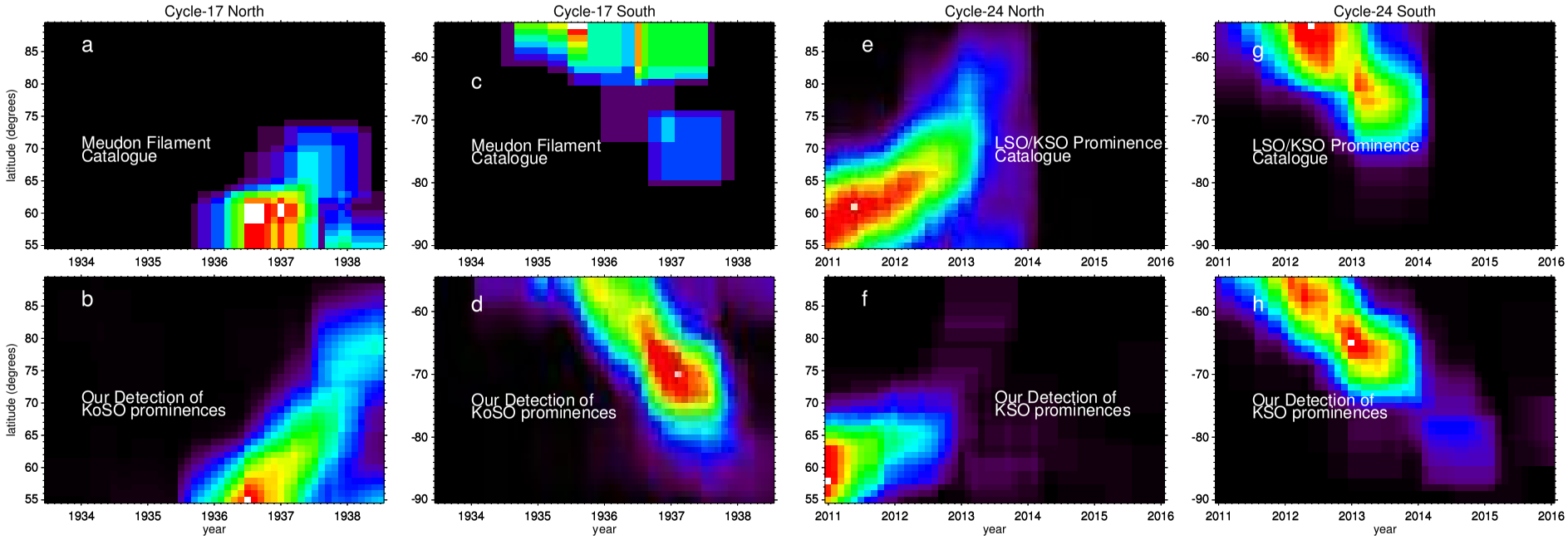

Figure 8.7: Comparison of polar rush between available catalogues and our detection. a) Density image of cycle-17 northern polar branch derived from Meudon filament catalogue; b) Density image of cycle-17 northern polar branch derived from our detection of KoSO prominences; c) Density image of cycle-17 southern polar branch derived from Meudon filament catalogue; d) Density image of cycle-17 southern polar branch derived from our detection of KoSO prominences; e) Density image of cycle-24 northern polar branch derived from LSO/KSO prominence catalogue; f) Density image of cycle-24 northern polar branch derived from our detection of KSO prominences; g) Density image of cycle-24 southern polar branch derived from LSO/KSO prominence catalogue; h) Density image of cycle-24 southern polar branch derived from our detection of KSO prominences.

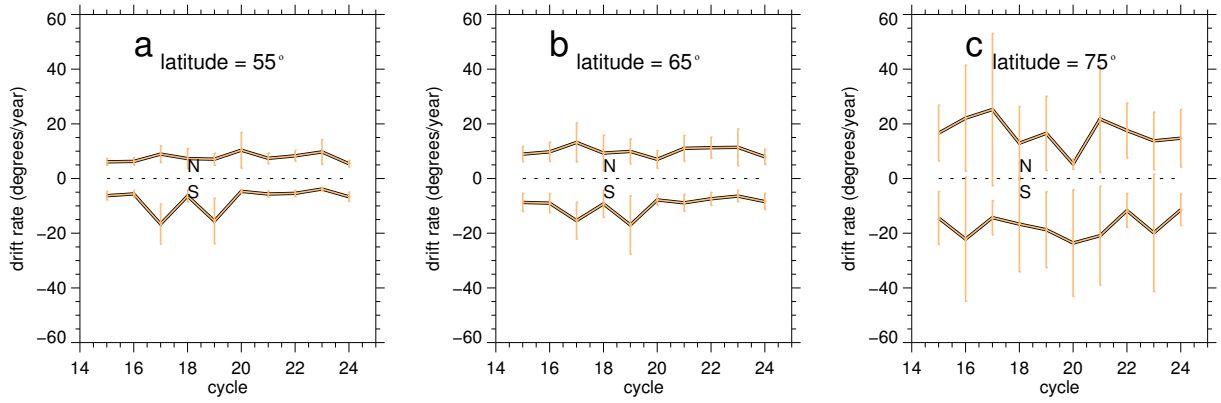

Figure 8.8: Cycle wise drift rate of polar prominences with error bars as vertical stretches in two latitude zones extracted from nonlinear fit. a)-c) show the variation of instantaneous drift rates (degrees/year) with solar cycle number at latitudes $55°, 65°, 75°$ respectively for both northern and southern hemispheres. It is worthing noting that the errors bars increase for higher latitudes indicating need for lower order polynomial fit.

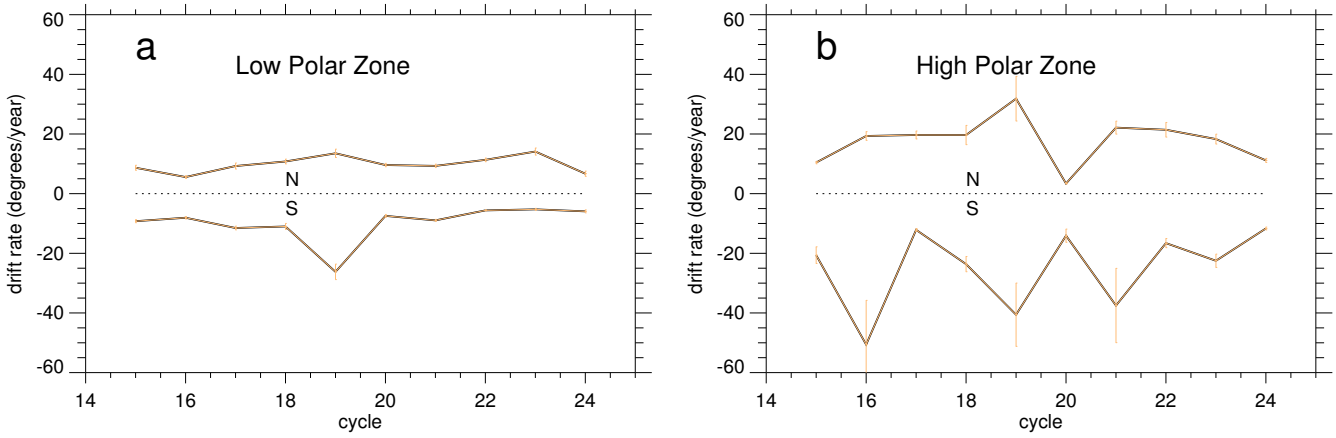

Figure 8.9: Cycle wise drift rate of polar prominences with error bars as vertical stretches in two latitude zones extracted from piecewise linear fit. a) The variation of drift rates (degrees/year) with solar cycle number for both northern and southern hemispheres in latitude LPZ ranging from 50° to a separator latitude from which there is change in linear fit; b) the variation of drift rates (degrees/year) with solar cycle number for both northern and southern hemispheres in latitude HPZ ranging from separator latitude to $\approx 85°$ from which there is change in linear fit. It can be observed that the piecewise linear fits successfully depicts cycle-to-cycle variation in drift rates along with north-south asymmetry taking in account the error bars. For both the latitude zones cycle 19 shows highest drift rate in northern hemisphere and it dominates south for latitude LPZ.

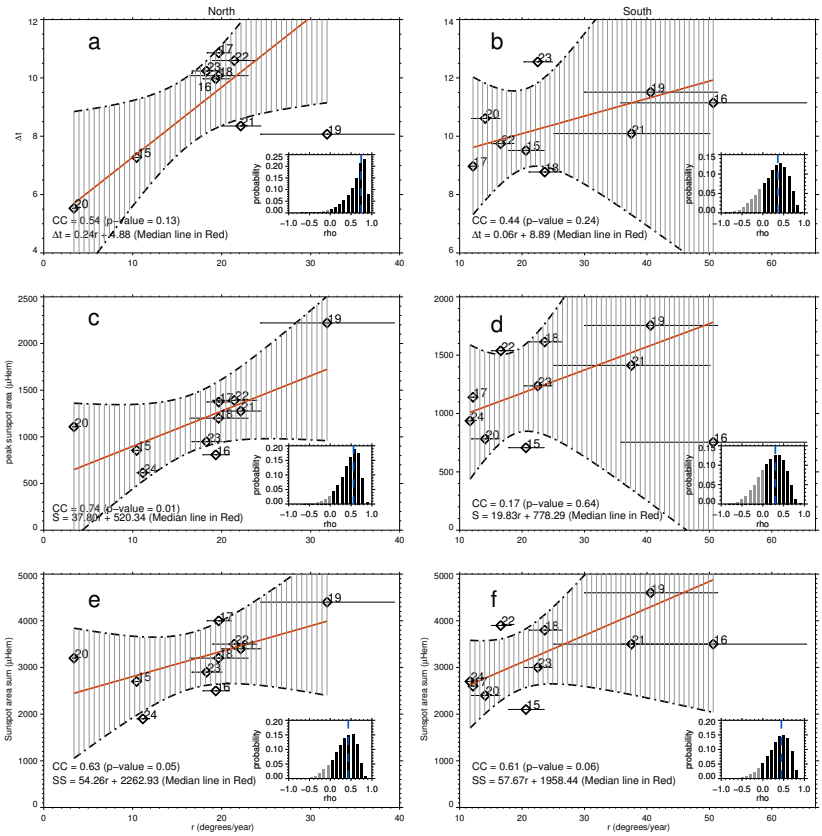

Figure 8.10: Hemisphere-wise correspondences of prominence poleward migration rates with sunspot cycle epoch and strength. a) and b) Depict plot of rate of polar migration (r) from HPZ straight line fit vs Δt, the time delay between the epoch of polar branch reaching poles for i^{th} cycle and epoch of sunspot area maxima for $(i+1)^{th}$ cycles for north and south respectively; c) and d) depict plot of rate of polar migration (r) from HPZ straight line fit vs 13 month running averaged peak sunspot hemispheric area (S) in same cycle for north and south respectively; e) and f) demonstrate plot of r vs sum of yearly averaged hemispheric sunspot area from cycle minima epoch to the time of first polar branch reaching the pole (SS) in same cycle for north and south respectively; Cycle numbers (i) are indicated beside the symbols. Uncertainties of poleward migration rates in HPZ are depicted by horizontal lines around the data points (diamond symbols). 95% posterior probability of slope and intercept lies within the grey shaded region bounded by dashed curves for all the panels. Red straight lines depicted in all the panels are constructed from median of slope, intercept posterior probability distribution. The posterior probability distributions of correlation coefficients (ρ) derived from Bayesian analysis are depicted as small barplots in different panels with median ρ as blue dashed line. The distribution area in grey depicts posterior probability for $\rho < 0$ and black for $\rho \geq 0$.

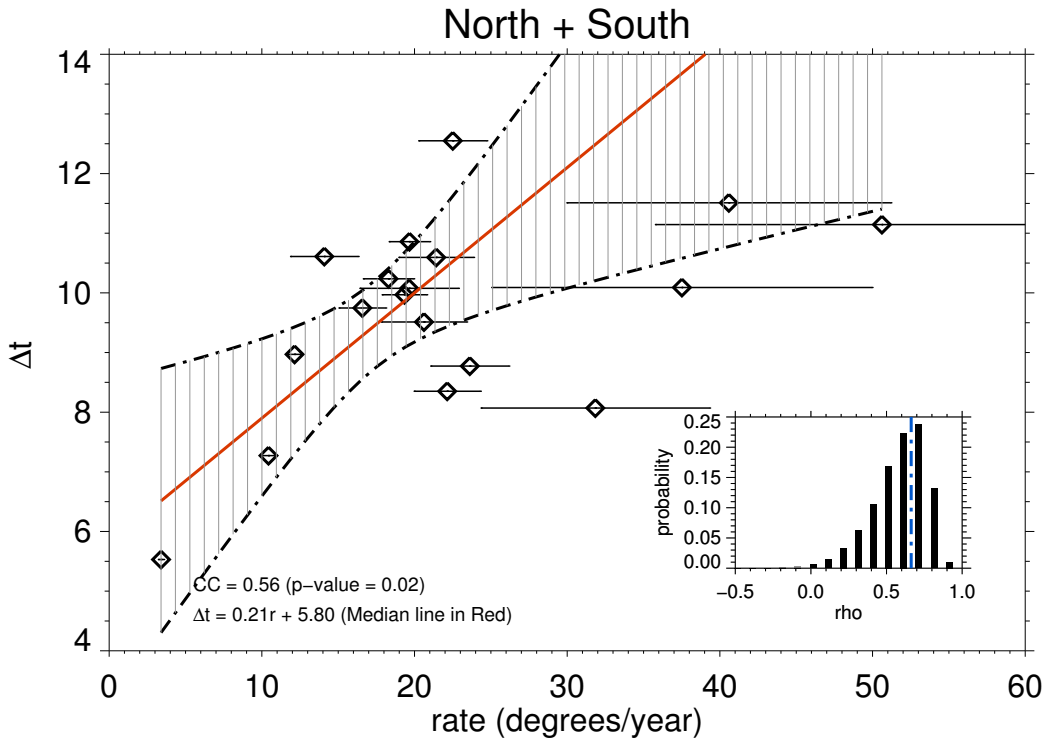

Figure 8.11: Plot of rate of polar migration (r) from HPZ straight line fit vs Δt when data points of Figure 8.10a and Figure 8.10b are combined. Uncertainties of poleward migration rates in HPZ are depicted by horizontal lines around the data points (diamond symbols). 95% posterior probability of slope and intercept lies within the grey shaded region bounded by dashed curves. Red straight lines is constructed from median of slope, intercept posterior probability distribution. The posterior probability distribution of correlation coefficient (ρ) derived from Bayesian analysis is depicted as small bar-plot in lower right corner. The location of blue dot-dashed line in probability distribution represents median ρ.

8.5 Discussion

As Ca II K_3 line, recorded in KoSO data, represents a slightly lower height range in chromosphere as compared to that for H_α, a difference in detection affecting polar rush might be expected. However, through the comparison of Meudon H_α filament catalogue and our detected Ca II K prominences, a close match in polar branches for several cycles were depicted. This confirmed no major influence of change of wavelength over the migration rate on statistical basis. Also, the the signature of filament poleward migration in H_α is limited to certain latitudes as shown by Chatterjee et al. [2017] from KoSO data because of projection effect, poor contrast near limb and artefacts. Also, clear correspondence between catalogue and detection from same data for overlapping cycles validated the presented detection technique. Information about prominences from KoSO Ca II K disc-blocked images in that sense acts as a complimentary dataset to the H_α filaments. It is also worth mentioning that manual detection in from same prominence dataset of KoSO Ananthakrishnan [1952] shows close agreement with the automated detection presented here, in terms of time-latitude distribution of prominences.

Though the fitting of polar branches has been done on combined dataset, each polar branch has major contribution of one of the three observatories. So, in the Tables 8.3 & 8.4 each polar branch of a cycle has been listed against one among KoSO, Meudon and KSO. The reason behind the high error-bars at higher latitudes while doing the 2nd degree polynomial fit is that the higher order coefficient is sensitive and the rate error is a nonlinear function of latitude. The separator latitudes while doing piece-wise linear fits gave an indication that rate change occurs near about 70° latitude. The smaller error-bars also confirms that indeed drift rates keep on increasing close to poles.

The smaller correlations between rate and the epoch delay as compared to that in Petrovay et al. [2017] has been caused by the small number of data points as north and south were treated separately. The smaller number of data points also reduced the statistical significance of correlation. These have been demonstrated by Figure 8.11 where north and south have been treated together similar to the one in Petrovay et al. [2017]. Because of this combined treatment, the region of 95% posterior probability

(Figure 8.11) shrunk as compared those in the Figure 8.10a, b. In addition to this, HPZ rates derived with piecewise linear fits has slightly higher uncertainties for cycle 16, 19, and 20 in south compared to others. This resulted in higher uncertainty interval depicted by 95% posterior probability in south as compared to north. However, the Bayesian analysis still supported the fact that the data points come from a population with positive correlation (Table 8.5) . As suggested by Petrovay et al. [2017], this relation could be used in conjunction with Waldmier effect [Waldmeier 1935, Petrovay et al. 2017] and "minmax3" rule [Cameron & Schüssler 2007] to predict epoch and amplitude of subsequent cycle maxima. Differences in poleward migration rates between north and south may have some implications in the double peak behaviour of solar cycles.

Also, integrated sunspot area from minima to first polar reversal proves to be a better candidate to define sunspot cycle strength when correlated with poleward drift rate. This has been depicted by more consistent statically significant point estimates of Pearson correlation and also the posterior probabilities (Table 8.5) of correlation derived from Bayesian analysis for both north and south.

Polar rush has important implication to meridional flow [Wang et al. 2002] and turbulent diffusion [Petrovay et al. 2017]. The computed polar migration rates as presented in this article, from the century-long prominence data may effectively constrain such parameters. For example, meridional flow for a solar cycle in the simulation by Wang et al. [2002] has been scaled according to the solar activity of the same cycle i.e. higher the activity more is the meridional flow rate. We indeed find some correlation of poleward migration rate and cycle strength. This may further imply that there is a correlation between rate of polar rush and meridional circulation.

Also as reported in Muñoz-Jaramillo et al. [2012], such study about proxy of polar field evolution is important as sunspot area combined with polar field evolution gives a complete picture of the long-term variation of solar hemispheric magnetic field. It has been shown before that polar faculae is a good proxy for polar magnetic field with 11 years average periodicity and also that the faculae count become maximum during solar minima [Sheeley 2008]. So, the long-term data of prominences as presented here combined with historical polar faculae data can prove to be important in predicting epoch and strength of future cycles.

8.6 Conclusions

In this work, we first presented the calibration and processing of raw disc blocked Ca II K dataset (1906 – 2002) from the Kodaikanal Solar Observatory. To improve the statistics of prominences we included the full disc H_α data from Meudon and Kanzelhohe observatory till April, 2018 starting from 1980. Salient points of this work are listed below.

- Disc centered, rotation corrected images and subsequent polar maps of same size with constant disc radius were produced for the entire available dataset. Using the same algorithm prominence locations were detected in all three datasets. To the best of our knowledge this is probably the first detailed result presented for century-long prominence observation for about 8 cycles from Kodaikanal and 3 cycles from Meudon and Kanzelhohe.

- Time-latitude distribution of detected prominences has been produced depicting a clear signature of polar rush for 10 cycles starting from 1906 till April, 2018 with initial ones mimicking those presented in Ananthakrishnan [1952] from same dataset. Cycle 20 was seen to have two northern polar branches with the second one being fainter and having higher migration rate. This is consistent with previous studies [Waldmeier 1973, Minarovjech et al. 1998a].

- Drift rates of polar prominences with latitude greater than 50° has been calculated with error bars through two different fitting functions namely 2nd degree polynomial and piece-wise linear (Tables 8.3, 8.4). Piece-wise linear function has seen to give much small error bar on rates for latitudes close to pole as compared to 2nd degree polynomial fit. Drift rates were found to be varying over time. This implies that the latitudes of polar prominences change non-linearly with time. These drift rates can provide essential inputs to constrain poleward flow rate in different dynamo model and thus might prove to be valuable for cycle prediction.

- Through piece-wise linear fit we found cycle to cycle variation of rates outside error bars for both the lower (LPZ) and higher (HPZ) latitude zones greater than 55° latitude. Also, on an average HPZ was seen to have more drift rate than

LPZ. In LPZ, cycle 19 dominated others for both north and south. In HPZ only northern hemisphere was seen to be dominated by cycle 19.

- Using the polar rush extracted from our prominence data, linear correlations between rate of polar-rush and delay between epochs of polar branch reaching pole and subsequent cycle sunspot area maxima were examined as depicted by Petrovay et al. [2017] using coronal green line data. Apparently, the point-estimates of Pearson correlations, when considered separately for north and south, were found to be statistically insignificant unlike in Petrovay et al. [2017]. However, posterior probability distribution of correlation coefficients generated from Bayesian analysis gave a hint that high chance ($\geq$ 83%) that the data points are derived from a population modelled by bivariate normal distribution with positive correlation. The combined treatment of north and south provided a good agreement with the result presented in Petrovay et al. [2017].

- The correlation of HPZ migration rate and sunspot cycle strength was calculated. When cycle amplitude was used as a measure of cycle strength, statistically significant point-estimate of correlation was found only for northern hemisphere and almost no correlation in south. When sunspot area, integrated between cycle minima and epoch of first polar branch reaching pole, was used as cycle strength measure correlations close to 0.6 were found for both north and south. This confirmed the findings presented in Makarov et al. [2001b]. Bayesian approach again depicted a high chance ($\approx$ 81%) of positive correlation with a median of 0.3 even for southern hemisphere "migration rate-cycle amplitude" pair.

- For all the variable-pairs Bayesian analysis, integrating the poleward migration rate uncertainties, provided uncertainty ranges of linear relations in terms of 95% posterior probability. All the median relations were found to have positive slope.

As future works, we would like to combine KoSO H_α data series with this long-term off-limb Ca II K dataset to associate filament morphologies and prominences eruptions. Coronal green line (5303Å) data [Sykora 1985, Minarovjech et al. 1998b, 2007, Petrovay et al. 2017] and space based datasets will be useful sources to add to KoSO prominence dataset for bringing continuity.

Chapter 9

Summary and Future scope

9.1 Summary

Work presented in this thesis blends together the optical design, related modelling of an upcoming space based solar telescope SUIT and analyses of long-term datasets with detection of features to be seen by SUIT. Kodaikanal Solar Observatory (KoSO) digitised spetroheliograms have been the test bed for the long-term study. Experience gained from these datasets will be worth in handling the data to be recorded by SUIT complemented by knowledge on SUIT image quality. The following points summarise the highlights of the work presented in different chapters of this thesis.

1. Optical design of SUIT has been optimised using design requirements and constraints such as resolution, focal length and dimension. Through optimisation an off-axis Ritchey Cretien design with a field corrector lens was derived.

2. Ghost image analysis was performed under non-sequential setting to check spurious pattern on the image plane generated from CCD back reflection and optical surface inter-reflection. Filter tilts and CCD coating thickness were optimised by minimising ghost flux.

3. Using MTF at 42 cycles/mm and 80% encircled energy diameter as image quality criteria, facbrication and alignment tolerances for SUIT optics were derived. An analysis was performed to find thermal tolerance assuming different temperature profiles through telescope tube. For this analysis, agin MTF at 42 cycles/mm was

used as image quality criteria and field corrector lens as compensator to relax the tolerance.

4. The imaging being in NUV, scattering is crucial. Optical surface micro-roughness and particulate contamination were considered as scattering contributors. Model parameters of Bi-directional Scattering Distribution Function (BSDF) were estimated from fit to experimental data. Simulation was performed to estimate the scatter to specular flux ratio and PSF wing broadening. Requirements on surface polish, clean-room environment for assembly were put forward to minimise the scatter. To restrict scatter from entrance windows from reaching optical apertures through first order specular reflection, primary and secondary baffles with internal vanes were designed for SUIT through analytical calculations. Effect of VELC payload package scatter and reflection on SUIT was analyzed.

5. As a part of CCD calibration, a plan for generating model flat-field was presented through LED sources placed before science filters. LED locations were optimised to meet the requirement of model flat uniformity and CCD coverage.

6. A plan for component-wise and integrated alignment for SUIT optics was devised. The plan incorporates theodolite, Zygo interferometer, alignment cubes and nodal aberration theory to find alignment errors through Zernike coefficients.

7. Plages were detected from KoSO century-long Ca II K digitised data. The automated detection was validated through correlation with 'plage index'. Generated plage area cycle was found to have high correlation with available MWO series. Carrington maps were generated for the entire series and correlated with SoHO/MDI maps of overlapping times confirming location correspondence between plages and magnetic concentrations.

8. Supergranules were detected from the KoSO Ca II K series using 'watershed method'. Morphological parameters such supergranule scale, circularity and fractal dimension were extracted. Temporal evolution of those parameters near active regions and in Quiet Sun were studied, producing contrasting correlations

with sunspot cycle. This could be a possible indication of different natures of global and local solar dynamo.

9. KoSO digitised H_α data (1914-2007) was calibrated and Carrington maps were generated. A semi-automatic technique was developed for filament detection from those Carrington maps. Latitudinal distribution of filament tilts were constructed, which can be compared with Joy's law of sunspot tilts. Using the time-latitude distribution of detected filaments, role of polar filaments in polar field reversal was demonstrated.

10. Prominences were detected for 10 solar cycles (from cycle 15) using a fully automated method from a combined series with a major share from KoSO Ca II K disc-blocked images (1906-2002). The identified location maps clearly depicted non-linear trends of prominence poleward migration for all the cycles. Piece-wise linear fits were applied to polar branches, which was found to be more efficient as compared to nonlinear fits in probing the change of migration rates. Bayesian analysis was done to understand the role which poleward migration can play in solar cycle prediction. The derived migration rates can also be important in constraining the meridional flow rate, an important parameter for solar dynamo simulation.

9.2 Limitation

The limitations of this study are listed below:

1. The coating properties of ghost image analysis were derived from limited number of parameters provided by the manufacturer such as transmission profile at normal incidence and, effective refractive index. However, a more detailed information on coating thickness and arrangement will provide more reliable results on ghost flux.

2. Baffle designs were made using two dimensional geometry. Though this suffices for primary baffle because of rotational symmetry, it is a crude assumption for

secondary baffle. Thus, a three dimensional ray tracing simulation should be performed in ASAP to optimise the vane positions for secondary baffle using the calculated vane positions as initial guesses. The optimisation should minimise first order reflections at baffle inner walls from all directions reaching optical apertures.

3. The Ca II K and H_α series are not yet ready for irradiance study. All the analyses were carried out on density images.

4. Current filament detection code is semi-automated and uses Carrington maps. However, fully automated technique applicable on full disc image is desirable as it will generate a better statistics of filaments.

9.3 Future scope

SUIT ghost flux and scatter to specular ratio being higher than requirement, post-processing schemes can be developed for improving the image quality. Mathematical model can be developed for SUIT to remove ghost patterns [Shestov, S. V. et al. 2019]. Also, in the case of SUIT as the scatter is narrow-angle, a PSF deconvolution [Seibert & Boone 1988] strategy can be developed to reduce the scatter and enhance the image contrast.

As KoSO data suffers from low density in later cycle, cross calibration with other available chromospheric datasets will enhance the statistics of detected features [Rybák et al. 2011]. Machine learning algorithms can be applied for automated filament detection using KoSO filaments detected from semi-automated method as training set. Further, small scale features such a brightening in chromospheric networks can be detected and it can be explored what connections their time-latitude distribution has with sunspot butterfly. SUIT data pipeline will also be benefited through implementation of such algorithms developed to detect similar features automatically.

Chapter 10

Appendix

10.1 UT-IST Correction

the Ca II K images in KoSO have been recorded by an instrument which causes image rotation as a function of time of a day on top of p-angle variation over a year (can be found using ephemerides). So, fitting p-angle from the pole marking to a function of time (IST), day of a year and comparing the same with measured p-angle, I could find correct time (Figure 10.1). If the time is in UT the p-angle will deviated from the fitted surface by a values of about 82.5 degrees.

$$p(day, time) = 26.3 \sin(2\pi \frac{day}{365.25} - 0.184) + 15(time - 5.833)$$

10.2 Alignment of Full-disc Image with Carrington Maps

The Ca II K images in KoSO have pole marking to mark north and south pole of rotation axis. However, sometimes those marking are consistent. Thus, a method is proposed here to alignment the full disc Ca II K images using Carrington maps as reference. It works as follows:

1. A Carrington rotation is selected which covers the date of the image to be aligned.

2. From the Carrington map a longitude band is selected centered at a Carrington longitude corresponding to the date of the image.

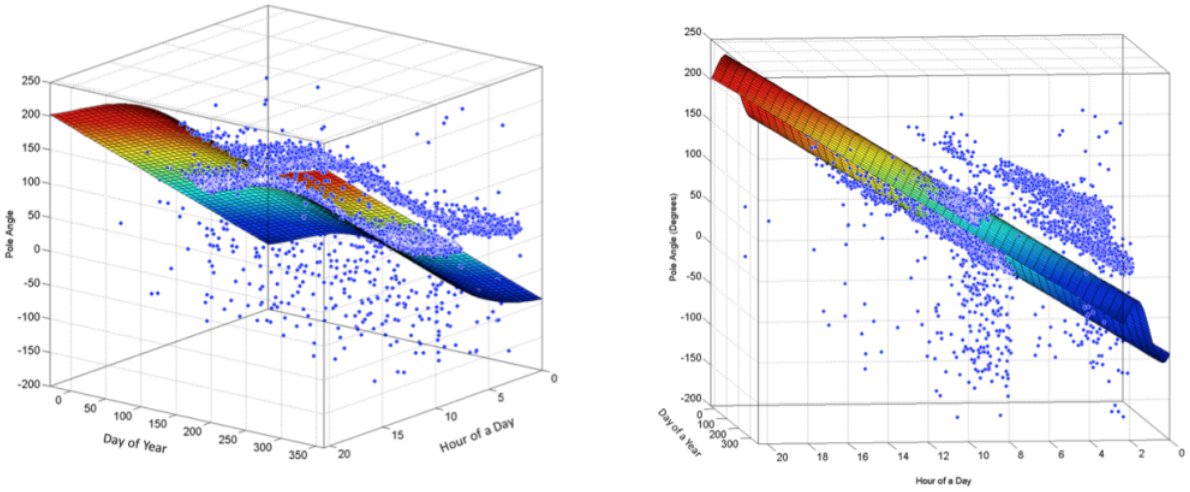

Figure 10.1: Pole-angle of KoSO Ca II K spectroheliograms as a function of day and time. Two panels show two different projections of same 3-dimensional plot. The 'o' symbols depict the p-angles corresponding to the north-south pole markings in raw images. The rainbow coloured surface is the fitted empirical function to differentiate UT time stamps from IST time stamps. *Left panel* especially shows the overlap of values of UT and IST time stamp values which can only be decoupled including another dimension i.e. p-angle.

3. If the image towards the beginning or end of a Carrington rotation, previous or next rotation is concatenated respectively to allow entire longitude range. In case of unavailability of previous or subsequent maps the bands are shrunk depending on their location in the grid.

4. The full-disc centered image is transformed to a rectangular grid of heliographic latitude and longitude. Subsequently, the heliographic map of the full-disc image is also limited in longitude coverage to match the size of the Carrington map band.

5. Heliographic map of the image and Carrington band are spatially correlated.

6. The image is rotated in 1° step-size. If the angle of rotation is less than 360°, steps 4-6 are repeated. Otherwise, the method goes to last step 7.

7. The angle corresponding to the maximum correlation gives the value of image rotation required to align the N-S of the full disc image.

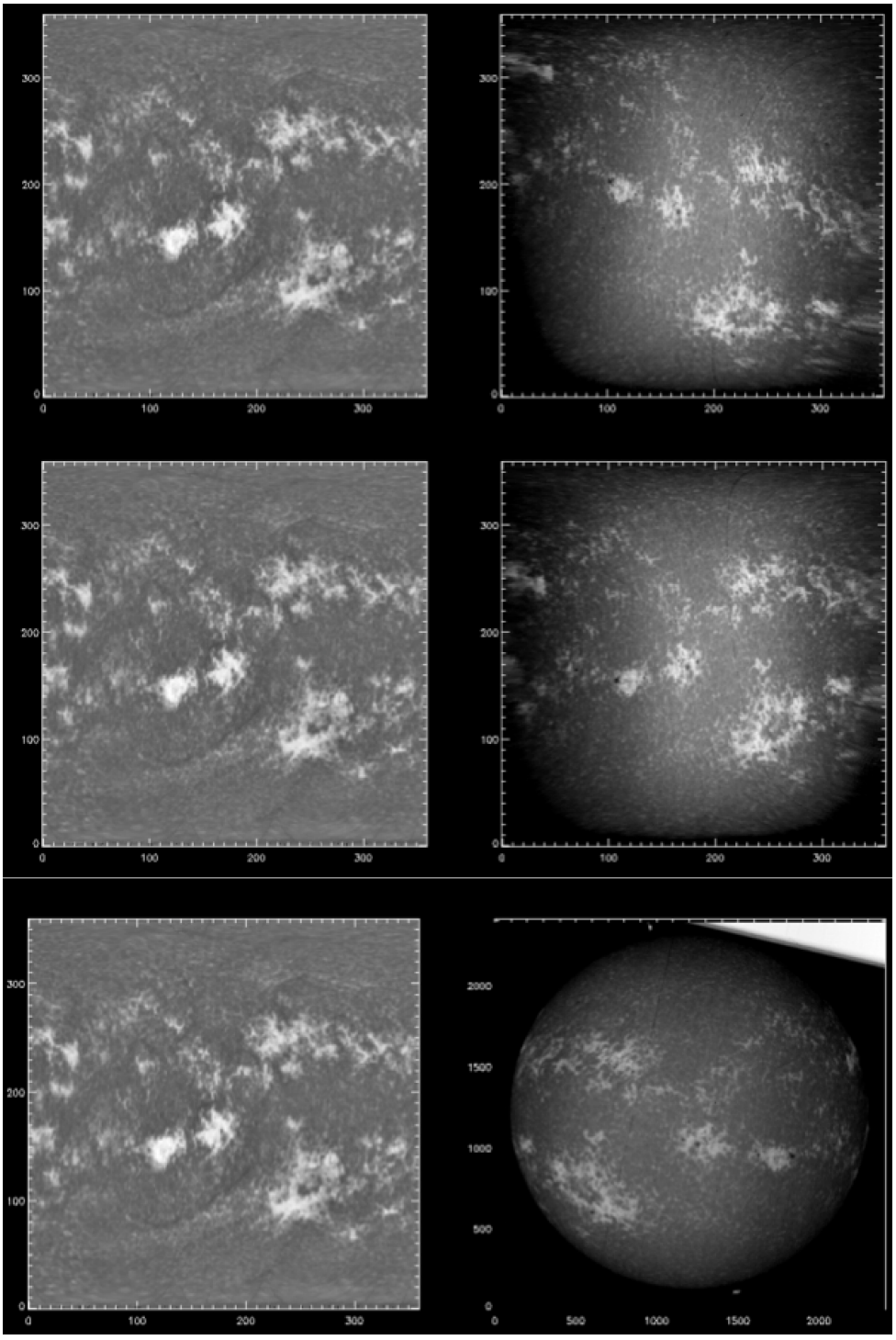

Figure 10.2: Steps of correlation with Carrington maps to align full-disc images. *Left panels* show bands of Carrington longitudes corresponding to full disc image. Top two images of *right panels* show heliographic projection of sea full disc image at two rotations. Bottom image of *right panel* shows the aligned full disc image.

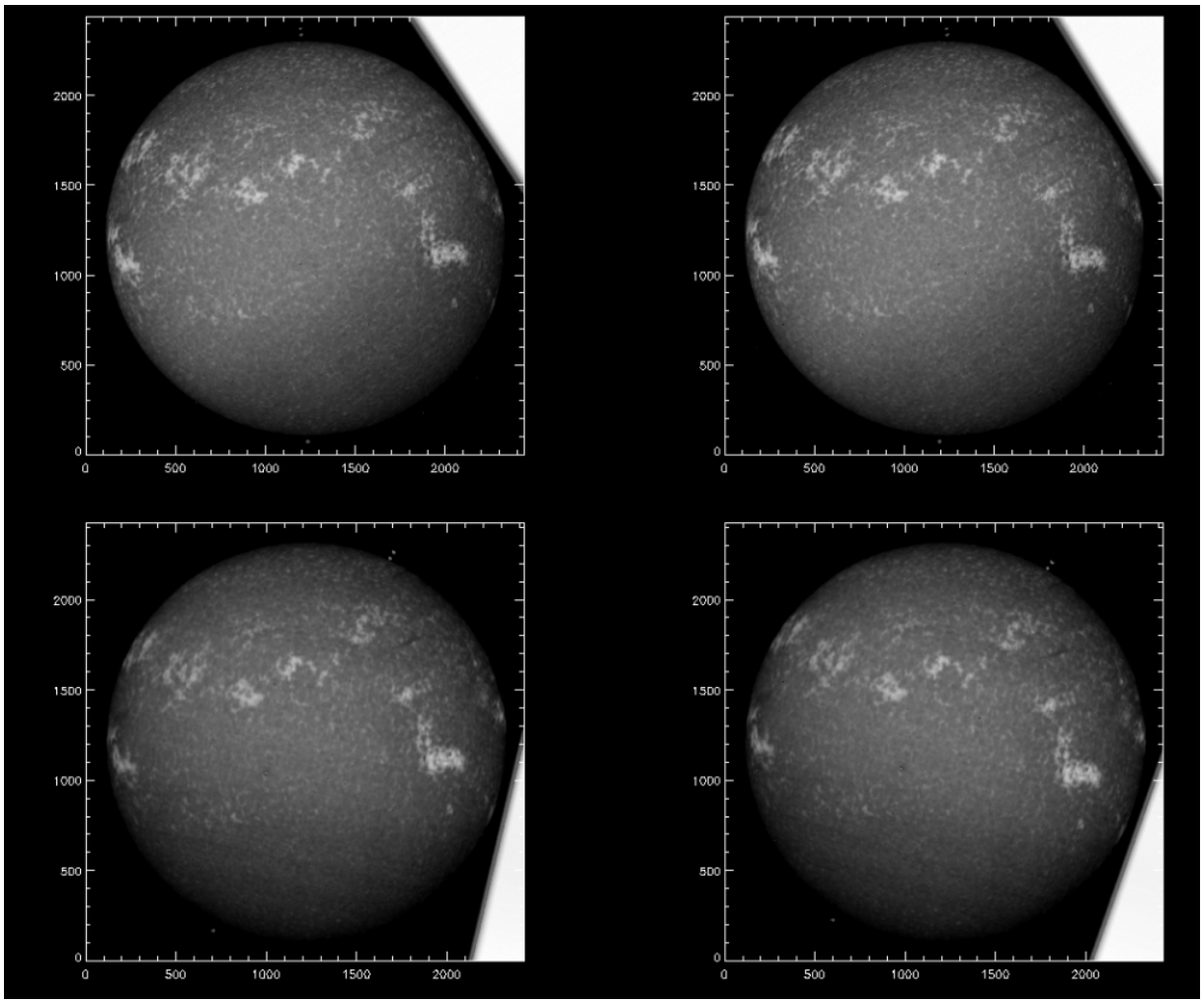

Figure 10.3: KoSO Ca II K full disc images captured on March 16, 1960 at two different times aligned using empirical p-angle formula (*right panel*) and Carrington map correlation (*left panel*).

The processing of alignment described above is depicted in Figure 10.2. This is to be noted that this method works even with reference Carrington maps where few image over entire rotation are imperfectly aligned. This is because of the fact that Carrington maps are generated only by sampling a heliographic longitude of band of [-30°, 30°] for each full disc image.

Figure 10.3 shows that alignment of images based on date, time (section 10.1) and correlation with Reference Carrington maps are more consistent than with pole markings.

Bibliography

Abetti, G. 1957, The sun.

Ananthakrishnan, R. 1952, *Nature*, 170, 156

Ananthakrishnan, R. 1954, Proceedings of the Indian Academy of Sciences - Section A, 40, 72

Babcock, H. W. 1961, *Astrophys. J.*, 133, 572

Bagalá, L. G., Bauer, O. H., Fernández Borda, R., Francile, C., Haerendel, G., Rieger, R., & Rovira, M. G. 1999, in ESA Special Publication, Vol. 448, Magnetic Fields and Solar Processes, ed. A. Wilson & et al., 469

Barata, T., Carvalho, S., Dorotovič, I., Pinheiro, F. J. G., Garcia, A., Fernandes, J., & Lourenço, A. M. 2018, Astronomy and Computing, 24, 70

Berghmans, D., et al. 2006, Advances in Space Research, 38, 1807 , magnetospheric dynamics and the international living with a star program

Berrilli, F., Ermolli, I., Florio, A., & Pietropaolo, E. 1999, *Astron. Astrophys.*, 344, 965

Bertello, L., Ulrich, R. K., & Boyden, J. E. 2010, *Solar Phys.*, 264, 31

Bogart, R. S., Hoeksema, J. T., & Scherrer, P. H. 1992, in Bulletin of the American Astronomical Society, Vol. 24, American Astronomical Society Meeting Abstracts #180, 814

Bonnin, X., Aboudarham, J., Fuller, N., Csillaghy, A., & Bentley, R. 2013, *Solar Phys.*, 283, 49

Born, M., et al. 1999, Principles of Optics: Electromagnetic Theory of Propagation, Interference and Diffraction of Light, 7th edn. (Cambridge University Press)

Bumba, V., Rusin, V., & Rybansky, M. 1990, *Solar Phys.*, 128, 253

Cameron, R., & Schüssler, M. 2007, *Astrophys. J.*, 659, 801

Carroll, R. J., Roeder, K., & Wasserman, L. 1999, Biometrics, 55, 44

Chae, J. 2004, *Solar Phys.*, 221, 1

Chapman, G. A., Cookson, A. M., & Dobias, J. J. 1997, *Astrophys. J.*, 482, 541

Charbonneau, P. 2010, Living Reviews in Solar Physics, 7

Chatterjee, S., Banerjee, D., & Ravindra, B. 2016, *Astrophys. J.*, 827, 87

Chatterjee, S., Hegde, M., Banerjee, D., & Ravindra, B. 2017, *Astrophys. J.*, 849, 44

Chatterjee, S., Mandal, S., & Banerjee, D. 2017, *Astrophys. J.*, 841, 70

Chatzistergos, T. 2017, PhD thesis, Max Planck Institute for Solar System Research, Göttingen, Germany <EMAIL>chatzistergos@mps.mpg.de</EMAIL>

Chatzistergos, T., Ermolli, I., Solanki, S. K., & Krivova, N. A. 2018, *Astron. Astrophys.*, 609, A92

Chen, P. F., Innes, D. E., & Solanki, S. K. 2008, *Astron. Astrophys.*, 484, 487

Choudhuri, A. R., Chatterjee, P., & Jiang, J. 2007, Physical Review Letters, 98, 131103

Choudhuri, A. R., Schussler, M., & Dikpati, M. 1995, *Astron. Astrophys.*, 303, L29

Church, E. L., & Takacs, P. Z. 1990, in , Vol. 1165, Scatter from Optical Components, ed. J. C. Stover, 31–41

Church, E. L., & Takacs, P. Z. 1995, in , Vol. 2541, Optical Scattering in the Optics, Semiconductor, and Computer Disk Industries, ed. J. C. Stover, 91–107

Church, E. L., Takacs, P. Z., & Leonard, T. A. 1990, in , Vol. 1165, Scatter from Optical Components, ed. J. C. Stover, 136–150

Colak, T., & Qahwaji, R. 2009, Space Weather, 7, n/a, s06001

Crouch, A. D., Charbonneau, P., & Thibault, K. 2007, *Astrophys. J.*, 662, 715

D'Azambuja, L., & D'Azambuja, M. 1948, Ann. Obs. Meudon. 6

Delaboudinière, J. P., et al. 1995, Solar Physics, 162, 291

Demarcq, J., Olivieri, G., Fruteau de Laclos, M., Marteaud, M., Nicolas, M., & Roussel, R. 1985, L'Astronomie, 99, 557

Dikpati, M., & Gilman, P. A. 2006, *Astrophys. J.*, 649, 498

—. 2007, *Solar Phys.*, 241, 1

Dittman, M. G. 2006, in , Vol. 6291, Society of Photo-Optical Instrumentation Engineers (SPIE) Conference Series, 62910R

Ermolli, I., Fofi, M., Bernacchia, C., Berrilli, F., Caccin, B., Egidi, A., & Florio, A. 1998, The Prototype RISE-PSPT Instrument Operating in Rome, ed. J. M. Pap, C. Fröhlich, & R. K. Ulrich (Dordrecht: Springer Netherlands), 1–10

Ermolli, I., Solanki, S. K., Tlatov, A. G., Krivova, N. A., Ulrich, R. K., & Singh, J. 2009, *Astrophys. J.*, 698, 1000

Ermolli, I., et al. 2013, Atmospheric Chemistry & Physics, 13, 3945

Evershed, J. 1907, *Mon. Not. Roy. Astron. Soc.*, 67, 477

—. 1908, *Mon. Not. Roy. Astron. Soc.*, 68, 515

—. 1917, Kodaikanal Observatory Bulletins, 3, 209

Evershed, J., & Evershed, M. 1917, Mem. Kod. Observ., 1, 55

Feigelson, E., & Babu, G. 2012, Modern Statistical Methods for Astronomy: With R Applications (Cambridge University Press)

Filip, J., Vávra, R., & Maile, F. J. 2017, in Proceedings of the 33rd Spring Conference on Computer Graphics, SCCG '17 (New York, NY, USA: ACM), 13:1–13:9

Filippov, B., & Koutchmy, S. 2008, Annales Geophysicae, 26, 3025

Fleck, B., et al. 2012, in American Astronomical Society Meeting Abstracts, Vol. 220, American Astronomical Society Meeting Abstracts #220, 207.01

Foukal, P. 1998, *Geophys. Res. Lett.*, 25, 2909

Foukal, P., Bertello, L., Livingston, W. C., Pevtsov, A. A., Singh, J., Tlatov, A. G., & Ulrich, R. K. 2009, Solar Physics, 255, 229

Foukal, P., & Lean, J. 1988, *Astrophys. J.*, 328, 347

Freniere, E. R. 1981, in , Vol. 257, Radiation scattering in optical systems, ed. G. H. Hunt, 19–28

Gandorfer, A., et al. 2011, Solar Physics, 268, 35

Garcia, A., Sobotka, M., Klvaňa, M., & Bumba, V. 2011, Contributions of the Astronomical Observatory Skalnate Pleso, 41, 69

Gelman, A., Carlin, J., Stern, H., Dunson, D., Vehtari, A., & Rubin, D. 2013, Bayesian Data Analysis, Third Edition, Chapman & Hall/CRC Texts in Statistical Science (Taylor & Francis)

Ghosh, A., et al. 2016, The Solar Ultraviolet Imaging Telescope onboard Aditya-L1

Gibson, S. E. 2018, Living Reviews in Solar Physics, 15, 7

Gilbert, H. R., Holzer, T. E., Burkepile, J. T., & Hundhausen, A. J. 2000, *Astrophys. J.*, 537, 503

Gilbert, H. R., Holzer, T. E., Burkepile, J. T., & Hundhausen, A. J. 2000, *Astrophys. J.*, 537, 503

Gopalswamy, N., Hanaoka, Y., & Hudson, H. S. 2000, Advances in Space Research, 25, 1851

Gopalswamy, N., Shimojo, M., Lu, W., Yashiro, S., Shibasaki, K., & Howard, R. A. 2003,

Astrophys. J., 586, 562

Gray, L. J., et al. 2010, Reviews of Geophysics, 48, RG4001

Hagenaar, H. J., Schrijver, C. J., & Title, A. M. 1997, *Astrophys. J.*, 481, 988

Hale, G. E. 1893, Memorie della Societa Degli Spettroscopisti Italiani, 21, 68

Hanaoka, Y. 2013, in Journal of Physics Conference Series, Vol. 440, Journal of Physics Conference Series, 012041

Hao, Q., Fang, C., Cao, W., & Chen, P. F. 2015, *Astrophys. J. Suppl.*, 221, 33

Harvey, J., & Munoz-Jaramillo, A. 2015, in AAS/AGU Triennial Earth-Sun Summit, Vol. 1, AAS/AGU Triennial Earth-Sun Summit, 111.02

Harvey, J., & Worden, J. 1998, in Astronomical Society of the Pacific Conference Series, Vol. 140, Synoptic Solar Physics, ed. K. S. Balasubramaniam, J. Harvey, & D. Rabin, 155

Harvey, J. E., Goshy, J. J., & Pfisterer, R. N. 2014, in , Vol. 9205, Reflection, Scattering, and Diffraction from Surfaces IV, 92050I

Harvey, J. E., Schröder, S., Choi, N., & Duparré, A. 2012, Optical Engineering, 51, 013402

Hastie, T., & Tibshirani, R. 1990, Generalized Additive Models, Chapman & Hall/CRC Monographs on Statistics & Applied Probability (Taylor & Francis)

Hathaway, D. H. 2015, Living Reviews in Solar Physics, 12, 4

Henney, C. J., & Harvey, J. W. 2001, AGU Spring Meeting Abstracts, SP51B

Hoeksema, J. T., Bush, R. I., Scherrer, P. H., Heck, C., Hurlburt, N., Shine, R., Tarbell, T., & Title, A. 1997, in Bulletin of the American Astronomical Society, Vol. 29, AAS/Solar Physics Division Meeting #28, 884

Hudson, H. 2010, Observations of solar and stellar eruptions, flares, and jets, ed. C. J. Schrijver & G. L. Siscoe (Cambridge University Press), 123

Ipson, S. S., Zharkova, V. V., Zharkov, S., Benkhalil, A. K., Aboudarham, J., & Fuller, N. 2005, *Solar Phys.*, 228, 399

Jamieson, T. H. 1981, Optical Engineering, 20, 202156

Jean-Pierre Wuelser, James R. Lemen, T. D. T. C. J. W. J. C. C. B. A. C. D. W. D. G. S. G. S. B. M. A. S. M. R. L. N. J. D. P. G. R. R. L. A. S. R. A. H. J. D. M. J. S. N. J.-P. D. G. E. A. F. A. M. B. P. B. F. B. J.-Y. C. G. C. F. D. A. J. M. L. R. M. M. M. M.-F. R. X. S. V. B. W. D. 2004, EUVI: the STEREO-SECCHI extreme ultraviolet imager

Jin, C., & Wang, J. 2015, *Astrophys. J.*, 806, 174

Joshi, N. C., Bankoti, N. S., Pande, S., Pande, B., & Pandey, K. 2009, *Solar Phys.*, 260, 451

Karttunen, H. 1996, Fundamental astronomy (Springer)

Kelly, B. C. 2007, *Astrophys. J.*, 665, 1489

Kelt, A., Harris, A., Jorden, P., & Tulloch, S. 2006, in Scientific detectors for astronomy 2005, ed. J. E. Beletic, J. W. Beletic, & P. Amico (Dordrecht: Springer Netherlands), 369–374

Kiepenheuer, K. 2012, Structure and Development of Solar Active Regions, International Astronomical Union Symposia (Springer Netherlands)

King, W. B. 1969, J. Opt. Soc. Am., 59, 1155

Kitai, R., et al. 2013, Data Science Journal, 12, WDS213

Kopp, G. 2016, Journal of Space Weather and Space Climate, 6, A30

Lee, M. D., & Wagenmakers, E.-J. 2014, Bayesian Cognitive Modeling: A Practical Course (Cambridge University Press)

Leighton, R. B. 1964, *Astrophys. J.*, 140, 1547

Lemen, J. R., et al. 2012, Solar Physics, 275, 17

Li, K. J. 2010, Monthly Notices of the Royal Astronomical Society, 405, 1040

Li, K. J., Li, Q. X., Gao, P. X., Mu, J., Chen, H. D., & Su, T. W. 2007, Journal of Astrophysics and Astronomy, 28, 147

Lin, G., Adiga, U., Olson, K., Guzowski, J. F., Barnes, C. A., & Roysam, B. 2003, Cytometry Part A, 56A, 23

Liu, K., Wang, Y., Shen, C., & Wang, S. 2012, *Astrophys. J.*, 744, 168

Livingston, W., & Harvey, J. 1971, in IAU Symposium, Vol. 43, Solar Magnetic Fields, ed. R. Howard, 51

Lockyer, W. J. S. 1908, *Nature*, 78, 174

—. 1922, *Mon. Not. Roy. Astron. Soc.*, 82, 323

—. 1931, *Mon. Not. Roy. Astron. Soc.*, 91, 797

Low, B. C. 1982, Reviews of Geophysics, 20, 145

Ma, H. 2013

Makarov, V. I., & Sivaraman, K. R. 1983, *Solar Phys.*, 85, 227

Makarov, V. I., Tlatov, A. G., Callebaut, D. K., Obridko, V. N., & Shelting, B. D. 2001a,

Solar Phys., 198, 409

Makarov, V. I., Tlatov, A. G., & Sivaraman, K. R. 2001b, *Solar Phys.*, 202, 11

—. 2003, *Solar Phys.*, 214, 41

Mandal, S., Hegde, M., Samanta, T., Hazra, G., Banerjee, D., & Ravindra, B. 2017, *Astron. Astrophys.*, 601, A106

Mandelbrot, B. 1982, The Fractal Geometry of Nature (Henry Holt and Company)

Marshall, J. L., & DePoy, D. L. 2013, Publications of the Astronomical Society of the Pacific, 125, 000

Martin, S. F. 1998, Solar Physics, 182, 107

Matzke, D., Ly, A., Selker, R., Weeda, W. D., Scheibehenne, B., Lee, M. D., & Wagenmakers, E.-J. 2017

McIntosh, P. S. 1972, Reviews of Geophysics and Space Physics, 10, 837

McIntosh, S. W., Leamon, R. J., Hock, R. A., Rast, M. P., & Ulrich, R. K. 2011, *Astrophys. J.*Letters, 730, L3

Meunier, N., Roudier, T., & Rieutord, M. 2008, *Astron. Astrophys.*, 488, 1109

Milby, E. 2009

Minarovjech, M., Rušin, V., & Saniga, M. 2007, *Solar Phys.*, 241, 263

—. 2011, Contributions of the Astronomical Observatory Skalnate Pleso, 41, 106

Minarovjech, M., Rybansky, M., & Rusin, V. 1998a, *Solar Phys.*, 177, 357

Minarovjech, M., Rybansky, M., & Rusin, V. 1998b, in Astronomical Society of the Pacific Conference Series, Vol. 150, IAU Colloq. 167: New Perspectives on Solar Prominences, ed. D. F. Webb, B. Schmieder, & D. M. Rust, 484

Mohler, O. C., & Dodson, H. W. 1968, *Solar Phys.*, 5, 417

Moss, W. 1946, Sol. Phys. Observ., 3, 119

Mouradian, Z., & Soru-Escaut, I. 1994, *Astron. Astrophys.*, 290, 279

Muñoz-Jaramillo, A., Sheeley, N. R., Zhang, J., & DeLuca, E. E. 2012, *Astrophys. J.*, 753, 146

Muenzer, H., Schroeter, E. H., Woehl, H., & Hanslmeier, A. 1989, *Astron. Astrophys.*, 213, 431

Muller, R., & Roudier, T. 1994, Solar Physics, 152, 131

Murdin, P., ed. 2000, Wilcox Solar Observatory

Naqvi, M. F., Marquette, W. H., Tritschler, A., & Denker, C. 2010, Astronomische Nachrichten, 331, 696

Nejad, S. M., Madineh, A. B., & Nasiri, M. 2013, Optik - International Journal for Light and Electron Optics, 124, 6480

Paniveni, U., Krishan, V., Singh, J., & Srikanth, R. 2010, Monthly Notices of the Royal Astronomical Society, 402, 424

Parenti, S. 2014, Living Reviews in Solar Physics, 11, 1

Petrovay, K., Nagy, M., GerjÃąk, T., & JuhÃąsz, L. 2017, Journal of Atmospheric and Solar-Terrestrial Physics,

Pevtsov, A. A., Virtanen, I., Mursula, K., Tlatov, A., & Bertello, L. 2016, *Astron. Astrophys.*, 585, A40

Plesseria, J.-Y., Mazy, E., Defise, J.-M., Rochus, P., Lemmens, E., & Vrancken, D. 2003, in , Vol. 5170, Techniques and Instrumentation for Detection of Exoplanets, ed. D. R. Coulter, 167–176

Pötzi, W., Temmer, M., Veronig, A., Hirtenfellner-Polanec, W., & Baumgartner, D. 2013, in EGU General Assembly Conference Abstracts, Vol. 15, EGU General Assembly Conference Abstracts, EGU2013–1459

Priest, E. 2014, A Description of the Sun (Cambridge University Press), 1–73

Priest, E. 2014, Magnetohydrodynamics of the Sun

Priyal, M., Banerjee, D., Karak, B. B., Muñoz-Jaramillo, A., Ravindra, B., Choudhuri, A. R., & Singh, J. 2014a, *Astrophys. J. Lett.*, 793, L4

Priyal, M., Singh, J., Ravindra, B., Priya, T. G., & Amareswari, K. 2014b, *Solar Phys.*, 289, 137

Rast, M. P. 2003, *Astrophys. J.*, 597, 1200

Rausaria, R. R., Gupta, S. S., Selvendran, R., Sundara Raman, K., & Singh, J. 1993a, *Solar Phys.*, 146, 259

Rausaria, R. R., Sundara Raman, K., Aleem, P. S. M., & Singh, J. 1993b, *Solar Phys.*, 146, 137

Ravindra, B., Priya, T. G., Amareswari, K., Priyal, M., Nazia, A. A., & Banerjee, D. 2013, *Astron. Astrophys.*, 550, A19

Reinsch, C. H. 1967, Numer. Math., 10, 177

Rieutord, M., & Rincon, F. 2010, Living Reviews in Solar Physics, 7, 2

Rimmer, M. P. 1978, A Tolerancing Procedure Based On Modulation Transfer Function (MTF)

Robert H. Barkhouser, R. G. O. 1999, Interferometric alignment and figure testing of large (0.5 m) off-axis parabolic mirrors in a challenging cleanroom environment

Rusin, V., Rybansky, M., Dermendjiev, V., & Stavrev, K. Y. 1994, Contributions of the Astronomical Observatory Skalnate Pleso Supplement, 24, 135

Rušin, V., Rybanský, M., Dermendjiev, V., & Stavrev, K. Y. 1988, Contributions of the Astronomical Observatory Skalnate Pleso, 17, 63

Ruzmaikin, A., Feynman, J., & Stoev, S. A. 2011, Journal of Geophysical Research (Space Physics), 116, A04220

Rybák, J., et al. 2011, Contributions of the Astronomical Observatory Skalnate Pleso, 41, 133

Scherrer, P., et al. 1997, in Bulletin of the American Astronomical Society, Vol. 29, AAS/Solar Physics Division Meeting #28, 894

Scherrer, P. H., & HMI Team. 2010, in Bulletin of the American Astronomical Society, Vol. 41, American Astronomical Society Meeting Abstracts #216, 873

Schlichenmaier, R., & Collados, M. 2002, A&A, 381, 668

Schrijver, C. J., Cote, J., Zwaan, C., & Saar, S. H. 1989, *Astrophys. J.*, 337, 964

Schrijver, C. J., Elmore, C., Kliem, B., Török, T., & Title, A. M. 2008, *Astrophys. J.*, 674, 586

Schwabe, H. 1844, Astronomische Nachrichten, 21, 233

Secchi, P. A. 1872, *Mon. Not. Roy. Astron. Soc.*, 32, 226

Seibert, J. A., & Boone, J. M. 1988, Medical Physics, 15, 567

Sheeley, Jr., N. R. 2008, *Astrophys. J.*, 680, 1553

Sheeley, Jr., N. R., Cooper, T. J., & Anderson, J. R. L. 2011, *Astrophys. J.*, 730, 51

Shestov, S. V., Zhukov, A. N., & Seaton, D. B. 2019, A&A, 622, A101

Shimojo, M. 2013, *Pub. Astron. Soc. Japan*, 65, S16

Simon, G. W., & Leighton, R. B. 1964, *Astrophys. J.*, 140, 1120

Singh, J., & Prabhu, T. 1985, Solar Physics, 97, 203

Skumanich, A., Smythe, C., & Frazier, E. N. 1975, *Astrophys. J.*, 200, 747

Solanki, S. K. 1999, in Astronomical Society of the Pacific Conference Series, Vol. 158, Solar and Stellar Activity: Similarities and Differences, ed. C. J. Butler & J. G. Doyle, 109

Solanki, S. K., & Fligge, M. 2002, Journal of Atmospheric and Solar-Terrestrial Physics, 64, 677

Solanki, S. K., Inhester, B., & Schüssler, M. 2006, Reports on Progress in Physics, 69, 563

Sonka, M., Hlavac, V., & Boyle, R. 2014, Image Processing, Analysis, and Machine Vision (Cengage Learning)

Spencer, G. H., & Murty, M. V. R. K. 1962, J. Opt. Soc. Am., 52, 672

Srikanth, R., Singh, J., & Raju, K. P. 2000, *Astrophys. J.*, 534, 1008

Stenflo, J. O. 2012, *Astron. Astrophys.*, 547, A93

Stix, M. 2004, The Sun: An Introduction, Astronomy and Astrophysics Library (Springer Berlin Heidelberg)

Stover, J. C., Schroeder, S., Staats, C., Lopushenko, V., & Church, E. 2016, in , Vol. 9961, Reflection, Scattering, and Diffraction from Surfaces V, 996102

Sundara Raman, K., Aleem, S. M., Singh, J., Selvendran, R., & Thiagarajan, R. 1994, *Solar Phys.*, 149, 119

Sundara Raman, K., Ramesh, K. B., & Selvendran, R. 2001, Bulletin of the Astronomical Society of India, 29, 77

Sýkora, J. 1970, *Solar Phys.*, 13, 292

Sykora, J. 1985, Bulletin of the Astronomical Institutes of Czechoslovakia, 36, 61

Tandberg-Hanssen, E. 1974, Geophysics and Astrophysics Monographs, 12

Tandberg-Hanssen, E. 1998, in Astronomical Society of the Pacific Conference Series, Vol. 150, IAU Colloq. 167: New Perspectives on Solar Prominences, ed. D. F. Webb, B. Schmieder, & D. M. Rust, 11

Tlatov, A. G., Kuzanyan, K. M., & Vasil'yeva, V. V. 2016a, in Astronomical Society of the Pacific Conference Series, Vol. 504, Coimbra Solar Physics Meeting: Ground-based Solar Observations in the Space Instrumentation Era, ed. I. Dorotovic, C. E. Fischer, & M. Temmer, 241

Tlatov, A. G., Kuzanyan, K. M., & Vasil'yeva, V. V. 2016b, *Solar Phys.*, 291, 1115

Tlatov, A. G., Pevtsov, A. A., & Singh, J. 2009, *Solar Phys.*, 255, 239

Tribble, A. C., Boyadjian, B., Davis, J., Haffner, J., & McCullough, E. 1996, in , Vol. 2864, Optical System Contamination V, and Stray Light and System Optimization, ed. A. P. M. Glassford, R. P. Breault, & S. M. Pompea, 4–15

Tripathi, D., et al. 2017, Current Science, 113

Verma, V. K. 2000, *Solar Phys.*, 194, 87

Vernazza, J. E., Avrett, E. H., & Loeser, R. 1981, *Astrophys. J. Suppl.*, 45, 635

Vincent, L., & Soille, P. 1991, IEEE Trans. Pattern Anal. Mach. Intell., 13, 583

Waldmeier, M. 1935, Astronomische Mitteilungen der Eidgenössischen Sternwarte Zurich, 14, 105

—. 1973, *Solar Phys.*, 28, 389

Wang, Y.-M., Lean, J., & Sheeley, Jr., N. R. 2002, *Astrophys. J. Lett.*, 577, L53

Xu, G.-G., Zheng, S., Lin, G.-H., & Wang, X.-F. 2016, *Astrophys. J.*, 827, 137

Xu, Y., Pötzi, W., Zhang, H., Huang, N., Jing, J., & Wang, H. 2018, *Astrophys. J. Lett.*, 862, L23

Zhang, Q. M., Chen, P. F., Xia, C., & Keppens, R. 2012, *Astron. Astrophys.*, 542, A52

Zhang, X., Zhang, D., Xu, S., & Ma, H. 2016, Opt. Express, 24, 26392

Zharkova, V., Ipson, S., Benkhalil, A., & Zharkov, S. 2005, Artificial Intelligence Review, 23, 209

Zharkova, V. V., & Schetinin, V. 2003, A Neural-Network Technique for Recognition of Filaments in Solar Images, ed. V. Palade, R. J. Howlett, & L. Jain (Berlin, Heidelberg: Springer Berlin Heidelberg), 148–154

Zirin, H. 1974, *Solar Phys.*, 38, 91